



SIMS 2011

**The 52nd International Conference of
Scandinavian Simulation Society**

**Västerås, Sweden
September 29-30, 2011**

ISBN: 978-91-977493-7-4



PROGRAM

52nd Scandinavian Simulation and Modeling Society Conference

**Mälardalen University, Västerås
September 29-30, 2011**

2011-09-29

09:15-12:00 Mälardalen University, Room Beta

Welcome

09.15-09.25 Rector Karin Röding

Keynotes: *Chairman Key-note speaker: Erik Dahlquist*

09.25-10.15 Smart adaptive systems in nonlinear multivariable control and diagnostics

*Prof. Esko Juuso
Oulu University, Finland*

10.15- 11:05 Energy at Iceland from a modeling perspective

*Mr. Jonas Ketilsson
R&D manager, Iceland energy agency, Iceland*

11:05-11:10 Short break

Session *Hydropower*

Chairman session on Hydro power: Mika Liukkonen, East Finland University

11:10- 11:35 The effect of compressibility of water and elasticity of penstock walls on the behavior of high head hydro power stations

Behzad Rahimi Sharefi, Wenjing Zhou, Bjørn Glemmestad, Bernt Lie,

Telemark University college, Porsgrunn, Norway

11:35-12:00 Modelling and control of a high head hydropower plant

Wenjing Zhou, Behzad Rahimi Sharefi, Bernt Lie, Bjørn Glemmestad

Telemark University college, Porsgrunn, Norway

12:00-13:00 LUNCH (with SIMS board meeting) Room: Kåren

13:00-18:00 Mälardalen University, Room Kappa

Session Water

Chairman session on Water treatment: Esko Juuso, Oulu University, Finland

13:00-13:25 Modeling of aluminum in water treatment process

Jani Tomperi and Esko Juuso

University of Oulu, Marja, Finnsugar, Finland

13:25 - 13:50 Considering culture adaptations to high ammonia concentration in ADM1

Wenche Bergland, Deshai Botheju, Carlos Dinamarca, Rune Bakke

Telemark University college, Porsgrunn, Norway

13:50-14:15 Dynamic modelling approach for detecting turbidity in drinking water

Petri Juntunen, Mikka Liukkonen, Markku Lehtola, Yrjö Hilttonen
University of Eastern Finland, Kuopio, Finland

14:15-14:40 Simulation of digestate nitrification based on cow manure

Deshaij Botheju, Yanni Qin, Knut Vasdal, Rune Bakke

Telemark University college, Porsgrunn, Norway

14:40-15:05 Trend analysis in dynamic modeling of water treatment

Esko Juuso

University of Oulu, Ilkka Laakso, StoraEnso Fine paper, Oulu, Finland

15:05-15:35 Coffee break

- Session** **Energy conv**
*Chairman session on Energy conversion: Rune Bakke,
Telemark Univ College*
- 15:35-16:00 Modeling and control of gas lifted oil field with five oil wells

*Roshan Sharma and Bjørn Glemmestad
Telemark University College
Kjetil Fjalestad
Statoil, Porsgrunn, Norway*
- 16:00-16:25 Stability Analysis of AGC in the Norwegian Energy System

*Ingvar Andreassen and Dietmar Winkler
Telemark University College, Porsgrunn, Norway*
- 16:25-16:50 Comparison of Control Limit Generation Approaches in
Desulphurization Plant Monitoring

*Riku-Pekka Nikula and Esko Juuso, University of Oulu, Anton
Laari
Helsinki Energy, Porkkalankatu, Finland*
- 16:50-17:15 Towards multi fuel SOFC plants

*Masoud Rokni, Lasse Clausen and Christian Bang-Møller,
Technical University of Denmark, Lyngby, Denmark*
- 17:30 - 18:00 SIMS Annual general assembly
- 19:00 Dinner at Djäkneberget Restaurant

2011-09-30

08:30-11:55 Mälardalen University Room Milos

Keynotes: Chairman key notes: Erik Dahlquist

08:30-09:20 New trends in Automation

*Mr. Erik Oja
Senior Vice President, head of Process Automation Division,
ABB AB*

09:20-10:10 Process industry center in linköping: Use of modeling for automation and control

Prof. Alf Isaksson

Linköping University and ABB Corporate Research

10:10-10:40 Coffee break

Session *Diagnosis*

Mälardalen University Room Kappa

Chairman session on Diagnostics: Prof. Rebei bel Fdhila, ABB Corporate Research and MDU

10:40-11:05 On-line application of diagnostics and maintenance on demand using simulation models

Elena Tomas Aparicio, Björn Widarsson, Erik Dahlquist

Mälardalen Univ, Sweden

11:05-11:30 Modeling Software for Advanced Industrial Diagnostics

Mika Liukkonen, Mikko Heikkinen, Yrjö Hiltunen, Teri Hiltunen, FosterWheeler, Jari Kapanen, Andritz

Univ Eastern Finland

11:30-11:55 Water contents of wood and peat based fuels by analysing the domain NMR data

Ekaterina Nikolskaya and Risto A. Kauppinen

Univ of Bristol UK

Leonid Grunin Mari

State Technical University

Yoshkar-Ola, Russia, Mika Liukkonen and Yrjö Hiltunen,

Eastern Finland University, Finland

11:55-12:55 Lunch

12:55-16:10 Mälardalen University Room Kappa

Session *Energy systems*

Chairman session on Energy systems: Eva Thorin, MDU

12:55-13:20 Modeling, Simulation and Control for an Experimental Four Tanks System using ScicosLab

Carlos Pfeiffer

Telemark University College, Porsgrunn, Norway

13:20-13:45 Simulation of a Bubble Plume in a Water Vessel With and Without Internal Liquid Recirculation

Rebei Bel Fdhila

Mälardalen University and ABB Corporate Research, Sweden

13:45-14:10 Dynamic modelling of a pulp mill with a BLG plant - effects in the chemical recovery cycle

Christian Hoffstedt and Niklas Berglin,

Innventia, Stockholm, Sweden

14:10-14:45 Retention time and nutrient tracking inside a digester for biogas production

Johan Lindmark and Eva Thorin, Rebei Bel Fdhila

Mälardalen University, Västerås, Sweden

Session

Solar and others

Chairman session on applications and tools: Fredrik Wallin, MDU

14:45-15:10 Developing a computer program for the estimation of the incoming sun beam by defining a special coefficient factor for Denizli, Turkey

G. Uckan, H. K. Ozturk, E. Cetin

Pamukkale University, Denizli, Turkey

15:10-15:35 OMSketch — Graphical Sketching in the OpenModelica Interactive

Mohsen Torabzadeh-Tari, Jhansi Reddy Remala, Martin

Sjölund, Adrian Pop, Peter Fritzson

Linköping University, Linköping, Sweden

15:35-16:00 Etiology of Rey generator stator core failure and study of its rehabilitation integrity

Kourosh Mousavi Takami

Pasad Parang Co., Tehran, Iran

16:00-16:10 Closing remarks - Esko Juuso, Erik Dahlquist

PROCEEDINGS

#	Authors	Title
1	Erik Dahlquist, Elena Tomas Aparicio and Björn Widarsson	On-line application of diagnostics and maintenance on demand using simulation models
4	Johan Lindmark, Rebei Bel Fdhila and Eva Thorin	Retention time and nutrient tracking inside a digester for biogas production
5	Mika Liukkonen, Mikko Heikkinen, Teri Hiltunen, Jari Kapanen and Yrjö Hiltunen	Modeling Software for Advanced Industrial Diagnostics
6	Ekaterina Ekaterina Nikolskaya, Mika Liukkonen, Risto Kauppinen, Leonid Grunin and Yrjö Hiltunen	WATER CONTENTS OF WOOD AND PEAT BASED FUELS BY ANALYSING TIME DOMAIN NMR DATA
7	Roshan Sharma, Kjetil Fjalestad and Bjørn Glemmestad	Modeling and control of gas lifted oil field with five oil wells
8	Rebei Bel Fdhila	Simulation of a Bubble Plume in a Water Vessel With and Without Internal Liquid Recirculation
9	Riku-Pekka Nikula, Anton Laari and Esko Juuso	Comparison of Control Limit Generation Approaches in Desulphurization Plant Monitoring
10	Behzad Rahimi Sharefi, Wenjing Zhou, Bjørn Glemmestad and Bernt Lie	THE EFFECT OF COMPRESSIBILITY OF WATER AND ELASTICITY OF PENSTOCK WALLS ON THE BEHAVIOR OF A HIGH HEAD HYDROPOWER STATION
11	Carlos Pfeiffer	Modeling, Simulation and Control for an Experimental Four Tanks System using ScicosLab
12	Wenjing Zhou, Behzad Rahimi Sharefi, Bernt Lie and Bjørn Glemmestad	Modelling and control of a high head hydropower plant
13	Jani Tomperi	Predictive model for residual aluminum in a water treatment process
15	Ingvar Andreassen and Dietmar Winkler	Stability Analysis of AGC in the Norwegian Energy System
17	Wenche Bergland, Deshai Botheju, Carlos Dinamarca and Rune Bakke	Considering Culture Adaptations to High Ammonia Concentration in ADM1
18	Christian Hoffstedt	Dynamic modelling of a pulp mill with a BLG plant - effects in the chemical recovery cycle
19	Petri Juntunen, Mika Liukkonen, Markku J. Lehtola and Yrjö Hiltunen	DYNAMIC MODELLING APPROACH FOR DETECTING TURBIDITY IN DRINKING WATER
22	Gokhan Uckan, Engin Çetin and Harun Öztürk	DEVELOPING A COMPUTER PROGRAM FOR THE ESTIMATION OF THE INCOMING SUN BEAM BY DEFINING A SPECIAL COEFFICIENT FACTOR FOR DENİZLİ/TURKEY
24	Mohsen Torabzadeh-Tari, Jhansi Reddy Remala and Peter Fritzson	OMSketch — Graphical Sketching in the OpenModelica Interactive Book, OMNotebook
25	Deshai Botheju, Yanni Qin, Knut Vasdal and Rune Bakke	Simulation of digestate nitrification based on cow manure
27	Esko Juuso and Ilkka Laakso	Trend analysis in dynamic modeling of water treatment
28	Masoud Rokni, Lasse Clausen and Christian Bang-Møller	TOWARDS MULTI FUEL SOFC PLANTS (full paper)
29	Kourosh Mousavi Takami	Etiology of Rey generator stator core failure and study of its rehabilitation integrity

Paper 1

Title: On-line application of diagnostics and maintenance on demand using simulation models

Erik Dahlquist, Elena Tomas Aparicio, Björn Widarsson
Mlardalens Hgskola, Sweden

Keywords: Diagnostics, modelling, simulation, boiler, CFB, decision support, BN

The need for early fault detection and effective maintenance operations in the industry makes us think about developing tools that can handle the uncertainty of the processes and improve the maintenance scheduling. Among other decision support tools, Bayesian Networks (BN) is a method that can handle the uncertainty in industrial processes. If we add on-line physical models to this method, a significant tool for plant personal to detect and analyze possible process faults can be obtained.

The aim of this project was to develop and demonstrate an application for diagnosis and decision support that is implemented and running on-line. The application was implemented in a Circulating Fluidizing Bed (CFB) at Mälarenergi AB.

First a model in Modelica language was built and verified towards process data. The differences between measured and simulated values for different variables were given as an input into a Bayesian Network model where the probability for different faults within the process was determined.

The advantage of the application is that the combination of model based diagnostics and decision support can be used to schedule equipment and sensor maintenance. Moreover the application is used on-line which allows evaluation of the system under real circumstances.

Results from running the system shows that several different type of faults could be determined simultaneous. 16 different variables were followed and analysed in parallel.

On-line application of diagnostics and maintenance on demand using simulation models

Elena Tomas Aparicio and Erik Dahlquist, Mälardalen University, Vasteras, Sweden, Björn Widarsson, Fvb, Vasteras, Sweden

Abstract:

The need for early fault detection and effective maintenance operations in the industry makes us think about developing tools that can handle the uncertainty of the processes and improve the maintenance scheduling. Among other decision support tools, Bayesian Networks (BN) is a method that can handle the uncertainty in industrial processes. If we add on-line physical models to this method, a significant tool for plant personal to detect and analyze possible process faults can be obtained. The aim of this project was to develop and demonstrate an application for diagnosis and decision support that is implemented and running on-line. The application was implemented in a Circulating Fluidizing Bed (CFB) at Mälarenergi AB. First a model in Modelica language was built and verified towards process data. The differences between measured and simulated values for different variables were given as an input into a Bayesian Network model where the probability for different faults within the process was determined. The advantage of the application is that the combination of model based diagnostics and decision support can be used to schedule equipment and sensor maintenance. Moreover the application is used on-line which allows evaluation of the system under real circumstances. Results from running the system shows that several different types of faults could be determined simultaneous. 16 different variables were followed and analyzed in parallel.

Key words: Modeling, diagnostics, BN, modelica, power plant

Introduction

In industrial processes there is an increasing need for fault detection, decision support and risk assessment in order to prevent disturbances and performance problems. Moreover an effective maintenance work is an essential condition to make use of resources in an optimal way. Different features for optimization, control, diagnostics and decision support are being developed in order to have a better control of the process. Process diagnostics tools are able to identify the possibilities for improvements, describe the current situation of the process and indicate the areas where improvements and cost savings can be made [1], [2], [3]. Process diagnostics methods have been discussed also in a Värmeforsk (Thermal Engineering Research Association) project [4].

Heat and power processes have high demands on safe and efficient operation routines, therefore these processes are excellent candidates to study in this context. These processes are controlled and supervised through a big number of signals which means that the probability for error in the measured values is high. Simulation software is widely used in the industry i.e. to evaluate the configuration of the system before applying changes in reality. However, the simulation is not an error detection or optimization tool in itself. The combination of simulation models with statistical models results in a powerful on-line tool for different applications as diagnosis, optimization, Model Predictive Control (MPC) and decision support [5]. A Värmeforsk (Thermal Engineering Research Association) project describing Dynamic Data reconciliation was published in 2009 [6], other projects describing this methods can be found in [7] and [8].

A Bayesian Networks model describes a process that contains uncertainty. Different works using Bayesian Networks (BN) as decision support are described in [9] and [10]. Moreover two Värmeforsk projects are dealing with it [11], [4]. The step between the data processing and the decision support is treated in this project. A similar project can be seen in [12]. Other statistical models that are commonly used are ANN (Artificial Neural Networks) and this can be seen in [13].

There are many studies regarding diagnostics and on demand based maintenance, for example in [14], however, the combination of model based diagnostics and physical models and decision support regarding maintenance with Bayesian Networks has not been described before.

Model based diagnostics

Model based diagnostics is a method of isolating faults. Having a model that represents a system it is possible to simulate scenarios with data from the process and compare the results from the real process with the simulated results. This type of fault diagnosis provides information about possible errors. The advantage of model based type fault isolation is that it is based in the design of the system and not in probabilities. The combination of a model based diagnostics and probability based tools like Bayesian Networks can result in an excellent tool for fault isolation. Bayesian Networks are widely applied in aerospace and automotive industries [15]. Bayesian Networks are based on Bayes' probability law and can be applied in many fields; diagnosis, prediction, risk managements, warning, modelling and sensor measurement [17]. The networks represent the probabilistic relationship between several variables. From the Bayesian Networks model the probability of occurrence of some error can be detected and warn the process operators of an abnormal situations. Moreover from the analysis it is possible to predict the need for maintenance operations.

Simulation model

The simulation model developed is a dynamic physical model. Process data like fuel flow, fuel composition, air flow and similar are fed to the model as input. From these the model predicts the variable values in the boiler, the exhaust gas train and the steam system. The measured values for the same values are then compared to the calculated ones and the deviation is trended.

The implementation of the system has been at Boiler 5 at Mälarenergi. This is a Foster Wheeler CFB boiler located in Västerås, Sweden (see Figure 1). It is a biomass fuelled 157 MW_{th} boiler that produces 540°C/173 bar steam with intermediate superheat of 540°C/41 bar. Boiler 5 was commissioned in 2001 and connected in parallel with boiler 4 (coal-dust fired boiler). Boiler 5 operates at the same pressures and temperatures as boiler 4 as they share a turbine.

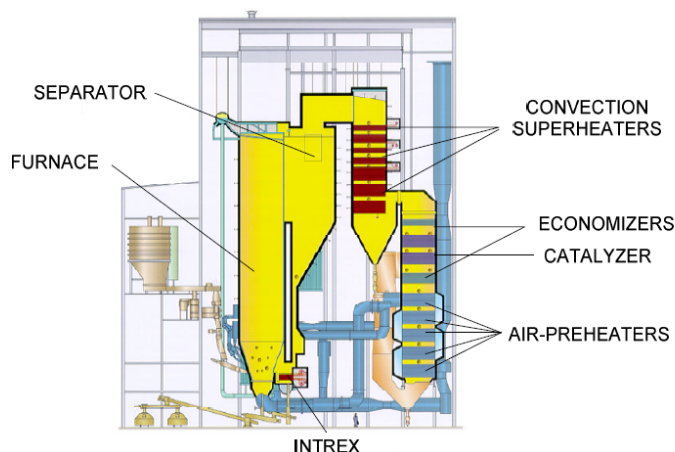


Figure1. Overview of Boiler

The fuel is a mixture of different biomass types: recycle wood, dry woodchips, trunk wood, saw-dust, bark, GROT (Branches, tops and roots), peat, Salix and ash from other furnaces. The fuel fed into the furnace is a result of different combinations of the mentioned biomass. A sample of each load is sent to the lab to obtain the elementary analysis and analysis of different contaminants. The fuel is fed through four feeding screws and the same numbers of screws are found in the bottom of the furnace to

remove the ashes. The ash is as well removed at the bottom of the integrated recycle heat exchanger (INTREX). Sand is continuously blown into the boiler in order to keep the bed material constants. The furnace contains two separators called cyclones where the flue gases are separated from the bed material (sand and ashes). The bed material ends up in the INTREX. The INTREX consists of two super-heaters: high pressure super-heater 3 (HPSH3) and intermediate pressure super-heater 2 (IPSH2). The super-heaters are places into two separate bubbling beds fluidized by high pressure air [12]. The steam temperature is as in the convection super heaters regulated by water injectors. When the boiler is operated at low loads there is not much bed material circulating through the cyclone and ending up in low solids circulation through the INTREX. In order to maintain the solids circulation trough the INTREX internal circulation from the furnace into the INTREX is used.

The convection part consists of three super-heaters, in order: high pressure super-heater 2 (HPSH2), high pressure super-heater 1 (HPSH1), intermediate pressure super-heater 1 (IPSH1). Injection water into the super-heaters controls the steam temperature.

The calculation sequence starts with initializing all constants, parameters and variables to zero or an initial value originally set in the program, i.e. the starting values. Thereafter the input data required for executing the calculations is entered. The input data are the boiler features, i.e. heat exchanger areas, U-values, flow rates, temperatures and concentrations, as well as other parameters and constants that are of interest for the calculations. The mass and energy balance equations as well as the reactions like combustion, heat transfer, fouling are calculated simultaneously for the complete model. The model has been developed in the DYMOLA/Modelica environment and has 22 blocks or modules as seen in (Figure 2). The equations are described in [6].

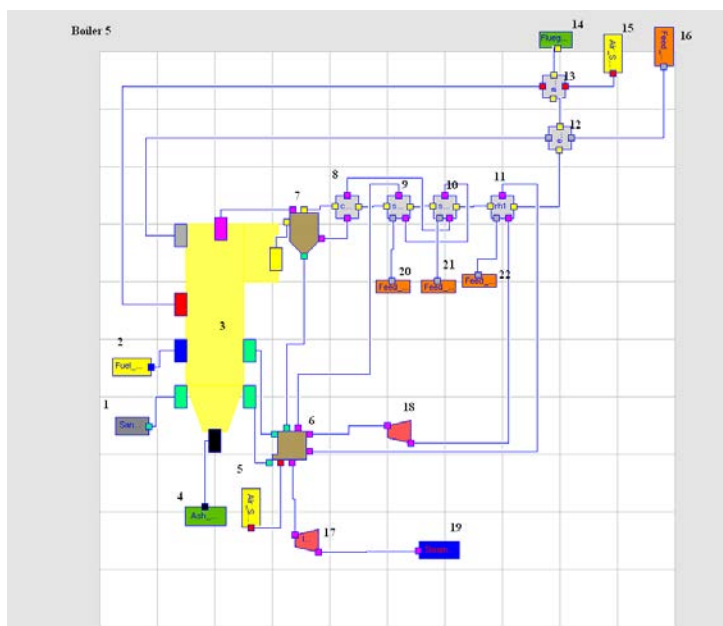


Figure 2. Boiler 5 model in DYMOLA. 1. Sand source, 2. Fuel source, 3. Boiler, 4. Ash sink, 5. Air source, 6. INTREX (HPSH3/IPSH2), 7. Cyclone, 8. HEX convection, 9. HPSH2, 10. HPSH1, 11. IPSH1, 12. Economizer, 13. HEX air gas, 14. Flue gas sink, 15. Air source, 16. Feed water source, 17. IP turbine, 18. Hp turbine, 19. Steam sink, 20. Feed water source into HPSH2, 21. Feed water source into HPSH1, 22. Feed water source into IPSH1.

By using physical models it is possible to compare the measured data to the data obtained from the simulation and give these deviations as input to a decision support tool with Bayesian Networks that will result in the probability for wrong measurement in the instruments as well as process faults. As

the equations for the complete system are solved simultaneously all parts of the processes are interlinked and affecting each other. Thus a fault in one sensor or one process part will affect all the others more or less. By following the trend for all variables we can make an intelligent guess that the variable that differs the most are probably the faulty one. As the diagnostics is relating to probabilities we therefor assume that this has the highest probability to be faulty. The second largest deviation then has the second highest probability etc. An alert may be sent to the maintenance and operator staff, which will do e.g. instrument recalibration or increase soot blowing etc. The true fault is then used to tune the BN to increase the prediction power by time. As we are primarily looking at trends of deviations the modelling fault becomes less important. If we have a bias it will not affect the diagnosis more than marginally. Other parameters or variables like the U-value of the heat exchangers will show up as faults, but can be correlated to e.g. soot blowing. The value just after soot blowing will be the most relevant from the model verification point of view. For heat exchangers with high fouling rates it may be a good idea to vary also the U-value in a similar way as we are varying the fuel composition.

System aspects

The simulation model is interfaced with Matlab/ Simulink that will get the historical data from the process server. In the same way the results from the simulation will be stored in the process database through Matlab/ Simulink. Figure 3 shows how the on-line application works.

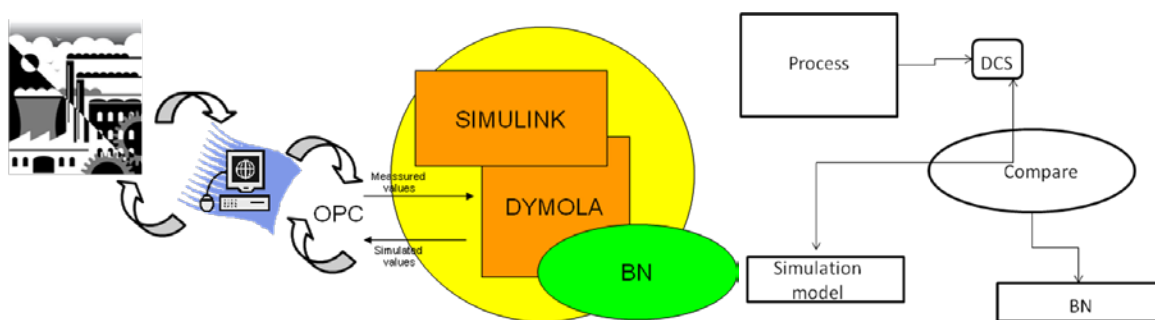


Figure 3. Application overview and Simulation in parallel with the process.

Data from the process is stored in the process database and is visualized in the operators display. OPC (Object link embedment for Process Control), which establishes the communication between plant data and plant equipment. A DYMOLA object is created in Matlab, which can be run using Matlab OPC server against ABB 800xA-environment at Mälarenergi. The results from the simulation are sent to the Data base and the difference between the simulated and the measured data is used as input data into a Bayesian Networks model.

Results and discussion

The model was tuned towards the real process by comparing simulation results to process data. This was performed during May and up to mid June 2010 when the plant was closed for the season. When the plant was starting up in September again the system was working and tests were made on-line during first the period 20-23rd September and later 24th September to 4th October continuously without any stops.

The first variable studied was steam temperature after HPSH2. During the first 24 hours the deviation between predicted and measured temperatures shows a stable temperature difference of 11 °C between the simulated and the measured data. This deviation can be due to a different fuel composition or a slightly different heat transfer than anticipated. The important fact is that the difference is relatively

constant. The downgoing peaks that are seen in Figure 4 after 36 hours, after 48 hours and the last day can be due to operation upsets or problems during the heat transfer operations.

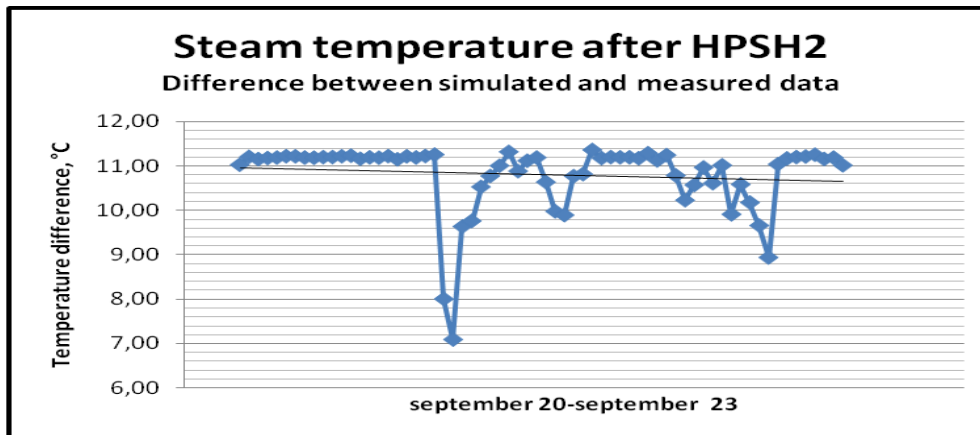


Figure 4. Difference between simulated and measured data for the variable steam temperature after HPSH2, situated just after the cyclone separator. 10 °C means a relative error of 1.2 %.

The rapid deviation indicates a problem for the operators to act directly. That the problem comes back could indicate that there are problems with fouling, and might need other actions like more frequent soot-blowing. We have not had possibility to really check the true cause, so at this moment we only can discuss possible explanations. By elongated tests, we hope to get a chance to verify a true cause later on. Principally the problem also could be poor sensor measurement. By checking if other sensors related to this one in the steam system behave in the same way, we can conclude that the problem is thermo-mechanical. On the other hand if they do not correlate, the problem may be the temperature meter. Principally there is no difference in these analyses if the deviation is large or small between the predicted value and the measured as long as the relation is constant. A problem still is that fouling is affecting especially the first heat exchangers, where there is a lot of dust. When we have frequent soot blowing we need to keep track on these and the time since last blow. This is for the actual heat transfer. If we look at the long term fouling, that is more or less irreversible fouling, this can be followed long term as an average value, or as the value just after last blow.

The second pair of variables is shown in Figure 5 and 6. In Figure 5 we see the flue gas temperature after the separator (principally a less efficient cyclone). In Figure 6 we see the temperature before the separator. As the flue gas is a continuum, these two should correlate. To some extent we see a correlation, but not a very strong one. This then indicates that the peaks seen are not related to varying fuel quality, but other type of effects. It is often not easy to identify the relations between different faults and the causes of these. Still, we can make assumptions which we can try to verify by systematic measurements and using the simulator to show what could be expected. The following could be an explanation: 1) The temperature in the flue gas after the separator is first increasing, which could be due to different heat transfer rate in the heat exchangers in the top of the separator the first 48 hours, but stabilizing thereafter. 2) It could also be a drift in a temperature sensor, which is then stabilizing. The strong peak after 18 hours may indicate some mechanical problem in the circulating fluidizing bed with respect to the fluidization. 3) A third cause could be due to combustion high up in the bed due to changes in particle size in the fuel during some period giving after-burning in the top of the separator. It is not self-evident which possible reason is most probable, but as the temperature is stabilising the temperature sensor is probably not the problem. The peak after 18 hours is another problem than the one causing the continuous increase in temperature. Fine fuel particles should have given a much faster increase and thus the most probable of the possible reasons is fouling of heat exchanger surfaces reducing the cooling of the gas. In Figure 6 we have the corresponding temperature before the separator. Here we can see a long term deviation of the temperature indicating a fouling of the temperature meter, and a possible future need for cleaning. We also see that there are several peak deviations indicating spontaneous burning high up in the bed now and then close to the sensor, but probably smoothened out so that this is not seen after the separator.

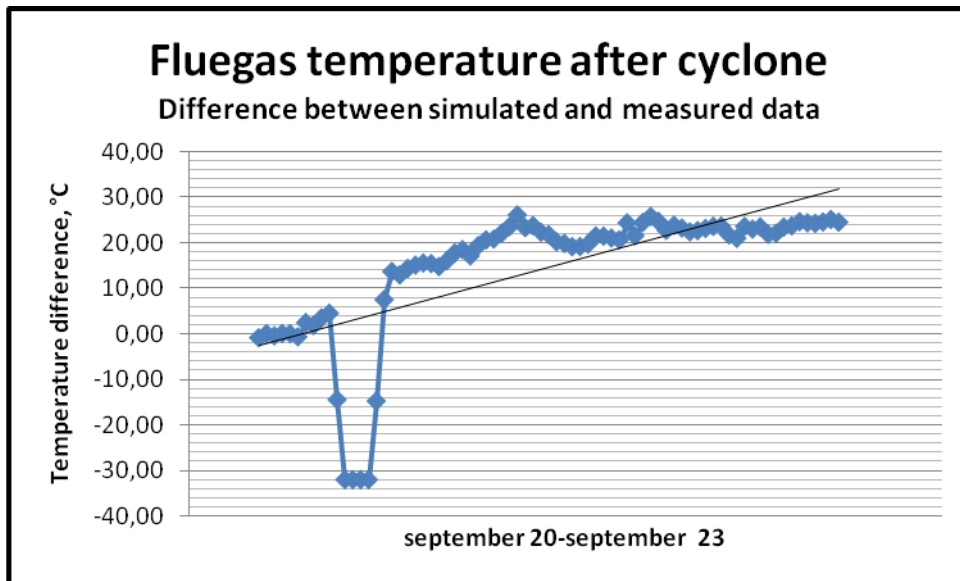


Figure 5. Difference between simulated and measured data for the variable flue gas temperature after cyclone. 10 °C means a relative error of 0.9 %.

In the simulation we assume a homogenous flow of gas through the exhaust gas channels, but in reality this may be much less stable than assumed. This probably can explain some of the differences. Still, this also can give information about the stability of the flow patterns in the real boiler, which might be of interest to study how e.g. different fuels can effect the flow pattern, as well as where the combustion take place. As fine particles can pass on with the exhaust gas and burn higher up in the boiler or even in the separator it might effect the fouling at different position in the exhaust gas system.

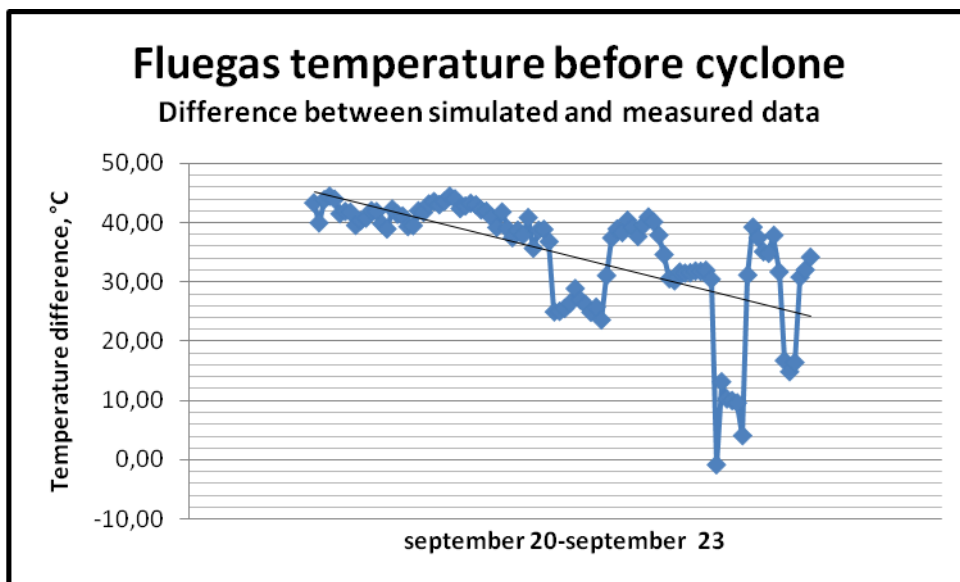


Figure 6. Difference between simulated and measured data for the variable flue gas temperature before cyclone. 10 °C means a relative error of 0.9 %.

The temperature of the flue gases after the cyclone increases over the studied period of time, while the temperature of the flue gases before the cyclone does not show any corresponding trend. This can indicate combustion in the actual separator. The difference between simulated and measured data for the variable fluegas moisture content, represented in Figure 7, shows an oscillating trend that indicates an alarming behaviour in the several hour to day time-perspective. This variation can be due to changes in the fuel composition, changing load, variations in the air flowrate (poor control),

instabilities in the boiler bed or error in sensor measurement. The plant was operated under different loads during the four days period (see Figure 8, from 125 to 165 MW). We don't see a strong correlation between load and moisture. Concerning moisture measurement we don't have detailed information as it was not measured frequently. Although the simulation also takes into account varying load, the solids management together with gas strokes with varying conditions is not seen in the simulation and could principally also explain variations.

However, it is possible to see that the difference is being reduced in the long term perspective, over several days. It could be varying moisture content in the fuel or even relation between C and H content in the fuel. More H gives more H_2O at combustion. It is not evident which alternative is the correct one, but the identification of the problem and some alternatives is a good starting point for further investigations. The first dip correlates in time to the temperature dip in temperature after the separator while the last dips correlate to disturbances in both steam temperature and temperature dips in temperature before the separator. As it is not correlating to the temperature after the separator it may indicate disturbances in the flow pattern in the exhaust gas channel causing a non-homogenous flow of moisture passing the sensor.

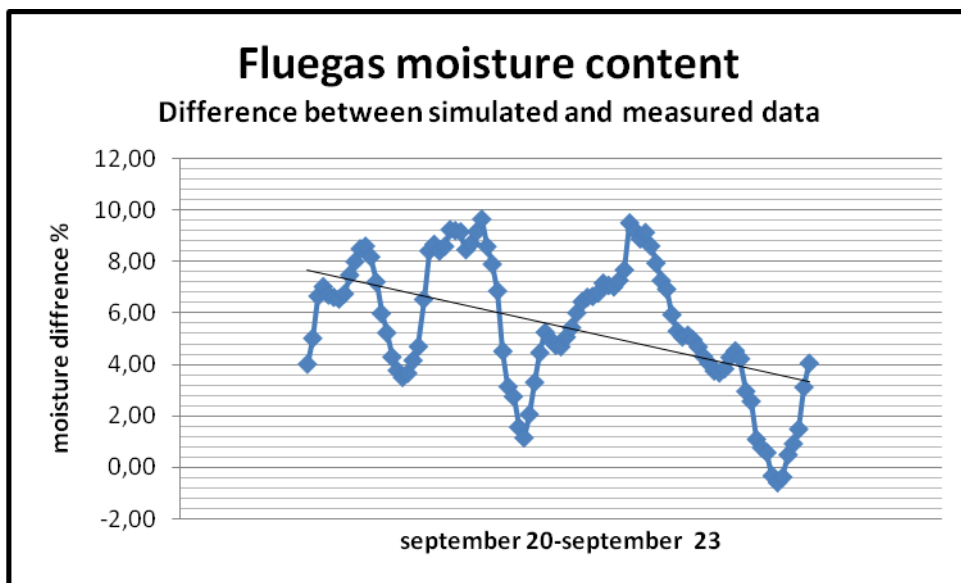


Figure 7. Difference between simulated and measured data for the variable fluegas moisture content.

The analysis made above is an example of how the difference between the values predicted from the model compared to measured values can be used to analyse and diagnose different type of short term or long term problems, both with respect to measurements as such, as well as thermo-mechanical problems in the actual process. In Figure 8 we see the curves together with the boiler load during the time period September 20- September 23. What we can conclude is that there seems to be a correlation between load on the boiler and the temperature before the cyclone, while there is no correlation between the moisture content and the other variables and the load. During the period September 24 to October 4 we made the calculations every one minute without taking the average over the hour. In figure 9 we see the results from this period comparing simulated data to measured data. The bottom curve is the boiler load measured as the fuel feed rate in kg/s. Above that is the temperature before the cyclone, steam temperature after HPSH2, flue gas temperature and at the top flue gas temperature after the cyclone. As can be seen in the figure the moisture content is not varying. For the gas temperatures we see that these gives lower measured temperatures than predicted at lower loads but higher than predicted at higher loads. The steam temperature after HPSH2 goes the opposite direction. One possible reason can be that we get different heat transfer at HPSH2 at the different loads as the fouling is higher at the higher load. For the higher than expected exhaust gas temperature it may also be due to combustion higher up in the system at the higher load. It might also be that the fuel composition is different at higher loads – dryer or finer particles, or just that the residence time in the bed is lower.

In the next section we will see how this reasoning can be structured in a Bayesian network, which gives the possibility to enhance the knowledge about what is going on inside the boiler in a structured way.

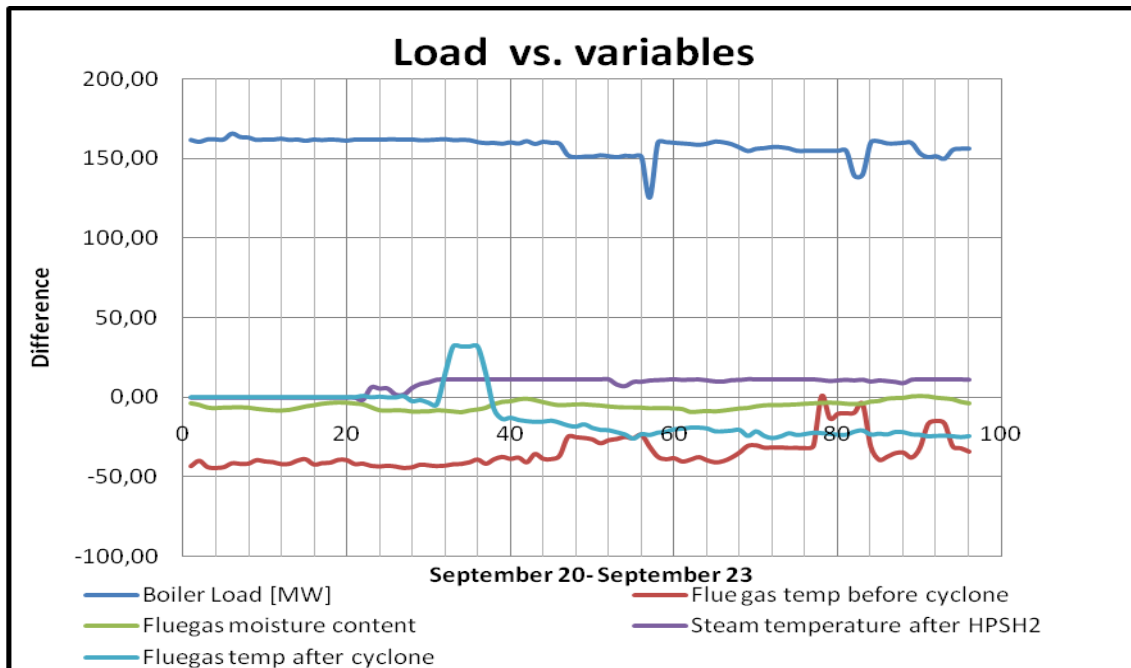


Figure 8 Boiler load vs. Variables during September 20- September 23. The bottom line is flue gas temp before the cyclone at “time 40”, the one above the flue gas temperature after the cyclone, then the moisture content in the flue gas, the steam temperature after HPSH2 and the curve at the top finally is the boiler load (MW).

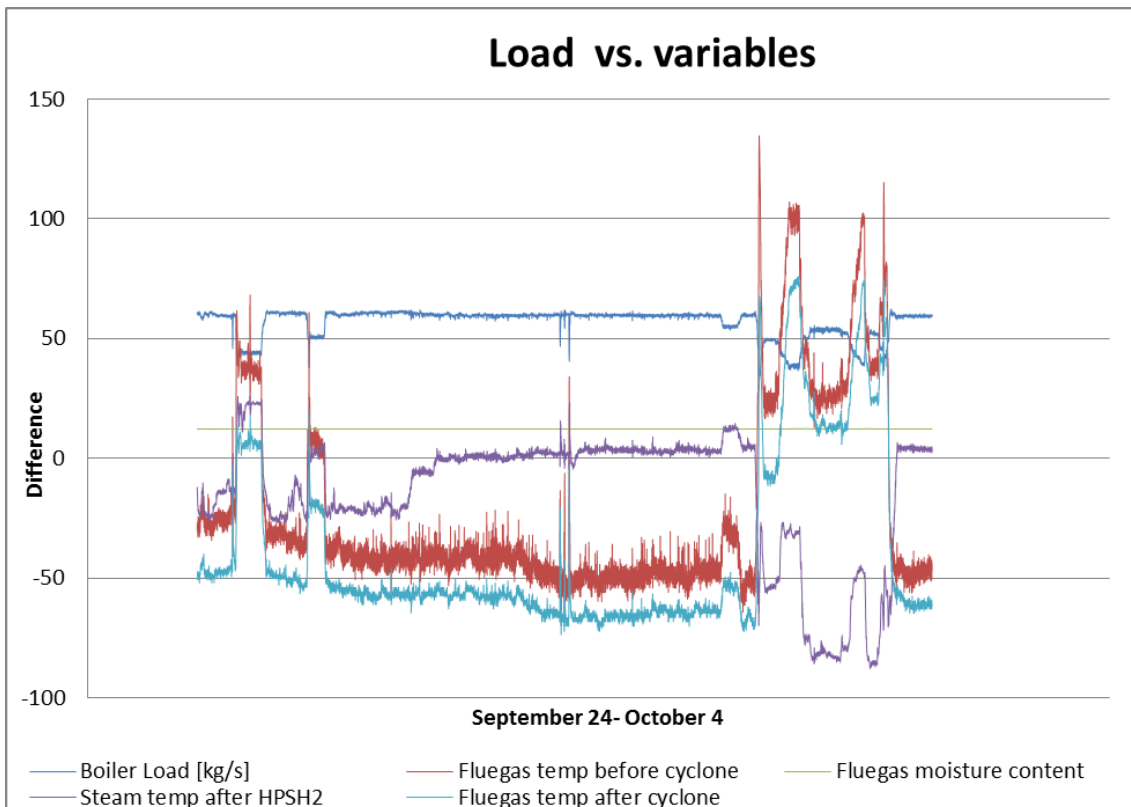


Figure 9. The second testperiod September 24 to October 4. Comparison between simulation and measured data every minute for all variables except for the fuel feed rate which is in [kg/s]. The curve at the bottom is the flue

gas temperature after the cyclone. Above that is the temperature before the cyclone, steam temperature after HPSH2, flue gas moisture and at the top we have the boiler load measured as the fuel feed rate in kg/s.

The possible causes to the deviation between predicted and measured values are configured in a BN and the probability for the different causes is later determined from experience.

Diagnostics results using Bayesian Networks

A test run of the Bayesian network with about 4 days of boiler operation September 20-23 gives the results seen in Figure 10. This time period was selected for testing the BN diagnostic system. The boiler was operating at varying load during the test period with loads between 70-90 % of nominal load because there was a time with low heat demand and operation without the steam turbine. The boiler is then cycled during the day, which gives a good indication if the model gives relevant values that correspond to the dynamics.

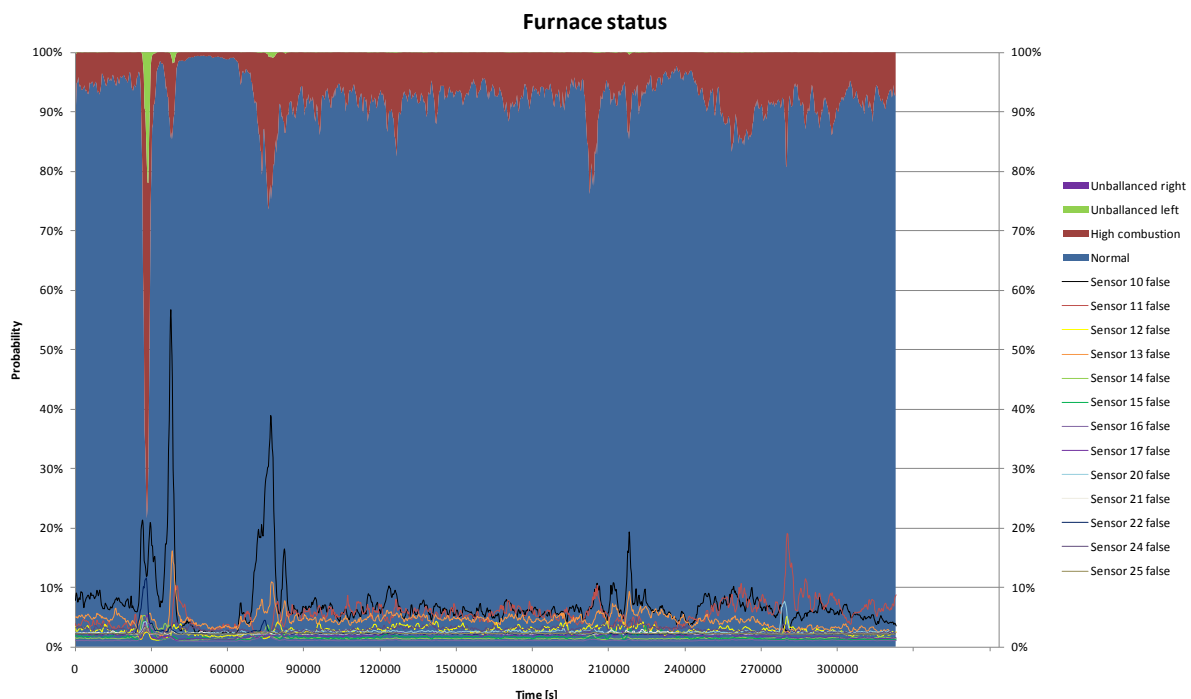


Figure 10. Probability for different type of faults in the CFB boiler for 16 variables as a function of time. Variables with the highest probability for faults are the same ones as seen in figures 8-11.

The coloured area in the graph shows the probability distribution of the node “Furnace status”. “Normal” dominates most of the time, but “High combustion” seems to be quite probable during short time periods. The problem with combustion high up in the boiler is mainly related to fine fuel particles and it can be discussed where the limit is when it becomes a real problem. There is also an indication of unbalance at the left side. Unbalances are usually caused by uneven fuel distribution and it is very interesting in a maintenance perspective. Process data from this time reveals short fuel feeder stops caused by problems in the fuel feeders.

The lines in the graph show the probability of faults in each of the 16 sensor signals. It is clear that some of them have a far more varying fault probability than others. In this situation, it can be interesting to investigate if sensor 10, 11 and 13 is correctly mounted and not disturbed by e.g. air nozzles.

The probability calculations are made by the program HUGIN where the correlation between different variables and the deviation between measured and simulated data are used as input data. The plot in Figure 10 also is one of the presentation views in the HUGIN program.

In figure 11 we see the display from Hugin for the time = 5 when there is very low probability for “high combustion”. There is a 95% probability for normal operations. In Figure 12 we see the presentation from the diagnostic system using the BN where there is a 20 % probability for normal operations but 63 % probability for “high combustion”. In Figure 13 finally we see that the operation looks more normal again. Here we have 78 % probability for normal operation again.

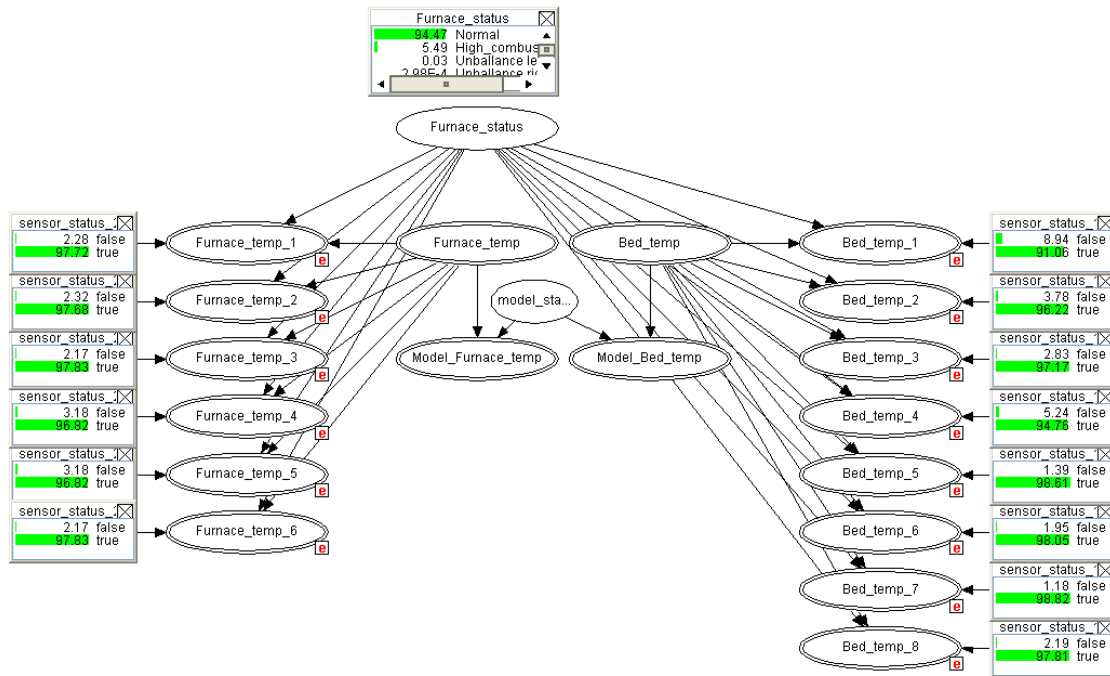


Figure 11. BN at $t=5$ with 95 % probability that furnace status is in state normal(not high combustion).

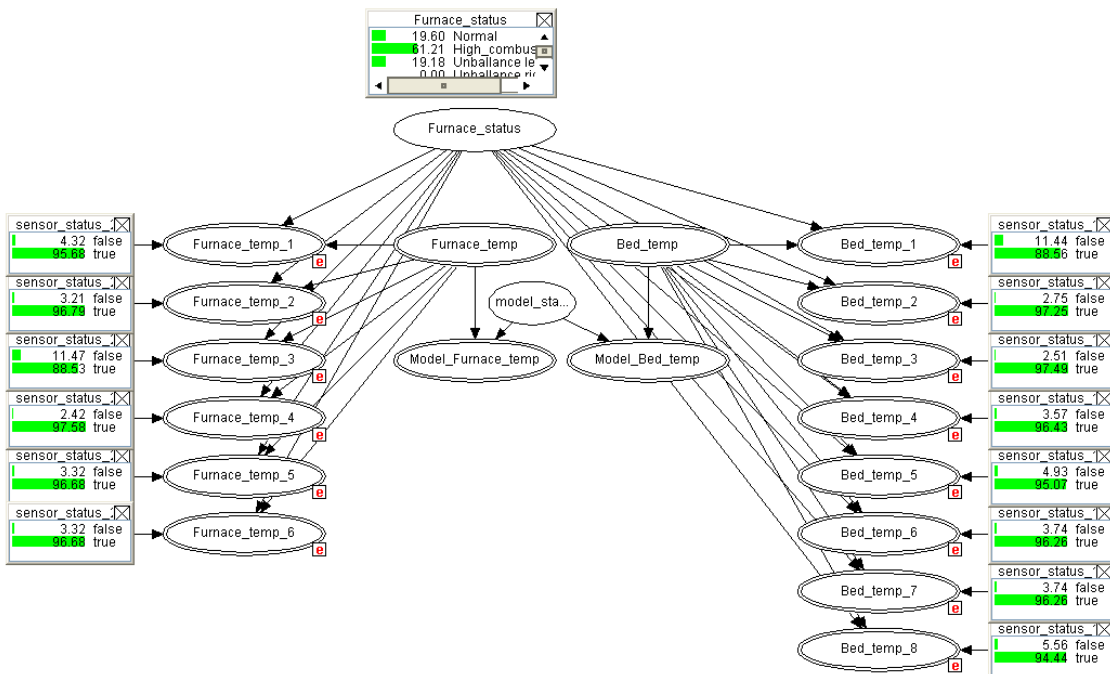


Figure 12. BN at $t=27900$ with 20 % probability that furnace status is in state normal (61 % probability for high combustion).

The boiler load is low when the analysis in Figure 16 is made and the situation here is probably caused by a problem with fuel feeding, causing uneven distribution of fuel.

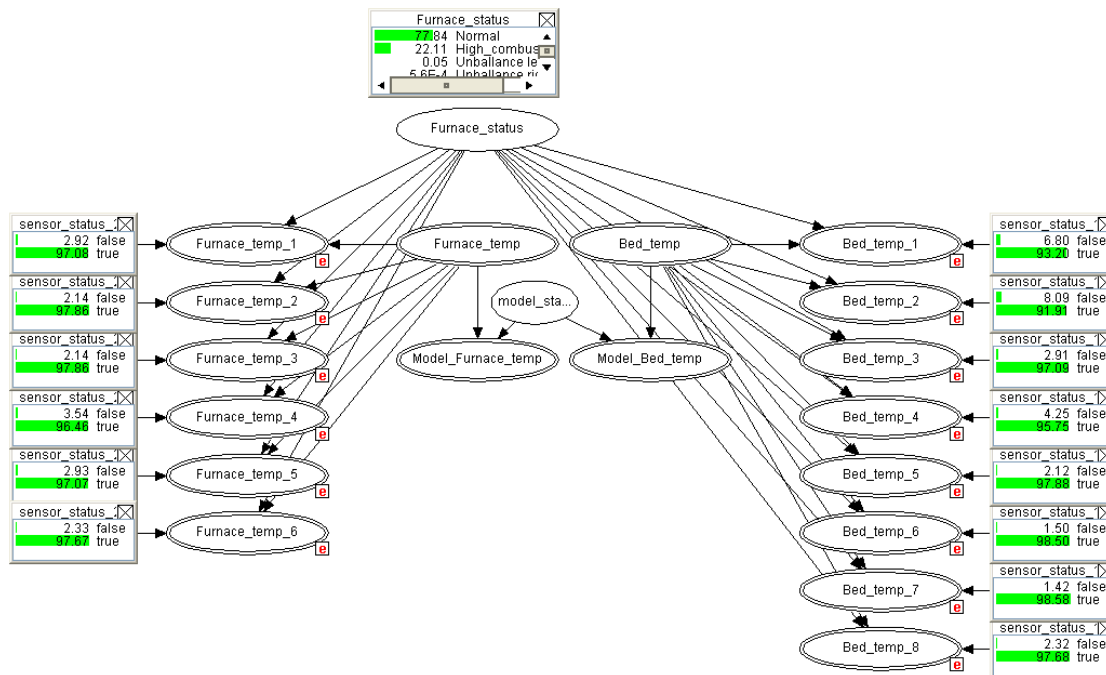


Figure 13. BN at $t=203\ 400$ with 78 % probability that furnace status is in state normal.

The load is in this case normal and the situation with higher temperature in the separator is probably caused by combustion of fine fuel material high up in the furnace.

Conclusions

From the results and discussions we can conclude that it is possible to operate a system on-line where a simulator with a complex physical model is running all the time continuously and calculating predicted values for the different variables in the boiler frequently. We have shown that the model can handle varying loads (Figure 8 and 9, 120-170 MW) and determine different type of upsets and faults (Figure 4- 7). The deviations have been fed to a Bayesian Network, where the probability for different type of faults is calculated from a BN correlating faults and reasons for the faults in a structured way (Figure 10-13). This BN configuration has to be determined for each specific plant, but the structure is principally the same. The cause of different faults is normally general for a certain type of equipment like a heat exchanger, a cyclone/separator, a fluidized bed etc. The advantage of the application is that the combination of model based diagnostics and decision support can be used to schedule equipment and sensor maintenance. Moreover the application is used on-line which allows evaluation of the system under real circumstances. Results from running the system shows that several different type of faults could be determined simultaneous. Refinement of the probability for the different measurements in relation to different causes are later performed by feeding back knowledge to the BN.

Acknowledgments:

We want to thank Varmeforsk (Thermal Engineering Research Association) for the financial support and valuable inputs from the reference group members. We also want to thank the staff at Malarenergi AB, and especially Peter Karlsson.

References:

- [1] Venkatasubramanian V, Rengaswamy R, Yin K, Kavuri S N; "A review of process fault detection and diagnosis Part I: Quantitative model-based methods",

- Computers and Chemical Engineering 27, pp 293-311, 2003.
- [2] Venkatasubramanian V, Rengaswamy R, Yin K, Kavuri S N; "A review of process fault detection and diagnosis Part II: Qualitative models and search strategies", Computers and Chemical Engineering 27, pp 313-326, 2003.
 - [3] Venkatasubramanian V, Rengaswamy R, Kavuri S N, Yin K; "A review of process fault detection and diagnosis Part III: Process history based methods", Computers and Chemical Engineering 27, pp 327-346, 2003.
 - [4] Widarsson B, Karlsson C, Nielsen, T, "Bayesian Networks applied to process diagnostics", Värmeforsk 882, Stockholm October 2004, ISSN 0282-3772.
 - [5] Avelin A, Jansson J, Dotzauer E. "Use of combined Physical and Statistical Models for On-line Applications in the Pulp and Paper Industry", Mathematical and Computer Modeling of Dynamical Systems: Methods, Tools and Applications in Engineering and Related Sciences, 1744-5051, v15-5, p. 425 – 434, 2009.
 - [6] Dahlquist E, Widarsson B, Lilja R, "Dynamisk dataåterförening - kvalitetssäkring av signaler", Värmeforsk 1050, Stockholm March 2008, ISSN 1653-1248.
 - [7] Karlsson C, Avelin A, Dahlquist E, "How to make better use of all the process data collected in process industry and power plants", 6th Eurosim Congress on Modeling and simulation, , Ljubljana, Slovenia, September 2007.
 - [8] Karlsson C, Dahlquist E;"Process and Sensor diagnostics", Värmeforsk 834, Stockholm October 2003, ISSN 0282-3772.
 - [9] Weidl, G., Madsen, A.L. and Dahlquist, E. (2002), "Bayesian Networks for Root cause analysis in process operation", European Journal of Operational Research, Special issue on "Advances in Complex System Modeling".
 - [10] Widarsson B, Dotzauer E; "Bayesian Networks-based early-warning for leakage in recovery boilers", Applied Thermal Engineering, v.28-7, p. 750-764, May, 2008.
 - [11] Widarsson B, Dotzauer E, Dahlquist E; "System för tidig läckagevarning i sodapanna", Värmeforsk 986, Stockholm, December 2006, ISSN 1653-1248.
 - [12] Man Cheol Kim, Poong Hyun Seong; "An analytic model for situation assessment of nuclear power plant operators based on Bayesian inference", Reliability Engineering & System Safety, Volume 91, Issue 3, March 2006, Pages 270-282
 - [13] Giovanni Cerri_, Sandra Borghetti, Coriolano Salvini, "Neural management for heat and power cogeneration plants", Engineering Applications of Artificial Intelligence 19 (2006) 721–730
 - [14] Ciarapica F.E. , G. Giacchetta: Managing the condition-based maintenance of a combined-cycle power plant: An approach using soft computing techniques. Journal of Loss Prevention in the Process Industries 19 (2006) 316–325
 - [15] Struss P, Provan G, de Kleer J, ; "Special issue on Model-Based Diagnostics", IEE Transactions on Systems, Man and Cybernetic part A:Systems and Humans, Volume 40, Issue5, , 870-873, September 2010.
 - [16] Jensen, F V, "Bayesian Networks and decision graphs"; Springer-Verlag 2001
 ISB 0-387-95259-4.
 - [17] Norsys Software Corp., Netica Tutorial, Norsys Software Corp.,
http://www.norsys.com/tutorials/netica/nt_toc_A.htm, 2010-12-02
 - [18] Fritzson, P., 2007, "Modelica – A unified Object-Oriented Language for Physical Systems Modeling, Language Specification Version 3.0", The Modelica Association.
 - [19] Dynasim AB, 2004-2009, 20090308, www.dynasim.com/dynasim.htm
 - [20] Modelon AB , Ideon Science Park , SE-22370 LUND, Sweden<http://www.modelon.se/>.
 - [21] Otter, M. and Elmquist, H., 2001; Modelica – Language, Library, Tools, Workshop and EU-Project RealSim.
 - [22] The Modelica Association, www.modelica.org/association,2009-03-08

Paper 4

Title: Retention time and nutrient tracking inside a digester for biogas production

Johan Lindmark, Rebei Bel Fdhila, Eva Thorin
Mälardalen University, Sweden

Keywords: Biogas, Mixing, Digester, CFD, Retention time, Nutrition

A large proportion of today's biogas plants are continuous stirred tank reactors (CSTR) and they are usually assumed to be perfectly mixed. Based on this assumption the retention time of the biogas plants and the organic loading rate are estimated. However, there can be large inconsistencies in the mixing parameters leading to local variations in the mixing pattern and in mixing intensity. These variations can lead to an uneven distribution of nutrients and microbiological activity inside the digester.

The digester is the heart of the biogas process where the organic material is broken down in steps to simpler compounds and finally to the energy rich gas methane. By controlling the environment for the microorganisms inside the digester the fermentation process can be improved with an increased capacity as a result. The mixing inside the digester is one of the most important measures of control available.

Several investigations have shown that the mixing inside the digester has a direct effect on the biogas yield and that the result is affected by the dry solid content of the mixture. At low dry solid content the mixing could possibly be handled by the naturally occurring mixing and only small improvements can be made by increasing the mixing.

Mixing becomes more important at higher total solid content and can affect the gas yield considerably. Previous studies, using a manure slurry with a total solid content of 10% as substrate, have shown that increased mixing can improve the gas yield by 29%, 22% and 15% compared to an unmixed digester by mixing with slurry recirculation, impeller mixing and gas injection respectively. Higher total solid contents can of course also lead to other problems in an unmixed digester like sedimentation or problems with a floating layer.

In this study the retention time and dispersion of the feed inside the digester at the Växtkraft biogas plant in Västerås, Sweden, is studied using Computational Fluid Dynamics (CFD) to understand the effect that the mixing has on the process. This work provides the distribution of nutrition and how the nutrient disperses inside the digester. The impact of mixing is evaluated by comparing experiments and simulations of the flow and mixing intensity with simulations of the nutrient content inside the digester.

Retention time and nutrient tracking inside a digester for biogas production

J. Lindmark¹, R. Bel Fdhila^{1,2}, E. Thorin¹

¹Mälardalens University, Energy division, School of Sustainable Development of Society and Technology, Västerås, Sweden; ²ABB AB, Corporate Research, SE - 721 78, Västerås, Sweden

Corresponding Author: J. Lindmark, Mälardalens University, School of Sustainable Development of Society and Technology, Box 883, 721 23 Västerås, Sweden: johan.lindmark@mdh.se

Abstract. A digester is practically a black box with too few possibilities to study what is going on inside. The continuous stirred tank reactor (CSTR) is a common digester design for biogas production which puts a high demand on the mixing configuration. This type of digester design is often assumed to be perfectly mixed which influences operational decisions e.g. residence time which can lead to problems in the process and low capacities. Chemical tracer methods have been used to study the mixing at biogas plants to give valuable information on retention time, active volumes and short-circuiting in plants already in operation but it is time-consuming and costly to make these types of evaluations. In this work the retention time and dispersion of the feed inside a digester is studied using a Computational Fluid Dynamic (CFD) model. A scalar is injected in the simulation to mimic the tracer method and to see the effect that the mixing has on dispersion of nutrient in a pneumatically mixed digester. The conclusions from this study are that large dead and stagnant zones can be found in the digester, as much as 30 %. The mixing configuration studied is limiting the dispersion of nutrient to 30 – 40 % of the digester because of the barrier that the column of bubble produces. One way to improve the dispersion could be to have two or more injection points. It takes the nutrient/feed around 125 seconds to follow the entire circulation path of the mixing and return to the starting point around the gas injectors.

Keywords: CSTR, CFD, HRT, biogas, mixing, digester, feed, nutrition, tracer

1 Introduction

A large proportion of today's biogas plants are continuous stirred tank reactors (CSTR) (De Baere 2010, Weil and 2010) and they are usually assumed to be perfectly mixed. Based on this assumption the retention time of the feedstock in the biogas reactor as well as the organic loading rate is estimated. However, there can be large inconsistencies in the mixing leading to variations in the mixing pattern and in mixing intensity (Karim et al. 2007, Lindmark et al. 2008). These variations can lead to stagnant zones, sedimentation, flotation and short-circuiting in the digester as well as an uneven distribution of nutrients and microbiological activity.

The digester is the heart of the biogas process where the organic material is broken down in steps to simpler compounds and finally to the energy rich gas methane. By controlling the environment for the microorganisms inside the digester the fermentation process can be improved with an increased biogas yield as a result. However, the biological process is complex and controlling it is a challenge.

The mixing inside the digester has been shown to be an important control measure of the process. Several investigations have shown that the mixing has a direct effect on the biogas yield but there are many contradicting opinions on how the mixing should be designed for best results. There are studies that show positive effects both from increasing (Karim et al. 2005a) and decreasing (Stroot et al. 2001) the mixing. High mixing intensities and shear have been shown to have negative effect on the microorganisms and the formation of flocks inside the digester (McMahon et al. 2001, Whitmore et al. 1987, Dolfing 1992).

The effects of mixing on the mass transfer and the digestion process are strongly connected to the content of total solids, viscosity and rheological properties of the digestate (Karim et al. 2005a, Karim et al. 2005b, Karim et al. 2005c) and this puts a high demand on the mixing equipment used (Yu et al. 2011). At low dry solid content the mixing could possibly be handled by the naturally occurring mixing and only small improvements can be made by increasing it (Karim et al. 2005a). Mixing becomes more important at higher total solid content and can affect the gas yield considerably. Previous studies, using a manure slurry with a total solid content of 10% as substrate, have shown that increased mixing can improve the gas yield by 29%, 22% and 15% compared to an unmixed digester by mixing with slurry recirculation, impeller mixing and gas injection respectively (Karim et al. 2005b). High total solid contents can of course also lead to other problems in an unmixed digester like sedimentation or problems with flotation.

The digester is basically a black box with few or no possibilities to evaluate the result of the mixing. The hydraulic retention time, the dispersion of the feed, stagnant zones and short-circuiting can be analyzed by using a tracer method. In this method you add a chemical tracer (e.g. lithium chloride) that is mixed with the injected liquid and by analyzing the concentration of this tracer at the outlet conclusions of the mixing quality can be drawn. This method is time-consuming and costly and that is why the use of a Computational Fluid Dynamic (CFD)

model has been proposed by many researchers as an alternative to this method (Meroney and Colorado 2009, Terashima et al. 2009).

In this study the retention time and dispersion of the feed inside a digester is studied using a CFD model. A tracer is injected in the simulation to see the effect that the mixing has on dispersion of nutrient. This work provides information on how the distribution of nutrition looks like and short-circuiting effects in a pneumatically mixed digester.

2 Computational model

To simulate the movement of the fresh feed inside a digester the volume of fluid (VOF) approach was chosen. A two phase gas/liquid, transient and turbulent model was built to visualize and analyze the local process changes at different time instants. The geometry of the digester was built, specifying appropriate boundary conditions at inlets and outlets. A passive scalar was injected through the liquid inlet as a tracer to be able to follow the dispersion of nutrient/feed inside the digester.

2.1 Digester Geometry

The simulated digester is a cylindrical CSTR with a radius of 8.5 m and a height of 19.5 m and a total liquid volume of 4 000 m³. Mixing of the liquid is done pneumatically by compressing biogas and distributing it through 12 injection pipes that release the gas at the bottom, in the center of the digester, the gas is then recovered at the top. The liquid inlet is situated near the bottom close to the side wall and the outlet at the bottom at the center of the digester. The inlet and outlet pipes were added as small sections of cuboids to facilitate that a good mesh quality could be produced.

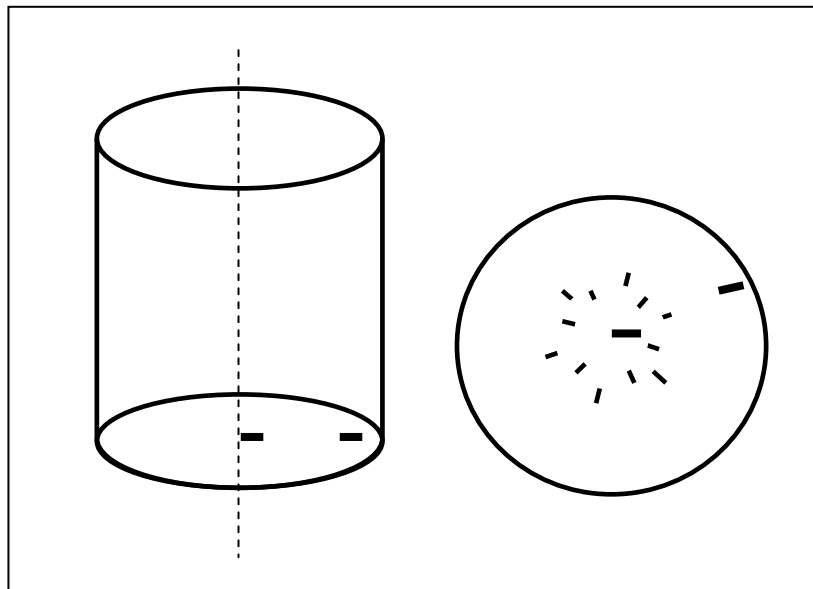


Figure 1. Illustration of the geometry that was used in the simulations. The left showing the shape of the digester with the positioning of the liquid outlet (centre) and liquid inlet (on the right hand side). The right picture is showing the top view of the digester bottom and the 12 gas injection points as well as the angles of the liquid inlet and outlet. The gas is injected facing out from the centre through the injection pipes and the liquid is pumped in and sucked out directed towards the centre.

The mesh was built up as a mixture of hexahedral and of tetrahedral cells, dividing the entire domain in 436 000 individual volumes in a structured way. A finer mesh was built at the bottom around the liquid inlet and outlet as well as around the gas injection pipes for better resolution in these areas where the gradients are high and the flow changes can be fast.

2.2 Boundary conditions

The gas inlets are all set to mass flow inlets with a specified mass flow rate. The liquid inlet and outlet are modeled as velocity inlets with the same fixed value to ensure that the introduced liquid is extracted. The gas outlet was set as a pressure outlet to allow the gas to be removed from the digester. The surface of the digestate was simulated as a free surface with a meniscus between the liquid and gas filled headspace. The boundary conditions are presented in Table 1.

Table 1. Boundary conditions.

Boundary	Type	value
Gas injection pipes	Mass flow inlet	0.01747 kg/s
Liquid inlet	Mass flow inlet	1.349 m/s
Liquid outlet	Mass flow inlet	-1.349 m/s
Gas outlet	Pressure outlet	-
Digester walls	No slip	-

2.3 Mathematical model

The VOF model was used to be able to track the two immiscible fluids using a single set of momentum equations. This model is used when the position of the interface between two fluids is of interest like in this case. The numerical solution can show the dispersal pattern of the feed and how much time it takes for the feed to reach the liquid outlet and be removed from the system. The turbulence is modelled using Reynolds stress model.

The model was set up using the physical properties of water because of the high water content (above 95 %) of the digester and the uncertainties in the property of the digestate. Thicker digestate puts a much higher demand on the mixing configuration and by using the properties of water we can see the imperfections in the mixing before they are magnified by higher TS. The physical properties of air were used for the properties of the injected gas.

To be able to track the flow of incoming feed a passive scalar in the liquid phase was injected through the liquid inlet after 327 seconds of the simulation and the concentration of the scalar in the digester are be tracked as it is mixed with the digestate. By analyzing the scalar in the different time steps the accumulation and deficiency of nutrients inside the digester can be visualized and recorded. Short-circuiting of the flow, leading to loss of fresh feed and nutrients, can be recorded at the vicinity of the liquid outlet.

2.4 Convergence

The flow is naturally transient however a stable solution is reached at approximately 5 minutes physical time. The flow was then frozen and the scalar was injected in a continuous manner with the liquid feed. At the inlet a scalar constant value of 1.0 was used.

3 Results and discussion

3.1 Mixing dynamics

The nutrient will follow the liquid circulation pattern which is produced by the mixing equipment and will be dispersed throughout the domain. To understand the mechanisms of the nutrient dispersion there is a need to study how the mixing is functioning and the flow field it produces. In the pneumatic configuration studied the gas is injected at the bottom and the buoyancy of the gas will cause the bubbles to rise towards the surface while transferring momentum to the liquid. The injected gas can be seen in figure 2 like a plume of rising bubbles.

The coarse mesh that we use influences certainly the size of these created bubbles or even gas pockets. The smaller the mesh cells the better accuracy of the gas bubbles description. However, we need to keep the mesh size under control to have a reasonable simulation time.

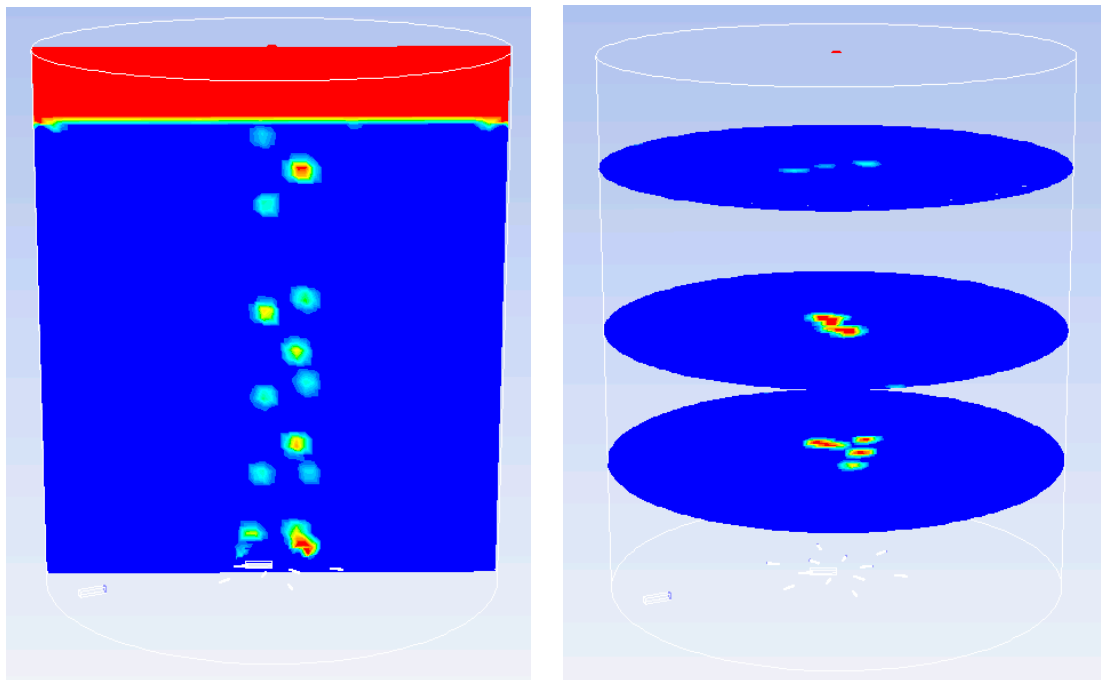


Figure 2. Tracking the flow of bubbles as volume fraction of gas in the liquid. The left figure is showing the bubbles or gas pockets path at the vertical mid-plane and the right figure is showing the volume fraction of gas in the tank at 5, 10 and 15 m from the bottom with the red colour representing the highest fraction of gas (5%) and blue the lowest (only liquid).

The results of the mixing and the flow fields can be seen in Figure 3, showing the velocity vectors and velocity contours inside the entire domain of the digester. The results clearly show that there is a good vertical circulation. There is a high liquid speed produced in the centre of the digester, up to 1 m/s, and there is a recirculation of liquid along the sides of the digester. However, there are areas that virtually have no mixing and large areas with very low liquid speed. There are some turbulent areas where numerous vortices are formed close to the free surface of the liquid and also at the bottom. The flow field ranges from a speed of 0 m/s to 1 m/s. The really high flows can be seen in the stream of bubbles while the periphery only has a speed of a couple of cm per second and totally stagnant zones in some places. The grey circle at the top of the digester outlines the meniscus of the digester and the vectors above that line illustrates the gas phase with the gas outlet in the centre of the top wall.

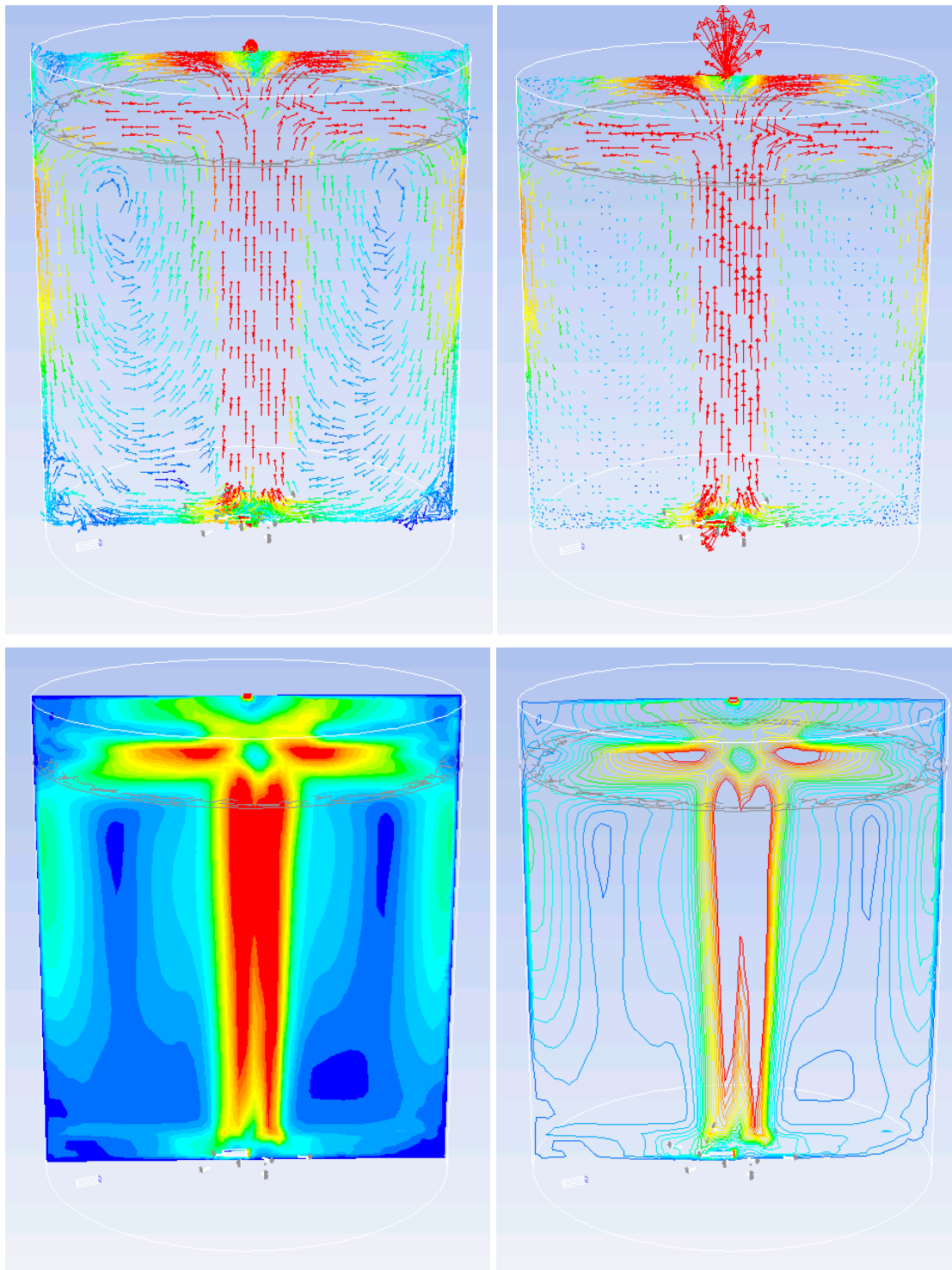


Figure 3. velocity vectors and velocity contours of the liquid phase. The figure is showing the velocity vectors in the digester to see in which direction the liquid is flowing with fixed vector size (top left) and also showing the real size of the vector (top right). The figure is also showing the velocity contours with (bottom left) and without filling (bottom right). The colour indicates a liquid speed range is between 0- 1 m/s (blue – red).

3.2 Tracking the dissolved nutrient

Tracking the dissolved nutrient inside the digester by means of the CFD tracer method shows a good vertical mixing of nutrient (Fig 4) as suggested by the mixing dynamics and earlier studies (Lindmark et al. 2008). However, the configuration of the feed/nutrient injection (from the left side in this figure) leads to an uneven distribution of nutrient. The scalar was first injected after 327 seconds of mixing so that the flow fields had time to stabilise and in this figure the nutrient dispersal can be seen at different time instants (from left to right). The second time illustrated (at 487 seconds) is approximately the time were the nutrient has made its way back to the injection point

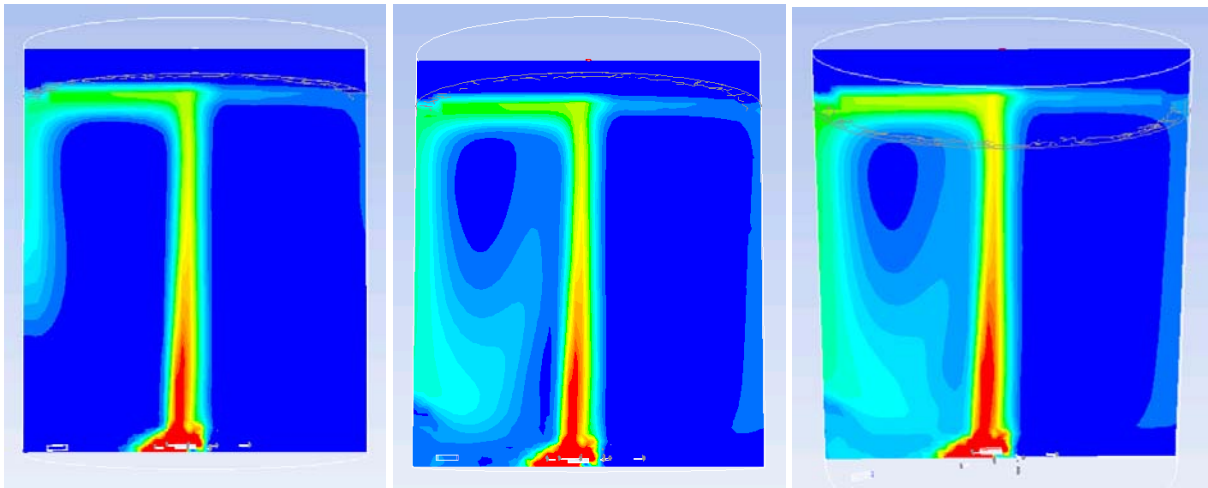


Figure 4. The scalar tracer at different time instants, shown as concentration of the scalar in the digestate. The figure shows the distribution of the nutrient at 407 (T_1), 487 (T_2) and 543 (T_3) seconds from left to right. Showing the dissolved nutrients path through the digester with the red colour representing the highest concentrations and blue the lowest (0-0.05).

To get more details on the nutrient dispersal the range of concentration was changed to 0 - 0.01 at time T_3 and also viewed in the z-direction at 2, 5, 10 and 15 m from the bottom (Fig 5). From this it can be concluded that the nutrient is only dispersed efficiently in around 30 - 40% of the digester and the rest of the volume is under-nourished. Overloading could possibly be a problem in the areas where we have the dispersion of nutrient since there will be an accumulating effect.

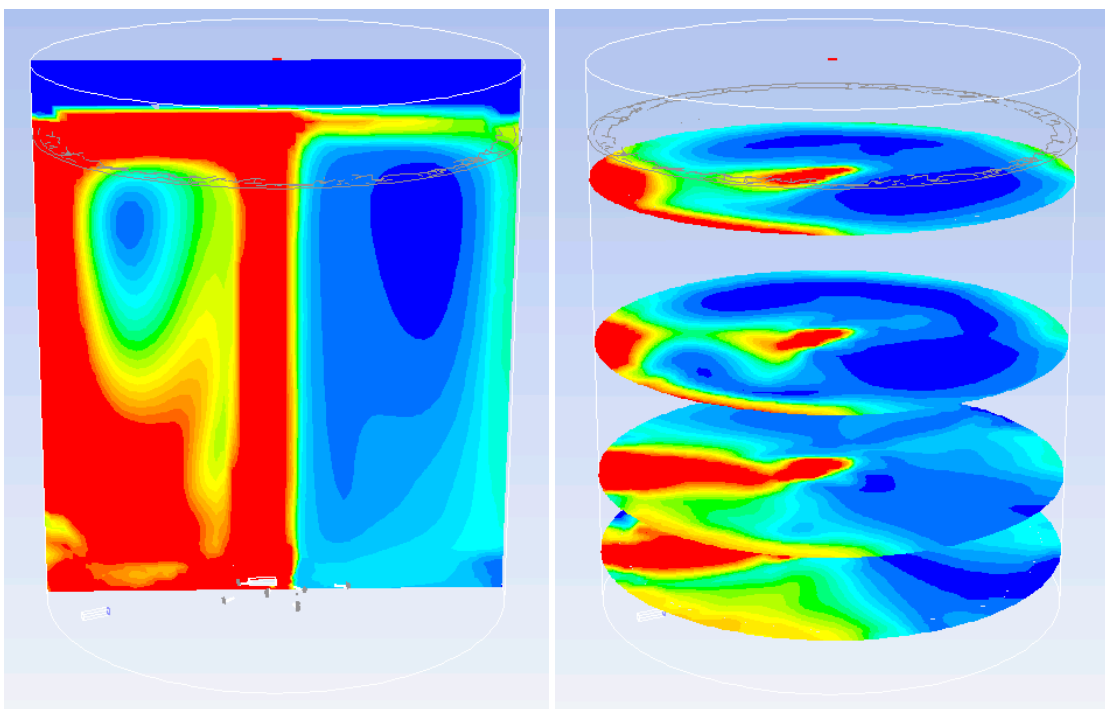


Figure 5. Dispersion and accumulation in the digester. Contours of the scalar concentration in the range 0 – 0.01.

Using a scalar as a tracer in the simulations has both benefits and drawbacks. Using a scalar is very similar to the use of the tracer method which means that it is accepted by the industry but it also gives a wide range of data concerning the dispersion of nutrient that the tracer method never could do. In the CFD simulation we can study the concentration of nutrient at every moment of the process and every part of the digester and visualize the results. When working with a passive scalar and using an imposed velocity boundary condition at the outlet, we need to set in advance a value for the scalar at that boundary. This means that the exact time when the scalar starts to be evacuated at the outlet is difficult to find out and evaluate operating parameters like e.g. the retention time. Because of this it is more appropriate to study dynamics in the system than for operational data like hydraulic retention time (HRT) and solid retention time (SRT) even though some conclusions about them can be drawn. By studying the concentration changes of the scalar at the gas injectors (positioned around the liquid

outlet) the turn over time can be seen as well as some effects of short-circuiting flows inside the digester (Figure 6). There is a stable concentration of the scalar around the gas injectors directly from the time of injection which is caused by short-circuiting and it is 1.15 % of the scalar mixed with the liquid that probably will be removed from the digester through the liquid outlet. At $T = 452$ there is a rapid increase in the concentration of the scalar after it has gone through the entire digester and returned to the source of the mixing, the turn over time. The turnover time of the scalar is consequently near to 125 seconds and the path the scalar will take can be seen in the velocity vectors in Figure 3.

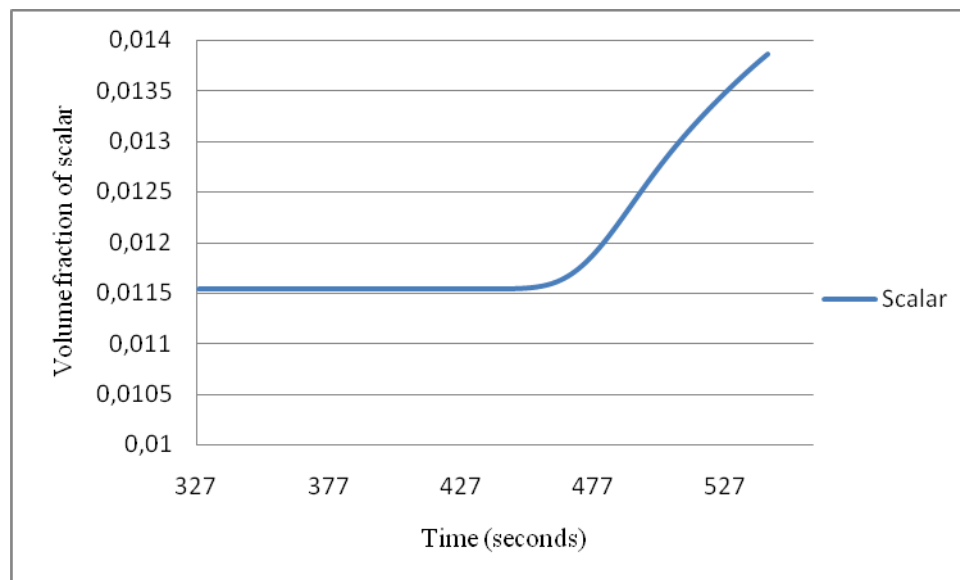


Figure 6. Turn over time of the digester. This figure shows the volume fraction of the scalar around the gas injectors changes with time.

From an engineering point of view it is very hard to control a biological process because there are so many factors influencing the process. There has been some work done to evaluate the effects of mixing both by microbiologists and engineers but there is as of yet no coherent picture on what actions to take to get the improved digestion process that everyone is aiming for.

The impact of mixing on parameters like temperature, pH and retention time in the digester seems to be a good starting point from which to analyze the effects of the mixing imperfections. One of the main possibilities for control is the addition of fresh feed but because of mixing imperfections we can have overloaded and undernourished zones in the digester at the same time even if the organic loading rate to the digester itself is adequate. There is also the possibility that inhibiting substances can accumulate in the digester and that inconsistencies in temperature and pH can form within the digester with local effects on the microorganisms. All these parameters have been extensively studied and there is a good theoretical basis from which to draw conclusion. By considering mass transfer, physical properties and the mixing in the digester the effects of the different parameters can be studied in every part of the digester, as a matrix.

Vesvikar and Al-Dahhan (2005) suggests that all areas with a mixing below 5 % of the maximum is stagnant or dead zones which has negative effects on the biogas plants capacity to produce biogas. In this simulation around 30 % of the total volume would fall under that category (two darkest shades of blue in figure 3). Except for the effect of mixing on mass transfer they also mean that these zones lead to the degradation of digester performance by increase in pH and temperature.

It is also possible to study the temperature range inside the digester through simulations but the pH is directly connected to the microbiological activity and the concentration of nutrient which makes it harder to predict. However, valuable information on the dynamics of the digestion could be gained by studying it.

4 Conclusion

There are large dead and stagnant zones in the digester and according to the preliminary simulations made on mixing dynamics result say it can be around 30 %.

The mixing configuration is limiting the dispersion of nutrient to 30 – 40 % of the digester because of the barrier that the column of bubble produces. One way to improve the dispersion could be to have two or more injection points.

It takes the nutrient/feed that is pumped in to the digester around 125 seconds to follow the entire circulation path of the mixing (Fig 3) and return to the zones around the gas injectors.

5 Acknowledgement

This study was funded by the European Regional Development Fund through the project Regional Mobilizing of Sustainable Waste-to-Energy Production (REMOWE) which is a part of the Baltic Sea Region programme.

6 References

- Dolfing, The energetic consequences of hydrogen gradients in methanogenic ecosystems, *FEMS Microbiol. Ecol.* 101 (1992), 183–187
- Karim, K., Varma, R., Vesvikar, M., and Al-Dahhan, M.: Flow pattern visualization of a simulated digester. *Water Research*, 38(17) (2004), 3659–3670.
- Karim, K., Klasson, K.T., Hoffmann, R., Drescher, S.R., DePaoli, D.W., Al-Dahhan, M.H., Anaerobic digestion of animal waste: Effect of mixing. *Bioresource Technology*, 96(14) (2005a), 1607–1612
- Karim, K., Hoffmann, R., Klasson, T., Al-Dahhan, M.H. Anaerobic digestion of animal waste: Waste strength versus impact of mixing. *Bioresource Technology* 96 (16) (2005b), 1771–1781
- Karim K., Hoffmann R., Klasson K.T., Al-Dahhan M.H., Anaerobic digestion of animal waste: Effect of mode of mixing, *Water Research*, 39 (15) (2005c), 3597–3606.
- Karim, K., Thoma, G. J., and Al-Dahhan, M. H.: Gas-lift digester configuration effects on mixing effectiveness. *Water Research*, 41(14) (2007), 3051–3060.
- Liang Yu, Jingwei Ma and Shulin Chen, Numerical simulation of mechanical mixing in high solid anaerobic digester, *Bioresource Technology*, 102 (2) (2011), 1012–1018
- Lindmark J., Bel Fdhila R., Thorin E., On modelling the mixing in a digester for biogas production. In *Proceedings of MATHMOD 09, 6th International Conference on Mathematical Modelling*, Vienna, Austria, 2009.
- McMahon, K.D., Stroot, P.G., Mackie, R.I., and Raskin, L., Anaerobic codigestion of municipal solid waste and biosolids under various mixing conditions-II: microbial population dynamics, *Water Res.* 35 (7) (2001), 1817–1827.
- Meroney, R.N., Colorado, P.E. CFD simulation of mechanical draft tube mixing in anaerobic digester tanks *Water Research*, 43 (4) (2009), 1040–1050
- Terashima M., Goel R., Komatsu K., Yasui H., Takahashi H., Li Y.Y., Noike T., CFD simulation of mixing in anaerobic digesters, *Bioresource Technology*, 100 (7) (2009), 2228–2233.
- Stroot, P.G., McMahon, K.D., Mackie, R.I., Raskin, L., in press. Anaerobic codigestion of municipal solid waste and biosolids under various mixing conditions-I. Digester performance, *Water Res.* 35(7) (2001), 1804–1816.
- De Baere, L., Mattheeuws, B., and Velghe, F. (2010). State of the art of anaerobic digestion in Europe, 12th World Congress on Anaerobic Digestion, October 31st –November 4th, Guadalajara, Mexico.
- Vesvikar, M.S., Al-Dahhan, M., Flow pattern visualization in a mimic anaerobic digester using CFD. *Biotechnology and Bioengineering* 89 (6) (2005), 719–732.
- Weiland, P., Biogas production: current state and perspectives, *Applied Microbiology and Biotechnology*, 85 (2010), 849–860.
- Whitmore, T.N., Lloyd, D., Jones, G. and Williams T.N., Hydrogen-dependent control of the continuous anaerobic digestion process, *Appl. Microbiol. Biotechnol.* 26 (1987), pp. 383–388.

Paper 5

Title: Modeling Software for Advanced Industrial Diagnostics

Mika Liukkonen, Mikko Heikkinen, Teri Hiltunen, Jari Kapanen, Yrjö Hiltunen
University of Eastern Finland, Finland

Keywords: Software, Process, Analysis

The energy efficiency of industry is recognized nowadays as a highly important matter because of tightening environmental legislation (Directive 2009/29/EC) and increasing fuel costs. One of the key issues in this respect is to minimize the emissions released from processes. The increasing demands for process efficiency and the efforts to reduce harmful emissions have generated a number of challenges for industrial plants, and new kind of tools are needed to meet those challenges. Process data archives provide a potential source of information which can be utilized in optimization, improvement of productivity and reduction of emissions. Data-driven modeling is currently considered a useful way of diagnosing industrial processes in a diverse field.

We have presented earlier a modelling and optimization system, which can be used in monitoring and optimization of power plants and which is implemented on the Matlab-software platform (Mathworks, Natick, MA, USA). The software has been under constant development, and it currently includes new tools which are considered useful in diagnosing, not only combustion processes, but also other industrial processes. In the paper we will concentrate on those parts which are the latest advancements in the software. These include correlation analysis, calculation of process lags, variable selection and multivariate regression modelling.

The software consists of the following main parts:

- Data import: import and export data, rename and preselect variables etc.
- Data pre-processing: remove constants, filter, interpolate, create derivatives, change resolution of data etc.
- Data visualization: simple plotting, scatter plots, histograms, statistics
- Correlations and lags: calculate correlations, define changing correlations, define time lags
- Variable selection: select the most important variables using regression
- Modelling: multivariate regression, artificial neural networks

We will demonstrate the use of the software by analyzing a data set from a 63 MWth circulating fluidized bed (CFB) boiler fired by demolition wood. The data set includes 49 variables, has a resolution of 15 minutes and covers a one month's operational period of the boiler.

In the search for solutions to current environmental problems, it is evident that industrial processes have to become more energy efficient and environmentally friendly. Energy plants, for example, will have to be able to produce their energy with less emissions of harmful gas in the future. This necessitates the development of novel systems for process diagnostics. The software presented here provides a fast way of analyzing a large amount of process data and the results show that it provides a useful modeling tool for industrial applications. The software can be utilized in advanced process diagnostics which can become a part of the service business of plant manufacturers, for example.

Modeling Software for Advanced Industrial Diagnostics

Mika Liukkonen*, Mikko Heikkinen*, Teri Hiltunen**
Jari Kapanen***, Yrjö Hiltunen*

**Department of Environmental Science, University of Eastern Finland, P.O. Box 1627, FIN- 70211 KUOPIO
(e-mail: mika.liukkonen@uef.fi).*

***Foster Wheeler Ltd, P.O. Box 201, FIN- 78201 Varkaus, Finland*

****Andritz Ltd., P.O. Box 34, FIN-57101 Savonlinna, Finland*

Abstract: Modern process industry is nowadays confronting many challenges. Increasing fuel and material costs, for example, have made it necessary to improve process performance and efficiency. On the other hand, new environmental legislation has created a pressure to reduce process emissions. As it seems that the interest on model-based control and optimization will be increasing in the future, process history can potentially provide a source of information to be utilized in the optimization, improvement of productivity and cost-efficiency and in the reduction of emissions, for example. In this paper we demonstrate a piece of modeling software for advanced industrial diagnostics. The software includes tools for importing and exporting data, pre-processing and visualization tools, a computational tool for lag calculations and tools for performing variable selection and modeling. The software is programmed into standalone software built up in the Matlab platform. We demonstrate the use of the software by two industrial data sets: one from a circulating fluidized bed boiler fired by demolition wood and another from a chemical pulping process. The results show that the software provides an efficient tool for advanced industrial diagnostics.

Keywords: Software, process, analysis, modeling

1. INTRODUCTION

The energy efficiency of industry is recognized nowadays as a highly important matter because of tightening environmental legislation (Directive 2009/29/EC) and increasing fuel costs. Growing demands for process efficiency and the efforts to reduce harmful emissions have generated a number of challenges for industrial plants, and new kind of tools are needed to meet those challenges. At the same time it seems that the interest on model-based control and optimization is increasing (Blanco et al., 2009). Process data archives provide a potential source of information which could be utilized more in such applications, e.g. in the optimization, improvement of productivity and cost-efficiency and reduction of emissions in processes.

There is an increasing availability of measurement and other data in the modern industry (Giudici & Figini, 2009). These data may be related to materials, process performance, process equipment, maintenance, control, produced quality and so forth. It seems, however, that the use of process data in process improvement has not achieved a standard role. In the pulp and paper industries, for example, the scope of modeling and simulation applications has been only partial, which is largely because of the complexity of the processes (Blanco et al., 2009). Another possible reason for this is the difficulty of data analysis caused by the characteristics of the industrial process data, e.g. the large volume of data and

variables affecting the process. Combustion processes, for instance, are multivariable and the interactions of variables have to be considered carefully, which makes it a challenging process to manage (Joronen & Kerschbaum, 2008). On the other hand, it seems that engineers and managers are having difficulties in handling the overflow of process data (Wang, 2007). For these reasons, new valid tools are needed for advanced industrial diagnostics.

Data mining and applied statistical methods are currently considered as useful tools for extracting knowledge from industrial data (Giudici & Figini, 2009) and data-driven modeling is currently considered an advantageous way of diagnosing industrial processes in a diverse field (Fortuna et al., 2007; Heikkinen et al., 2009; Kadlec et al., 2009; Kalogirou, 2003; Liukkonen et al., 2011 a-b). We have presented earlier a modeling and optimization system (Heikkinen et al., 2009), which can be used in monitoring and optimization of power plants and which is implemented on the Matlab-software platform (Mathworks, Natick, MA, USA). The software has been under constant development, and it currently includes new tools which are considered useful in diagnosing, not only combustion processes, but also other industrial processes. In the paper we will concentrate on those parts which are the latest advancements in the software. These include correlation analysis, calculation of process lags, variable selection and multivariate regression modeling.

The software developed for advanced diagnostics can support efforts to improve process performance, as it can be utilized as a part of a performance analysis to discover complex dependences between process variables. We demonstrate the use of the software by analyzing two data sets from real industrial processes, one from a 63 MW_{th} circulating fluidized bed (CFB) boiler fired by demolition wood and another from a chemical pulping process.

2. COMPUTATIONAL METHODS

The software developed for advanced industrial diagnostics consists of the following main parts:

- *Import*: import and export data, rename and preselect variables etc.
- *Pre-processing*: remove constants, filter, interpolate, create derivatives, change resolution of data etc.
- *Visualization*: simple plotting, scatter plots, histograms, statistics
- *Correlations and lags*: calculate correlations, determine changing correlations, determine time lags
- *Variable selection*: select the most important variables using regression
- *Modeling*: multivariate regression, artificial neural networks

2.1 Pre-processing tools

Erroneous or missing data can complicate modeling, and therefore pre-processing is an important step of data analysis. Pre-processing of large datasets is often laborious manual work, however, which may multiply the time spent for analyses. For this reason, diagnostics software includes several sophisticated tools for different steps of preparing data.

Filtering of unreliable data is an essential pre-processing operation, which is often performed manually. Therefore, when datasets are large and the variables are filtered by thresholds, a practical filtering tool can save plenty of time. The advanced diagnostics software includes fixed boundary, low-pass and moving average techniques for filtering, and has a separate graphical interface for filtering. The software also includes tools for removing unreliable rows and constants conveniently.

Many data centric modeling methods require a complete data matrix, which means that the possible missing data must be compensated. Several methods have been proposed for that purpose (Little & Rubin, 1987; Schafer, 1997). A method used commonly and programmed also in this software is the simple linear interpolation algorithm, which fills the gaps in a table by drawing a straight line between two neighboring values and returning the appropriate values along that line. Despite this, all the modeling and statistical methods embedded to the software are programmed to accept missing data.

Derivative variables or soft sensor type of variables are used commonly for analyzing process data. Therefore a calculator tool for creating new derivative variables is included to the software.

2.2 Determination of process lags

Process lags can be considerable in the process industry and should therefore be considered carefully in the analysis. When dealing with relatively slow fluid flows, for instance, data associated with each time stamp may not be comparable as such. Process lags can be determined using a cross-correlation method, in which the correlations between variables are calculated in a time window.

The correlation coefficients between two variables are calculated in each time step and the maximum absolute value of these coefficients represents the process lag between these two variables. The lags between individual variables constitute a matrix, which can be used in determining the final lags with respect to each variable. Some of these maximum correlations may be insignificant (i.e. these lags are unreliable), however, so the final process lags are calculated by using the lags indicated by the most considerable correlations.

2.3 Variable selection

The aim of selecting variables is at selecting a subset p from the set of P variables without appreciably degrading the performance of the model and possibly improving it. Although exhaustive subset selection methods involve the evaluation of a very large number of subsets, the number to be evaluated can be reduced significantly by using suboptimal search procedures (Whitney, 1971). Therefore they are ideal for large data sets.

Sequential forward selection is a simple suboptimal method for selecting variables in which the variables are included in progressively larger subsets so that the prediction performance of the model is maximized. To select p variables from the set P :

- 1) Determine the variable that yields the best value for selected criterion.
- 2) Search for the variable that yields the best value with the variable(s) selected in stage 1.
- 3) Repeat stage 2 until p variables have been selected or a stopping criterion has been met.

2.4 Modeling tools

Multivariate regression can be used to model the relationship between two or more explanatory variables and a response variable by fitting an equation to observed data samples. A model with N observations and P variables is defined by (1):

$$y_i = b_0 + b_1x_{i1} + b_2x_{i2} + \dots + b_px_{ip} + \varepsilon_i, \text{ for } i = 1, 2, \dots, N \quad (1)$$

where y denotes the value of the response variable, x is the value of the predictor (explanatory) variable, b_0 is a constant, $b_1 \dots b_p$ equal the unknown coefficients to be estimated, and ε comprises the uncontrolled factors and experimental errors of the model. The fitting is performed by minimizing the sum of the squares of the vertical deviations from each data point to

the line that fits best for the observed data, which is known as least squares fitting.

The software also includes a modeling tool based on self-organizing maps (SOM) (Kohonen, 2001), which can be used for discovering and analyzing process states and optimizing processes. The use of the SOM tool in the monitoring of process states and process optimization has been demonstrated by Heikkinen et al. (2009).

3. RESULTS

3.1 Modeling of NO_x in a CFB boiler

Process and data

Fluidized bed combustion is a technology designed principally for converting solid fuels such as coal, peat, biomass or waste derived fuels into energy. Fuel flexibility and the ability to burn low-grade fuels are major advantages generally associated with fluidized bed combustion (Basu, 2006; Koornneef et al., 2007): circulating fluidized bed boilers (CFBs) can burn a wide spectrum of fuels without a major reduction in performance. For instance, the fuel flexibility allows CFBs to co-combust a wide variety of solid fuels, including fossil fuels such as coal, biomass-derived fuels such as wood and agricultural residue, peat, and even waste fuels like demolition wood (Coda Zabetta, 2009).

Nevertheless, fuel flexibility may also pose new challenges. The use of demanding heterogeneous fuels such as biomass not only increases the need for monitoring the process but also complicates the development of new methods for diagnosing and monitoring it. The quality of demolition wood, for example, tends to vary considerably depending on its origin and preparation before combustion, which makes the control of the CFB process demanding. In addition, varying quality of fuel can have undesired consequences such as an increased level of emissions, which are produced in complex chemical reactions. The effects of individual operating parameters on the released emissions cannot be easily separated from each other, which means that combustion management has to take all these effects into account (Joronen & Kerschbaum, 2008).

Process data for the present purpose were extracted from a database attached to a 63 MW_{th} CFB boiler fired by demolition wood. The size of the data matrix used as an example is 3 000 x 49 (3 000 rows, 49 variables in columns), covering thus a month (31 days) of operation.

Selection of variables

The data set is first averaged to have a resolution of 15 minutes. Then, constant variables are removed, because they do not bring any additional value to the model. The missing values of data (less than 0.5 % of input data) are replaced using linear interpolation.

Next, ten variables are selected using the NO_x concentration of flue gas as the model output. The results can be seen in Fig. 1. The NO_x model consisting of the ten selected

variables yields a correlation of 0.88 with the observed NO_x content.

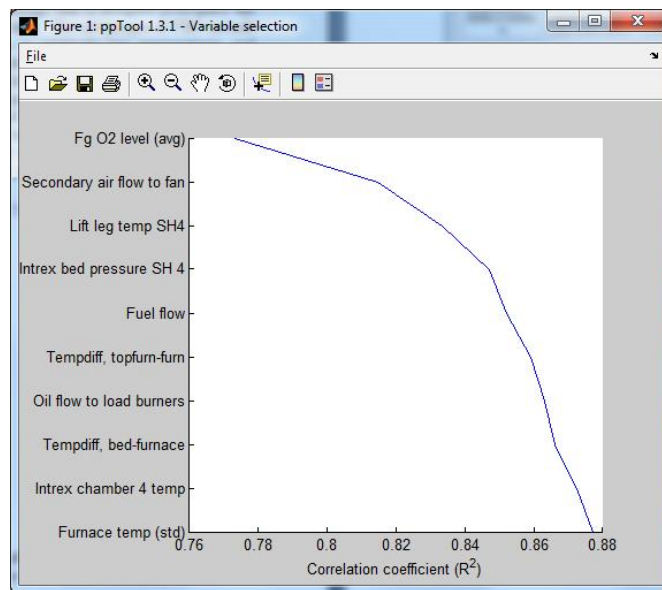


Fig. 1. A window showing the results of variable selection in the CFB case.

The model

The regression tool window of the advanced diagnostics software is presented in Fig. 2. The model for NO_x is constructed using the variables obtained by the variable selection tool. As can be seen, the regression tool outputs the model coefficients, the goodness of fit and two plots representing the performance of the model.

3.2 Modeling of pulp brightness in a chemical pulping process

Process and data

Chemical pulp production is performed by cooking the raw wood material together with chemicals to dissolve the binding agent (lignin), which ties the fibers together, from the wood. The remaining wood fibers form the chemical pulp, which is the principal material for producing paper and board. (www.prowledge.com)

The first phases of producing chemical pulp are the debarking of the logs in a debarking drum, chipping of the debarked logs, and screening of the wood chips. Cooking of the chips occurs in a large digester. In the sulfate method the chips are cooked in an alkaline chemical solution, or *liquor*, after which the pulp is washed. The pulp is brown in color at this stage, so it can be bleached to improve its brightness and cleanliness. This occurs either by removing or brightening the colored substances, e.g. residual lignin, in the pulp. Various bleaching chemicals can be used such as oxygen, chlorine dioxide or hydrogen peroxide. After bleaching the pulp is screened, dried and baled. (www.prowledge.com)

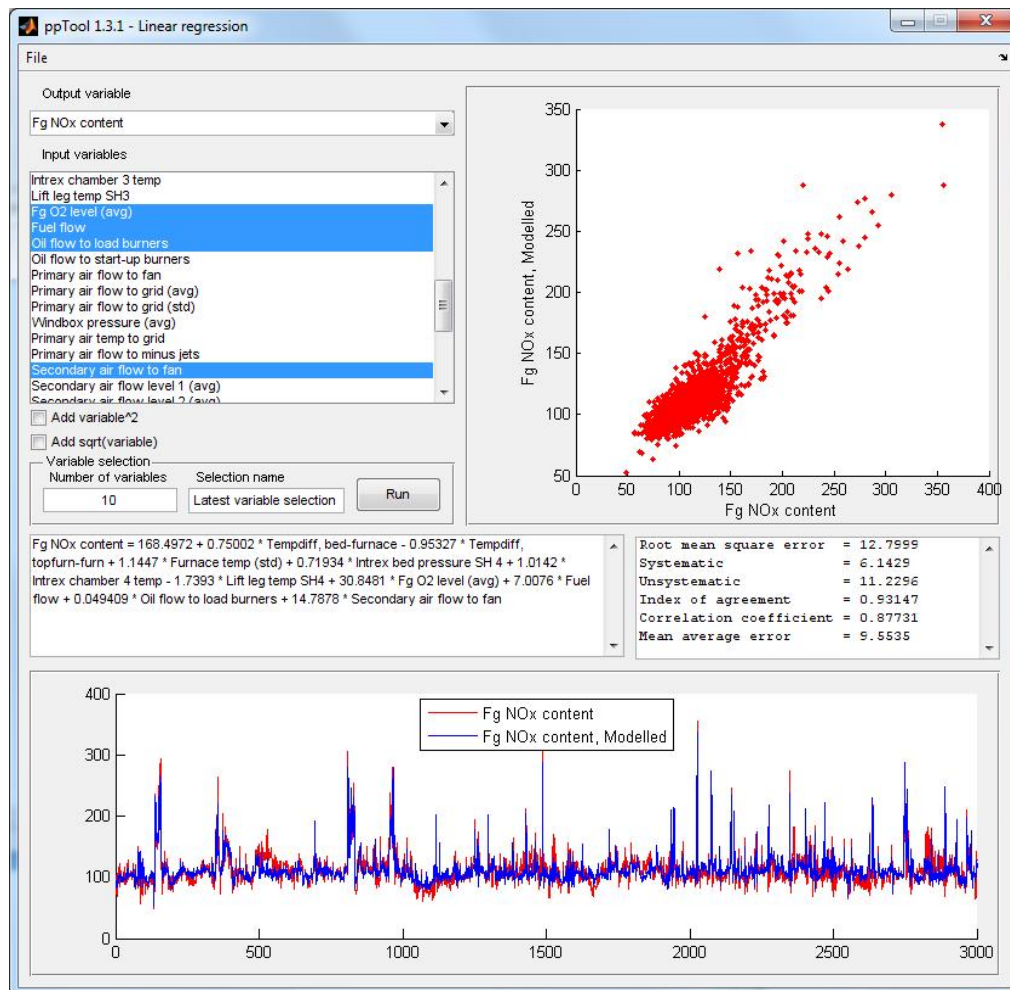


Fig. 2. The regression tool window of the software and a model for the NO_x content of flue gas in a CFB boiler using the selected variables.

The process data used in this study was extracted from databases of a sulfate pulp mill. All the variables potentially affecting the brightness of the pulp in the bleaching stage of the process are included to the dataset. The time period is one year and the resolution of the data is 15 minutes. The size of the complete dataset is 35 040 rows.

Determination of process lags

Outliers and unreliable data are marked as missing data using the software. It would be possible to estimate the process lags on a theoretical basis if flows and volumes are given. In this case, however, the process lags between the main stages of bleaching are estimated using the software tool. Brightness of the pulp in the sequential stages of the bleaching process was chosen for analysis, because brightness is measured in every stage and it is considered an important quality parameter.

The software calculates the correlations between variables within a given time window. In this case, the time dimension is 40 (10 hours). In other words, the correlation is calculated

40 times for each variable, with 40 different time dimensions within a 10-hour period of time. Thus the software is given the assumption that the length of the lag can be anything between 0 and 10 hours. The dimension which yields the largest absolute value of the correlation coefficient represents the lag. Then, the first brightness parameter (*D stage brightness*), which is measured at the beginning of the bleaching process, is defined as the reference variable to be able to compare the resulting lags between variables. The information of the resulting matrix, which can be seen in Fig. 3, comprises the lags between all variables and can be used in estimating the lags with respect to the reference variable. Finally, the determined process lags are those indicated by the most considerable correlations. The process lags determined for the variables which indicate the brightness of the pulp in different stages of the bleaching process are shown in Table 1.

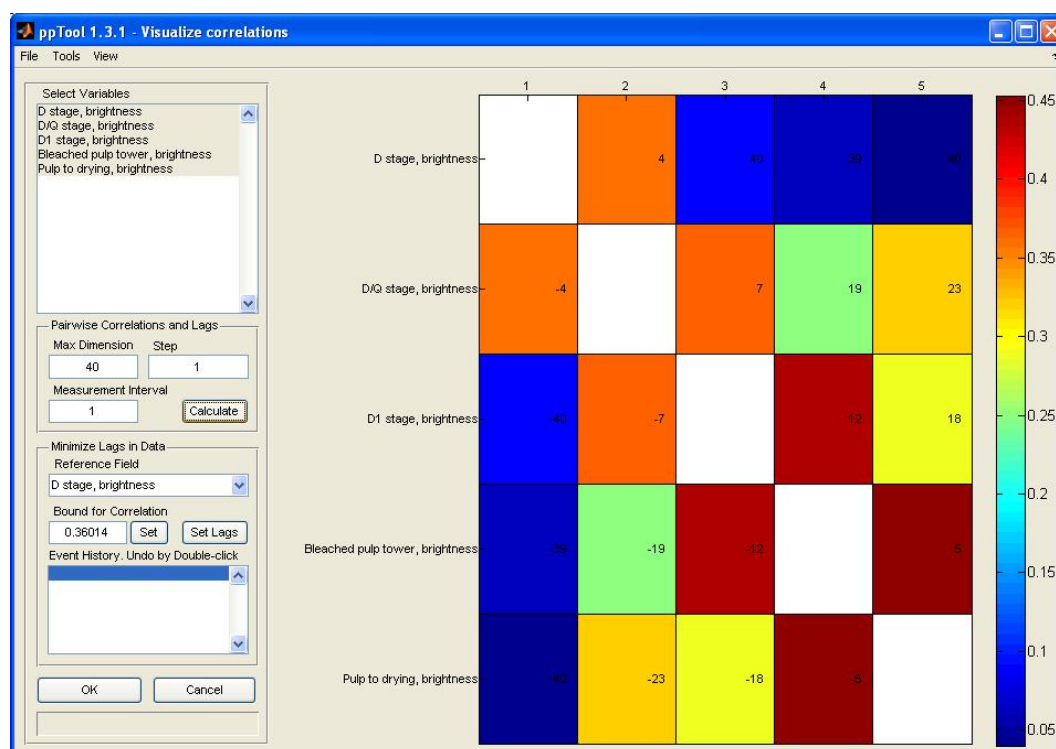


Fig. 3. The graphical interface of the lag analysis tool based on cross correlation. Colors represent the correlation coefficient between variables and a value inside a cell shows the number of data rows indicating the length of the lag (the dimension in which the absolute value of the correlation coefficient is largest).

Table 1. The calculated process lags.

Variable	Lag (data rows)	Lag (hours)
D stage brightness	0	0
D/Q stage brightness	4	1
D1 stage brightness	11	2.75
Bleached pulp tower, brightness	23	5.75
Pulp to drying, brightness	28	7

Table 2. Results for modeling the brightness of pulp.

	Original dataset	Embedded dataset
Root mean square error	0.461	0.379
Index of agreement	0.642	0.812
Correlation coefficient	0.521	0.708
Mean average error	0.354	0.230

The model

The multivariate regression tool of the software is used for the modeling of brightness in bleached pulp. Bleaching chemicals, kappa variables and brightness variables are used as inputs (10 variables). Two models are calculated; (a) using the original dataset and (b) using a dataset in which the variables are embedded using the information from the lag

calculations. The results (see Table 2) indicate that the model based on the embedded dataset yields better results. The correlation coefficient, for example, is raised from 0.52 to 0.71.

4. DISCUSSION

While new solutions are being sought to create cleaner alternatives at all fronts, it is evident that also industrial processes have to become more energy efficient and environmentally friendly. Energy plants, for example, will have to be able to produce their energy with less emissions of harmful gas in the future. This can be difficult because of numerous affecting variables and the complex dynamics present in the combustion process. Minimization of process emissions is a major issue also in chemical pulping, but optimizing the process may also decrease the consumption of energy and chemicals. As in most continuous processes, the derivation of dependences can be difficult in the chemical pulping process, because the lags are not known thoroughly and the control loops are complex.

For these reasons novel systems for advanced process diagnostics are needed. The software presented here provides a fast way of analyzing a large amount of process data and the results show that it provides a useful modeling tool for industrial applications. The software can be utilized in advanced process diagnostics which can become a part of the service business for manufacturers of process equipment and devices, for example.

The performance analyses of processes often include data analyses to discover the best possible control strategy based on variable interdependences, which can be complex and

multivariable. Naturally performing these analyses cannot be fully automated, since they require empirical knowledge of the process, which only an experienced process expert can possess. The software has been designed for analyzing large data sets, which are typical for process industry, since measurement data are usually collected all the time from different process stages. Nonetheless, constructing data-based and especially non-linear models requires specialized expertise from the software users, not only on the modeling methods but also on the process itself. The generic modeling tool may thus be used by process experts, who are able to analyze and validate the results before taking them into operational use. On the other hand, a skilled process expert can automate laborious data processing stages using the software, which facilitates the routine and regular analysis work and so enables more efficient performance analyses.

5. CONCLUSIONS

The software proposed for advanced industrial process diagnostics can support efforts to improve process performance and to determine the optimal control strategy, for example. The software exploits process history, which offers a useful source of information and which can help in the improvement of process efficiency or in the reduction of process emissions, for example. The software can be utilized as a part of a performance analysis to discover complex dependences between process variables.

ACKNOWLEDGMENTS

The authors would like to thank the Finnish Funding Agency for Technology and Innovation (*Tekes*) for funding two research projects, *Enefir* and *Dynergia*, which have provided the framework for the research.

REFERENCES

- Basu, P. (2006). *Combustion and Gasification in Fluidized Beds*. CRC Press, United States of America.
- Blanco, A., Dahlquist, E., Kappen, J., Manninen, J., Negro, C., Ritala, R. (2009). Use of Modelling and Simulation in the Pulp and Paper Industry. *Mathematical and Computer Modelling of Dynamical Systems*, 15(5), 409-423.
- Coda Zabetta, E., Hiltunen, M., Moulton, B., Hotta, A. (2009). Biomass and Waste Co-combustion – European Experience. In *Proc. Electric Power Conference*, Rosemont, Illinois, USA. Available via: http://www.fwc.com/publications/tech_papers/files/TP_F_IRSYS_09_01.pdf
- Fortuna, L., Graziani, S., Rizzo, A., Xibilia, M.G. (2007). *Soft Sensors for Monitoring and Control of Industrial Processes*. Springer-Verlag, London.
- Giudici, P., Figini, S. (2009). *Applied Data Mining for Business and Industry*, 2nd edition. John Wiley & Sons, Ltd.
- Heikkinen, M., Hiltunen, T., Liukkonen, M., Kettunen, A., Kuivalainen, R., Hiltunen, Y. (2009). A Modelling and Optimization System for Fluidized Bed Power Plants. *Expert Systems with Applications*, 36, 10274-10279.
- Joronen, T., Kerschbaum, R. (2008). Advanced Controls – Fuzzy Logic for Fluidized Bed Boiler. *AT&P journal*, PLUS2, 24-28.
- Kadlec, P., Gabrys, B., Strandt, S. (2009). Data-driven Soft Sensors in the Process Industry. *Computers and Chemical Engineering*, 33, 795-814.
- Kalogirou, S.A. (2003). Artificial Intelligence for the Modeling and Control of Combustion Processes: A Review. *Progress in Energy and Combustion Science*, 29, 515-566.
- KnowPulp® – Learning Environment for Chemical Pulping and Automation. Prowledge Oy, www.prowledge.com
- Kohonen, T. (2001). *Self-Organizing Maps*. 3rd ed. Springer-Verlag Berlin Heidelberg, New York.
- Koornneef, J., Junginger, M., Faaij, A. (2007). Development of Fluidized Bed Combustion - An Overview of Trends, Performance and Cost. *Progress in Energy and Combustion Science*, 33, 19-55.
- Little, R.J.A., Rubin, D.B. (1987). *Statistical Analysis with Missing Data*. John Wiley & Sons, New York.
- Liukkonen, M., Heikkinen, M., Hiltunen, T., Hälikkä, E., Kuivalainen, R., Hiltunen, Y. (2011a). Artificial Neural Networks for Analysis of Process States in Fluidized Bed Combustion. *Energy*, 36(1), 339-347.
- Liukkonen, M., Hiltunen, T., Hälikkä, E., Hiltunen, Y. (2011b). Modeling of the Fluidized Bed Combustion Process and NO_x Emissions Using Self-Organizing Maps: An Application to the Diagnosis of Process States. *Environmental Modelling & Software*, 26(5), 605-614.
- Schafer, J.L. (1997). Analysis of Incomplete Multivariate Data. *Monographs on Statistics and Applied Probability*, no 72. Chapman & Hall, London.
- Wang, K. (2007). Applying Data Mining to Manufacturing: the Nature and Implications. *Journal of Intelligent Manufacturing*, 18, 487-495.
- Whitney, A.W. (1971). A Direct Method of Nonparametric Measurement Selection. *IEEE Transactions on Computers*, C-20, 1100-1103.

Paper 6

Title: WATER CONTENTS OF WOOD AND PEAT BASED FUELS BY ANALYSING TIME DOMAIN NMR DATA

Ekaterina Nikolskaya, Mika Liukkonen, Jukka-Pekka Männikkö, Risto Kauppinen, Leonid Grunin, Yrjö Hiltunen
University of Eastern Finland, Finland

Keywords: NMR, Water content, Biofuels, Wood, Peat

The water content (WC) of fuel in particular is one of the most important quality parameters for biofuels, such as wood and peat. However, a good online method to quantify the water content is currently unavailable because of complex nature of biological water. For example in wood, water can be mainly in three different forms; liquid in pores (free water), physical and chemical bonded in cell walls (bonded water) and vapour in pores. Water can also be on the surface of wood, when water content is above 60%, or in the ice form, when temperature is below 0 °C. Earlier water content measurements from biofuels using NMR have shown that it could be potentially the method-of-choice for quantifying water. Important questions to be addressed include whether NMR method are cost effective and practical in industrial settings.

A portable low-resolution nuclear magnetic resonance (NMR) analyzer has been purchased at the University of Eastern Finland for testing the NMR method for applicability for industrial measurements of water content. The permanent magnet of 0.5 T has dimension of 140x190x150 mm weighting 19 kg. Water content measurements were made over a broad range of moisture contents for several genuine fuels from an energy company. The wood and peat samples were ground into powder for NMR samples. The sample volume was approximately 1.5 cm³. NMR measurements were compared with the standard method for water content determination, in which the mass of the sample is measured before and after oven drying at reduced pressure.

Free Induction Decay (FID) signals were acquired for all samples and three values for each magnitude FID were calculated as follows: (1) the long time constant component A_l of FID. (2) The short time constant component A_s of FID. (3) The ratio of A_l / A_s . The A_s and A_l values and (A_l/A_s) ratio were calculated for all samples. The reference water content was determined as a function of the (A_l/A_s) ratio for each sample. There was a clear 2th order relationship between these values ($R^2 = 0.987$). Water content values of fuels using NMR data and the model were in good agreement with water content measurements with the standard test employing oven drying. The correlation coefficient between these two methods was 0.997 and the RMS error 1.14 %. The errors can be partly due to procedures used in NMR measurement and partly due to the oven drying method. The same measurements have been made for peat samples.

The current results show that one can use the same model for a variety of samples, which indicates that the NMR method can be used without additional calibration both for different kinds of samples. The calibration needs to be performed only once for given NMR probe and NMR device setup, which makes the method user-friendly and fast to implement.

The results of the study demonstrate that the NMR method is as accurate as the gold-standard test. Importantly, NMR water content measurement can be performed in 15 seconds, in contrast to the oven drying which takes up to 20 hours. Our results show that the NMR

Water Contents of Wood and Peat Based Fuels by Analyzing Time Domain NMR data

Ekaterina Nikolskaya*, Mika Liukkonen*, Risto A. Kauppinen***, Leonid Grunin** and Yrjö Hiltunen***

*Department of Environmental Science, University of Eastern Finland, P.O. Box 1627, FIN- 70211 KUOPIO
(e-mail: firstname.lastname@uef.fi).

** Mari State Technical University, Yoshkar-Ola, Russia
(e-mail: mobilenmr@hotmail.com)

*** University of Bristol, Bristol, UK

Abstract: The time-domain nuclear magnetic resonance relaxometer (TD-NMR) was used to determine water contents of wood and peat based fuels and their mixtures. Measurements were made over a broad range of water contents for various fuels. NMR results were compared to the values estimated by standard method, where mass of a sample is measured before and after oven drying at reduced pressure. Water content measurements using these two methods were in a good agreement. The correlation coefficient for all samples was 0.99 and the standard deviation 2.5 %. These results demonstrate that the TD-NMR method is fast and accurate and it can be used without additional calibration for any wood and peat based fuels.

Keywords: Water content, Nuclear magnetic resonance, Gravimetric method, Wood, Peat, Solid fuels

1. INTRODUCTION

In recent years, the increasing use of biomass as a fuel in the production of energy and the tightening environmental legislation have created a need for faster and more exact determination of biomass properties. Generally speaking, the most important fuel characteristics are the calorific value, chemical composition, moisture content, ash content, composition of ash, melting behavior of ash and fuel handling properties such as density and particle size [1]. In terms of international emissions trading, the moisture content, the carbon content in dry matter and the calorific value are the variables included in the calculation of emission factors for solid biofuels.

The water content of fuel in particular is one of the key parameters for biofuel quality, because it affects directly the accessible amount of energy. Nyström and Dahlquist [2] have gleaned potential methods, such as X-ray, near infrared spectroscopy (NIR), radio frequency measurements (RF), microwave measurements (MW) and nuclear magnetic resonance (NMR), bear potential to become useful for process control. However, moisture content is usually determined by a standard method, where the mass of the sample is measured before and after oven drying [3].

Nuclear magnetic resonance (NMR) is a new respectable method for measuring the water content [4-9]. NMR equipment have been used in moisture content measurements mostly in laboratory conditions, in which it has been applied to wood, food supplies, soil samples, oil and coal [10-14].

Nyström and Dahlquist [2] propose that all methods, including the NMR method, should be calibrated for every biofuel mixture used. The recent results of Merela et. al. [4] confirmed that the NMR method is comparable in terms of its accuracy and reliability to the gravimetric method, regardless of the species of wood. The results [4] demonstrate that the water or moisture content in wood samples can be determined instantly based on its mass and the amplitude of its NMR FID signal.

The results of our earlier paper [15] also demonstrate that time-domain nuclear magnetic resonance (TD-NMR) method is fast and accurate and, importantly, it can be used without additional calibration for wood-based fuels. On the other hand, it would be interesting to know whether this concerns also different fuel types and their mixtures. Peat, for example, is widely used in Finland for producing energy, and it is often burned in combination with wood-based fuels. Thus, a generic measurement not sensitive to fuel type would be a great advancement. In addition, actual online measurements for moisture and other important biomass properties have not been implemented using the NMR method.

The objective of this study was to examine the potential of a TD-NMR method to measure water content in wood and peat based fuels and their mixtures. In this paper we present more results concerning the measurement of wood fuels, which support the earlier findings [15]. Furthermore, we present results for measuring the water content of peat and fuel mixtures of wood and peat.

2. MATERIAL AND METHODS

2.1 Fuel samples

Water content measurements were performed over a broad range of moisture contents for three genuine fuels from an energy company. The wood samples were ground into powder (the particle size about 3 mm). The sample volume in NMR tubes was approximately 0.6 cm³. The summary of the samples is shown in Table 1.

Water content in wood is defined in terms of the initial weight of wood sample and the final weight of the sample after oven drying to constant weight at 105±2°C and it can be calculated using the following equation:

$$WC\% = \frac{\text{Original weight of wood} - \text{oven dry weight of wood}}{\text{Original weight of wood}} \times 100\% \quad (1)$$

Table 1. The summary of the samples for modelling

Sample	Description	WC range, %
Wood	milled to 2-3 mm of particle size	12-69
Peat	sifted by 4 mm sieve	38-64
Mixture of wood and peat	- 50% of sifted peat and 50% of milled wood	23-57
	- 90% of sifted peat and 10% of sifted wood	39-65
	- Original mixtures (sifted by 4 mm sieve) with content of approximately 10% of wood	9-56

2.2 NMR measurements

The TD-NMR measurements were done using a mobile NMR analyzer Spin Track [16] with a ¹H resonance frequency of 25 MHz. The permanent magnet of 0.6 T has dimension of 140x190x150 mm weighting 19 kg. The diameter of sensor hole was 10 mm. Free Induction Decays (FID) were recorded with an acquisition rate of 3 Mega samples per second; excitation pulse duration was 3.7 microseconds. Digital receiver console provided quadrature acquisition with the ringing time of around 12-16 microseconds.

The measurements were performed at room temperature. After the NMR analysis was completed, water contents were determined by oven drying of each NMR sample at 105°C over night.

Complex FID signals were acquired for all samples and magnitudes of FIDs were calculated using the following equation:

$$Magn = \sqrt{\text{Re}^2 + \text{Im}^2} \quad (2)$$

where Re is the real part and Im the imaginary part of a FID. The shape of the FID signal from wet wood sample with the water content value of 61 % is shown in Figure 1.

A long time constant component A_{long} for each FID signal was calculated as the average value of FID magnitudes in the range from 40 μs to 160 μs (area of magnitude values is marked by red color in Figure 1).

3. RESULTS AND DISCUSSION

TD-NMR device was used to determine water contents of wood and peat based fuels and their mixtures. Measurements were made over a broad range of water contents for various fuels. FID of wood sample can be presented as a two-component signal (See Figure 1), where the short time constant component A_{short} is the NMR signal from bulk matter and water rigidly bonded to the material structure. The long time constant component A_{long} arises from free water. It seems that the size of long time constant component increases with the water content. Typical FIDs of wood and peat samples are shown in Figures 2 and 3, respectively. The results of repeated measurements are summarized in Table 2.

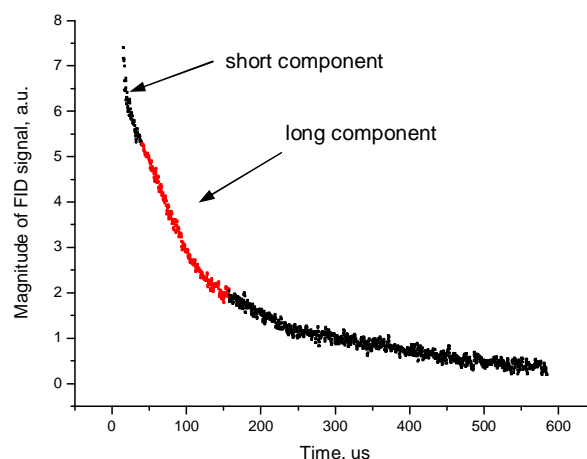


Figure 1. Magnitude of a Free induction decay (FID) signal from a wood sample with WC = 61 %. Magnitude values, which have been used for calculation of long time constant component A_{long} , are marked by red color

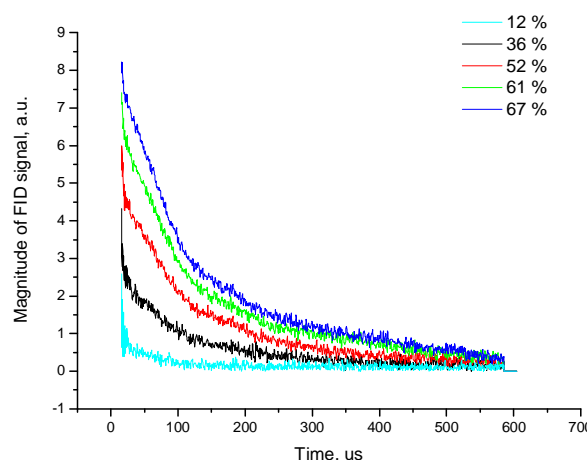


Figure 2. Magnitudes of FID signals from five wood samples with different water contents.

Table 2. Results of repeated measurements.

Sample	Water content (%)	Std of A_{long} (%) ^{a)}	Std of water content (%) ^{b)}
Wood	20	2.92	0.27
Wood	56	1.24	0.38
Peat	42	2.09	0.38
Peat	44	1.56	0.56

a) Standard deviation of 10 separate NMR measurements using the same sample.

b) Calculated using equation (3).

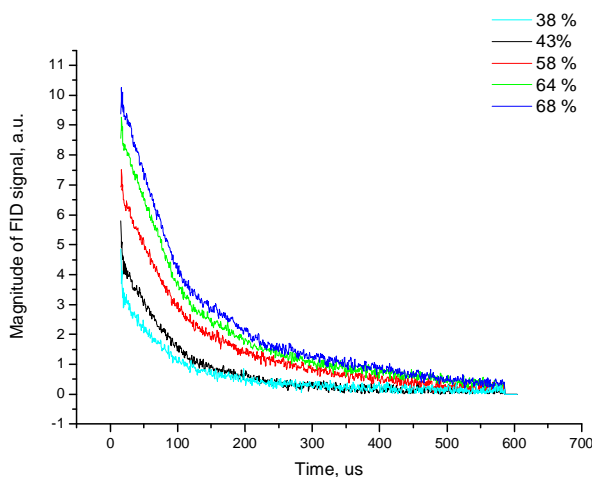


Figure 3. Magnitudes of FID signals from five peat samples with different water contents.

However, if the same model can be used for both wood and peat samples, the FIDs have to be similar with the same water contents. The FIDs of a wood and a peat samples with almost the same water contents are presented in Figure 4. As can be seen, the FIDs are almost identical, which indicate the usability of the NMR method in cases of different solid fuels.

NMR measurements were compared with the standard method for water content determination, in which the mass of the sample is measured before and after oven drying at reduced pressure. The mean values of the long components A_{long} were calculated for all samples. In Figure 5, the reference water content is plotted as a function of the mean value for each sample. There is a clear 2nd order relationship between these values. In our final model, the water content of the sample can be determined as follows:

$$WC = a * A_{long}^2 + b * A_{long} + c, \quad (3)$$

where $a = -2.458 \times 10^{-5}$, $b = 0.0778$ and $c = 7.3396$. Water content measurements using NMR and equation (3) are in a good agreement with water content measurements with the standard method employing oven drying, as can be seen in Figure 6. The correlation coefficient between these two methods for all samples is 0.99 and the standard error 2.5 %. The errors can be partly due to procedures used in NMR measurement and partly to the oven drying method. Repeated measurements by the same sample (See Table 2) show that the error in the A_{long} is not more than 3 % and so the absolute error in water content value using equation (3) is less than 0.5 %, which is consistent with data reported for the alternative methods [3].

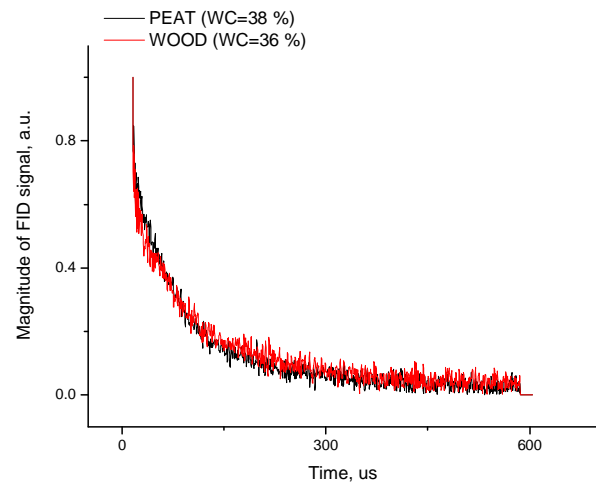


Figure 4. Magnitudes of FID signals from a wood (red line) and peat (black line) samples with similar water contents.

4. CONCLUSIONS

In the present paper, water content measurements based on NMR were performed over a broad range of moisture for wood and peat fuels. The results of the study demonstrate that the NMR method is as accurate as the gold-standard test. Importantly, NMR water content measurement can be performed very fast, in contrast to the oven drying which takes up to 20 hours.

The current results also show that one can use the same model for wood and peat fuels without additional calibration. The calibration needs to be performed only once for given NMR probe and NMR device setup, which makes the method user-friendly and fast to implement. The results indicate that the NMR method can be successfully applied to water content measurements of wood and peat based fuels with a great potential for industrial scale application.

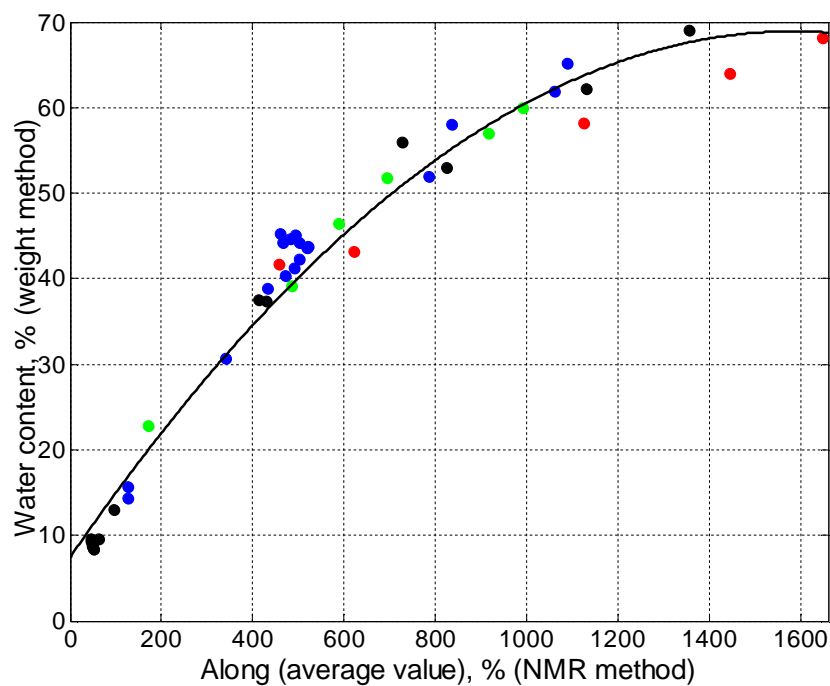


Figure 5. Water content measured by oven drying method as a function of the sum of FID. The solid line is a 2nd order fit to the measured points.

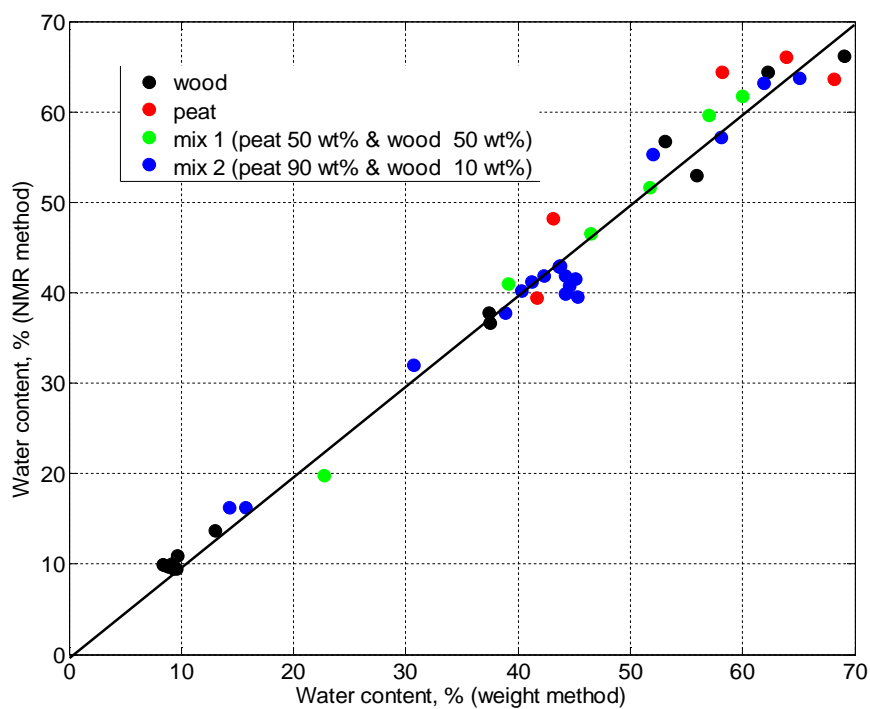


Figure 6. A comparison of the measurement of water content in wood samples using NMR and oven drying methods.

ACKNOWLEDGMENTS

The authors would like to thank the Finnish Funding Agency for Technology and Innovation (*Tekes*) for funding a research project, *Dynergia*, which has provided the framework for the research.

REFERENCES

1. Demirbas A. Biofuels. Biofuels. Securing the Planet's Future Energy Needs. 2nd Printing. 2009, X, 336 p.
2. Nystrom J, Dahlquist E. Methods for determination of moisture content in woodchips for power plants - a review. *Fuel* 2004;83: 773-779.
3. Standard Numbers CEN/TS 14774/15414. Solid biofuels. Methods for the determination of moisture content.
4. Merela M, Oven P, Sersa I, Mikac U. A single point NMR method for an instantaneous determination of the moisture content of wood. *Holzforschung* 2009;63: 348-351.
5. Barale PJ, Fong CG, Green MA, Luft PA, McInturff AD, Reimer JA, Yahnke M. The use of a permanent magnet for water content measurements of wood chips. *IEEE Transactions on Applied Superconductivity* 2002;12:975-978.
6. Rosenberg E, Schatvet J, Høydal K. In-kiln measurements of moisture content in timber at Moelven Våler AS. Third European COST E15 Workshop on wood drying: softwood drying to specific end-uses, Helsinki, Finland; 2001. p.1-9.
7. Elder T, Labbe N, Harper D, Rials T. Time domain-nuclear magnetic resonance study of chars from southern hardwoods. *Biomass & Bioenergy* 2006; 30: 855-862.
8. Grunin L, Blumich B. Resolving chemical shift spectra with a low-field NMR relaxometer. *Chemical Physics Letters* 2004; 397: 306-308.
9. Blumich B, Perlo J, Casanova F. (2008) Mobile single-sided NMR. *Progress in Nuclear Magnetic Resonance Spectroscopy* 52:197-269.
10. Hartley, I.D., Kamke, F.A., Peemoeller, H. (1994) Absolute moisture content determination of Aspen wood below the fiber saturation point using pulsed NMR. *Holzforschung* 48: 474-479.
11. Grunin YB, Grunin LY, Nikolskaya EA. Pulsed NMR method for determining the thermodynamic characteristics of adsorption processes in biopolymers, *Russian Journal of Physical Chemistry A* 2007; 81: 1165-1169.
12. Grunin L.Y., Nikolskaya E.A., Karasev D.V. Application of Solid Echo pulse sequence for measurement of solid fat content by proton magnetic relaxation method. *Factory laboratory. Diagnostics of materials.* 2009. V.75. №12. P.37-39.
13. ISO 10565:1998. Oilseeds - Simultaneous determination of oil and water contents - Method using pulsed nuclear magnetic resonance spectrometry.
14. Grunin L.Y., Kanarskij A.V., Sochkova I.N. Kanarskaya Z.A., Ahmadyshin R.A. Express-method of determination of protein in yeast and yeast products by NMR relaxometer. *Factory laboratory. Diagnostics of materials.* 2008. V.74. №1. P.13-15
15. Männikkö JP, Grunin L, Nikolskaya E, Kauppinen RA, Hiltunen Y. Time domain nuclear magnetic resonance analyzer for water content determination of wood fuels. Submitted to *Fuel*.
16. Resonance Systems Ltd, Available from: <http://www.nmr-design.com/index.php>.

method can be successfully applied to water content measurements of wood fuels with a great potential for industrial scale application.

Paper 7

Title: Modeling and control of gas lifted oil field with five oil wells

Roshan Sharma, Kjetil Fjalestad, Bjørn Glemmestad
Telemark University College, Norway

Keywords: Gas lifted oil wells, cascade control, droop control, dynamic modeling, simulation

Distribution and control of lift gas available for a cluster of gas lifted wells in an oil field is necessary for maximizing total oil production. This paper describes a simple dynamic model of the oil field developed from mass balances at different sections of the oil wells. Dynamic behavior of the oil wells is studied by open loop simulations. For proper distribution of the available gas, the pressure of the common gas distribution manifold and the lift gas flow rates through each gas lift choke valves should be controlled when there is variation in the supply of the lift gas. Four control strategies namely cascade control, droop control, droop control with integral action and pressure control with one swing producer are presented. The total available lift gas will be completely utilized by the five oil wells without demanding any extra gas requirement.

Modeling and Control of Gas Lifted Oil field with five oil wells

Roshan Sharma*, Kjetil Fjalestad** and Bjørn Glemmestad*

* Department of Electrical Engineering, Information Technology and Cybernetics, Telemark University College, Porsgrunn, Norway

e-mail: roshan.sharma@hit.no , bjorn.glemmestad@hit.no

** Statoil Research Center, Porsgrunn, Norway

e-mail: kfja@statoil.com

Abstract: Distribution and control of lift gas available for a cluster of gas lifted wells in an oil field is necessary for maximizing total oil production. This paper describes a simple dynamic model of the oil field developed from mass balances at different sections of the oil wells. Dynamic behavior of the oil wells is studied by open loop simulations. For proper distribution of the available gas, the pressure of the common gas distribution manifold and the lift gas flow rates through each gas lift choke valves should be controlled when there is variation in the supply of the lift gas. Four control strategies namely cascade control, droop control, droop control with integral action and pressure control with one swing producer are presented. The total available lift gas will be completely utilized by the five oil wells without demanding any extra gas requirement.

Keywords: Gas lifted oil wells, cascade control, droop control, dynamic modeling, simulation

1. Introduction

Production of oil from a naturally flowing oil well causes a gradual reduction of the reservoir pressure as time passes. As long as the reservoir pressure is sufficient to counter balance the sum of the different pressure losses occurring along the flow path of the fluid (eg: hydrostatic and frictional pressure drop), the oil stream from the reservoir reaches the surface without the need of any external assistance (Takacs, 2005). However, as more fluid is extracted from the reservoir, the reservoir pressure reduces to a value less than the total pressure losses in the well and the fluid flow from the reservoir stops. The well is said to be 'dead' when the well's reservoir pressure cannot lift the liquid column produced from the reservoir and the production of oil stops (American Petroleum Institute, 1994).

Among several artificial lifting methods, this paper focuses on the use of continuous flow gas lifting mechanism. In continuous flow gas lifting, a high pressure natural gas supplied by a compressor is continuously injected into the tubing from the annulus at a proper depth (see Figure 2). The injected gas reduces the density of the multiphase fluid (mixture of oil, gas and water) in the tubing thereby reducing the flow resistance (flowing pressure losses) in the tubing and enabling flow again (Brown and Beggs, 1977).

An oil well responds differently to low and high gas lift injection rate as shown in Figure 1. As the lift gas flow rate is increased from low injection flow rate, the oil production increases, becomes maximum at some optimal lift gas flow rate and then start to decrease again. This is due to the fact

that at very high gas injection rate, the effect of the frictional losses (which is a function of the square of the lift gas velocity) in the tubing will be dominant and the bottom hole pressure will start to increase. It is also due to increase in the back-pressure caused by the accumulation of more and more gas in the tubing due to increased lift gas injection rate. This behavior of gas lifted oil well demands for design and development of a control system that will control the gas flow rate injected into the tubing for controlling the oil produced from the well.

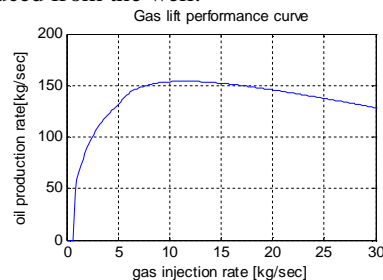


Figure 1: Gas lift performance curve of a typical oil well

Moreover, for a field with multiple oil wells where lift gas is supplied from a common source (see Figure 3), it is important to distribute the lift gas among the oil wells properly. Lift gas flow rates for each oil well and the pressure in the gas distribution manifold should be controlled.

The main objective of this paper is to develop a simple model of a gas lifted oil field with five oil wells, study the dynamic behavior of the oil field under varying operating conditions and then use the model for designing, developing and simulating four different control strategies for proper distribution of the lift gas. For all the simulation results in the paper, MATLAB has been used as the tool for simulation.

Automatic control of gas lifted oil well has been studied by various authors. Automation system for gas lifted wells operating under constraints of high availability of lift gas has been proposed by Camponogara et al. (2010). Instability of gas lifted oil wells and strategies to control the heading problems have been studied by Jansen et al. (1999), Plucenio (2002), Eikrem et al. (2002 and 2004a), Dalsmo et al. (2002), Imsland et al. (2003), Plucenio et al. (2006) and Scibilia et al. (2008). Control of gas lifted oil well along with optimization using non-linear MPC has been proposed by Plucenio et al. (2009). Sliding Mode Control (SMC) strategies have been proposed by Di Bernardo et al. (2002), Anguola et al. (2005a), Pagano et al. (2008) and Pagano et al. (2009) to control the production choke valve for controlling the slug flow oscillations in the oil well. Non-linear model-based back stepping control applied for stabilization of unstable flow in oil wells has been proposed by Kaasa et al. (2007).

2. Simple dynamic model of oil well

A simple model of a gas lifted oil well is developed taking into account all the components of a typical gas lifted oil well as shown in Figure 2.

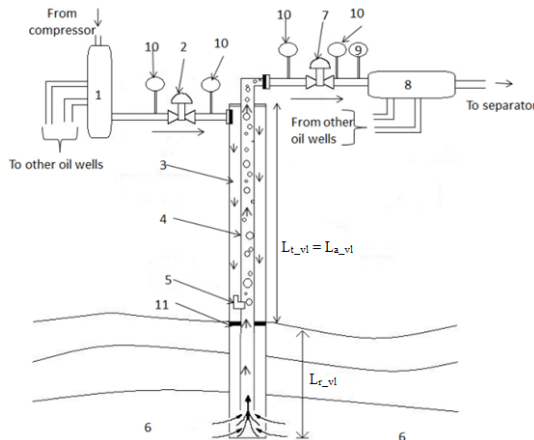


Figure 2: Different components of a gas lifted oil well

1. Lift gas distribution pipeline
2. Gas lift choke valve
3. Annulus
4. Tubing
5. Gas injection valve
6. Reservoir
7. Production choke valve
8. Gathering manifold
9. Multiphase meter
10. Pressure and temperature transducers
11. Packer

$L_{t-vl} = L_{a-vl}$ = vertical length of tubing/annulus above the gas injection point

L_{t-vl} = vertical length of tubing below the gas injection point

Figure 3 shows a schematic of an oil field with five oil wells and with a common gas distribution pipeline and a common gathering manifold. The compressor outputs a highly pressurized lift gas for injection (w_{gc}) into the gas distribution pipeline. The lift gas enters into the annulus of each well from this common gas distribution manifold. The flow rate of the lift gas to be injected into each well (w_{ga}^i , superscript i denotes i^{th} oil well for all symbols) is controlled by the gas lift choke valve present in the well head of each oil well.

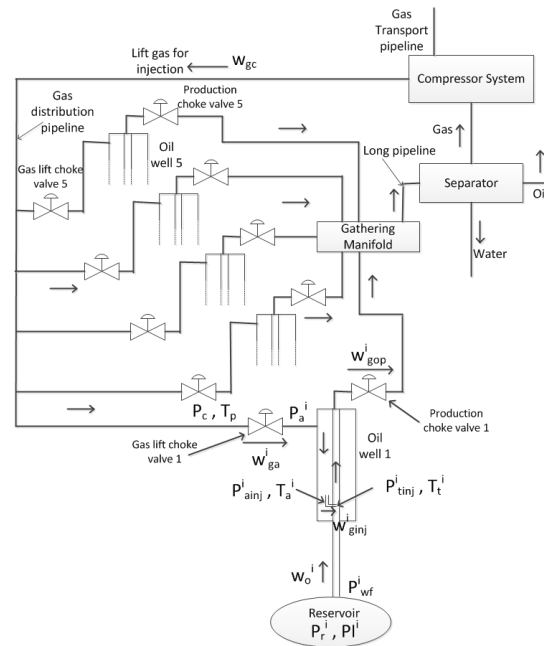


Figure 3: Schematic for an oil field with five oil wells

From the annulus, the high pressure lift gas is injected into the tubing (w_{ginj}^i) at a proper depth through the gas injection valve (see Figure). The gas injection valve is designed in a way that the back flow of fluid into the annulus from the tubing does not occur through it. The injected gas mixes with the multiphase fluid (crude oil, water and gas produced from the reservoir, w_o^i) in the tubing at the point of injection thereby reducing its density and the weight of the liquid column in the tubing. This causes the differential pressure between the reservoir (P_r^i) and bottom hole pressure (P_{wf}^i) to be increased causing the liquid column to flow upwards to the surface. The production choke valve controls the flow rate of the multiphase fluid (w_{gop}^i) produced from the reservoir. In this paper, it is left at 100% fully open and has not been implemented for control purpose. The mixture of the gas, water and oil flowing out of each of the wells through the production choke valves is collected together in the common gathering manifold and finally

transported to the separator where they are separated into their respective phases. The gas is then sent back to the compressor system and recycled to be used for lifting purpose. For simplifying the flow of the gas and fluid, a simple flow chart is shown in Figure 4.

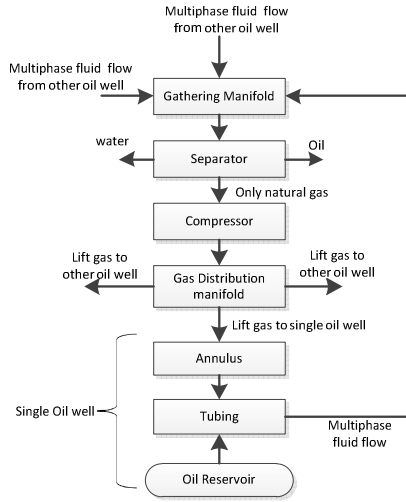


Figure 4: Flow chart of the simple model of oil field

Pressure and temperature transducers measure the pressure and temperature both downstream and upstream the production choke valve and gas lift choke valve. A multiphase flow meter is installed downstream the production choke valve and is used to measure the flow rate of oil, gas and water individually. The packer is used to seal the bottom of the casing annulus, which funnels all of the production into the tubing string, so all of the available gas energy is utilized to lift the fluid.

For the purpose of gas injection distribution and control, friction losses in the pipelines have not been taken into account as it might not be of importance for the sole purpose of control. Also it will be simpler to implement control strategies with a simple model of the process given that the model sufficiently reflects the necessary dynamics of the system needed for control purpose. All phases of the multiphase fluid are assumed to be evenly distributed with no slugging. The temperature of lift gas and the multiphase fluid is assumed to be constant at 280 K at all sections of the pipelines and the reservoir pressure is kept constant at 150 bar. It is also assumed that flashing does not occur.

The four states used in the model are the mass of gas in the distribution pipeline (m_{gp}), mass of gas in the annulus (m_{ga}^i), mass of gas in the tubing above injection point (m_{gt}^i) and the mass of liquid (oil) in the tubing above injection (m_{ot}^i). If w_{gc} is the total mass flow rate of lift gas

supplied by compressor and entering into the gas distribution pipeline (considered as input disturbance) and w_{ga}^i is the mass flow rate of gas injected into annulus i.e. mass flow rate leaving the gas distribution pipeline, then the mass balance in gas distribution manifold gives,

$$\dot{m}_{gp} = w_{gc} - \sum_{i=1}^5 w_{ga}^i \quad (1)$$

Mass flow rate through the gas lift choke valve (w_{ga}^i) is obtained by using the standard flow equation developed by Instrument Society of America (ANSI/ISA S75.01, 1989),

$$w_{ga}^i = N_6 C_v(u_1^i) Y_1^i \sqrt{\rho_{gp} \max(P_c - P_a^i, 0)} \quad (2)$$

$N_6=27.3$ is the valve constant, u_1^i is valve opening of the i^{th} gas lift choke valve expressed in percentage, P_c and P_a^i are the pressures upstream and downstream of the i^{th} gas lift choke valve, ρ_{gp} is the density of gas in the distribution pipeline which is a function of the upstream pressure P_c , Y_1^i is the gas expansion factor and $C_v(u_1^i)$ is the valve characteristic as a function of its opening.

We assume the gas expansion factor (Y_1^i) to be:

$$Y_1^i = 1 - \alpha_y \left(\frac{P_c - P_a^i}{\max(P_c, P_c^{\min})} \right) \quad (3)$$

$$\alpha_y = \text{constant} = 0.66$$

P_c^{\min} is the minimum pressure in the gas distribution pipeline. Valve characteristic as a function of its opening ($C_v(u_1^i)$) is modeled by three linear equations as shown in Equation (4). The function in Equation (4) is fitted to the data supplied by the choke supplier.

$$C_v(u_1^i) = \begin{cases} 0 & u_1^i < 5 \\ 0.111u_1^i - 0.556 & 5 < u_1^i < 50 \\ 0.5u_1^i - 20 & u_1^i > 50 \end{cases} \quad (4)$$

Using gas law, the pressure upstream (P_c) and downstream (P_a^i) the gas lift choke valve can be found from the mass of gas,

$$P_c = \frac{zm_{gp}RT_p}{MA_pL_{p,tl}} \quad (5)$$

$$P_a^i = \frac{zm_{ga}^iRT_a^i}{MA_a^iL_{a,tl}^i} \quad (6)$$

A_p and A_a^i are the cross sectional area of the gas distribution pipeline and annulus, $L_{p,tl}$ and $L_{a,tl}^i$ are the true/actual lengths of the gas distribution pipe and the annulus, M is the molar mass of the lift gas, R is the universal gas constant, T_p is the

average temperature of lift gas in the common gas distribution pipeline, T_a^i is the average temperature of lift gas in the annulus of the i^{th} well and z is the gas compressibility factor. The gas compressibility factor given by Equation (7) is expressed as a polynomial function of gas pressure P in bar (assuming constant temperature of 280K at the bottom of the sea). It is curve fitted (LSQ-method) to calculations from PVTsim (PVTsim, 2008) using the lift gas composition and assuming constant temperature.

$$z = -2.572 \times 10^{-8} P^3 + 2.322 \times 10^{-5} P^2 - 0.005077 P + 1 \quad (7)$$

Average density of the gas in the distribution pipe ρ_{gp} from definition is,

$$\rho_{gp} = \frac{m_{gp}}{A_p L_{p,tl}} \quad (8)$$

Applying mass balance in annulus yields,

$$\dot{m}_{ga}^i = w_{ga}^i - w_{ginj}^i \quad (9)$$

w_{ginj}^i is the mass flow rate of gas injected into the tubing from the annulus through the gas injection valve at the point of injection i.e. mass flow rate of gas leaving the annulus and w_{ga}^i is the mass flow rate of gas entering the annulus through the gas lift choke valve. The mass flow rate of the gas injected into the tubing from the annulus (w_{ginj}^i) is,

$$w_{ginj}^i = K^i Y_2^i \sqrt{\rho_{ga}^i \max(P_{ainj}^i - P_{tinj}^i, 0)} \quad (10)$$

K^i is the gas injection valve constant, P_{ainj}^i is the pressure upstream the gas injection valve in the annulus and P_{tinj}^i is the pressure downstream the gas injection valve in the tubing, ρ_{ga}^i is the average density of gas in the annulus. Y_2^i is the gas expandability factor given by,

$$Y_2^i = 1 - \alpha_Y \left(\frac{P_{ainj}^i - P_{tinj}^i}{\max(P_{ainj}^i, P_{ainj}^{min})} \right), \alpha_Y = 0.66$$

P_{ainj}^{min} is the minimum pressure of lift gas in the annulus at the point of injection into the tubing. P_{ainj}^i is given by adding hydrostatic pressure drop to P_a^i as,

$$\begin{aligned} P_{ainj}^i &= P_a^i + \rho_{ga}^i g L_{a,vl}^i \\ P_{ainj}^i &= P_a^i + \frac{m_{ga}^i g L_{a,vl}^i}{A_a^i L_{a,tl}^i} \end{aligned} \quad (11)$$

$L_{a,vl}^i$ is the vertical depth of the annulus from the well head to the point of injection. Density of gas in the annulus (ρ_{ga}^i) is a function of the average gas pressure,

$$\rho_{ga}^i = \frac{M(P_a^i + P_{ainj}^i)}{2zRT_a^i} \quad (12)$$

Denoting the pressure upstream the production

choke valve in the tubing head to be P_{wh}^i , the average gas pressure \bar{P}_G^i in the tubing above point of injection is,

$$\bar{P}_G^i \approx \frac{P_{wh}^i + P_{tinj}^i}{2} \quad (13)$$

The volume of gas present in the tubing above the gas injection point (V_G^i) can be found by subtracting the volume of oil present inside the tubing from the total volume of the tubing above the gas injection point.

$$V_G^i = A_t^i L_{t,tl}^i - m_{ot}^i / \rho_o$$

A_t^i is the inner cross sectional area of the tubing, $L_{t,tl}^i$ is the actual length of tubing above the gas injection point and ρ_o is the density of crude oil which is assumed to be 700 kg/m³. Using gas law,

$$\bar{P}_G^i V_G^i = z \frac{m_{gt}^i}{M} RT_t^i$$

Putting the value of \bar{P}_G^i from Eq. (13) we get,

$$\frac{P_{wh}^i + P_{tinj}^i}{2} V_G^i = z \frac{m_{gt}^i}{M} RT_t^i \quad (14)$$

T_t^i is the average temperature of the fluid/gas in the tubing

Pressure in the tubing downstream the gas injection valve (P_{tinj}^i) can be found by adding the hydrostatic pressure to well head pressure in tubing as,

$$P_{tinj}^i = P_{wh}^i + \rho_m^i g L_{t,vl}^i \quad (15)$$

ρ_m^i is the average density of the mixture of the oil and gas in the tubing above the gas injection point and is given by,

$$\rho_m^i = \frac{m_{gt}^i + m_{ot}^i}{A_t^i L_{t,tl}^i}$$

Solving Equations (14) and (15) we get,

$$P_{wh}^i = \frac{zm_{gt}^i RT_t^i}{MV_G^i} - \frac{\rho_m^i g L_{t,vl}^i}{2} \quad (16)$$

$$P_{tinj}^i = \frac{zm_{gt}^i RT_t^i}{MV_G^i} - \frac{\rho_m^i g L_{t,vl}^i}{2} + \rho_m^i g L_{t,vl}^i \quad (17)$$

The bottom hole pressure or well flow pressure P_{wf}^i is obtained by adding hydrostatic pressure drop to P_{tinj}^i as,

$$P_{wf}^i = P_{tinj}^i + \rho_o g L_{r,vl}^i \quad (18)$$

$L_{r,vl}^i$ is the vertical length of the tubing below the gas injection point up to reservoir opening. The mass flow rate of crude oil flowing from the reservoir into the tubing (w_o^i) is calculated using the PI (Productivity Index) model of the well (Brown and Beggs, 1977, American Petroleum Institute, 1994).

$$w_o^i = PI^i \max(P_r^i - P_{wf}^i, 0) \quad (19)$$

P_r^i is the reservoir pressure which is assumed to be constant at 150 bar. The valve constant of the

production choke valve is assumed to be at least 10 times more than that of the gas lift choke valve. The mass flow rate of the mixture of gas and oil through the production choke valve (w_{gop}^i) is given by,

$$w_{gop}^i = 10N_6 C_v(u_2^i) Y_3^i \sqrt{\rho_m^i \max(P_{wh}^i - P_s, 0)} \quad (20)$$

u_2^i is the valve opening of production choke valve which is kept at full 100% open. $C_v(u_2^i)$ satisfy Equation (4) replacing u_1^i by u_2^i . P_s is the pressure of the common gathering manifold assumed to be at 30 bars i.e. it is the pressure downstream the production choke valve. Y_3^i is gas expandability factor given by,

$$Y_3^i = 1 - \alpha_Y \left(\frac{P_{wh}^i - P_s}{\max(P_{wh}^i, P_{wh}^{min})} \right), \quad \alpha_Y = 0.66$$

P_{wh}^{min} is the minimum pressure in the tubing at the well head.

Mass fraction is utilized to estimate the flow rates of oil (w_{op}^i) and gas (w_{gp}^i) through the production choke valve individually as,

$$w_{gp}^i = \frac{m_{gt}^i}{m_{gt}^i + m_{ot}^i} w_{gop}^i \quad (21)$$

$$w_{op}^i = \frac{m_{gt}^i}{m_{gt}^i + m_{ot}^i} w_{gop}^i \quad (22)$$

Finally, mass balances of oil and gas inside the tubing above the gas injection point are:

$$\dot{m}_{gt}^i = w_{ginj}^i - w_{gp}^i \quad (23)$$

$$\dot{m}_{ot}^i = w_o^i - w_{op}^i \quad (24)$$

3. Open Loop Simulation Results

For the open loop simulation without controllers for the five oil wells of the field, the total lift gas mass flow rate is considered to be the input disturbance to the system. The dynamic behavior of the cluster of oil wells are studied and analyzed under varying conditions of input disturbance. MATLAB has been used as the tool for all simulation results. In the open loop simulation, the differential equations of the model of the oil field are solved using the built-in ODE solvers (ode15s with default settings) in MATLAB. The productivity index PI and gas injection valve constant K are calculated using the values of the average oil produced from each well which are obtained from analyzing a year's data of the real oil field and are listed in Table 1.

Table 1: Annual average oil production of real oil field

Well No.	Well 1	Well 2	Well 3	Well 4	Well 5	unit
Avg. Oil production	77.77	68.84	68.4	88.47	29.16	Kg/sec

The well parameters used for simulation are listed in Table 2.

Table 2: Well Parameters used for simulation

Parameters	Well1	Well2	Well3	Well4	Well5	Unit
L_{p_tl}	13000					meter
L_{a_tl}/L_{t_tl}	2758	2559	2677	2382	2454	meter
L_{a_vl}/L_{t_vl}	2271	2344	1863	1793	1789	meter
ID_a	9.63	9.63	9.63	9.63	9.63	Inch
ID_t	6.18	6.18	6.18	6.18	6.18	Inch
OD_t	7.64	7.64	7.64	7.64	7.64	Inch
L_{r_vl}	114	67	61	97	146	meter
P_r	150					bar
P_s	30					bar
w_{gc}	40000 (at normal operation)					Sm ³ /hr
PI (1.0e+4)	2.51	1.63	1.62	4.75	0.232	$\frac{kg/hr}{bar}$
K	68.43	67.82	67.82	69.26	66.22	$\frac{\sqrt{\frac{kgm^3}{bar}}}{hr}$

ID = Internal Diameter, OD = Outer Diameter

3.1 Simulation at normal supply of lift gas

For the normal operation, 40000 Sm³/hr of lift gas is supplied by the compressor. At $t = 15$ hours, w_{gc} is reduced to 36000 Sm³/hr and at $t = 35$ hours, it is increased back to 40000 Sm³/hr.

Decrease in the supply of lift gas causes the pressure of the gas distribution manifold to decrease from 200 bar to around 183.5 bar as shown in Figure 5(a).

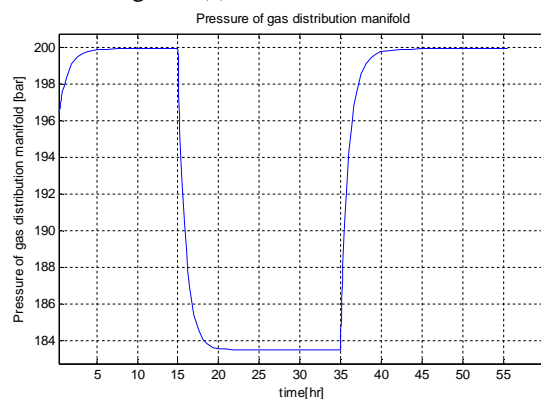


Figure 5(a): Pressure of gas in the distribution pipeline at normal supply of lift gas

However, one of our objectives is to maintain the pressure of the distribution pipeline constant irrespective of the fluctuations in the gas supply from the compressor. The total gas is distributed among the five oil wells as shown in Figure 5(b).

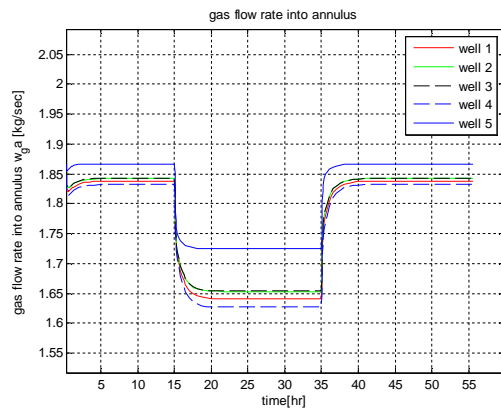


Figure 5(b): Distribution of lift gas among oil wells at normal supply of lift gas

The bottom hole pressure of the wells and the density of mixture of oil and gas in the tubing tend to increase (Figure 5(c) and Figure 5(d) respectively) with the decrease in the gas supply and vice versa.

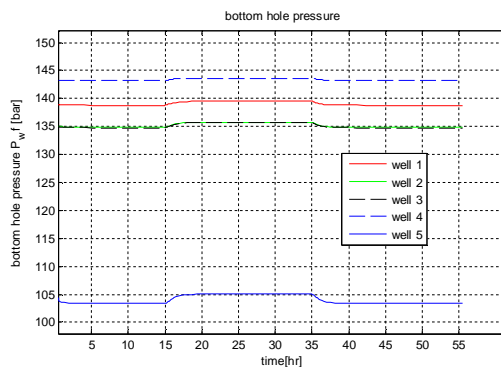


Figure 5(c): Bottom hole pressure at normal supply of lift gas

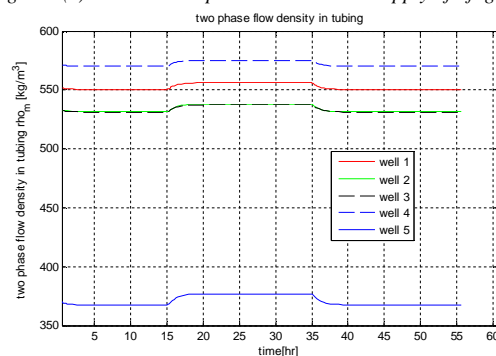


Figure 5(d): Density of liquid in tubing at normal supply of lift gas

3.1.1 Model Validation

The graph of the total oil production from each oil well obtained by the open loop simulation of the mathematical model of the oil field can be compared with the actual oil production values obtained from real oil field. As can be seen from Figure 5(e), at nominal operating condition ($35 < t < 15$ hrs), well 4 produces the highest (about 90 kg/sec), well 5

produces the least (about 30 kg/sec), well 1 produces about 78 kg/sec and well 2 and well 3 produce about 68 kg/sec. These values obtained from model simulation are very similar to the values obtained from analyzing real field data (look Table 1) which suggests the correctness in the development of the model of the oil field and in the calculation of the values of PI and K of the wells.

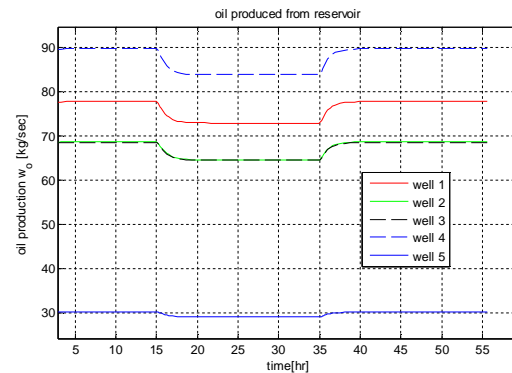
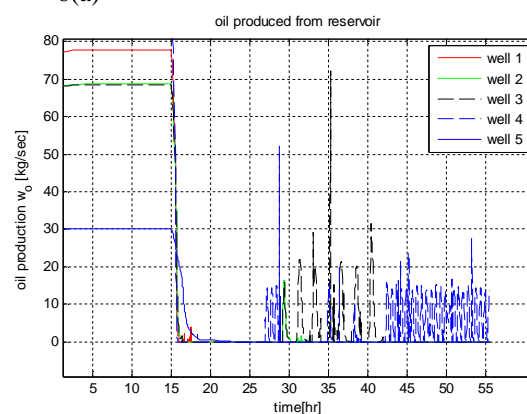


Figure 5(e): Production of oil from reservoir at normal supply of lift gas

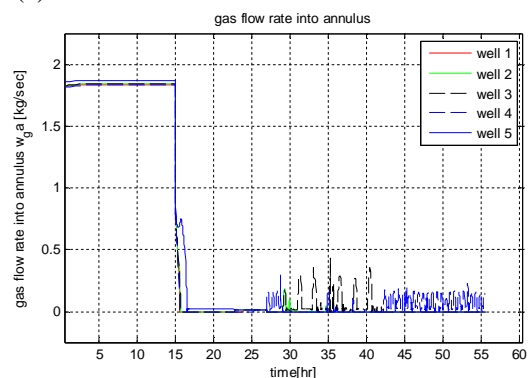
3.2 Simulation at very low supply of lift gas

In this case, at $t = 15$ hours, the gas supplied by the compressor is considerably reduced to a very low value of about $500 \text{ Sm}^3/\text{hr}$ from its normal operating condition.

6(a)



6(b)



6(c)

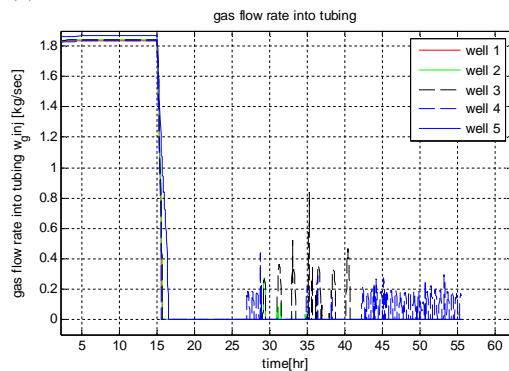


Figure 6: Simulation results (Figures 6(a)-6(c)) for very low supply of lift gas

Under very low supply of lift gas, the production of oil from the wells show oscillating behavior as seen in Figure 6(a)-6(c). As also explained by Jansen et al. (1999), Plucenio (2002), Eikrem et al. (2002 and 2004a), Dalsmo et al. (2002), Imsland et al. (2003) Plucenio et al. (2006) and Scibilia et al. (2008), this instability is due to the fact that as the gas starts to fill up the annulus, the pressure in the annulus at the point of injections starts to build up. But at the same time, in the tubing, due to the weight of the fluid, the pressure at the point of injection is high enough to keep the gas injection valve closed. When enough gas is accumulated in the annulus, the pressure difference across the gas injection valve will be sufficient to open the valve and then the lift gas flows into the tubing causing the fluid to rise up through the tubing. However, the flow of gas from annulus in the tubing causes the pressure of gas in the annulus to decrease slowly. As this happens, the pressure upstream the gas injection valve continues to decrease and after some time reaches to a value lower enough to close the gas injection valve. The flow of lift gas from annulus to tubing then stops. Accumulation of gas in the annulus starts again and thus the cycle repeats again.

This paper however does not focus on the control of the well instability. We assume that the lift gas is available in sufficient amount for the wells to operate at or near/around the nominal operating condition.

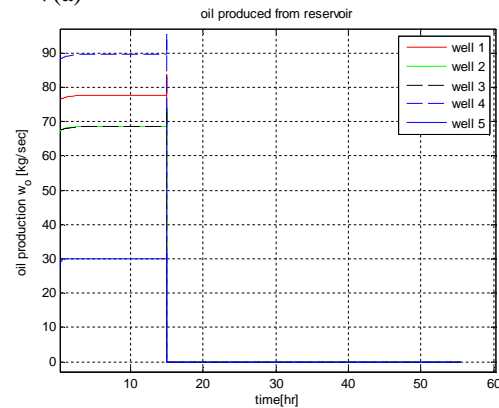
3.3 Simulation at very high gas supply

In this case, at $t = 15$ hours, the gas supplied by the compressor is considerably increased to a very high value of about $50 \times 10^4 \text{ Sm}^3/\text{hr}$ (assuming that it is within compressor's maximum rate) from its normal operating gas flow rate. Under very high supply of gas, the production of oil from the reservoir instead of increasing suddenly falls to zero as shown in Figure 7(a). This is due

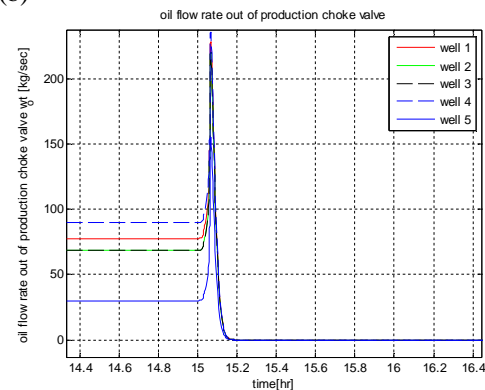
to injection of a high amount of gas into the tubing causing a large accumulation of the gas in the tubing (more than 4000 kg) above the point of injection (see Figure 7(d)). The back pressure due to this huge accumulated gas in the tubing causes the bottom hole pressure to increase and attain a value greater than the reservoir pressure of 150 bar as shown in Figure 7(c). The production of oil then stops completely. Previously accumulated oil in the tubing will flow out of the production choke valve and then the tubing will be void of oil containing only gas as shown in Figure(b).

The well head pressure in the tubing P_{wh} increases to about 140 bar. The pressure drop across the production choke valve is about 110 bar through which only gas flows without any oil

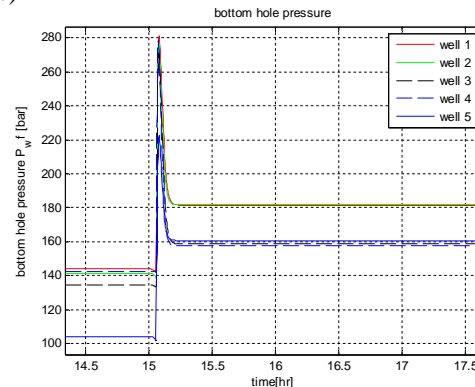
7(a)



7(b)



7(c)



7(d)

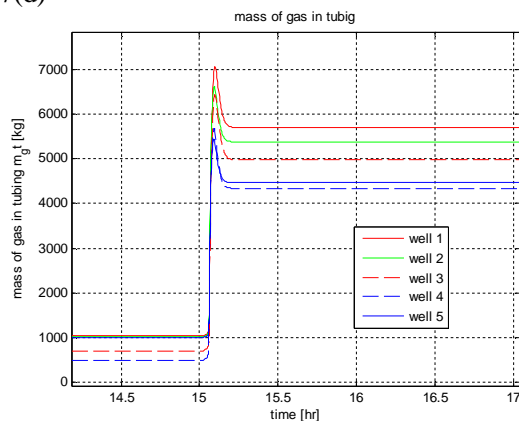


Figure 7: Simulation results (Figures 7(a)-7(d)) for very high supply of lift gas

4. Control System for oil wells

If the flow rate of the lift gas supplied by the compressor decreases, the pressure of the gas distribution manifold will also decrease. To achieve proper distribution of the total lift gas, a suitable control system must be designed to enable flow control (sufficient valve pressure drop) to each of the wells. The main interest of designing the control system is to:

- keep the pressure of the gas distribution manifold close to the set point by manipulating flows through gas lift choke valves.
- distribute the available lift gas to maximize total oil production.

We have tested four feedback control strategies for achieving the control system objective. They are:

- *Cascade Control Strategy*
- *Simple Droop Control Strategy*
- *Droop Control with integral action*
- *Pressure control with one swing producer*

For simulating all the four control strategies, the ordinary differential equations of the model of the oil field are solved by using Euler forward method with a time step of 0.9 second.

5.1 Cascade Control Strategy

In cascade control strategy, a pressure transducer measures the pressure of the common gas distribution manifold which is then taken as feedback to a pressure controller. The set point to this pressure controller (PC) is 200 bar. There are five flow controllers (FC) controlling the flow rates of the lift gas through each of the five gas lift choke valves. The nominal set points to each of these flow controllers are 8000 Sm³/hr of lift gas. The output of the pressure controller gets added to these nominal set points of five flow

controllers, the result of which is then given as the current set point to the five flow controllers. The schematic diagram of the control system with the cascade control strategy is shown in Figure 8.

In real oil fields, due to long gas distribution pipeline (13 km for this case), the change in pressure due to input disturbance from compressor takes certain time. The PI controllers are tuned in a way that it takes at least 25-30 minutes for the controllers to track the pressure set point and flow rate set point. Skogestad tuning method (Skogestad, 2003) is utilized for obtaining the initial values for controller parameters K_p and T_i which later are finely tuned by trial and error method and are listed in Table 3. Second order system with two time constants without delay is considered for tuning process. Instead of linearizing and expressing the non-linear system as linear state space model, the process gain and the time constant of the non-linear process to be used with Skogestad tuning method are found by performing step responses with the non-linear model.

Table 3: K_p and T_i values for cascade control strategy

Well no.		Well 1	Well 2	Well 3	Well 4	Well 5
FC	K_p	1e-4	2e-4	5e-4	4e-4	7e-4
	T_i	700 sec	839 sec	650 sec	520 sec	735 sec
PC		$K_p = 5000, T_i = 800$ sec				

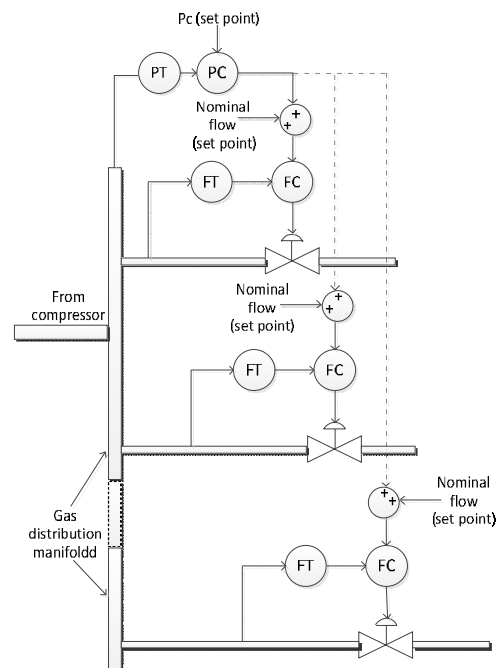
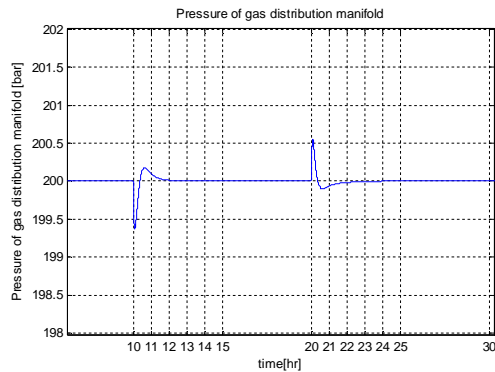


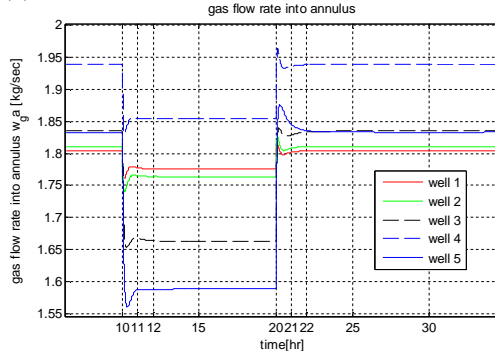
Figure 8: Schematic for cascade control strategy

At $t = 10$ hour, the lift gas flow rate is reduced to $36000 \text{ Sm}^3/\text{hr}$ and increased back to $40000 \text{ Sm}^3/\text{hr}$ at $t = 20$ hours. The pressure in the gas distribution manifold tracks the set point and remains at 200 bars as shown in Figure 9(a). The distribution of the total available gas into the five oil wells is shown in Figure 9(b). The control strategy utilizes the available gas supplied by the compressor fully, without demanding any extra lift gas as shown in Figure 9(d). Control signal generated by the flow controllers i.e. the percentage of valve opening for each valve is shown in Figure 9(c).

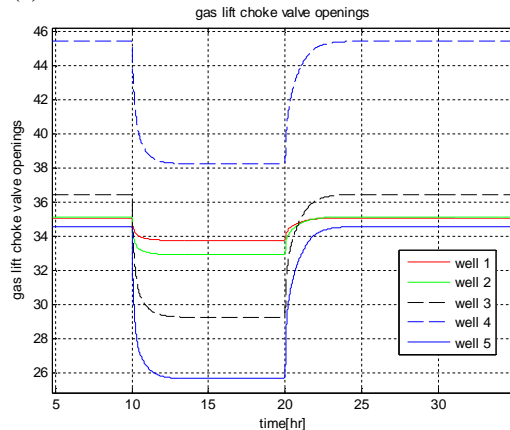
9(a)



9(b)



9(c)



9(d)

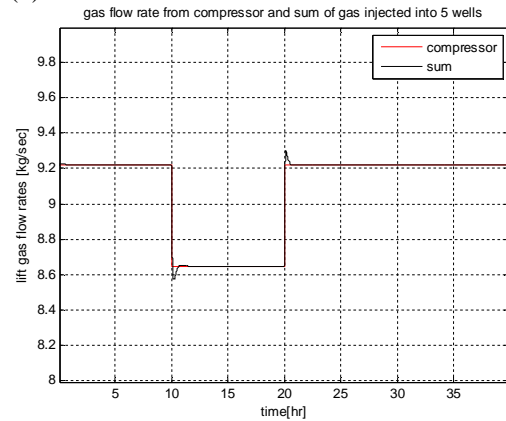


Figure 9: Simulation results (Figures 9(a) - 9(d)) for cascade control strategy.

5.2 Droop Control Strategy

Droop control strategy is a widely and successfully used control structure in the electricity power industries to control the frequency of the common power grid where multiple generators/turbines are connected in parallel (Schavemaker and Sluis, 2008). Since the five oil wells in the gas lifted oil field share the common gas distribution manifold, it can be considered analogous to the electric grid-generators system. In the case of grid-generator system, frequency is controlled by adjusting power supplied by each generator. For the case of lift gas distribution, using the droop control strategy, the change in the gas distribution manifold pressure is compensated by changing the gas flow rates into the wells by making use of a well-defined one to one relation between lift gas flow rates and gas distribution manifold pressure as shown in Figure 10. The graph has a positive slope so that when pressure is decreased, the flow rates are also decreased and vice versa. The slope of the relationship also called droop determines the regulation factor for the gas lift flow rates.

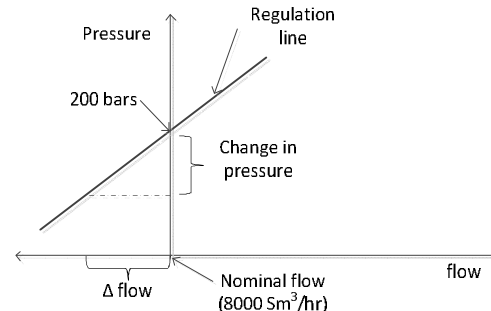


Figure 10: Pressure-flow relationship for droop control

Each of the oil well depending on its productivity index will be assigned a certain regulation factor (R) which is generally expressed in percentage.

$$R_i = 1 \times \frac{PI_i}{\sum_{i=1}^5 PI_i}, i = 1,2,3,4,5 \quad (25)$$

A schematic showing the droop control strategy is shown in Figure 11.

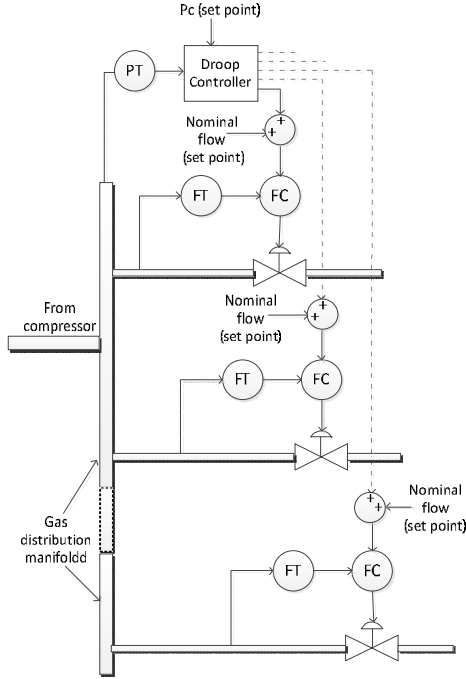


Figure 11: Schematic for droop control strategy

Mathematically, the slope of the line which is the droop/regulation is,

$$R_i = \frac{\frac{\Delta P_c}{P_{c,nom}^i}}{\frac{\Delta w_{ga}^i}{w_{ga,nom}^i}}, i = 1,2,3,4,5$$

ΔP_c is the pressure deviation, Δw_{ga}^i is the flow rate deviation, $P_{c,nom}^i$ is nominal pressure (200 bar) and $w_{ga,nom}^i$ is the nominal gas lift flow rate (8000 Sm³/hr). Pressure deviation (ΔP_c) is,

$$\Delta P_c = P_c - P_{c,nom}$$

Then Δw_{ga}^i can be found using the droop value as,

$$\Delta w_{ga}^i = \frac{1}{R_i} \frac{w_{ga,nom}^i}{P_{c,nom}^i} \Delta P_c, i = 1,2,3,4,5 \quad (26)$$

5.2.1 Simple droop control

For simple droop control strategy, Equation (26) is added to the nominal flows for each flow controller to determine the current set point ($w_{ga,S,P}^i$) for the 5 flow controllers.

$$w_{ga,S,P}^i = w_{ga,nom}^i + \Delta w_{ga}^i \quad (27)$$

The values of K_p and T_i for the five PI controllers used for controlling flows are calculated, first by using Skogestad tuning rules (Skogestad, 2003) and later fine tuning by trial and error method and are listed in Table 4.

Table 4: K_p and T_i values for simple droop control strategy

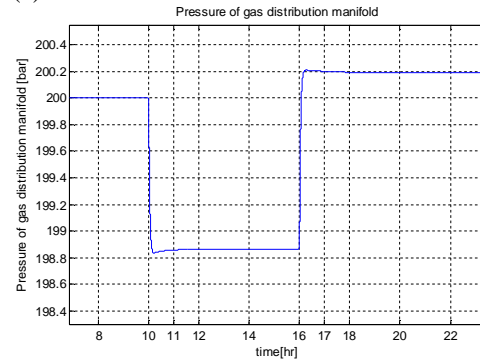
Well no.		Well 1	Well 2	Well 3	Well 4	Well 5
FC	K_p	8.2	7.12	9.15	6.8	9
	T_i	20 sec	25 sec	28 sec	31 sec	19 sec

It must however be noted that the droop control does not bring the pressure in the gas distribution pipe strictly to the nominal operating value. The whole idea of the simple droop control is to let the pressure float around the nominal value by manipulating the gas flow rates through the gas lift choke valve bounded by the regulation factors.

In Figure 12, at $t = 10$ hours, the gas supplied by compressor is reduced from 40000 Sm³/hr to 36000 Sm³/hr because of which the gas distribution manifold pressure floats around 198.8 bar (close to nominal value) despite the application of huge disturbance. At $t = 16$ hours, it is increased to 42000 Sm³/hr and the pressure floats around 200.2 bar (close to nominal value).

Oil well number 5 has the lowest productivity index value i.e. the lowest droop (see Eq. 25). Since the nominal flow rates for all the oil wells are considered to be same, due to its lowest droop, oil well 5 will contribute the most in the regulation of the pressure (see Eq. 26) as can also be seen from Figure 12(b).

12(a)



12(b)

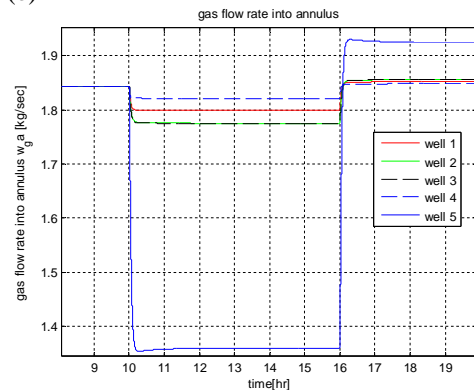


Figure 12: Simulation results (Figures 12(a)-12(b)) for simple droop control strategy.

5.2.2 Droop control with integral action

Integral action in droop control ensures that the pressure set point is exactly tracked. To obtain the integral action in the droop control strategy, Equation (26) is added to the current gas flow rate (w_{ga}^i) through the gas lift choke valve and updated at each sampling time of the simulation to obtain dynamic set points to the flow controller.

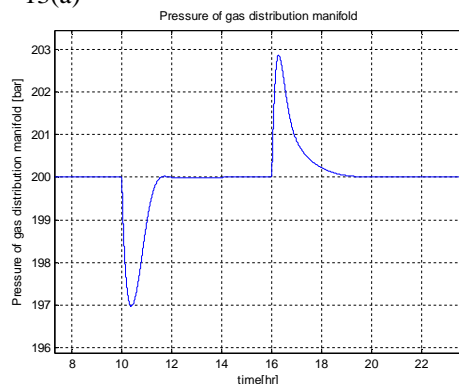
$$w_{ga,S.P}^i = w_{ga}^i + \Delta w_{ga}^i \quad (28)$$

The values of K_p and T_i for the five PI controllers used for controlling flows are calculated, first by using Skogestad tuning method (Skogestad, 2003) and later fine tuning by trial and error method and are listed in Table 5.

Table 5: K_p and T_i values for droop with integral action

Well no.		Well1	Well 2	Well 3	Well 4	Well 5
FC	K _p	1.8	1.6	1.5	2	0.2
	T _i	150 sec	115 sec	128 sec	109 sec	80 sec

13(a)



13(b)

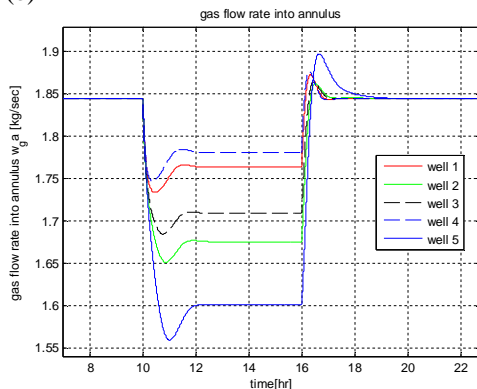


Figure 13: Simulation results (Figures 13(a)-13(b)) for droop control with integral action.

In Figure 13, at $t = 10$ hours, the gas supplied by compressor is reduced from 40000 Sm^3/hr to 36000 Sm^3/hr and at $t = 16$ hours, it is increased back to 40000 Sm^3/hr . The pressure in the gas distribution manifold and the flow rates

increased back to 40000 Sm^3/hr . However, instead of floating around the nominal pressure value like in the simple droop case, the controller due to the integral action keeps the pressure exactly at 200 bar.

Figure 13(b) shows the distribution of the gas flow rates through individual valve for controlling the pressure.

5.3 Pressure control with one swing producer

In pressure control with one swing producer, the gas lift choke valve of one oil well which produces the least is dedicated for controlling the pressure in the gas distribution pipeline.

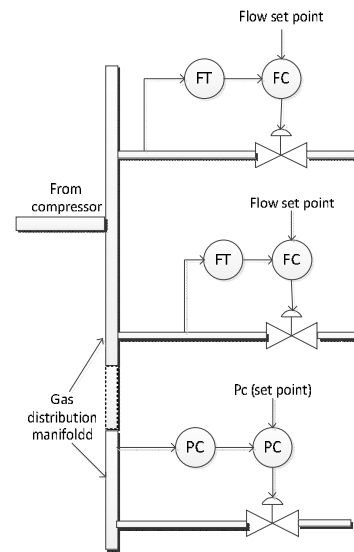


Figure 14: Schematic for pressure control with one swing producer

All other oil wells will have fixed set points for their respective flow controllers except the dedicated oil well whose gas injection flow rate can vary to bring the pressure to its set point. A schematic diagram of the pressure regulating valve control strategy is shown in Figure 14.

The values of K_p and T_i for the five PI controllers used for controlling flows and pressure are calculated, first by using Skogestad tuning method (Skogestad, 2003) and later fine tuning by trial and error method and are listed in Table 6.

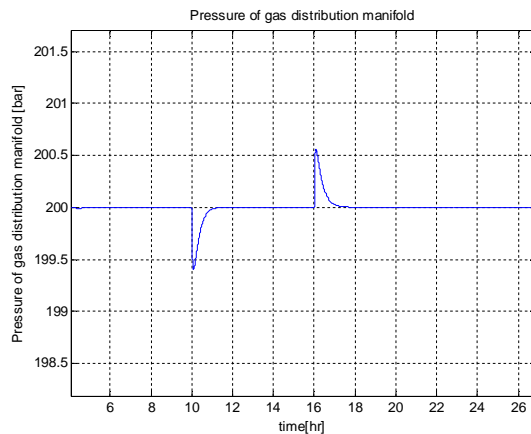
Table 6: K_p and T_i for pressure regulating valve strategy

Well no.		Well1	Well 2	Well 3	Well 4	Well 5
FC/ PC	K _p	3	2	3.5	4	10.8
	T _i	95 sec	105 sec	110 sec	90 sec	1000 sec

In Figure 15, at $t = 10$ hours, the gas supplied by compressor is reduced from 40000 Sm^3/hr to 36000 Sm^3/hr and at $t = 16$ hours, it is increased back to 40000 Sm^3/hr . The pressure in the gas distribution manifold and the flow rates

through valve 1 to valve 4 are tracking their respective fixed set points. The gas flow rate of the fifth oil well which has the pressure controlling gas lift valve is changing to keep the pressure constant i.e. it is taking the sole responsibility of keeping the pressure of the gas distribution manifold constant when there is change in the flow rate of the supplied lift gas.

15(a)



15(b)

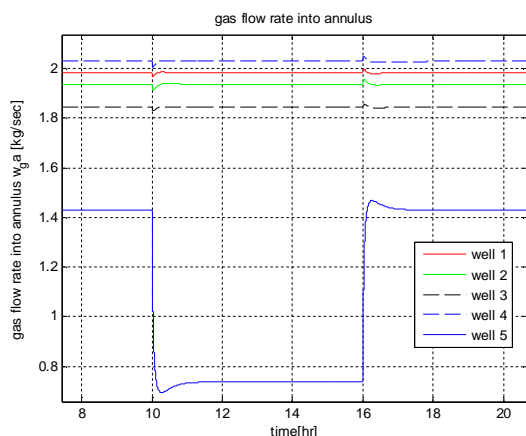
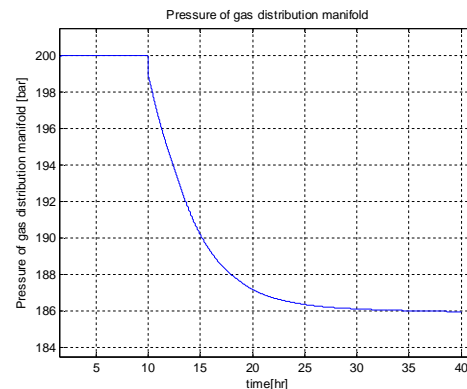


Figure 15: Simulation results (Figures 15(a)-15(b)) for pressure control with one swing producer.

One disadvantage of this control strategy is that it is not suitable for all operating conditions. It can be shown through simulation (see Figure 16) that this strategy will not always be able to track the set points. When a large input disturbance (gas flow rate reduced to 33000 Sm³/hr from 40000 Sm³/hr at $t = 10$ hrs), is applied, fully 100% closing (0% opening) of the dedicated pressure regulating valve is not able to increase the pressure to follow the set point and the pressure continuously falls down as shown in Figure 16(a) and Figure 16(b).

16(a)



16(b)

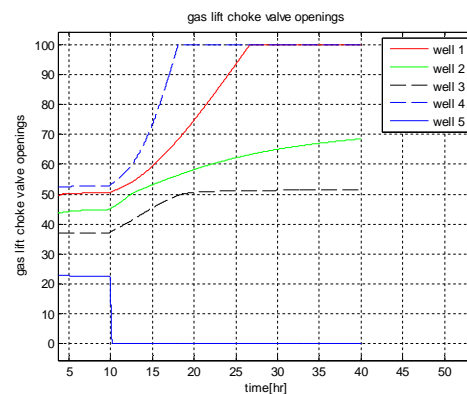


Figure 16: Disadvantage of pressure control with one swing producer

Conclusion

This paper provides a simple dynamic model representing an oil field with five gas lifted oil wells. Dynamic behavior of the oil wells is studied by open loop simulations. Among the four control strategies, the pressure control strategy with one swing producer cannot meet the control objectives when the input disturbance to the process is large, making it unsuitable for such operating conditions. Droop control strategy is considered to be new for the oil industries. Cascade control strategy as well as both droop control structures operates properly to meet the control objectives under varying input disturbances. In cascade control strategy, there is no priority of which well should take more responsibility in meeting the control objectives. However, in case of droop control strategy, the oil well with the lowest Productivity Index value will have the highest contribution for regulating the pressure and in case of the pressure control strategy with one swing producer, only the dedicated valve takes the full responsibility to meet control objectives.

If the floating of the pressure of the gas

distribution manifold by a small value about its set point is acceptable, then simple droop control strategy can be used. By introducing integral action in the simple droop control, the controller can exactly track the pressure set point without floating around the set point.

Cascade control strategy has been successfully implemented in different industrial processes since many years. Details about the cascade control structure are readily available in literature, which can be useful for further modifications and troubleshooting. So, the use of cascade control structure is recommended.

The control structures are tested under the effect of measurement noise by adding white Gaussian noise to the pressure measurement. All the four control strategies are stable to the measurement noise.

References

- American Petroleum Institute (1994). *API gas lift manual, Book 6 of the Vocational Training series, Third Edition*, American Petroleum Institute, Exploration and Production Department, Washington, DC 20005-4070, USA.
- Angulo, F., di Bernardo, M., Fossas, E. and Olivar, G. (2005a). *Feedback control of limit cycle: a switching control strategy based on nonsmooth bifurcation theory*. IEEE Transactions on Circuit and Systems-I, Vol.52, Issue 2, pp.366-378.
- ANSI/ISA S75.01, (1989). *Flow Equations for Sizing Control Valves, Standards and Recommended Practices for Instrumentation and Control*, 10th edition, Vol. 2.
- Brown, K.E. and Beggs, H.D. (1977). *The technology of artificial lift methods, Volume 1, Inflow Performance, Multiphase flow in pipes, The flowing well*. PennWell Publishing Company, Tulsa, Oklahoma, ISBN 0-87814-031-X.
- Camponogara, E., Plucenio, A., Teixeira, A.F. and Campos, S.R.V. (2010). *An automation system for gas-lifted oil wells: Model identification, control and optimization*. Journal of Petroleum Science and Engineering, Vol.70, Issue 3-4, pp. 157-167.
- Dalsmo, M., Halvorsen, E. and Slupphaug O. (2002). *Active feedback control of unstable wells at the Brage field*. SPE annual technical conference and exhibition, San Antonio, Texas, 29 Sep.- 2 Oct.
- Di Bernardo, M., Garofalo, F., Lanelli, L. and Vasca, F. (2002). *Bifurcations in piecewise smooth feedback systems*. International. Journal of. Control, Volume 75, Issue 16-17, pp. 1243-1259.
- Eikrem, G.O., Foss, B., Imsland, L., Hu, B. and Golan, M. (2002). *Stabilization of gas lifted wells*. In: Proceedings of the 15th IFAC World Congress on Automatic Control, Part 1. IFAC. Barcelona, Spain.
- Eikrem, G.O., Imsland, L., and Foss, B.A. (2004a). *Stabilization of gas lifted wells based on state estimation*. In: Proceedings of the International Symposium on Advanced Control of Chemical Processes. IFAC. Hong Kong, China.
- Imsland, L.S, Foss, B.A. and Eikrem, G.O. (2003). *A state feedback controller for a class of positive systems: Application to gas lift stabilization*. In: Paper 422 CD-Rom Proceedings of the 7th European Control Conference, 1-4 Sept., Cambridge, UK.
- Jansen, B., Dalsmo, M., Nøkleberg, L., Havre, K., Kristiansen, V. and Lemetayer, P. (1999). *Automatic control of unstable gas lifted wells*. SPE Paper 56832, presented at the SPE annual conference and exhibition, Houston, Texas, 3-6 October.
- Kaasa, G.O., Alstad, V., Zhou, J. And Aamo, O.M. (2007). *Nonlinear model-based control of unstable well*. Modeling, Identification and Control, Vol, 28, No. 3, pp. 69-79.
- Pagano, D.J., Plucenio, A., Traple A. and Gonzaga C.A. (2008). *Controlling oscillations and re-starting operations in gas-lift wells*. In: Proceeding of the XVI Brazilian Conference on Automatica CBA, Brazil.
- Pagano, D.J., Plucenio, A. and Traple, A. (2009). *Slug-flow control in submarine oil-risers using SMC strategies*. 7th IFAC International Symposium on Advanced Control of Chemical Processes, Vol. 7, Part 1, DOI: 10.3182/20090712-4-TR-2008.00091.
- Plucenio, A. (2002). *Stabilization and optimization of an oil well network operating with continuous gas-lift*. In: Proceedings of the SPE International Student Paper Contest at the SPE Annual Technical Conference and Exhibition, San Antonio, TX, USA.
- Plucenio, A., Mafra, G.A. and Pagano, D.J. (2006). *A control strategy for an oil well operating via gas lift*. In: Proceedings of the International Symposium on Advanced Control of Chemical Process, Gramado, Brazil – April 2-5.
- Plucenio, A., Pagano, D.J., Camponogara, E., Traple, A. and Teixeira, A. (2009). *Gas-lift optimization and control with non-linear MPC*. 7th IFAC International Symposium on Advanced Control of Chemical Processes, Vol. 7, Part 1, Turkey.
- PVTsim. (2008). *PVT simulation program developed for reservoir engineers, flow assurance specialists, PVT lab engineers and process engineers* [online]. Available at: <<http://www.pvtsim.com>> [Accessed: 20 January 2011]
- Schavemaker, P. and Sluis, L.V.D. (2008). *Electrical Power system Essentials*. Published by John Wiley & Sons, Ltd. ISBN 978-0470510278.
- Scibilia, F., Hovd, M. and Bitmead, R.R. (2008). *Stabilization of Gas-Lift Oil Wells using Topside Measurements*. In: Proceedings of the 17th IFAC World Congress, Seoul, South Korea, July 6-11, pp: 13907-13912.
- Skogestad, S. (2003). *Simple analytical rules for model reduction and PID controller tuning*, Journal of Process Control, Vol 13, Issue 4, pp. 291-309.
- Takacs, G. (2005). *Gas lift manual*. Published by: PennWell Corporation, ISBN 0-87814-805-1

Paper 8

Title: Simulation of a Bubble Plume in a Water Vessel With and Without Internal Liquid Recirculation

Rebei Bel Fdhila
ABB, Sweden

Keywords: computational fluid dynamics, bubbly flow, bubble plume, pseudo-turbulence, liquid recirculation

Bubbly flows are encountered in a large number of industrial applications including chemical, biological, metallurgical, nuclear and environmental processes among others. Bubble plumes have important properties, as cleaners in continuous casting when they transport the undesired non metallic particles to the surface of the melt, as mixers because of their buoyancy induced recirculation in fermentors for example or as turbulence producers due to their oscillating interfaces and zigzagging and unstable motion which creates its own turbulence and agitation needed by many processes, etc.

Small bubbles of micrometric size in liquids have been thoroughly studied. Well established mathematical models for isolated bubbles or for cases where the void fraction is very small exist and are used to simulate these flows when encountered. Larger bubbles are not spherical. Depending on their size they become ellipsoidal, oblate, spherical caps ... and can even have very fast changing shapes depending on the flow where they are immersed. For these categories the mathematical models are less accurate and do not cover all flow configurations. In this study we consider bubbles in the range [1-10mm] and a maximum local gas volume fraction of 10%. Computational fluid dynamics (CFD) is used to study the effect of bubble size, gas flow rate and internal liquid recirculation induced by immersed pumps. The turbulent fluid flow and continuity equations are numerically solved using a commercial package based on finite volumes approach.

Our simulations have addressed a lab facility used in [1] where a cylindrical vessel of 1m diameter and 1.5 m height was filled with water until 0.85m height. The air injector was moveable and positioned at the bottom and the gas flowrate was adjustable.

Some of the published cases are simulated and compared with the measured data. It was found that when the internal liquid recirculation is sufficiently intense compared to the flow induced by the bubbles the simulation results are in agreement with the measured quantities in [1]. However, for the cases where the bubbles are the governing force we show that there is no agreement between the predictions and the experimental results.

This contribution is to underline that for these flow regimes encountered in several processes, not considering properly the pseudo-turbulence (the turbulence induced by the bubbles) is a major limitation for flow predictions. A simple implementation of the basic model of this turbulence phenomena as described in [2] can improve significantly the simulated results.

1. Bel Fdhila, R., Sand, U., Rahmani, M. A., Yang, H., Eriksson, J.-E., "Model Study of Combined Gas and Electromagnetic Stirring in a Ladle Furnace", 4th International Conference on Modelling and Simulation of Metallurgical Processes in Steelmaking (STEELSIM), 27th June – 1st July 2011, Düsseldorf, Germany
2. Sato, Y., Sekoguchi, K., "Liquid Velocity Distribution In Two-Phase Bubbly Flow", Int. J. Multiphase Flow, vol.2, pp. 79-95, 1975.

Simulation of a Bubble Plume in a Water Vessel With and Without Internal Liquid Recirculation

Rebei Bel Fdhila^{1,2}

¹Mälardalen University, Energy division, School of Sustainable Development of Society and Technology, Västerås, Sweden

²ABB AB, Corporate Research, SE - 721 78, Västerås, Sweden
email: rebei.bel_fdhila@se.abb.com

ABSTRACT

Abstract

Understanding and modelling bubbly flows has been and continues to be a major challenge to be able to predict several industrial processes where this flow configuration is governing.

In this study we consider bubbles in the range [1-10mm] and a maximum local gas volume fraction of 10%. Computational fluid dynamics (CFD) is used to study the effect of gas flow rate, bubble size and internal liquid recirculation induced by immersed pumps. The turbulent fluid flow and continuity equations are numerically solved using a commercial package based on finite volumes approach.

Our simulations have addressed a lab facility used in [1] where a cylindrical vessel of 1m diameter and 1.5 m height was filled with water until 0.85m height. The air injector was moveable and positioned at the bottom and the gas flowrate was adjustable.

Some of the published cases are simulated and compared with the measured data. It was found that when the internal liquid recirculation is sufficiently intense compared to the flow induced by the bubbles the simulation results are in sufficient agreement with the measured quantities in [1]. However, for the cases where the bubbles are the governing force we show that there is no agreement between the predictions and the experimental results.

This contribution is to underline that for these flow regimes encountered in several processes, not considering properly the pseudo-turbulence (the turbulence induced by the bubbles) and the bubble size distribution are a major limitation for flow predictions. A simple implementation of the basic model of this turbulence phenomena as described in [2] can improve significantly the simulated results.

Introduction

Bubbly flows are encountered in a large number of industrial applications including chemical, biological, metallurgical, nuclear and environmental processes among others. Bubble plumes have important properties, as cleaners in continuous casting when they transport the undesired non metallic particles to the surface of the melt, as mixers because of their buoyancy induced recirculation in fomenters for example or as turbulence producers due to their oscillating interfaces and zigzagging and unstable motion which creates its own turbulence and agitation needed by many processes, etc.

small bubbles of micrometric size in liquids have been thoroughly studied. Well established mathematical models for isolated bubbles or for cases where the void fraction is very small exist and are used to simulate these flows when encountered. Larger bubbles are not spherical.

Depending on their size they become ellipsoidal, oblate, spherical caps ... and can even have very

fast changing shapes depending on the flow where they are immersed. For these categories the mathematical models are less accurate and do not cover all flow configurations.

Generally, the real process occurs in very large and opaque vessels or in a hostile environment where observations and detailed measurements are often not possible. We are driven to use laboratory models where the size can be significantly smaller and the fluids chosen more friendly as water and air in the present case.

In this investigation we use computational fluid dynamics (CFD) to study the bubbly flow in a lab facility used in [1] where a cylindrical vessel of 1 m diameter and 1.5 m height was filled with water until 0.85 m height. The air injector positioned at the bottom is moveable and the gas flow rate was adjustable and internal water vertical flow induced by immersed pumps.

In the present paper we limit ourselves to evaluate the predictions of the commercial code ANSYS Fluent without using additional modules as the one accounting for bubble break-up and coalescence or for the turbulence purely induced by the bubble presence. We consider millimetric bubbles, a given air flow rates and water flow rates from the pumps chosen among the cases measured in [1].

Simulated Lab water model facility and flow characteristics

The model facility is presented below in Figure 1. The vessel is a cylinder of 1.5 m height and 1 m diameter. The initial water layer is 0.85 m high. The air is injected at the center and the immersed two pumps are operating upwards at the vicinity of the wall. The air injector has many holes of 0.5 mm diameter and the bubbles are around 1 mm diameter at their release. Away from the injection zone, the bubbles become significantly bigger due to the coalescence phenomena. Six flow configurations have been considered: central injection of 15 and 30 l/mn air with and without activated pumps. When both gas injection and water pumps are on the bubble plume is attracted to the wall and consequently occupies a significantly larger volume of the vessel compared to when the plume is rising vertically without any interaction with the pumps induced water flow. The resulting flow pattern is shown in Figure 2.

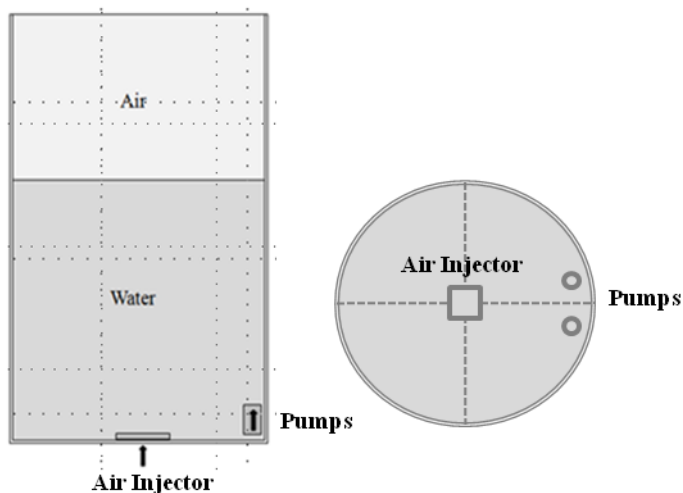


Figure 1. Experimental facility



Figure 2. Flow pattern in the water model

Flow modelling

Mathematical model

The two-phase air/water mixture is modelled using the Eulerian/Eulerian approach where both phases are treated as continua. This allows all flow quantities as velocities, turbulence variables and volume fractions to be defined at every point and at every instant.

Coalescence and break-up are not considered as well as the pseudo-turbulence induced by the bubbles.

The model consists of two continuity equations, one for each phase, two three dimensional momentum equations and the Reynolds stress model to describe the turbulence.

Continuity equation for phase (q)

$$\frac{\partial}{\partial t}(\alpha_q \rho_q) + \nabla \cdot (\alpha_q \rho_q \vec{u}_q) = 0$$

Momentum equation for phase (q)

$$\frac{\partial}{\partial t}(\rho_q \alpha_q \vec{u}_q) + \nabla \cdot (\rho_q \alpha_q \vec{u}_q \vec{u}_q) = -\nabla \alpha_q p_q + \nabla \alpha_q \cdot \overline{\overline{\tau_q}} + \alpha_q \rho_q \vec{g} + \alpha_q \vec{F}_q$$

The index q stands for water or air. α_q , ρ_q , \vec{u}_q , $\overline{\overline{\tau_q}}$, \vec{F}_q and \vec{g} are respectively, the local volume fraction, density, velocity, stress tensor, interaction forces of phase (q) and the gravity.

In the water model the gas bubbles are of millimetric size in the range 1-15mm equivalent diameter approximately. We use the universal drag law formulation [3], where the drag coefficient depends on the diameter. As detailed in [3], for bubbles between 1 and 5mm

diameter the Schiller-Naumann drag model is used: $C_D = \frac{24}{Re} (1 + 0.15 Re^{0.687})$, for bubbles

with a diameter smaller than 10mm we use the Ishii-Zuber model: $C_D = \frac{2d_b}{3} \sqrt{g \frac{\Delta \rho}{\sigma}}$. For

larger bubbles we use the spherical cap model: $C_D = \frac{8}{3}$. Re is the bubble Reynolds

number, d_b is the bubble diameter, $\Delta \rho$ is the phasic density difference and σ is the surface tension.

Computational model & boundary and flow conditions

We used a hexahedral mesh of around 500 000 cells. The air is injected with a constant velocity and a uniform bubble size, 1 or 10mm diameter. The top of the cylinder is taken as pressure outlet boundary condition. The pumps are modelled using fixed value zone condition where we specify a velocity. The flow is transient and the "steady" solution is obtained after a large simulation time reached using adaptive time stepping.

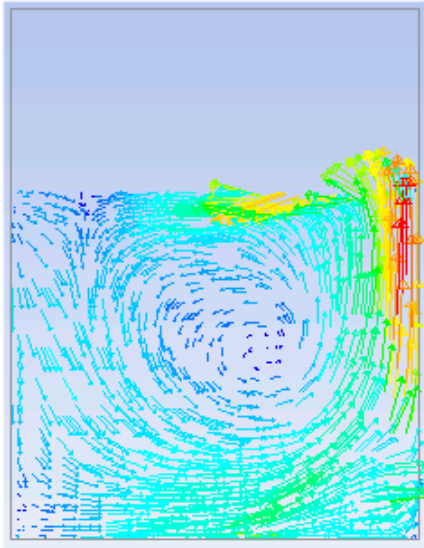


Figure 3. Liquid velocity field for 10 mm bubbles and 2m/s pump induced velocity

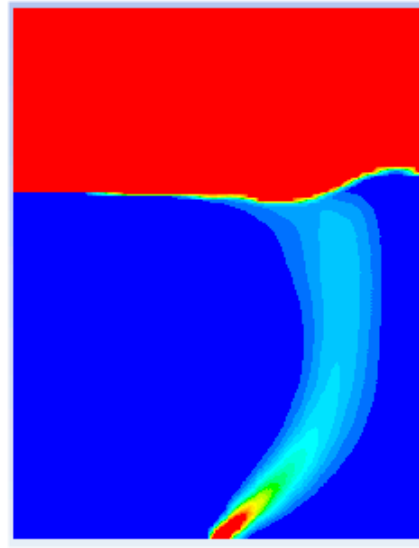


Figure 4. Gas plume structure for 10 mm bubbles and 2m/s pump induced velocity

Results

The figures 3 and 4 show clearly that the simulated liquid vortex and gas plume structure are similar to the flow picture in figure 2. The immersed pumps are situated at the bottom right of the figures and provide a rising liquid flow stream which clearly attracts the gas plume and both build a sustained stable liquid vortex. The qualitative comparison seems convincing of the high accuracy of the numerical predictions, however, we will see below that the quantitative comparison brings a lot of differences with the measurements to the light.

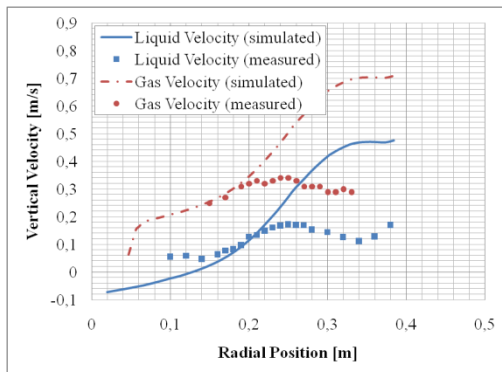


Figure 5. Liquid and Gas velocities for 10 mm bubbles, 15 l/mn gas flow rate and 2m/s pump induced liquid velocity

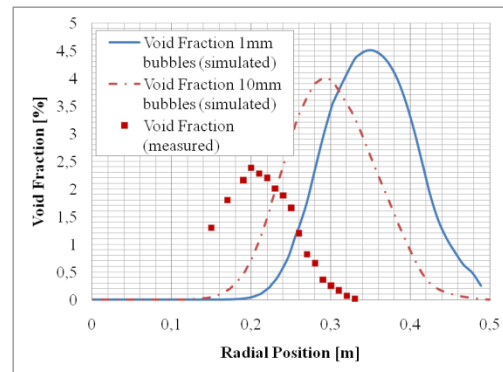


Figure 6. Gas volume fraction for 15 l/mn gas flow rate and 2m/s pump induced liquid velocity

In figure 5 far from the pumps situated near the wall the simulated gas and liquid velocities are in good agreement with the measurements, however, when we approach the high speed liquid stream induced by the pumps the simulated values are clearly over estimated. In the other hand the calculated slip velocity shows a good agreement with the experimental data in the whole flow domain.

Figure 6 shows the differences between the simulated and the measured cases in terms of void fraction. For larger bubbles there is a gas plume shift to the left and at the same time a reduction of the magnitude approaching interestingly the experimental profile. This is an encouraging result since we know that the bubbles in reality are approximately between 1 and 15 mm diameter but in our simulation we assume a constant size due to the lack of exact data.

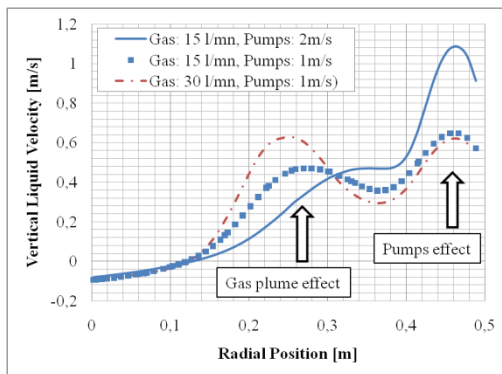


Figure 7. Effect of the gas flow rate and the pump velocities on the liquid velocity profile for 10 mm bubbles.

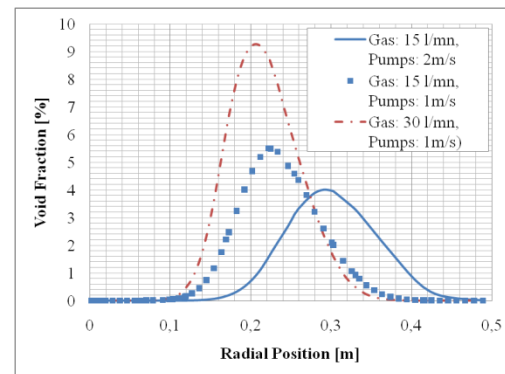


Figure 8. Effect of the gas flow rate and the pump velocities on the gas volume fraction profile for 10 mm bubbles.

Both figures 7 and 8 underline the strong interaction between the gas plume and the liquid induced stream. Higher pump effect attracts the plume more towards the wall and higher gas flow rate gives more independence to the plume because the gravity forces become more important than inertial forces and tend to push the gas towards the vessel axis where the injection point is situated.

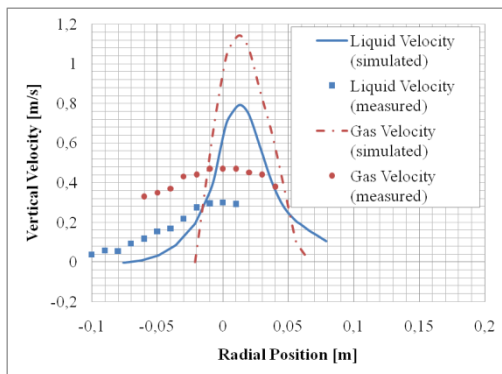


Figure 9. Liquid and Gas velocities for 10 mm bubbles and 15 l/mn gas flow rate without pump effect

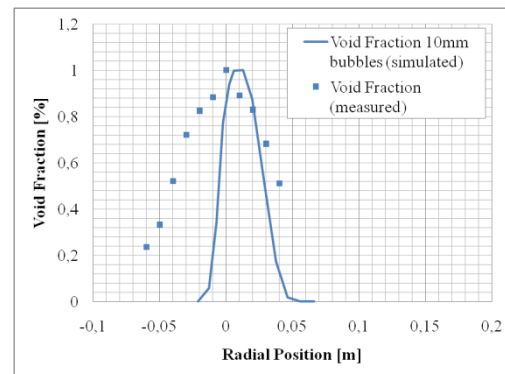


Figure 10. non dimensional gas volume fraction for 10mm bubbles and 15 l/mn gas flow rate without pump effect

Flow results without any pump induced liquid recirculation are presented in figures 9 and 10. There are substantial differences between simulated and measured data. Both velocities and void fraction profiles are not comparable to the measurements because of the rough assumption of the bubble size but also because of the way we model the

turbulence of the liquid. We use the Reynolds stress model where the turbulence is mainly generated by the gradients in the liquid velocity. When the pumps are not operating the turbulence induced by the bubbles (pseudo-turbulence) is much larger than the turbulence created by the gradients and needs to be modelled in a different way than the Reynolds stress model. Both figures 9 and 10 show that in the simulation results the plume is much more confined proving that the turbulent dispersion is underestimated.

Conclusions

Eulerian/Eulerian approach is used to simulate a bubble plume in a cylindrical vessel partly filled with water with and without liquid recirculation induced by internal vertical pumping. The gas is injected at the bottom center and the simulations have been performed using two bubble sizes 1 and 10mm, two gas flow rates 15 and 30 l/min and three induced liquid velocities from the pumps 0, 1 and 2m/s. The numerical predictions show that the vertical liquid stream has a sucking effect on the gas plume and that the flow patterns simulated and seen in the experiment are very resembling to each other. The pumping widens the bubble plume, redistributes it better in the vessel volume and allows the bubbles to have a longer contact time with the liquid.

A closer quantitative analysis shows that the predictions are far from perfect but still acceptable when the pumps are operating. Without pumped liquid the gas bubbles rise almost vertically and introduce the major amount of turbulence (pseudo-turbulence) in the liquid. The Reynolds stress model which is based on gradient generated turbulence is not sufficient and an approach similar to Sato and Sekoguchi (1975) is needed to account for the bubble induced turbulence.

The bubbles size distribution has also proved to be essential in order to capture the plume dynamics, and a model as the population balance for the dispersed phase would be beneficial for this case study. Both turbulence and bubble coalescence and break-up will constitute the continuation of this work.

References

1. Bel Fdhila, R., Sand, U., Rahmani, M. A., Yang, H., Eriksson, J.-E., "Model Study of Combined Gas and Electromagnetic Stirring in a Ladle Furnace", 4th International Conference on Modelling and Simulation of Metallurgical Processes in Steelmaking (STEELSIM), 27th June – 1st July 2011, Düsseldorf, Germany
2. Sato, Y., Sekoguchi, K., "Liquid Velocity Distribution In Two-Phase Bubbly Flow", Int. J. Multiphase Flow, vol.2, pp. 79-95, 1975.
3. ANSYS FLUENT user guide 2010.

Paper 9

Title: Comparison of Control Limit Generation Approaches in Desulphurization Plant Monitoring

Riku-Pekka Nikula

Fault detection, statistical process control, desulphurization plant, University of Oulu, Finland

Keywords: process monitoring

Early detection of faults and changes in the operation of an industrial plant brings financial benefits, improves safety and facilitates the observance of environmental regulations. In this study, statistical approaches to generation of control limits for process measurements are considered. Exceedings of the limits are monitored to detect an abnormal state in the process. Methods which are capable of updating the limits in real time according to the current operating mode give a practical solution to continuous monitoring. In a case study, statistical methods are used in desulphurization plant monitoring. Two reactors of the plant are monitored using control limits generated by different methods. The results show that a fault connected to operation of the other reactor can be detected by combining the control limit exceedings of the measurements in both reactors. Graphical presentation of the combined control limit exceedings offers promising assistance for operator's decision making.

Comparison of Control Limit Generation Approaches in Desulphurization Plant Monitoring

Riku-Pekka Nikula*, Anton Laari**, Esko Juuso*

*Control Engineering Laboratory, P.O.Box 4300, FI-90014 University of Oulu, Finland
(e-mail: riku-pekka.nikula@oulu.fi, esko.juuso@oulu.fi)

**Helsinki Energy, Porkkalankatu 9-11, FI-00090 Helsinki, Finland
(e-mail: anton.laari@helen.fi)

Abstract: Early detection of faults and changes in the operation of an industrial plant brings financial benefits and facilitates the observance of environmental regulations. In this study, statistical approaches to generation of control limits for process measurements are discussed. Points falling outside of the limits are monitored to detect an abnormal state in the process. A method which is capable of updating the limits recursively gives a practical solution to continuous real time monitoring. In a case study, statistical methods are used in desulphurization plant monitoring. Two parallel reactors of the plant are monitored using control limits generated by different methods. The results show that an abnormality on the other reactor can be detected by generating an alarm balance for both of the reactors and combining the balances. Graphical presentation for the divergence of the reactors offers promising assistance for process monitoring.

Keywords: process monitoring, fault detection, statistical process control, desulphurization plant

1. INTRODUCTION

In process industry, plotting graphs and presenting the data visually is a common method for interpretation of process performance. Converting measurement data into a graphical presentation is an essential step towards quick understanding of processes. Process operators are the ones who observe and make decisions in the control of a process. Therefore, it is practical to represent the process data in a way that is easy and fast to interpret. Providing information of a process unit or a variable, in which a change is occurring and the time when the process change occurs, is often the most useful information for diagnosis of the change. Inspection of several control charts simultaneously or crowded charts may bring confusion to diagnosis. Therefore, combining information from several sources, whether they are whole process units or process variables, brings assistance to process monitoring.

According to Qin and Li (1999) typical process changes can be classified into three categories: (i) unmeasured, normal process disturbances; (ii) slow process degradation which may or may not lead to a process fault; and (iii) abnormal process changes which prohibit the process to function normally. Chemical plants are typically subjected to small disturbances in the compositions or flow rates of the feed streams. Such disturbances can be largely balanced by the process controllers. Disturbances that cannot be compensated for may be large fluctuations in process inputs, or may be sensor, controller or equipment failures (De Veaux et al. 1994). The actual magnitudes and types of process shifts are difficult to predict. Therefore, the detection methods should

have an excellent overall performance in a broad shift domain, which means being effective in detecting both small and large process shifts. In online detection, it is desirable to detect the change in real time as soon as it occurs. Detection of a change is based on the design of stopping rules or proper choices of statistic and threshold. A good detector is sensitive to change, but does not induce many false alarms. A good design is usually defined as one which will minimize the failure and delay at a fixed false alarm rate (Venkatasubramanian et al. 2003).

Use of statistical process control (SPC) techniques such as Shewhart, cumulative sum (CUSUM) and exponentially weighted moving average (EWMA) control charts have been widely studied in process monitoring, see Hossain et al. (1996), Corbett and Pan (2002), Reynolds and Stoumbos (2004). The Shewhart chart is designed to identify single extreme values. CUSUM and EWMA charts are used to identify shifts in the mean level. Performances of EWMA-charts and CUSUM-charts are often quite close (Reynolds and Stoumbos, 2004). The use of control charts alone does not enable identification of trouble causes in a process. An issue concerning control charts is the assumption of independent and identically distributed observations. In reality, process data is seldom normally distributed. However, it is impractical to design control charts especially for many kinds of distributions. The justification for the use of control limits based on the normal distribution comes from the central limit theorem (Oakland and Hollowell, 1990, p. 102).

An industrial plant may have thousands of measurement positions. Because of the large number of variables involved, it is not practical to monitor each variable separately. Processes have often some level of redundancy and significant correlation may exist either among a set of variables or between the predictor and response variables. This redundancy can be exploited to reduce the dimensionality of the monitoring problem. The problem can be simplified with dimension reduction techniques such as principal component analysis or partial least squares (De Veaux et al. 1994). This facilitates detection of an out of control process but at the same time it complicates the root cause analysis. With these techniques it is often unclear on which original variables the new point is out of control.

Monitoring of an alarm balance is another way to exploit the redundancy of variables. In that case, process variables are monitored individually by some statistical method. The amount of points of each variable falling outside limits is summed up to a collective alarm balance consisting of several variables. The concept of alarm balance is presented in the study of Talonen and Sirola (2009). Alarm balance enables monitoring a process in parts or subsections. In addition, changes in the process can be presented in a user-friendly way. However, in case of several variables on the alarm balance, the variables causing the change have to be identified with other means. Knowledge and experience of the process is needed for the diagnosis of root causes.

This study focuses on different statistical methods to generation of control limits. Seven methods are compared and their suitability to monitoring with alarm balance is evaluated. The methods are applied on measurements from two parallel reactors of the Salmisaari desulphurization plant in Helsinki, Finland. Redundancy of the measurements is exploited to find differences in operation of the reactors. The methods are tested during an actual fault case and during a normal in-control state in the plant. A visual approach based on the alarm balances is used for assistance of process monitoring.

2. METHODS

Seven approaches to the generation of control limits are evaluated. Methods I and II are based on defining the limits based on median absolute deviation from the median (MAD). Method III is based on the approach presented by Talonen and Sirola (2009). Methods IV and V are based on cumulative sum charts. Methods VI and VII are based on distribution of the data. Specifically, it means defining the limits based on 25th and 75th percentiles of the data. The points outside the generated control limits are monitored by an alarm balance.

2.1 Sliding Window Approach

In all the methods, except IV and VI, a sliding window approach is used. N consecutive data points are used in computation. The current data point is the last data point of a sliding window. An exception is method I, in which the

current point is the midpoint of the window. As a new data point comes, the sliding window slides one point forward and the oldest point from the previous window is dropped. With a sliding window, only current data is utilized and the older historical data does not have an influence on generation of control limits at the current time step.

2.2 Methods I and II

The median \tilde{x} of a data sequence $\{x_k\}$ is obtained by first rank-ordering it from smallest to largest, i.e. $x_{(1)} \leq x_{(2)} \leq \dots \leq x_{(N-1)} \leq x_{(N)}$ and then taking either the middle value (if N is odd) or the average of the middle two values (if N is even). The MAD scale estimate, is defined as

$$S = 1.4826 \text{median}\{|x_k - \tilde{x}|\}, \quad (1)$$

where the factor 1.4826 was chosen so that the expected value of S is equal to the standard deviation σ for normally distributed data (Huber 1981, p. 107).

A point is outside a control limit if $|x_t - \tilde{x}| > t \cdot S$, where x_t is the current data point and t is a user-defined threshold. This approach is called Hampel identifier and it is normally used in outlier detection. The approach is called Hampel filter, when it is applied to a sliding data window. More discussion can be found in the papers of Pearson (2002) and Liu et al. (2004). The method assumes independent and identically distributed data.

Method I introduces delay to real time monitoring, because x_t is the midpoint of sliding window. However, this approach was chosen, because it is normal practice in outlier detection (Pearson 2002). In method II, x_t is the last point of the window, and thus monitoring is real time.

2.3 Method III

Method III is based on the approach presented by Talonen and Sirola (2009). Six-sigma-rule used in quality control is adapted to the generated control limits. The control limit (CL) is generated every time step for each process variable. Correlations among other process signals are taken into account by recursive formula of alarms in a certain area. The phases used to define the control limit are presented in (2), (3), (4), and (5).

$$\mu_t = \sqrt{\frac{1}{N} \sum_{k=0}^{N-1} (x_t - x_k)} \quad (2)$$

$$\sigma_t = \sqrt{\frac{1}{N-1} \sum_{k=0}^{N-1} (x_t - x_k - \mu_t)^2} \quad (3)$$

$$CL_t = c_t \cdot [d \cdot \sigma_t + d_{DB} \cdot \tilde{x}_{DB} + d_{MM} \cdot (\max_{DB} - \min_{DB})] \quad (4)$$

$$c_t = \frac{1 + A_{all}(t) + A_t(t)}{1 + A_{all}(t)} \quad (5)$$

Variable μ_t is moving average at a time point t ; x_k is the k^{th} data point of the sliding window; σ_t is moving standard deviation; \tilde{x}_{DB} is median of moving standard deviations; d , d_{DB} and d_{MM} are user-defined coefficients; \max_{DB} and \min_{DB} are maximum and minimum values of the signal stored in a data base. A_{all} is all alarms in a certain process area and A_i is alarms of the variable i in a certain time period. An alarm means that a point is outside control limit. For any signal, the parameter $c_i \geq 1$. According to Talonen and Sirola (2009), good initial values for d and d_{DB} are between one and three based on three-sigma rule. By practical experience good initial values for d_{MM} are between 0.001 and 0.004. Upper and lower (UCL and LCL) control limits for a variable are defined as

$$UCL_t = \mu_t + CL_t, \quad (6)$$

$$LCL_t = \mu_t - CL_t. \quad (7)$$

2.4 Methods IV and V

Methods IV and V are based on cumulative sum charts, which are used to evaluate the deviation of measurement values from the mean. Since processes are inherently stable, cumulating process data can give information about longer-term trends (Oakland and Followell, 1990, p. 282). Cumulative sums to positive C^+ and negative C^- directions are presented in (8) and (9)

$$C_t^+ = \max \left[0, x_t - \left(\mu_0 + \frac{d \cdot \sigma}{2} \right) + C_{t-1}^+ \right], \quad (8)$$

$$C_t^- = \max \left[0, \left(\mu_0 - \frac{d \cdot \sigma}{2} \right) - x_t + C_{t-1}^- \right], \quad (9)$$

where the target value μ_0 is zero and standard deviation σ is one due to the fact that variables have been normalised to zero mean and unit variance. Coefficient d is used to define how large shifts are desired to be detected. The cumulative sum is set to zero if the control limit H is exceeded. The control limit H is user-defined and constant. It is not updated based on data.

Method IV uses all the historical data for the normalisation of data and computation of cumulative sum, whereas method V uses data from a small time period. In method V, x_t is normalised at every time step based on the current sliding window. Variables H , d , μ_0 , and σ stay constant. Cumulative sum charts rely upon the assumption of independent and identically distributed observations.

2.5 Methods VI and VII

Methods VI and VII find the 25th percentile q_1 and the 75th percentile q_3 from the data. A range is defined based on q_1

and q_3 and the range is weighted with a user-defined parameter w . The upper and lower (UL and LL) control limits are defined in (10) and (11). If w is zero, $x_t > q_3$ or $x_t < q_1$ cause an alarm. In method VI, all the data is used to define the limits. Method VII uses sliding window to define the limits for data.

$$UL = q_3 + w(q_3 - q_1) \quad (10)$$

$$LL = q_1 - w(q_3 - q_1) \quad (11)$$

2.6 Alarm Balance

For each process variable an alarm balance A is created. Alarm balance is a recursive sum of points outside control limits. Coefficient λ is a forgetting factor, $0 < \lambda \leq 1$. In this study, $\lambda = 1$. $\#UCL_t$ and $\#LCL_t$ are the amount of points outside limits (0 or 1) on the current time point t .

$$A_t = \lambda \cdot A_{t-1} + (\#UCL_t - \#LCL_t) \quad (12)$$

In this study, parallel reactors are monitored. Therefore, separate alarm balances for them are created. Only output temperatures are monitored, but the alarm balances could have several variables combined from a certain process area as was presented in Talonen and Sirola (2009). In this study, the divergence of the reactors is monitored by comparing the reactors with (13). If the divergence $A_t^{\text{divergence}}$ grows, it is a sign of deviating operation between the two parallel reactors.

$$A_t^{\text{divergence}} = |A_t^{\text{reactor1}} - A_t^{\text{reactor2}}| \quad (13)$$

3. CASE STUDY

3.1 Desulphurization Process

The Salmisaari Power Plants consist of two units. Boiler K1 is a combined heat and power (CHP) plant. Boiler K7 generates only heat. The ratio of electricity generation to heat generation is normally fixed. Since the consumption of energy at different times of a year and a day does not always correspond to this ratio, it is possible to adjust the power plants to generate electricity and heat according to the need of each moment. The power plants reach an efficiency of nearly 90% in combined heat and power generation.

The Salmisaari desulphurization plant removes approx. 80% of sulphur dioxide from combustion gases of the power plants. The plant uses half-dry method, in which the chemical reactions occur in solid, liquid and gaseous phases. The plant has two parallel reactors. Combustion gases are cleaned from solid particles in electrostatic precipitator before arriving to the desulphurization plant (reactors). Alkaline slurry, which includes calcium hydroxide and reaction product, is sprayed to the gases in the reactors. Particles of slurry and sulphur dioxide molecules react partly in the reactor and the products fall to the bottom of the reactor. The reaction continues in dust filters, in which dust is collected from gas by means of

fabric filter. The cleaned gas flows through a blower to the chimney stack and out. The reaction product at the bottom of the reactor is collected and used in making of slurry. Performance of the desulphurization plant is critical to the power plants. The emission standards of sulphur dioxide have to be precisely followed. Therefore, increase in sulphur dioxide emissions or an interruption in the use of the desulphurization plant may consequently cause unwanted reduction in energy generation. Even lawsuits are possible.

During the period under review, an abnormal state emerged in the process due to a mechanical defect in the slurry pump of reactor 2. The slurry pump output pulsed abnormally. Eventually, this disturbance caused an interruption to the use of desulphurization plant. The process is operated basically so that the output temperatures from the reactors are kept invariable by pumping of right amount of slurry to the reactor nozzles. Slurry delivery problems have an effect on reactor performance, and therefore such problems may be seen through real time measurements in a reactor. In this study, output temperature data of the reactors are utilized.

3.2 Desulphurization Plant Data

Traditionally, data from in-control state of a process is used to obtain process mean \bar{X} and control limits for monitoring purposes. Future readings are assessed against the knowledge from the in-control process. Output temperatures from reactors were checked with traditional range and mean charts to find if they are in statistical control. The principles for the charts can be found in Oakland and Followell (1990), for instance. In-control time periods were not found. Therefore, two time periods, in which data points lie within the range $\bar{X} \pm 3\sigma$, were chosen to tune the methods and test the methods in a faultless state. \bar{X} and σ were computed for these periods separately. In addition, sulphur dioxide emissions from desulphurization plant were on an accepted level and faults were not reported on these periods. These matters were chosen to represent an in-control process. During the slurry pump induced fault, the range $\bar{X} \pm 3\sigma$ was not obeyed.

Table 1 describes the used data without any preprocessing. $T1$ and $T2$ represent reactor 1 and reactor 2 output temperatures, respectively. One minute rate of sampling was used. Skewness shows that data was not evenly distributed on both sides of the mean aside from $T1$ during the fault period, which was close to zero. Data was not normally distributed. Data lengths are different between the periods due to the fact that same length data, where points lie within $\bar{X} \pm 3\sigma$, were not easily found. In principle, variations and level changes were wanted, because real processes are not stable all the time. This complicated the choice of data periods. Before applying the monitoring methods, data was normalised to zero mean and unit variance.

Table 1. Description of data

period	tuning period		faultless period		fault period	
variable	$T1$	$T2$	$T1$	$T2$	$T1$	$T2$
\bar{x} (°C)	76.85	76.83	77.36	77.56	78.78	78.11
σ	0.77	0.71	0.68	0.81	0.56	1.00
skewness	-0.76	-1.00	0.86	0.88	-0.01	2.97
length (min)	17280	17280	18720	18720	12960	12960

To evaluate the type of abnormality in fault period Figure 1 is plotted. In Figure 1, output temperatures of both reactors are plotted. Moving average is calculated using $N=100$. It can be seen that $T2$ falls over $+3\sigma$ from the mean near the 6,990th point, which could be interpreted as a first sign of the fault. Later, near the 8900th point, the moving average starts to fluctuate largely. The points of $T2$ lie outside $+3\sigma$ from the mean 301 times (minutes) and outside -3σ from the mean 19 times during the period. The points of $T1$ lie outside $+3\sigma$ from the mean 37 times and outside -3σ from the mean 14 times during the period. The fault makes $T2$ chance occasionally to abnormal levels and the spread of the readings is wide. $T1$ is mainly in-control with some fluctuations.

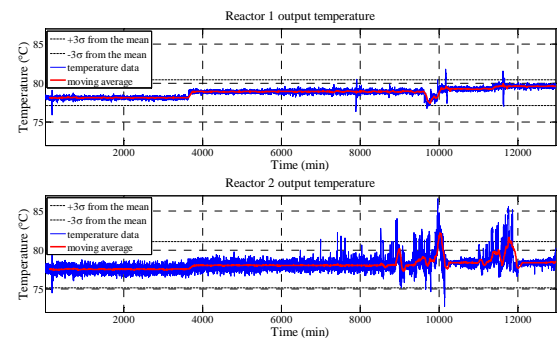


Figure 1. Fault period.

3.3 Comparison Principles for the Methods

Basically, the methods were compared by monitoring the amount of points outside control limits. In tuning, five settings with different percentages of points outside control limits were chosen. As it was mentioned earlier, the data had level changes in all the chosen periods. Based on that, the methods should find some points outside control limits also during an in-control process state. Using tuning period, it was chosen that settings from 1 to 5 would have 1%, 0.5%, 0.2%, 0.1%, and 0% of the points outside control limits at most. It means not over 172, 86, 34, 17, and 0 data points outside the control limits were allowed.

The percentages of points outside control limits were monitored in fault period and faultless period. During fault period, the methods find more than 1%, 0.5%, 0.2%, 0.1%, and 0 % of the points outside control limits with the defined settings on $T2$ to detect the abnormality. On the contrary, less than 1%, 0.5%, 0.2%, 0.1%, and 0 % of the points outside

control limits should be found on $T1$ and during the faultless period on both $T1$ and $T2$.

Besides the percentages of points outside limits, the divergence defined in (13) was monitored. The maximum divergence of variables on faultless period and fault period was checked. Then the divergences of periods were compared and their ratio checked. Finally, the alarm balances and divergences were monitored visually to affirm the functionality in visual presentation.

4. RESULTS AND DISCUSSION

4.1 Tuning the Methods

The methods were tuned using tuning period data described in Table 1. As it was mentioned, five settings were searched for. The settings are presented in Table 2. In Table 2, M means method, S means setting, and P means user-defined parameters. For the methods with sliding window N , the tested sizes were $N=10,20,\dots,100$ min. Method I was an exception due to the fact that the current point was the midpoint in a window. Tested sizes were $2 \cdot N + 1$ in that case. During the tuning, $t=\{1,2,\dots,10\}$ were tested on method I and $t=\{1,2,\dots,25\}$ on method II. On method III, $d=\{1,2,3\}$, $d_{DB}=\{1,2,3\}$, and $d_{MM}=\{0.001,0.002,\dots,0.004\}$ were tested. On methods IV and V, $d=\{1,2,\dots,10\}$ and $H=\{1,2,\dots,10\}$ were tested. On method VI, $w=\{0.1,0.2,\dots,0.3\}$ were tested. On method VII, $w=\{0.25,0.5,\dots,1.6\}$ were tested.

Table 2. Settings

M	I	II	III	IV	V	VI	VII
$S1$	10, 4	60, 5	70,1,3,0.002	3,7	20,4,1	2	90,3
$S2$	70, 4	50, 7	20,1,3,0.001	4,2	60,5,1	2	50,3.75
$S3$	80, 5	40, 10	40,3,1,0.001	4,5	50,5,2	2.2	30,5.25
$S4$	40, 5	70, 14	80,3,3,0.004	4,10	90,4,8	2.2	30,7.25
$S5$	20, 10	60, 22	10,3,1,0.001	5,5	10,3,5	2.6	50,15.75
P	N,t	N,t	N,d,d_{DB},d_{MM}	d,H	N,d,H	w	N,w

Table 3 shows the percentage of points outside the control limits with the chosen settings. It can be seen that the percentages differ notably between the temperatures with some settings. As Table 1 shows, the tuning data is not similar for both of the temperatures. The settings are not optimal for a single variable, but when the two chosen redundant variables are monitored with similar settings these settings are valid. The settings were chosen so that the percentage of points outside the control limits for both variables would be as close as possible to the planned percentage but not over. Methods IV and VI had the largest difference between variables $T1$ and $T2$ with settings 1 and 2. Method IV had the largest difference also on setting 3. These methods use all the data from a period at once, and obviously this has an influence on the results. Differences in $T1$ and $T2$ data prove to be significant in that case. With other methods the differences of $T1$ and $T2$ were below 0.10 percentage units, except on methods I and V with setting 1. Last-mentioned could be explained by small N on setting 1 on methods I and V compared to other methods with sliding

window. On setting 4, method III had the biggest difference between $T1$ and $T2$ from all the methods.

Table 3. The percentage of points outside control limits

method	variable	setting 1	setting 2	setting 3	setting 4	setting 5
I	$T1$	0.78	0.40	0.20	0.10	0.00
	$T2$	0.57	0.31	0.12	0.08	0.00
II	$T1$	0.89	0.34	0.17	0.06	0.00
	$T2$	0.95	0.43	0.19	0.10	0.00
III	$T1$	0.99	0.47	0.13	0.05	0.00
	$T2$	1.00	0.48	0.20	0.10	0.00
IV	$T1$	0.66	0.28	0.10	0.05	0.00
	$T2$	0.97	0.46	0.19	0.09	0.00
V	$T1$	0.98	0.47	0.18	0.10	0.00
	$T2$	0.75	0.41	0.17	0.09	0.00
VI	$T1$	0.00	0.00	0.00	0.00	0.00
	$T2$	0.34	0.34	0.02	0.02	0.00
VII	$T1$	0.98	0.42	0.17	0.10	0.00
	$T2$	0.94	0.49	0.20	0.08	0.00

4.2 Results from Faultless Period

The methods were tested in normal operation of the plant. Faultless period data described in Table 1 was used. Results are presented in Table 4. Table 4 shows the percentage of points outside control limits with the chosen settings. If the planned percentages 1%, 0.5%, 0.2%, 0.1%, and 0% are not exceeded, the chosen settings are valid for the period. The results show that only method IV with setting 1 exceeded the planned percentage on $T2$. Tables 4 and 3 show that the percentage of points outside control limits was generally smaller in faultless period than in tuning period. This suggests a successful tuning of the methods. The difference of $T1$ and $T2$ percentages were the largest on method III, except on setting 4 the difference was largest on method I. A large difference refers to difference in operation of the reactors, which is not desirable in a faultless period. The difference was zero or 0.01 percentage units in several settings. This suggests parallel variation in the temperatures, although little bit divergence exists.

Table 4. The percentage of points outside control limits

method	variable	setting 1	setting 2	setting 3	setting 4	setting 5
I	$T1$	0.00	0.06	0.02	0.01	0.00
	$T2$	0.00	0.13	0.04	0.04	0.00
II	$T1$	0.29	0.06	0.00	0.00	0.00
	$T2$	0.39	0.13	0.01	0.00	0.00
III	$T1$	0.38	0.07	0.03	0.01	0.00
	$T2$	0.73	0.33	0.10	0.02	0.00
IV	$T1$	0.67	0.01	0.00	0.00	0.00
	$T2$	1.00	0.16	0.04	0.01	0.00
V	$T1$	0.11	0.17	0.04	0.04	0.00
	$T2$	0.24	0.25	0.06	0.04	0.00
VI	$T1$	0.00	0.00	0.00	0.00	0.00
	$T2$	0.07	0.07	0.01	0.01	0.00
VII	$T1$	0.32	0.06	0.01	0.00	0.00
	$T2$	0.42	0.17	0.04	0.01	0.00

4.3 Results from Fault Period

The methods were tested on data from the period, in which the mechanical fault occurred on the slurry pump of reactor 2. Table 5 shows the percentage of points outside control limits with different methods. If the percentage is larger than planned on the settings on $T2$, a fault can be detected. The planned percentage of points outside control limits should not be exceeded on $T1$, because the fault does not emerge on reactor 1 measurements. Method I with settings 2 and 4; method III with settings 3 and 4; method IV with settings 2,3, and 4; and method VI with settings 1,2, and 3 showed promising results concerning the detection of the fault.

Table 5. The percentage of points outside control limits

method	variable	setting 1	setting 2	setting 3	setting 4	setting 5
I	$T1$	0.00	0.46	0.31	0.05	0.01
	$T2$	0.00	0.81	0.35	0.29	0.01
II	$T1$	0.34	0.06	0.01	0.01	0.00
	$T2$	0.69	0.19	0.06	0.01	0.00
III	$T1$	1.04	0.63	0.04	0.03	0.00
	$T2$	1.92	1.13	0.22	0.11	0.00
IV	$T1$	0.19	0.32	0.14	0.07	0.06
	$T2$	0.66	1.22	0.65	0.38	0.47
V	$T1$	0.16	0.23	0.09	0.08	0.00
	$T2$	0.44	0.42	0.19	0.08	0.00
VI	$T1$	0.18	0.18	0.12	0.12	0.03
	$T2$	4.12	4.12	3.77	3.77	3.28
VII	$T1$	0.61	0.13	0.04	0.01	0.00
	$T2$	0.73	0.43	0.12	0.05	0.00

4.4 Comparing the Results in Faultless and Fault Periods

The percentages of points outside control limits of the faultless and fault periods were monitored for the upper limit and the lower limit separately. Tables 6 and 7 show how many percentage units the amount of points outside limits differs when fault period is compared to faultless period. If the value is positive, the percentage of points outside the limit is larger in fault period than in faultless period, and vice versa if the value is negative. In Table 6, value of $T2$ should be as large as possible and value of $T1$ should be close to zero. Also the ratio of $T2$ to $T1$ is significant. It should be as large as possible. Therefore, method I with setting 4; method II with setting 3; method III with setting 3; method IV with setting 3; method V with setting 3; method VI with setting 5; and method VII with setting 2 are the most valid.

Table 6. The difference in upper limit

Method	Variable	Setting 1	Setting 2	Setting 3	Setting 4	Setting 5
I	$T1$	0.00	0.21	0.14	0.02	0.00
	$T2$	0.00	0.51	0.22	0.22	0.00
II	$T1$	0.08	-0.04	0.00	0.00	0.00
	$T2$	0.45	0.08	0.04	0.01	0.00
III	$T1$	0.49	0.37	0.00	0.00	0.00
	$T2$	1.25	0.80	0.14	0.09	0.00
IV	$T1$	-0.59	0.14	0.06	0.04	0.05
	$T2$	-0.27	1.04	0.61	0.36	0.45
V	$T1$	0.05	0.06	0.04	0.04	0.00
	$T2$	0.18	0.18	0.15	0.06	0.00
VI	$T1$	0.16	0.16	0.11	0.11	0.03
	$T2$	3.69	3.69	3.46	3.46	3.06
VII	$T1$	0.29	0.00	0.00	0.00	0.00
	$T2$	0.45	0.31	0.08	0.03	0.00

Type of the fault was such that more points were outside upper limit than outside lower limit. Therefore, Table 7 has smaller differences in $T2$ than in Table 6. Table 7 is open to more interpretations than Table 6. Interpretation of the results by evaluating the largest number ≥ 0 in $T2$ is one approach. Method I with setting 2; method II with setting 3; method III with settings 4 and 5; method IV with settings 2 and 5; method V with setting 1; method VI with settings 1 and 2; and method VII with setting 4 had the largest number ≥ 0 in $T2$.

Table 7. The difference in lower limit

Method	Variable	Setting 1	Setting 2	Setting 3	Setting 4	Setting 5
I	$T1$	0.00	0.19	0.15	0.03	0.01
	$T2$	0.00	0.17	0.08	0.03	0.01
II	$T1$	-0.03	0.03	0.01	0.01	0.00
	$T2$	-0.14	-0.02	0.01	0.00	0.00
III	$T1$	0.18	0.18	0.01	0.03	0.00
	$T2$	-0.06	-0.01	-0.02	0.00	0.00
IV	$T1$	0.10	0.17	0.08	0.03	0.01
	$T2$	-0.07	0.02	0.00	0.01	0.02
V	$T1$	0.00	0.00	0.01	0.00	0.00
	$T2$	0.01	-0.01	-0.02	-0.02	0.00
VI	$T1$	0.02	0.02	0.01	0.01	0.00
	$T2$	0.37	0.37	0.30	0.30	0.22
VII	$T1$	0.00	0.07	0.03	0.01	0.00
	$T2$	-0.14	-0.05	0.00	0.01	0.00

4.5 Divergence of the Reactors

Divergence $A_i^{divergence}$ of the reactors was monitored and maximum divergence of faultless and fault periods were monitored as well. Table 8 shows the ratio of maximum divergences between faultless and fault periods with different settings on the methods. The larger the ratio is, the larger the difference of reactors is in fault period compared to faultless period. If maximum divergence was zero in faultless period, it caused division with zero. Therefore, method I with setting 5 has the entry '1/0' and no ratio as an example.

Table 8. Ratio of maximum divergence

method	setting 1	setting 2	setting 3	setting 4	setting 5
I	0/0	2.60	2.73	4.25	1/0
II	3.09	2.36	4.00	2/0	0/0
III	7.33	6.07	2.42	8.00	0/0
IV	1.88	7.83	26.67	44.00	49/0
V	1.79	1.52	9.50	2.33	0/0
VI	34.92	34.92	397.00	397.00	365/0
VII	1.55	6.11	2.86	6.00	0/0

The results in Table 8 give advice for the choice of settings to visual monitoring. The larger the ratio is, the larger the fault period abnormality is in visual monitoring. The best approach is method VI; the second best approach is method IV; the third best approach is method V. With method II, the best ratio is 4.00, which is lower than other methods at their best have. Therefore, it shows the difference between normality and abnormality worst in visual monitoring.

Fig. 2 shows the divergences of method I with setting 4 and method VI with setting 3 during fault period and faultless period. Figure shows that the divergence of method I has occasionally grown during faultless period, whereas divergence of method VI had only one change during faultless period. Fig. 2 illustrates that method VI is more unambiguous than method I in visualising an abnormal process state. The magnitude of divergence is also distinct with the methods. The fault period plots show that both methods start detecting divergence at the same time near the 6,990th point and the divergence is progressively growing. Some decreases in divergence can be seen as well.

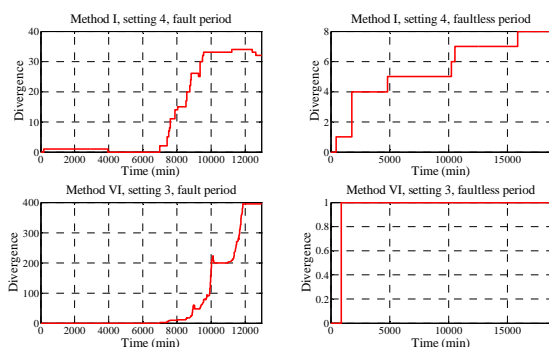


Fig. 2. Divergences during fault and faultless periods.

4.6 Discussion

The results in Table 5 suggest that methods I, III, IV, and VI could be able to find an abnormality with certain settings. Table 6 suggests that method I has the best performance on setting 4. With setting 4, method I has the best ratio (=11) of T_2 and T_1 differences. Methods III, IV and VI have the best performance on setting 3. With setting 3, methods IV and VI have the best ratio of T_2 and T_1 differences (=10.17 and =31.45, respectively); method III has no difference in T_1 and the most distinct difference in T_2 . In Table 6, method VI had even better ratio on setting 5 (=102) than on setting 3, but Table 5 suggests that setting 5 is not valid. Due to the

interpretation diversity, the results in Table 7 were found secondary to the selection of the most valid method.

Table 8 suggests that methods I, III, and IV function best on setting 4 with the largest ratios. Method VI functions best with setting 3, and not with setting 4 due to too many points outside limits on T_1 during the fault period. It should be noticed that Table 6 suggests setting 3 for methods III and IV, whereas Table 8 suggests setting 4. Based on Table 6, methods III and IV with settings 3 and 4 are both functioning well, whereas Table 8 suggests that setting 4 is notably better than setting 3 especially on method III. As a conclusion, the best approaches are methods I, III, and IV with setting 4, and method VI with setting 3. Therefore, tuning approaches with 0.1% and 0.2% of points outside control limits are the most valid from the tested settings.

Considering the suitability of the methods to real time monitoring, method III is the best. It is real time and setting 4 uses only an 80 minute sliding window. The computation of limits is fast, when only a short period of data is needed. Method I causes delay due to the fact that the monitored point is the midpoint in a sliding window. Setting 4, which is the best, causes 40 minute delay. Methods IV and VI use all the data from the monitored periods at once. These approaches are computationally heavy, if all the data is used in computation every time new data arrives. Methods V and VII, which are derivatives of IV and VI, could be a compromise solution with larger window sizes than was tested.

It has to be mentioned that the current settings are not optimal. The purpose of the study was to compare the methods, and not so much finding the optimal settings. For instance, method VI is very sensitive to tuning. Therefore, settings 1 and 2 or 3 and 4 have the same w , although the planned percentage of points outside the limits differs. Tuning of w should be done in smaller steps, but then again this kind of sensitivity brings problems. The settings are very case-specific, which is not the best option especially if several process variables are using the same settings.

Based on the results, method III with setting 4 is the most valid approach. 0.11% of the points fell outside the control limits in T_2 , whereas 0.03% was the corresponding percentage in T_1 . 0.1% of the points outside limits was defined to indicate an out-of-control period. Therefore, the detection of the abnormality was not very explicit.

Fig. 3 and 4 show the best method with the most optimal setting for monitoring purposes according to the results. The faultless period is monitored in Fig. 3. The fault period is monitored in Fig. 4. In Fig. 3 and 4, the upper part shows the divergence of the reactors, whereas the lower part shows the alarm balances of temperatures. Fig. 3 shows that only three occasional changes in divergence are detected during the faultless period. It means that the operation of the reactors was quite similar. The two changes in alarm balance of T_2 occurred during four minute periods near the 2,750th and 4,390th point. The last change occurred at 9,970th point in alarm balance of T_1 . The time between the alarms is so large that it clearly is not a sign of progressive abnormality.

However, such alarms may be worthy of closer analysis. With the used setting, at most 0.1% of points outside control limits were allowed and less was detected, which refers to an in-control process.

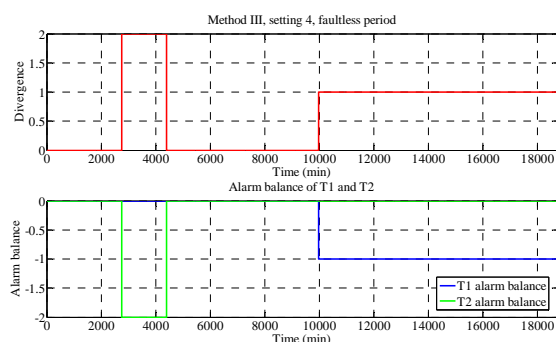


Fig. 3. The monitoring approach during faultless period.

Fig. 4 shows that divergence starts growing progressively near the 6,990th point. The growing ends near the 9,620th point. The period is less than 44 hours in length, because one minute sampling rate was used. The divergence of the reactors grew from 0 to 16. Roughly speaking, it is one alarm in 2 hours and 3 quarters of an hour. Therefore, this approach needs a lot of time to detect this kind of an abnormality, which may be unfavourable. However, an approach which does not cause false alarms is favourable. It is well-known that monotonous tasks, such as checking of numerous alarms, actually increase the risk of missing what should be detected (Oakland and Followell, 1990, p. 75).

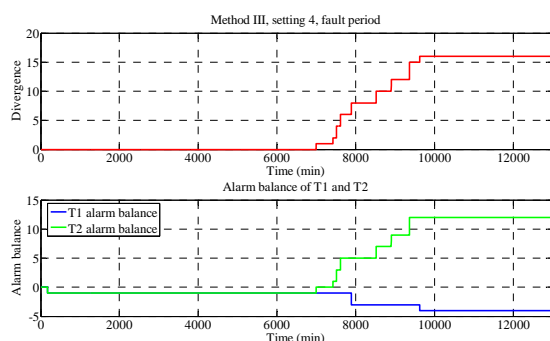


Fig. 4. The monitoring approach during fault period.

Although, the progressively growing divergence shows difference in the operation of the reactors, the cause for the difference can be only found with the help of process knowledge. Alongside with the presented approach, monitoring the difference of slurry flow rates to both of the reactors could have defined the origin of the fault more specifically. The current approach monitors only one variable from both of the reactors. More variables could be monitored and combined to compare parallel process units. However, this goes beyond the scope of this study.

The flow conditions in the channels after the reactors may vary. Single oscillations in temperature measurements may result from irregularity in temperature distribution or a faulty sensor. The output temperature sensors of the reactors are located similarly on the side of the outlet channels. T1 and T2

are created from a minimum measuring result of four sensors per channel. Therefore, sporadic temperature oscillations up in a single sensor do not have an effect in monitoring. If all the measured temperatures oscillate up, then the minimum temperature oscillates up as well. Oscillation down on a single sensor may cause a faulty minimum value. Such matters should be kept in mind with this approach.

5. CONCLUSIONS

In this study, seven statistical approaches to desulphurization plant monitoring were compared. Control limits for two process variables were generated and points outside these limits were detected. Alarm balance was used to monitor the variables. Difference between two parallel process units, namely reactors, was monitored by combining alarm balances of the variables. Four methods indicated that a process abnormality could be found with certain settings. Tuning the methods so that at most 0.1% or 0.2% of points lie outside control limits in normal operation gave the best results. Method III, which is based on calculation of moving average, moving standard deviation, median and the difference of maximum and minimum value weighted with user-defined parameters, was the most valid approach. Although difference in the operation of the reactors was found, root cause analysis needs additional process knowledge and brainstorming. Finding of the best settings for the methods needs more work.

REFERENCES

- Corbett, C.J., and Pan, J. (2002). Evaluating environmental performance using statistical process control techniques. *European journal of operational research*, vol. 139 (1), 68-83.
- De Veaux, R.D., Ungar, L.H., and Vinson, J.M. (1994). Statistical approaches to fault analysis in multivariate process control. *American control conference proceedings*, vol. 2, 1274-1278.
- Hossain, A., Choudhury, Z.A., and Suyut, S. (1996). Statistical process control of an industrial process in real time. *IEEE transactions on industrial applications*, vol. 32 (2), 243-249.
- Huber, P.J. (1981). *Robust Statistics*. John Wiley & Sons, New York.
- Liu, H., Shah, S., and Jiang, W. (2004). On-line outlier detection and data cleaning. *Computers and chemical engineering*, vol. 28 (9), 1635-1647.
- Oakland, J.S., and Followell, R.F. (1990). *Statistical process control: a practical guide*, 2. ed.. Heinemann Newness, Oxford.
- Pearson R.K. (2002). Outliers in process modeling and identification. *IEEE transaction on control systems technology*, vol. 10 (1), 55-63.
- Qin, S.J., and Li, W. (1999). Detection, identification, and reconstruction of faulty sensors with maximized sensitivity. *AIChE Journal*, vol. 45 (9), 1963-1976.
- Reynolds, M.R., Jr., and Stoumbos, Z.G. (2004). Control charts and the efficient allocation of sampling resources. *Technometrics*, vol. 46 (2), 200-214.

- Talonen, J., and Sirola, M. (2009). Generated control limits as a basis of operator-friendly process monitoring. *Proceedings of the 5th IEEE International workshop on intelligent data acquisition and advanced computing systems*, 468-472.
- Venkatasubramanian, V., Rengaswamy, R., Kavuri, S.N., and Yin, K. (2003). A review of process fault detection and diagnosis part III: process history based methods. *Computers and chemical engineering*, vol. 27 (3), 327-346.

Paper 10

Title: THE EFFECT OF COMPRESSIBILITY OF WATER AND ELASTICITY OF PENSTOCK WALLS ON THE BEHAVIOR OF A HIGH HEAD HYDROPOWER STATION

Behzad Rahimi Sharefi, Wenjing Zhou, Bjørn Glemmestad, Bernt Lie
Telemark University College, Norway

Keywords: Hydropower, Modeling and Simulation, Finite Volume Method

A high head hydropower generation unit typically consists of reservoir, waterway (head-race tunnel, surge shaft, penstock, turbine case and draft tube, and tail-race), turbine, and generator. The overall system is highly non-linear and its controller is usually designed for stability and best performance at the best-efficiency operating point using a linearized model. For having a stable operation and acceptable performance at the other operating points it may be necessary to change the controller parameters when the operating point of the system changes.

It is important to be able to model and simulate the system as accurately as possible. With an accurate model, a designed controller can be tested more reliably for stability and performance in different operating points. Different models with different degrees of complexity have been published [1]. The simple models consider rigid penstock walls with incompressible water column in the penstock. A more accurate model can be obtained if a penstock with elastic walls and compressible water column in the penstock is considered. Such a penstock can be modeled by two nonlinear partial differential equations. These equations can be linearized and solved by the Method of Characteristics (MOC) [2]. Numerical methods can also be used for solving these equations. Some software solutions such as WHAMO [3] and Hydro-Plant Library [4] are available for numerical simulations.

In this paper, first various parts of a typical high head hydropower generation unit and their functionality will be described briefly. Then modeling and numerical methods available for simulation of such system will be described in some detail. Specifications of the system under study will be as follows:

- elastic walls and compressible water column in the penstock
- rigid (inelastic) walls and incompressible water in other parts of the waterway (due to less pressure variations or short distances)
- the standard IEEE1992 model for turbines [5]
- synchronous generator connected to an infinite bus
- conventional PID controller with speed droop characteristics

In simulation of the penstock with elastic walls and compressible water column, the emphasis will be on the Finite Volume Method of Computational Fluid Dynamics [6]. The overall system will be simulated and the effect of compressible water in the penstock and with elastic penstock walls will be studied.

References:

[1]. Nand Kishor et al. "A Review on Hydropower Plant Models and Control." *Renewable and Sustainable Energy Reviews* 11 (2007) 776–796.

THE EFFECT OF COMPRESSIBILITY OF WATER AND ELASTICITY OF PENSTOCK WALLS ON THE BEHAVIOR OF A HIGH HEAD HYDROPOWER STATION

Behzad Rahimi Sharefi, Wenjing Zhou, Bjørn Glemmestad, Bernt Lie

Faculty of Technology, Department of Electrical Engineering, Information Technology and Cybernetics,
Telemark University College, P. O. Box 203, N-3901 Porsgrunn, Norway

Abstract: This paper considers modeling of a high-head hydropower generation unit when compressibility of the water and elasticity of the penstock walls are taken into account. Finite Volume Method and MATLAB are used to simulate the behavior of the penstock in this model. Various important parameters for simulation such as the number of grid volumes in the spatial discretization of the penstock as well as ODE solver options in MATLAB are examined by simulation, and are discussed. The simulation model thus obtained is validated using available charts for pressure rise in case of uniform gate closure. Then available models for the other parts of the waterway (inelastic models) are included to give an interface to the elastic penstock model. Finally, the model of the whole power generation unit with a classic transient droop controller and a synchronous generator connected to an infinite bus is simulated in MATLAB.

Key words: Hydropower, Hydroelectricity, Water Hammer, the Finite Volume Method, Simulation and Modeling of Dynamic Systems, Power System Dynamics

List of Symbols

Symbol	Description [Units]
a	Speed of the pressure waves in the water inside penstock [m/sec]
A	Cross-section area [m ²]
A_C, A_S and A_{TWT}	Cross-section area of the conduit, surge shaft and tail water tunnel respectively [m ²]
A_p^{atm}	Cross-section area of empty penstock (constant with axial location along the penstock) [m ²]
$A_{p,i}$	Cross-section area of the penstock as a function of only pressure at location X_i [m ²]
β	Compressibility of water = $4.5e-10$ [Pa ⁻¹]
β_p^{eq}	Equivalent compressibility due to penstock walls elasticity [Pa ⁻¹]
β_p^{total}	Total compressibility due to water compressibility and penstock walls elasticity [Pa ⁻¹]
C	Index referring to the conduit
C_v	Valve coefficient [m ³ /sec / Pa ^{0.5}]
CV_{2i+1}	Control volume for continuity equations, located between X_{2i} and X_{2i+2} (for $i=1, \dots, N-1$)
CV_{2i+2}	Control volume for momentum equations, located between X_{2i+1} and X_{2i+3} (for $i=1, \dots, N-2$)
δ	Transient droop [-]
Δx	Length of the control volumes for application of the mass or momentum conservation [m]
D	Pipe inner diameter [m]
e	Pipe thickness [m]

E	Young's modulus of elasticity [Pa]
f	Fanning friction factor [-]
f_C, f_S and f_{TWT}	Fanning friction factor of the conduit, surge shaft and tail water tunnel respectively [-]
$F_{p,2i+2}$	Pressure gradient force acting on the water column inside the control volume CV_{2i+2} [N]
$F_{G,2i+2}$	Gravity force acting on the water column inside the control volume CV_{2i+2} [N]
$F_{F,2i+2}$	Friction force acting on the water column inside the control volume CV_{2i+2} [N]
g	Gravity acceleration = 9.8 [m/sec ²]
h_{DT}	Height of the draft tube [m]
h_{HW}	Height of water column in the reservoir for simulations of Section 66 [m]
h_R	Height of water column in the head water reservoir [m]
h_{TW}	Height of water column in the tail water reservoir [m]
H_t	Turbine head [m] or [% of design head]
H_{td}	Turbine design head [m]
J	Momentum of inertia of turbine and generator rotor [Kg. m ²]
$\mathcal{K}_C, \mathcal{K}_{HW}, \mathcal{K}_{TW},$ \mathcal{K}_{TWT}	Friction coefficient in conduit, penstock interfaces in the head water and tail water and tail water tunnel respectively, so that the friction force on the water column inside these parts is found from the relation $\mathcal{K}\dot{m}^2$ [N. sec ² /Kg ²]
\mathcal{K}_S	Coefficient in surge shaft which accounts for both friction and variations of the water column length [N. sec ² /Kg ²]
ξ_{2i+2}	A friction coefficient; friction force applying on the control volume CV_{2i+2} is given by $\xi_{2i+2}V_{P,2i+2}$ [N. sec/m]
ℓ_S	Variable length of the water column in the surge shaft [m]
L	Length [m]
L_C, L_P, L_S, L_{TWT}	Length of the conduit, penstock, surge shaft and tail water tunnel respectively [m]
μ	Poisson's ratio [-]
m	Mass [Kg]
\dot{m}	Mass flow rate [Kg/sec]
\dot{m}_C	Mass flow rate of the conduit [Kg/sec]
$m_{P,2i+1}$	Mass of the water inside the control volume CV_{2i+1} [Kg]
$\dot{m}_{P,i}$	Penstock flow rate at location X_i [Kg/sec]
\dot{m}_{HWDI}	Mass flow rate at location X_4 (Figure 2) which is a state of the penstock model and can be used as an input by the head water system model. "HWDI" refers to "head water system input from the downstream". [Kg/sec]

\dot{m}_{HWDO}	Mass flow rate at location X_2 (Figure 2) which is a state of the head water system and can be used as an input by the penstock model. “HWDO” refers to the “head water system output to the downstream”. [Kg/sec]
\dot{m}_{TWUI}	Mass flow rate at location X_{2N-2} (Figure 2) which is a state of the penstock model and can be used as an input by the tail water system model. “TWUI” refers to “tail water system input from the upstream”. [Kg/sec]
\dot{m}_{TWUO}	Mass flow rate at location X_{2N} (Figure 2) which is a state of the tail water system model and can be used as an input by the penstock model. “TWUO” refers to “tail water system output to the upstream”. [Kg/sec]
N	Number of the Δx lengths along the penstock $N = L_p/\Delta x$
P	Index referring to the penstock
p	Pressure [Pa]
p_i	Penstock pressure at location X_i [Pa]
p_{HWDI}	Pressure at location X_3 (Figure 2) which is a state of the penstock model and can be used as an input by the head water system model. “HWDI” refers to “head water system input from the downstream”. [Pa]
p_{HWDO}	Pressure at location X_1 (Figure 2) which is a state of the head water system and can be used as an input by the penstock model. “HWDO” refers to the “head water system output to the downstream”. [Pa]
p_{TWUI}	Pressure at location X_{2N-1} (Figure 2) which is a state of the penstock model and can be used as an input by the tail water system model. “TWUI” refers to “tail water system input from the upstream”. [Pa]
p_{TWUO}	Pressure at location X_{2N+1} (Figure 2) which is a state of the tail water system model and can be used as an input by the penstock model. “TWUO” refers to “tail water system output to the upstream”. [Pa]
p^{atm}	Atmospheric pressure = $1\text{e}+5$ [Pa]
$p_{\text{CI}}, p_{\text{CX}}$ and p_{SX}	Pressures at the conduit inlet, conduit outlet and surge shaft outlet [Pa]
P_t	Turbine output power [W]
Π	Internal perimeter [m]
Π_p^{atm}	Internal perimeter of empty penstock (constant with axial location along the penstock) [m]
Π_C, Π_S and Π_{TWT}	Internal perimeter of the conduit, surge shaft and tail water tunnel respectively [m]
$\Pi_{p,2i+2}$	Internal perimeter of the penstock at X_{2i+2} [m]
Q_t	Turbine volumetric flow rate [m ³ /sec] or [% of rated discharge]
Q_{td}	Turbine rated volumetric discharge [m ³ /sec]
R	Index referring to the head water reservoir
R	Pipe inner radius [m]

ρ	Water density [Kg/m ³]
ρ^{atm}	Water density at atmospheric pressure =1000 [Kg/m ³]
ρ_i	Water density along the penstock at location X_i [Kg/m ³]
S	Index referring to the surge shaft
σ	Permanent droop [-]
TWT	Index referring to the tail water tunnel
θ	The angle that pipe makes with the horizon [rad]
θ_C, θ_S and θ_{TWT}	The angle with the horizon of the conduit, surge shaft and tail water tunnel respectively [rad]
$v_{P,i}$	Water velocity along the penstock at location X_i [m/sec]
X_i	Grid locations in every $\Delta x/2$ length of the penstock as shown in the Figure 2
Y_{GV}	Guide vanes opening [% or degrees]
ω_m^{design}	Turbine design mechanical speed [rad/sec]
V_S	RMS voltage of the infinite bus [V]
ω_s	Electric angular velocity on the infinite bus [rad/sec]
n_p	Number of the generator poles
r	Resistance of the phase winding [Ω]
r_e	Equivalent resistance of the infinite bus [Ω]
x_e	Equivalent reactance of the infinite bus [Ω]

1 Introduction

A high head hydropower generation unit is a highly non-linear system and its controller is usually designed for stability and best performance at the most efficient operating point using a linearized model. For having a stable operation and acceptable performance at the other operating points it may be necessary to change the controller parameters when the operating point of the system changes. It is important to be able to model and simulate the system as accurately as possible. With an accurate model, a designed controller can be tested more reliably for stability and performance in different operating points. Different models with different degrees of complexity have been published [1]. The simple models consider rigid penstock walls with an incompressible water column in the penstock. A more accurate model can be obtained if a penstock with elastic walls and compressible water column in the penstock is considered. Such a penstock can be modeled by two nonlinear partial differential equations. These equations can be linearized and solved by the Method of Characteristics [2]. Numerical methods can also be used for solving these equations. Some software solutions such as WHAMO [3] and the Hydro-Plant Library [4] are available for numerical simulations.

In this paper, a complete model for the hydropower generation unit is introduced which takes the compressibility of the water and elasticity of the penstock walls into account. The penstock model is validated by the charts available in the literature. Then the whole model is

simulated with a classic speed controller and a synchronous generator with voltage control loop to show the closed loop operation of the model.

2 Various Parts of a High Head Hydropower Generation Unit

Figure 1 shows a simple schematic drawing of the various parts of a typical high head hydropower generation plant. *Power house* (and other parts of the plant) is usually located inside mountains and can be accessed through additional tunnels that are not shown in the drawing. The *reservoir* in the upstream of the plant could have been created by the water stored behind a dam. In the following a brief description about other parts of the plant will be given:

Intake: *Intake* is equipped with a *trash rack* that prevents big solid objects entering into the waterway of the plant. Intake is usually equipped with a *gate valve* for maintenance purposes.

Conduit: *Conduit* (also known as *head race tunnel* [5] and *transfer tunnel* [6]) is a tunnel which conveys the water from the reservoir to the near of the power house. Length of the conduit might be a few kilometers. In some projects [6] length of the conduit can be as large as 45 kilometers. At the end of the conduit (near the surge shaft) the cross-section area of the conduit increases and hence the water velocity is reduced. This part of the conduit is equipped with *sand traps* and a finer trash rack to further filter solid objects in the water stream.

Surge Shaft: The surge shaft serves as a temporary storage (or source) of water in case of decrease (or increase) of water flow in the power house so that the huge amount of water in the conduit finds enough time to decelerate (or accelerate). So the surge shaft reduces the magnitude of the pressure surges (known as the “water hammer” effect [2]) that can happen in the waterway due to inertia of the water flowing inside the conduit.

Penstock: The penstock is a pipe (e.g. steel pipe) which connects the conduit and the surge shaft to the power house. The penstock (also known as “pressure shaft” [5]) has usually much greater slope than the conduit so that much of the water pressure builds up in the penstock. Due to these higher pressures, it is desirable to model the penstock with elastic walls and compressible water inside. Such a model will be introduced in the next section. Penstock may be equipped with isolating valves for maintenance.

Turbine: *Turbine* converts the potential and kinetic energy of the water flowing through the *turbine case* into mechanical energy. The converted energy is transferred into the generator by the common rotating shaft of the *turbine runner* and the generator rotor.

There are various types of the hydraulic turbines among which the *Pelton* turbines and the *Francis* turbines are the types that are used in the high head plants [2]. In the Pelton turbine, all the potential energy of the water first is converted into kinetic energy in jets of water. This energy is further converted into mechanical energy when these jets of water strike the *buckets* on the turbine runner. Jet nozzles control the flow rate of the water through the Pelton turbine. In the Francis turbine, whole the runner chamber is filled with water and the water flowing through the *runner passages* transfers its potential and kinetic energy to the runner. *Guide vanes* control the water flow rate through the Francis turbine.

Draft tube, tail water tunnel and tail water reservoir: *Draft tube* conveys the water flowing out of the Francis turbine runner passages to the tail water tunnel. The Figure 1 in fact shows the arrangement of a plant with Francis turbine. Tail water tunnel usually has positive slope to ensure that turbine is always submerged into the water to prevent cavitation. The difference between the water surface elevation in the head water reservoir and the tail water determines the *gross head* of the plant. When the *head losses* due to the friction between the water and the walls of the waterway are subtracted from the gross head, the result is called the “*net head*” of the plant and equals to the *turbine head* at the steady state operation conditions.

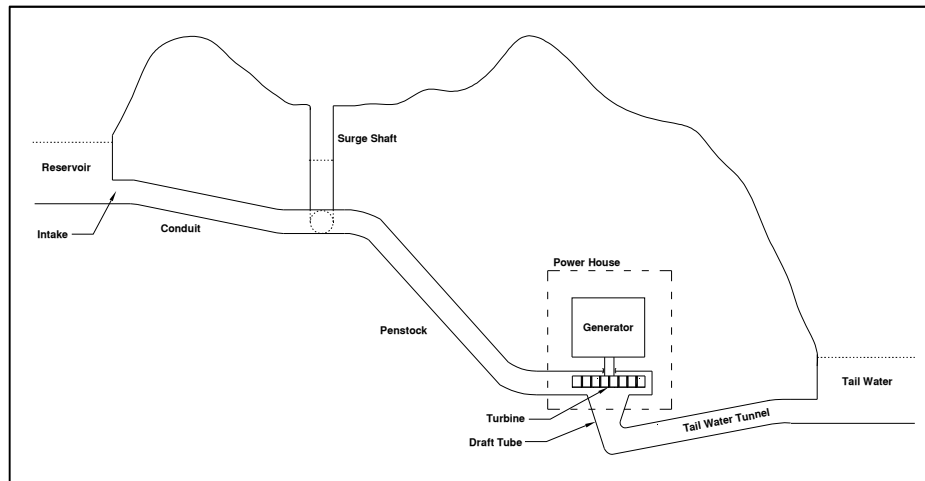


Figure 1 Schematic Drawing of a High Head Hydropower Generation Plant.

3 The Penstock Model

3.1 Problem Description

Compressible water flow inside a penstock with elastic walls is governed by two partial differential equations [2]. These PDEs are obtained by applying the mass and momentum conservation laws to a 1D infinitely small control volume along the penstock axis [7]. Numerical solution methods for these equations need both temporal and spatial discretization. Software such as WHAMO [3] which is a tool for simulation of water flow in pipe networks uses a finite difference scheme for discretizing the governing partial differential equations. In this scheme, the partial derivative terms are replaced by their equivalent “difference relations” and so the differential equations turn into difference equations. There is an alternative scheme referred to as the “Finite Volume Method” or simply “FVM”. This method (applied to a 1D problem such as fluid flow in a pipe) avoids the partial differential equations from the beginning by dividing the whole pipe volume into several control volumes along the pipe axis and then applying conservation laws to derive two ordinary differential equations for each control volume: One of the equations is an exact representation of the conservation of mass (continuity equation) and the other one is an exact representation of the conservation of momentum [8]. “Advantage of FVM is that the discretized governing equations retain their physical interpretation, rather than possibly distorting the physics due to numerical discrimination of each derivative term.” [9]¹

The idea of control volumes in FVM is better described by referring to Figure 2. The whole penstock length is divided into $2N$ equal segments. The first segment is between the locations X_1 and X_2 and the last segment is located between X_{2N} and X_{2N+1} . It is possible to define the volume determined by each two adjacent pipe segments located between X_{2i+1} and X_{2i+3} ($i=1, \dots, N-2$) as a control volume for application of both mass and momentum conservation laws, but this can cause the discretized momentum equations to have unrealistic behavior for spatially oscillating pressures [8]. The solution to this possible problem which is suggested in [8] is to use a so called “staggered grid”. Staggered grid for the penstock in the Figure 2 means to define the volume determined by each couple of pipe segments located between X_{2i+1} and X_{2i+3} (for $i=1, \dots, N-2$) as a control volume for application of the momentum conservation and

¹ It seems that instead of the word “discredited”, the word “discretized” should have been used by the source.

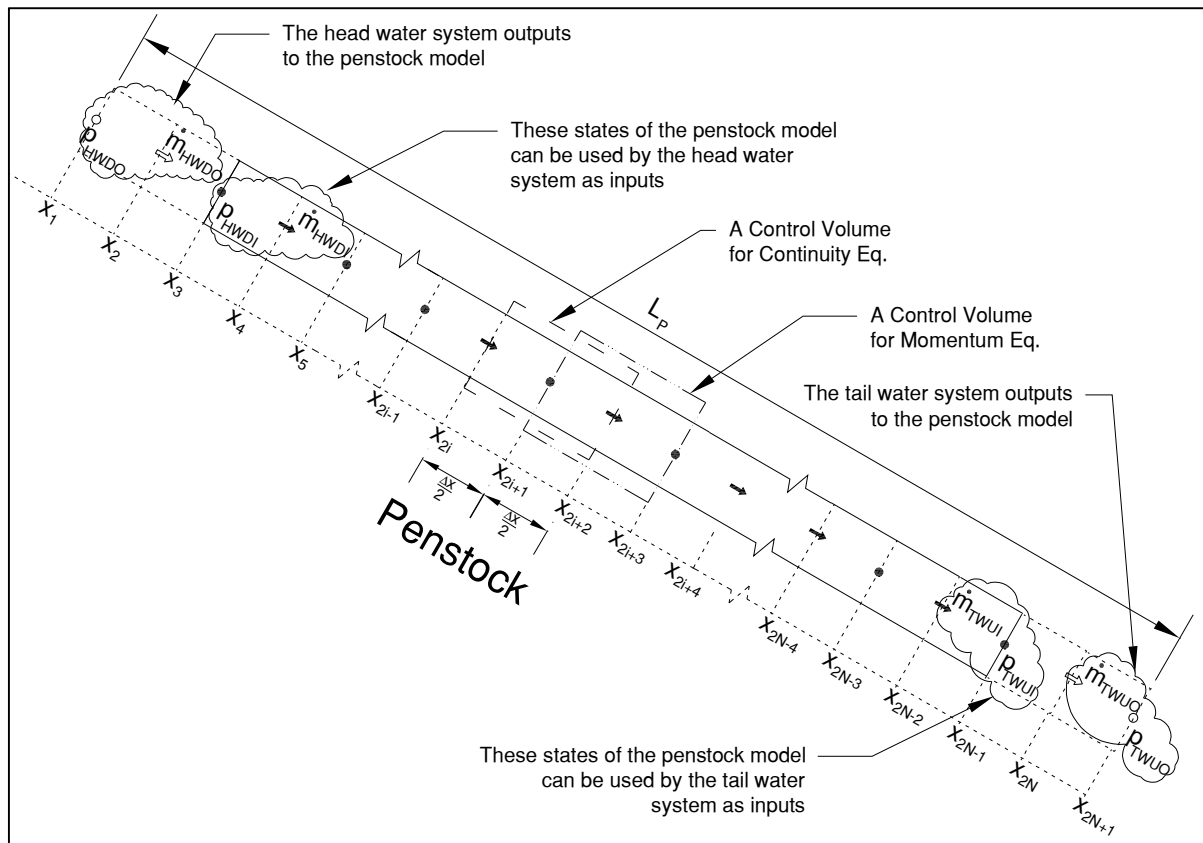


Figure 2 Control Volumes for Application of Mass and Momentum Conservation Laws in a Penstock.

define the volume determined by each couple of pipe segments located between X_{2i} and X_{2i+2} (for $i=1, \dots, N-1$) as a control volume for application of the mass conservation.

The state variables along the pipe which usually appear in the literature of Computational Fluid Dynamics are mass density and velocity of fluid particles. In this paper however it's been decided to use the pressure and mass flow rate as the state variables. The latter variables are more interesting than the former ones in a hydropower application. In addition, choosing the mass flow rate as the state has the advantage that in the steady-state condition the mass flow rate in the whole waterway of the plant will be the same (the surge shaft level will be constant in the steady-state condition and hence the mass flow rate in the conduit and penstock will also be the same). Hence determining the steady-state value of the states will be much easier.

The state "pressure" will be considered spatially constant along the whole length of a control volume for mass conservation and the state "mass flow rate" will be treated as being spatially constant along the whole length of a control volume for application of the momentum conservation. In [8] alternatively "density" and "velocity" are considered to be spatially constant inside their relevant control volumes. These states are indicated at the center of their related control volumes in Figure 2. Pressures are shown by bold dots and mass flow rates are shown by bold arrows. The differential equations governing these states will be introduced in the section 3.3. The cross-section area of the penstock when pressure inside and outside of the penstock is equal to the atmospheric pressure (i.e. when the penstock is empty) will be considered constant along the penstock axis throughout this paper. The amount of variation of the penstock cross-section area due to water pressure inside the penstock will be discussed in the next section.

The pressure and mass flow rate variables at locations X_1, X_2, X_{2N} and X_{2N+1} are shown with hollow dots and arrows. This denotes that these variables will not be governed by the penstock equations. They will be determined by the head/tail water system models and will be treated as inputs in the penstock model. States of the penstock model at locations X_3, X_4, X_{2N-2} and X_{2N-1} will be available as outputs to the neighboring systems (head/tail water). Variables at these eight locations are named after their neighboring systems (“HWDI” refers to “the head water system input from the downstream”, “HWDO” refers to “the head water system output to the downstream”, “TWUI” refers to “the tail water system input from the upstream” and “TWUO” refers to “the tail water system output to the upstream”).

3.2 Water Density and Pipe Cross-Section Area as a Function of Pressure

The relationship between water density and pressure can be concluded from definition of the compressibility factor for fluids. The compressibility factor β is defined by the following relation:

$$\beta = \frac{1}{\rho} \frac{\partial \rho}{\partial p} \quad \text{Eq. 1}$$

Relationship for density of water at location $X = X_i$ along the penstock can then be found by integrating both sides of the Eq. 1 (assuming that β for the water is constant in the range of pressures and temperatures which is common in the hydropower applications). The result is given in the Eq. 2 below:

$$\rho_i = \rho^{\text{atm}} e^{\beta(p_i - p^{\text{atm}})} \quad \text{Eq. 2}$$

The relationship for changes in the pipe inner radius (ΔR) and changes in the pipe cross-section area (ΔA) as a function of the pressure difference between the inside and the outside of the pipe (Δp) is given in [7] for a pipe which is anchored against longitudinal movement. This relationship is presented by the Eq. 3 below:

$$\frac{\Delta A}{A} = 2 \frac{\Delta R}{R} = \frac{D(1 - \mu^2)}{eE} \Delta p \quad \text{Eq. 3}$$

Again, integrating of the Eq. 3 will result in an exponential function in terms of pressure for A. The result is given below:

$$A_{P,i} = A_P^{\text{atm}} e^{\beta_P^{\text{eq}}(p_i - p^{\text{atm}})} \quad , \quad \beta_P^{\text{eq}} = \frac{D(1 - \mu^2)}{eE} \quad \text{Eq. 4}$$

Here also it is assumed that β_P^{eq} is constant in the range of pressures and temperatures that it is dealt with in hydropower applications.

The relations in Eq. 2 and Eq. 4 can be combined to give the following:

$$A_{P,i} \rho_i = A_P^{\text{atm}} \rho^{\text{atm}} e^{\beta_P^{\text{total}}(p_i - p^{\text{atm}})} \quad \text{Eq. 5}$$

Here $\beta_p^{\text{total}} = \beta_p^{\text{eq}} + \beta$ is the total compressibility due to compressibility of the water and elasticity of the penstock walls. β_p^{total} is related to the speed of sound in the water inside the penstock as follows: [7]

$$a = 1/\sqrt{\rho^{\text{atm}}\beta_p^{\text{total}}} \quad \text{Eq. 6}$$

In the range of pressures and elasticity which is common in the hydropower applications, it is valid to assume that the values of A , ρ or the product $A \times \rho$ change linearly with pressure. So the following approximations can be used for Eq. 2, Eq. 4 and Eq. 5:

$$\begin{aligned} \rho_i &\approx \rho^{\text{atm}}[1 + \beta(p_i - p^{\text{atm}})] \\ A_{P,i} &\approx A_P^{\text{atm}}[1 + \beta_p^{\text{eq}}(p_i - p^{\text{atm}})] \\ A_{P,i} \times \rho_i &\approx A_P^{\text{atm}}\rho^{\text{atm}}[1 + \beta_p^{\text{total}}(p_i - p^{\text{atm}})] \end{aligned} \quad \text{Eq. 7}$$

3.3 Governing Equations

3.3.1 Continuity Equations

Continuity equations are the result of application of the mass conservation law to the control volumes CV_{2i+1} enclosed between penstock cross-sections at locations X_{2i} and X_{2i+2} (for $i=1, \dots, N-1$). Mass conservation simply states that the rate of change of the fluid mass inside the control volume with time is equal to the net rate of mass flow into the control volume. The amount of the mass of water inside the control volume CV_{2i+1} is given by the following relation:

$$m_{P,2i+1} = \int_{X=X_{2i}}^{X_{2i+2}} \rho_{2i+1} A_{P,2i+1} dX = \rho_{2i+1} A_{P,2i+1} \Delta x \quad \text{Eq. 8}$$

In calculation of the integral term it has been assumed that pressure and hence density and cross-section area are spatially constant inside the control volume. It is of great importance for the later analysis that the value of $A \times \rho$ at the boundaries of a control volume for continuity (X_{2i} and X_{2i+2}) be assumed equal to the mean value of that function in the two adjacent control volumes (Bold dots in Figure 3 (a)):

$$\rho_{2i+2} A_{P,2i+2} = (\rho_{2i+1} A_{P,2i+1} + \rho_{2i+3} A_{P,2i+3})/2 \quad \text{Eq. 9}$$

Considering Eq. 8, the mass conservation law results in the following differential equations for the control volumes CV_{2i+1} ($i = 1, \dots, N-1$):

$$\Delta x \frac{d}{dt} (\rho_{2i+1} A_{P,2i+1}) = \dot{m}_{P,2i} - \dot{m}_{P,2i+2} \quad \text{Eq. 10}$$

By using Eq. 7, the derivative term in the above equation will turn into:

$$\frac{d}{dt}(A_{P,2i+1}\rho_{2i+1}) = \frac{d}{dp_{2i+1}}(A_{P,2i+1}\rho_{2i+1}) \frac{dp_{2i+1}}{dt} = \beta_P^{total} A_P^{atm} \rho^{atm} \frac{dp_{2i+1}}{dt} \quad \text{Eq. 11}$$

Substituting the Eq. 11 into the Eq. 10 will result in *the final form of the continuity equations* as follows:

$$\Delta x \beta_P^{total} A_P^{atm} \rho^{atm} \frac{dp_{2i+1}}{dt} = \dot{m}_{2i} - \dot{m}_{2i+2} \quad (i = 1, \dots, N-1) \quad \text{Eq. 12}$$

3.3.2 Momentum Equations

Momentum conservation for the control volume CV_{2i+2} enclosed between penstock cross-sections at locations X_{2i+1} and X_{2i+3} (for $i=1, \dots, N-2$) states that the rate of change (with time) of the momentum (in the X direction i.e. conventional direction of the water flow) of the water flowing inside the control volume at a particular time t is equal to the rate of the net momentum flowing into the control volume by mass transport at boundary surfaces $X = X_{2i+1}$ and $X = X_{2i+3}$ plus sum of the forces that apply to the water column inside the control volume at the X direction along the penstock axis at that time.

The amount of momentum of the water column in the control volume CV_{2i+2} is as follows:

$$\int_{CV_{2i+2}} v \, dm = \int_{CV_{2i+2}} v (A \rho \, dX) = \int_{CV_{2i+2}} (v A \rho) \, dX = \int_{CV_{2i+2}} \dot{m} \, dX = \dot{m}_{P,2i+2} \Delta x \quad \text{Eq. 13}$$

In deriving the above relation it is assumed that the mass flow rate in the X direction inside the control volume is spatially constant and equal to $\dot{m}_{P,2i+2}$. This assumption is indicated in Figure 3 (b). By this assumption velocity throughout the control volume will be piecewise constant because the product $A \times \rho$ is assumed to be piecewise constant between X_{2i+1} and X_{2i+3} (Figure 3 (a)). The velocity at X_{2i+2} can be considered equal to:

$$v_{P,2i+2} = \dot{m}_{P,2i+2} / (A_{P,2i+2} \rho_{2i+2}) \quad \text{Eq. 14}$$

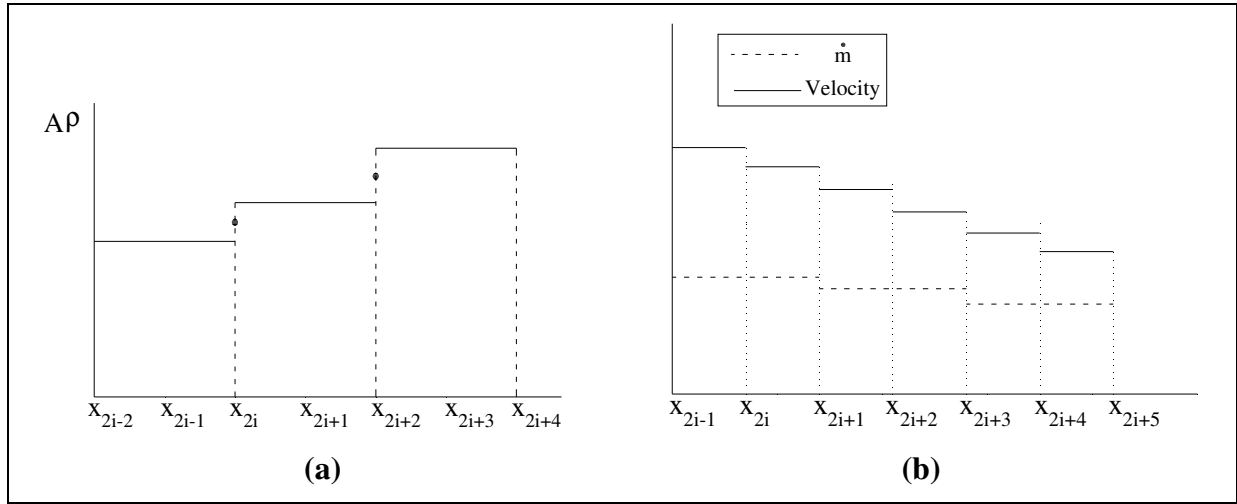


Figure 3 (a) Values of the Product $A \times p$ Inside the Control Volumes for Mass Conservation and at the Boundary Points of the Control Volumes. (b) Variations of Mass Flow Rate and Velocity inside Control Volumes for Momentum.

The momentum in the X direction along the penstock which is flowing into the control volume CV_{2i+2} due to mass transport is equal to:

$$\dot{m}_{p,2i+1} v_{p,2i+1} - \dot{m}_{p,2i+3} v_{p,2i+3} \quad \text{Eq. 15}$$

Forces that act on the water column are due to pressure difference between locations x_{2i+1} and x_{2i+3} , weight of the water column and friction between the water and the penstock wall. The force due to pressure difference at locations x_{2i+1} and x_{2i+3} is given in the following relation:

$$F_{p,2i+2} = A_{p,2i+2} (p_{2i+1} - p_{2i+3}) \quad \text{Eq. 16}$$

Relations giving the amount of gravity and friction forces for the water column inside control volume CV_{2i+2} are as follows respectively:

$$F_{G,2i+2} \cong \Delta x A_{p,2i+2} \rho_{2i+2} g \sin \theta_p \quad \text{Eq. 17}$$

$$F_{F,2i+2} = \xi_{2i+2} v_{p,2i+2} \quad \text{Eq. 18}$$

The coefficient ξ_{2i+2} is given in the following relation:

$$\xi_{2i+2} = -\frac{1}{2} f_p \Delta x \Pi_{p,2i+2} \rho_{2i+2} \text{sign}(v_{p,2i+2}) v_{p,2i+2} \quad \text{Eq. 19}$$

Now the momentum conservation law can be formulated for the control volume CV_{2i+2} using Eq. 13 to Eq. 19:

$$\Delta x \frac{d\dot{m}_{p,2i+2}}{dt} = \dot{m}_{p,2i+1} v_{p,2i+1} - \dot{m}_{p,2i+3} v_{p,2i+3} + F_{p,2i+2} + F_{G,2i+2} + F_{F,2i+2} \quad \text{Eq. 20}$$

The Upwind Difference Scheme

The relation in Eq. 14 gives the value of the water velocity at locations X_{2i+2} ($i=1,\dots,N-2$). The relation for velocity and mass flow rate at locations X_{2i+1} ($i=1,\dots,N-1$) is not given yet. In computational fluid dynamics, a so called “Upwind Difference Scheme” is often used for this case for stability purposes [8]. According to this scheme, the relation for velocity at a boundary of a control volume for momentum depends on the direction of the flow at that location. The following will show how to determine these relations.

The relations for mass flow rate at a boundary of a control volume for the momentum will be as follows:

$$\dot{m}_{P,2i+1} = (\dot{m}_{P,2i} + \dot{m}_{P,2i+2})/2 \quad , \quad \dot{m}_{P,2i+3} = (\dot{m}_{P,2i+2} + \dot{m}_{P,2i+4})/2 \quad \text{Eq. 21}$$

For the analysis, it is necessary to rewrite Eq. 20 in terms of $(dv_{P,2i+2}/dt)$. This is achieved by the use of Eq. 9, Eq. 10 and Eq. 14:

$$\Delta x \quad A_{P,2i+2} \quad \rho_{2i+2} \quad \frac{d v_{P,2i+2}}{dt} + \left(\frac{\dot{m}_{P,2i} - \dot{m}_{P,2i+4}}{2} - \xi_{2i+2} \right) v_{P,2i+2} =$$

$$\dot{m}_{P,2i+1} v_{P,2i+1} - \dot{m}_{P,2i+3} v_{P,2i+3} + F_{G,2i+2} + F_{P,2i+2} \quad \text{Eq. 22}$$

If water velocity at both boundaries of the control volume (at locations X_{2i+1} and X_{2i+3}) be positive in the X direction, then the upwind difference scheme requires that $v_{P,2i+1}$ and $v_{P,2i+3}$ in Eq. 22 be replaced with $v_{P,2i}$ and $v_{P,2i+2}$ respectively. So referring also to Eq. 21, Eq. 22 will turn into the following:

$$\Delta x \quad A_{P,2i+2} \quad \rho_{2i+2} \quad \frac{d v_{P,2i+2}}{dt} + \left(\frac{\dot{m}_{P,2i} + \dot{m}_{P,2i+2}}{2} - \xi_{2i+2} \right) v_{P,2i+2} =$$

$$\left(\frac{\dot{m}_{P,2i} + \dot{m}_{P,2i+2}}{2} \right) v_{P,2i+1} + F_{G,2i+2} + F_{P,2i+2} \quad \text{Eq. 23}$$

Hence Scarborough's condition for stability [8, p. 112] is satisfied and Eq. 22 and Eq. 23 will have a stable answer for steady-state velocity values in case of known pressures.

If water velocity at both boundaries of the control volume be negative in the X direction, then the upwind difference scheme requires that $v_{P,2i+1}$ and $v_{P,2i+3}$ in Eq. 22 be replaced with $v_{P,2i+2}$ and $v_{P,2i+4}$ respectively. Then Eq. 22 will turn into the following:

$$\Delta x \quad A_{P,2i+2} \quad \rho_{2i+2} \quad \frac{d v_{P,2i+2}}{dt} + \left(-\frac{\dot{m}_{P,2i+2} + \dot{m}_{P,2i+4}}{2} - \xi_{2i+2} \right) v_{P,2i+2} =$$

$$\left(-\frac{\dot{m}_{P,2i+2} + \dot{m}_{P,2i+4}}{2} \right) v_{P,2i+1} + F_{G,2i+2} + F_{P,2i+2} \quad \text{Eq. 24}$$

Again Scarborough's condition will be satisfied.

For satisfaction of Scarborough's condition it is not necessary that flow at both ends of the control volume be in the same direction. In fact, $\dot{m}_{P,2i} + \dot{m}_{P,2i+2} \geq 0$ for Eq. 23 and

$\dot{m}_{P,2i+2} + \dot{m}_{P,2i+4} \leq 0$ for Eq. 24 are sufficient conditions. If none of these conditions hold for a particular control volume, one can neglect the transported momentum terms for that particular control volume at that time which will result in the following equation:

$$\Delta x A_{P,2i+2} \rho_{2i+2} \frac{d v_{P,2i+2}}{dt} - \xi_{2i+2} v_{P,2i+2} = F_{G,2i+2} + F_{P,2i+2} \quad \text{Eq. 25}$$

So regarding the above discussion *the final form of the momentum equations* for $i=1,2,\dots,N-2$ will be as follows:

$$\Delta x \frac{d \dot{m}_{P,2i+2}}{dt} + a_{2i+2}^{\{2i+2\}} v_{P,2i+2} = a_{2i}^{\{2i+2\}} v_{P,2i} + a_{2i+4}^{\{2i+2\}} v_{P,2i+4} + F_{G,2i+2} + F_{p,2i+2} \quad \text{Eq. 26}$$

Here $a_{2i}^{\{2i+2\}}$, $a_{2i+2}^{\{2i+2\}}$ and $a_{2i+4}^{\{2i+2\}}$ are obtained from the following table:

	if $\dot{m}_{P,2i} + \dot{m}_{P,2i+2} \geq 0$	if $\dot{m}_{P,2i+2} + \dot{m}_{P,2i+4} \leq 0$	else
$a_{2i+2}^{\{2i+2\}}$	$\frac{\dot{m}_{P,2i+2} + \dot{m}_{P,2i+4}}{2} - \xi_{2i+2}$	$-\frac{\dot{m}_{P,2i} + \dot{m}_{P,2i+2}}{2} - \xi_{2i+2}$	$-\xi_{2i+2}$
$a_{2i}^{\{2i+2\}}$	$\frac{\dot{m}_{P,2i} + \dot{m}_{P,2i+2}}{2}$	0	0
$a_{2i+4}^{\{2i+2\}}$	0	$-\frac{\dot{m}_{P,2i+2} + \dot{m}_{P,2i+4}}{2}$	0

According to Figure 2, p_{HWD0} and \dot{m}_{HWD0} are the inputs of the penstock model from the head water system. p_{HWD0} is only needed to calculate $A_{P,2}$, ρ_2 and $A_{P,2}\rho_2$. The penstock segment between the locations $X = X_1$ and $X = X_3$ can be considered with inelastic walls and incompressible water model when Δx is very small. In this case the pressure p_{HWD0} will no longer be needed for the penstock model. The same is true for p_{TWU0} and the following relations can be used:

$$A_{P,2} = A_{P,2N} = A_P^{atm}, \quad \rho_2 = \rho_{2N} = \rho^{atm}$$

The set of ordinary differential equations given by Eq. 12 and Eq. 26 define the penstock model with compressible water and elastic walls.

4 Head Water and Tail Water

4.1 Head Water System

Figure 4 shows details of the head water system which consists of reservoir, conduit, surge shaft and a new part added in this paper as an interface to the elastic penstock model. This part represents the first Δx length of the penstock. Incompressible water and inelastic walls will be considered in the model of head water system. Applying mass and momentum conservation laws will result in a system of differential equations for the head water system given by Eq. 27 to Eq. 29 below:

$$\frac{d\ell_s}{dt} = \frac{\dot{m}_C - \dot{m}_{\text{HWDO}}}{A_S \rho^{\text{atm}}} \quad \text{Eq. 27}$$

$$L_C \frac{d\dot{m}_C}{dt} = -A_C(p_{\text{HWDO}} - p_{\text{CI}}) + \rho^{\text{atm}} g L_C A_C \sin \theta_C - \mathcal{K}_C \dot{m}_C^2 \quad \text{Eq. 28}$$

$$\Delta x \frac{d\dot{m}_{\text{HWDO}}}{dt} = -A_P^{\text{atm}}(p_{\text{HWDI}} - p_{\text{HWDO}}) + \rho^{\text{atm}} g \Delta x A_P^{\text{atm}} \sin \theta_P - \mathcal{K}_{\text{HW}} \dot{m}_{\text{HWDO}}^2 \quad \text{Eq. 29}$$

p_{CI} And p_{HWDO} in the above equations can be found from the following relation:

$$p_{\text{CI}} = p^{\text{atm}} + \rho^{\text{atm}} g h_R \quad \text{Eq. 30}$$

$$p_{\text{HWDO}} = \left(\frac{A_C}{L_C} + \frac{A_P^{\text{atm}}}{\Delta x} + \frac{A_S}{\ell_S} \right)^{-1} \left[\left(\frac{A_C}{L_C} p_{\text{CI}} + \frac{A_P^{\text{atm}}}{\Delta x} p_{\text{HWDI}} + \frac{A_S}{\ell_S} p^{\text{atm}} \right) + \right. \\ \left. \rho_{\text{atm}} g (A_C \sin \theta_C - A_P^{\text{atm}} \sin \theta_P + A_S \sin \theta_S) - \frac{\mathcal{K}_C}{L_C} \dot{m}_C^2 - \frac{\mathcal{K}_S}{\ell_S} (\dot{m}_{\text{HWDO}} - \dot{m}_C)^2 + \frac{\mathcal{K}_{\text{HW}}}{\Delta x} \dot{m}_{\text{HWDO}}^2 \right] \quad \text{Eq. 31}$$

\mathcal{K}_C and \mathcal{K}_{HW} are friction coefficients and \mathcal{K}_S accounts for both the friction and the variation of the length of the water column inside the surge shaft. These coefficients are defined below:

$$\mathcal{K}_S = \frac{f_s \ell_S \Pi_S \text{sign}(\dot{m}_{\text{HWDO}} - \dot{m}_C)}{2 A_S^2 \rho^{\text{atm}}} + \frac{1}{A_S \rho^{\text{atm}}} \quad \text{Eq. 32}$$

$$\mathcal{K}_C = \frac{f_C L_C \Pi_C \text{sign}(\dot{m}_C)}{2 A_C^2 \rho^{\text{atm}}} , \quad \mathcal{K}_{\text{HW}} = \frac{f_P \Delta x \Pi_P^{\text{atm}} \text{sign}(\dot{m}_{\text{HWDO}})}{2 (A_P^{\text{atm}})^2 \rho^{\text{atm}}} \quad \text{Eq. 33}$$

p_{HWDI} is an input from the penstock model. \dot{m}_{HWDI} of the penstock is not used by the inelastic model of the head water system.

A special case is also introduced by the Figure 4. This case will be used for validation of the elastic penstock model in this paper. Equations governing this special case are Eq. 29 plus the following relation which will replace Eq. 31:

$$p_{\text{HWDO}} = p^{\text{atm}} + \rho^{\text{atm}} g h_R \quad \text{Eq. 34}$$

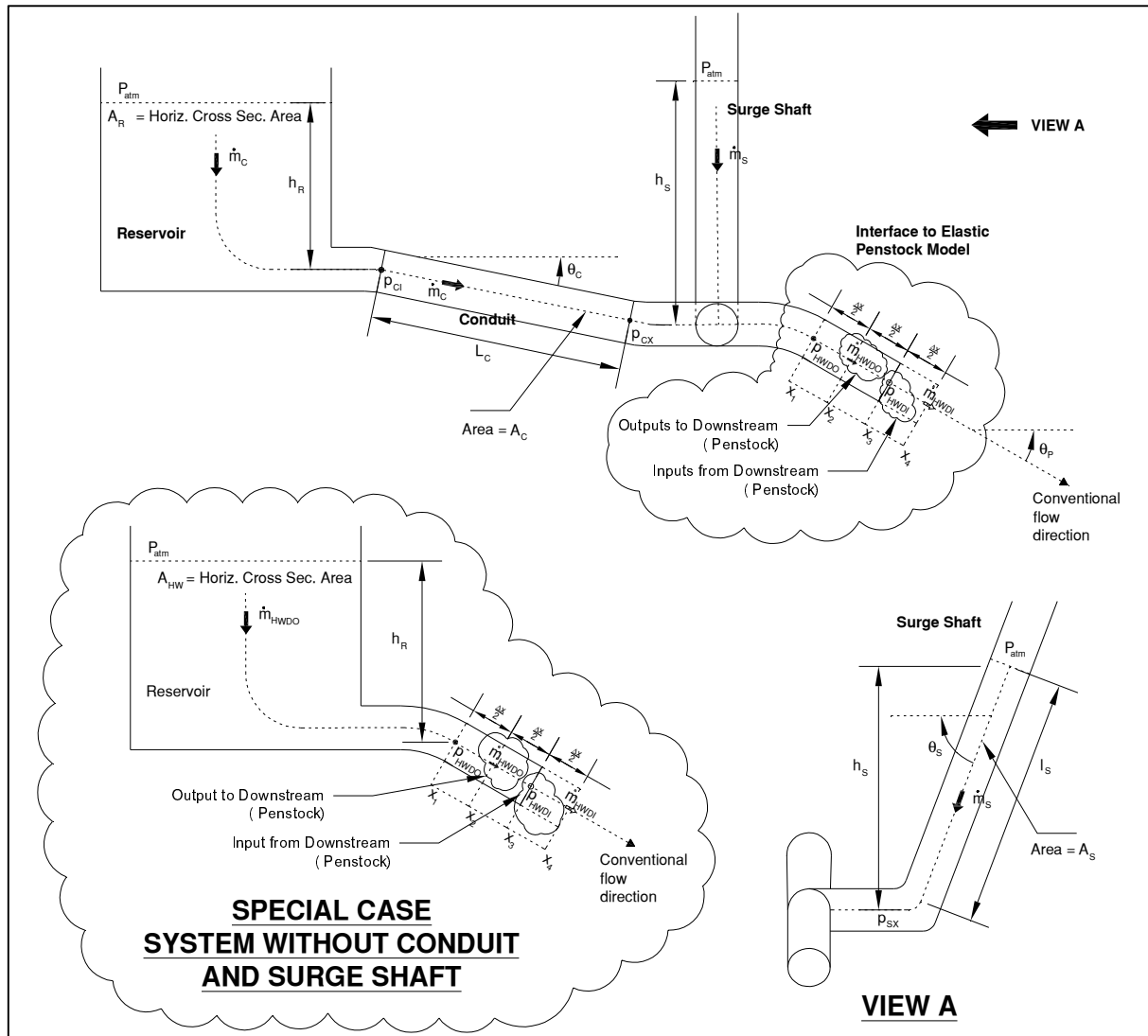


Figure 4 Details of the Head Water System.

4.2 Turbine, Draft Tube and Tail Water System

Figure 5 shows details of the system consisting of turbine, draft tube, tail water tunnel and tail water reservoir. Just as for the head water case, an interface part to the elastic penstock model is added in this paper. The governing equation of the system will be as follows:

$$\Delta x \frac{dm_{TWUO}}{dt} = -A_P^{atm} (p_{TWUO} - p_{TWUI}) + \rho^{atm} g \Delta x A_P^{atm} \sin \theta_P - \mathcal{K}_{TW} \dot{m}_{TWUO}^2 \quad \text{Eq. 35}$$

Here

$$P_{TWUO} = \left(1 + \frac{L_{TWT}}{\Delta x} \frac{A_P^{atm}}{A_{TWT}}\right)^{-1} \left(\rho^{atm} g (H_t - h_{DT}) + p_{TWTX} + \frac{L_{TWT}}{\Delta x} \frac{A_P^{atm}}{A_{TWT}} p_{TWUI}\right)$$

$$+\rho_{\text{atm}} g L_{\text{TWT}} \left(\sin \theta_{\text{TWT}} + \frac{A_{\text{P}}^{\text{atm}}}{A_{\text{TWT}}} \sin \theta_{\text{P}} \right) + \left(\mathcal{K}_{\text{TWT}} - \frac{L_{\text{TWT}}}{\Delta x} \mathcal{K}_{\text{TW}} \right) \frac{\dot{m}_{\text{TWUO}}^2}{A_{\text{TWT}}} \quad \text{Eq. 36}$$

$$p_{\text{TWTX}} = p^{\text{atm}} + \rho^{\text{atm}} g h_{\text{TW}} \quad \text{Eq. 37}$$

$$\mathcal{K}_{\text{TW}} = \frac{f_{\text{P}} \Delta x \Pi_{\text{P}}^{\text{atm}} \text{sign}(\dot{m}_{\text{TWUO}})}{2 (A_{\text{P}}^{\text{atm}})^2 \rho^{\text{atm}}} , \quad \mathcal{K}_{\text{TWT}} = \frac{f_{\text{TWT}} L_{\text{TWT}} \Pi_{\text{TWT}} \text{sign}(\dot{m}_{\text{TWUO}})}{2 A_{\text{TWT}}^2 \rho^{\text{atm}}} \quad \text{Eq. 38}$$

The term H_t in Eq. 36 (difference of the pressure at the turbine inlet and outlet [m]) is a function of \dot{m}_{TWUO} and turbine guide vanes opening. H_t is approximately proportional to \dot{m}_{TWUO}^2 for fixed guide vanes opening. p_{TWUI} is the input from the penstock model and \dot{m}_{TWUI} does not appear in the equations of tail water system.

Again a special case is introduced in Figure 5. In this case, the penstock ends in a valve which is open to the atmospheric pressure. The valve could be for example nozzles of a Pelton turbine. This special case in conjunction with the special case in Figure 4 will be used for validating the penstock model. Equations for the special case system are Eq. 35 plus the following equation which will replace Eq. 36:

$$p_{\text{TWUO}} = p^{\text{atm}} + \frac{\dot{m}_{\text{TWUO}} |\dot{m}_{\text{TWUO}}|}{\rho^{\text{atm}^2} C_v^2} \quad \text{Eq. 39}$$

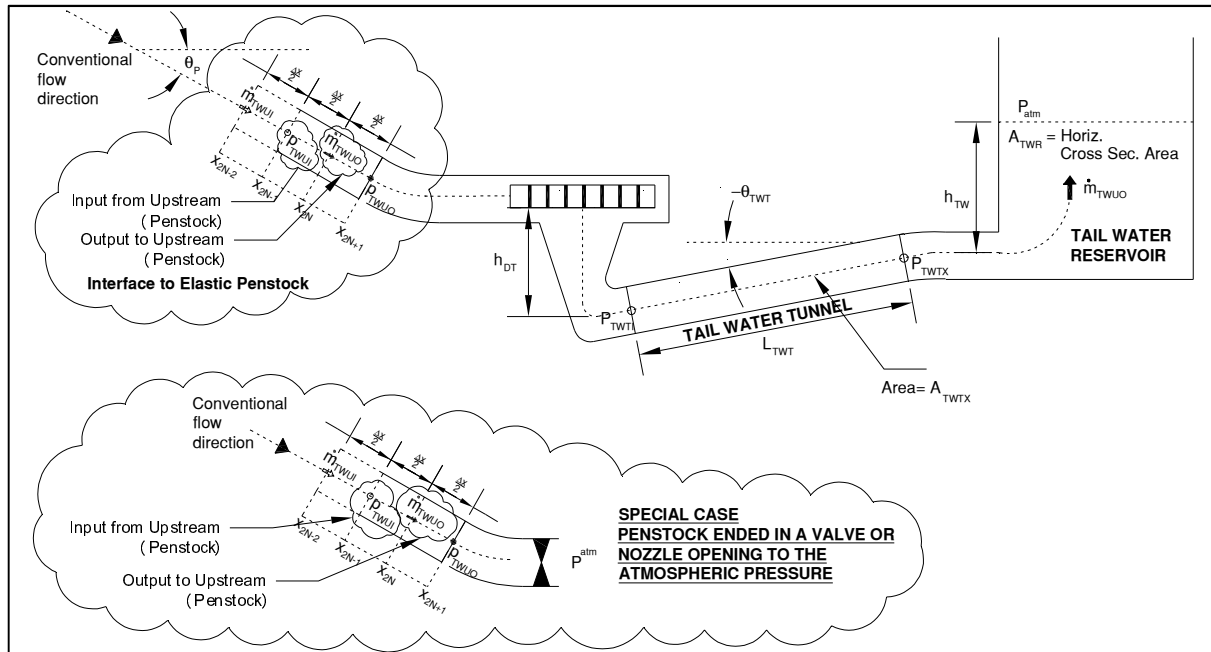


Figure 5 Details of the Turbine, Draft Tube and Head Water System.

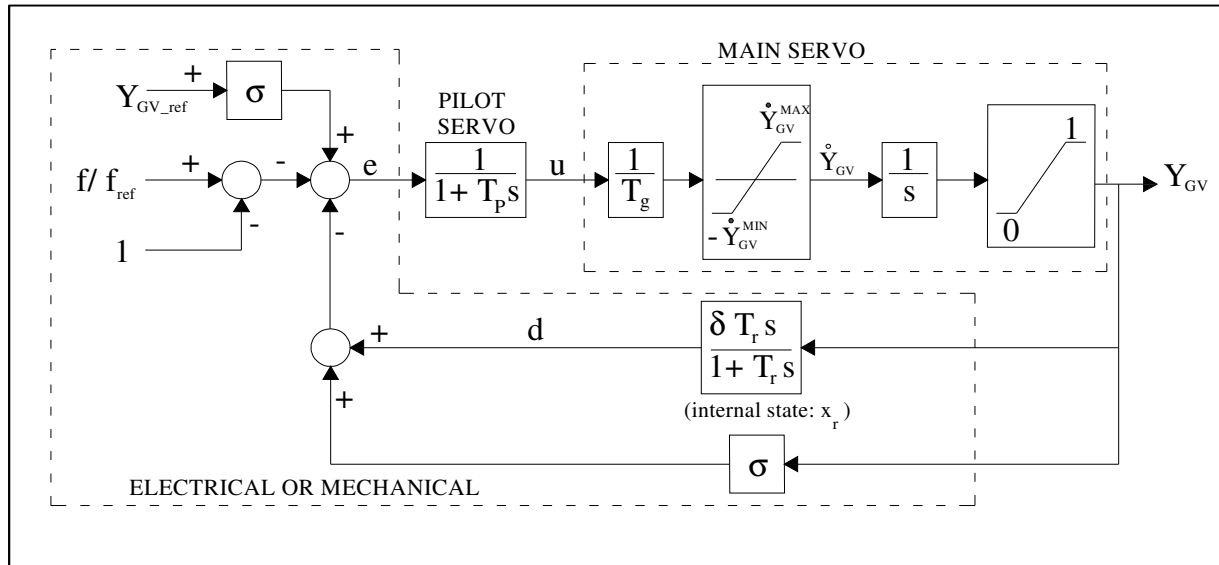


Figure 6 Block Diagram of the Turbine Controller [10].

5 Turbine Controller and Generator

A classic transient droop controller [10] with block diagram shown in Figure 6 will be used for closed loop simulations. Turbine output power is given by the following relation:

$$P_t = \eta_t \rho^{\text{atm}} g H_t Q_t \quad \text{Eq. 40}$$

Here η_t (turbine efficiency) is a function of H_t , Q_t and rotational speed of the turbine in general. A detailed model of the turbine can be found in [11].

A synchronous generator with one damper winding in the q axis will be considered with connection to the infinite bus as shown in Figure 7. Model of the generator can be found in [10, pp. 453-457]. Parameters of the generator used for simulations in this paper are given in Appendix I. $R_e + jX_e$ is the equivalent network impedance. Block diagram of the voltage controller (exciter) for this generator is given in Figure 8.

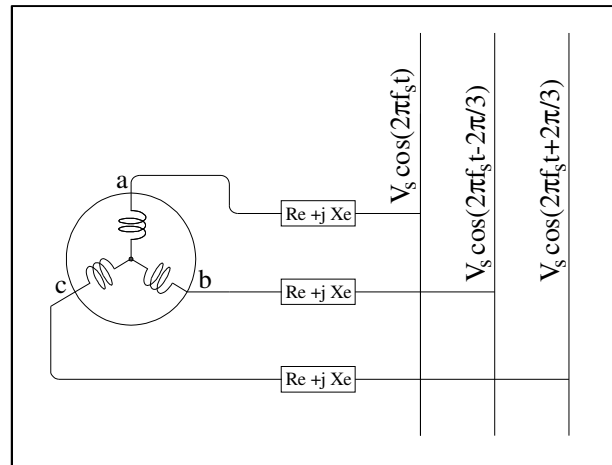


Figure 7 The Generator Connected to The Infinite Bus

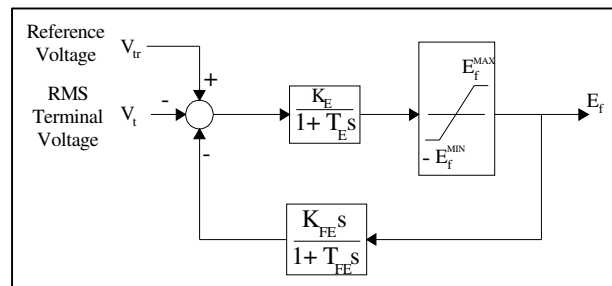


Figure 8 The Voltage Controller (Exciter) Block Diagram

6 Validation of the Penstock Model

In this section the model of the penstock with elastic walls and compressible water will be validated by application to the classic problem of reservoir-penstock-valve. Consider the system shown in the Figure 9. When the valve closes, the pressure before the valve increases and a pressure wave travels back to the reservoir. When this wave reaches the water surface at the reservoir, it is reflected as a

negative wave and travels toward the valve. The time that it takes for the pressure wave to travel from the valve to the reservoir and then back to the valve is equal to:

$$\frac{2 \times L_P}{\text{Speed of the pressure wave}}$$

The height h_{TW} of the reservoir is considered to be much less than the length L_P of the penstock in deriving the above relation. The speed of the pressure wave inside penstock is equal to the speed of sound inside the water in penstock for which a relation was given in Eq. 6 [7]. This can be one of the criteria for validation of the penstock model. Time for traveling of the pressure waves (and hence speed of the waves) can be found from the results of simulations and then it can be compared to the value obtained from Eq. 6. Maximum pressure rises before the valve when the valve starts closing from the steady-state condition with a uniform rate and reaches the complete closed position, are tabulated by Allievi [2]. Allievi charts can be used as another criterion for validation of the penstock model. The maximum pressure rise found by simulation can be compared to the charts. Details of the reservoir and valve with penstock interfacing parts are shown in the special cases of Figure 4 and Figure 5; their governing equations were derived in Section 4. Four different scenarios will be considered for simulation of the Penstock-Valve problem. The following parameters are the same for all the four scenarios:

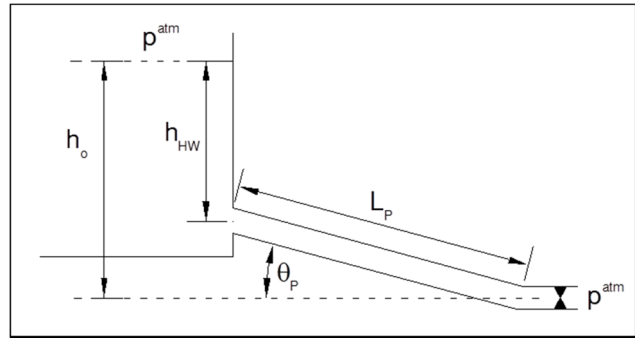


Figure 9 The Classic Penstock-Valve Problem.

$$L_P = 1000 \text{ [m]} , h_o = 100 \text{ [m]} , h_{HW} = 0 \text{ [m]} , \beta_P^{total} = 10^{-9} [Pa^{-1}]$$

$$A_P^{atm} = 7 \text{ [m}^2\text{]} , f_P = 0.04$$

Valve closing times and steady-state initial velocity of water will be different for each scenario as follows:

	T [sec]	v_o [m/sec]	Relative pressure rise $Z = (h_o + h)/h_o$ (from Allievi Charts [2])
Scenario #1	1	1	2
Scenario #2	3	1	1.6
Scenario #3	5.2	1	1.3
Scenario #4	3	4	3.8

The valve coefficient C_V for full valve opening can be calculated for each scenario considering the values for A_P^{atm} and v_o .

The valve starts closing at $t=50$ second in each scenario. Result of the simulation for the above scenarios is included in Figure 10 to Figure 14 respectively. In Figure 10 to Figure 13 the values of head rise are in close agree with z values in the above table.

The result of simulation for the fourth scenario however is different. The value of head rise in this case is more than expected ($3.47e+6 / 7.7e+5=4.5$ whereas a value of 3.8 is expected from

Allievi chart). The reason may be because of the higher velocity which causes higher losses due to friction. The steady state value of the head before the valve (before the time 50 sec when the valve starts to close) is less than the other cases. For examining this guess, the case is simulated again with zero friction factor and the result is given in Figure 14. It appears that with zero friction, the head rise is exactly in agree with the Allievi chart.

As mentioned earlier, another criterion for validating the penstock model could be to find the speed of the pressure waves from the simulation. β_p^{total} is taken to be $10^{-9} [Pa^{-1}]$ which shall result in a speed of sound equal to 1000 [m/sec] according to Eq. 6. The simulation results shall reflect this value for the pressure waves. In Figure 10 to Figure 14, the time difference between two consecutive peaks is 2 seconds (except for the peaks that coincide with valve closure) and this agrees with the value $2L_p/a$.

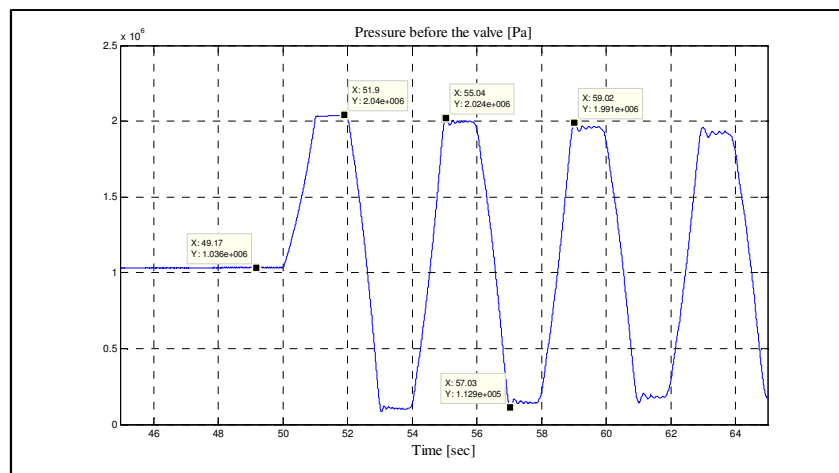


Figure 10 Result of Simulation of the Penstock-Valve for Scenario #1 (T=1 sec).

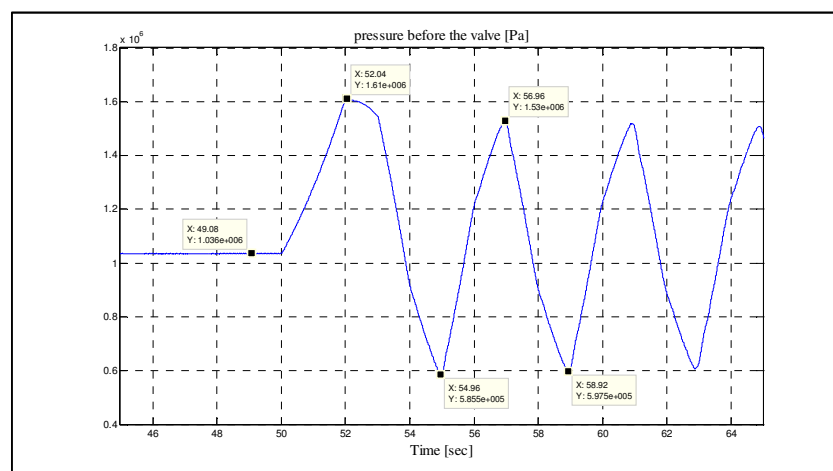


Figure 11 Result of Simulation of the Penstock-Valve for Scenario #2 (T=3 sec).

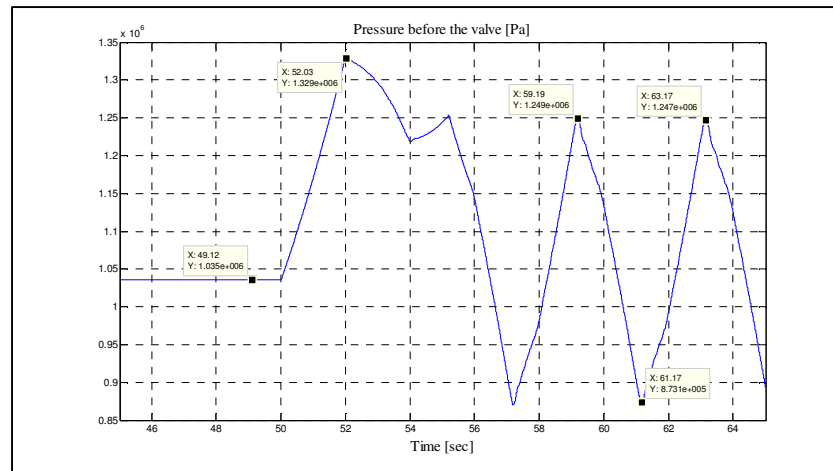


Figure 12 Result of Simulation of the Penstock-Valve for Scenario #3 ($T=5.2$ sec).

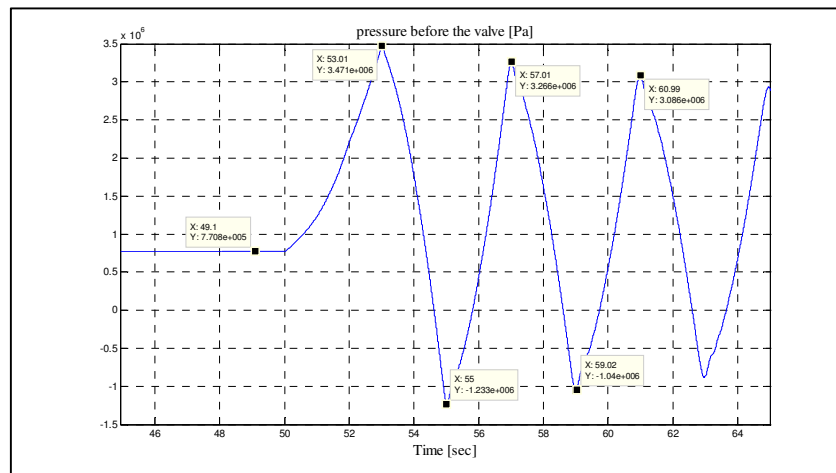


Figure 13 Result of Simulation of the Penstock-Valve for Scenario #4 ($T=3$ sec and $v_0=4$ [m/sec] with $f_p = 0.04$).

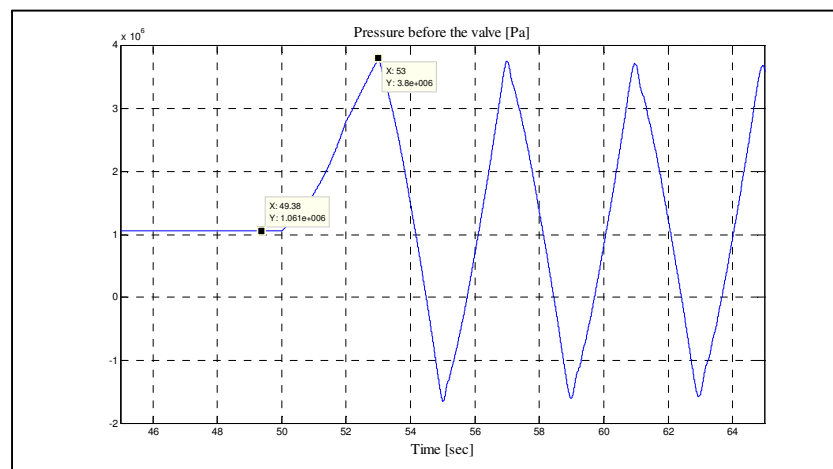


Figure 14 Result of Simulation of the Penstock-Valve for Scenario #4 ($T=3$ sec and $v_0=4$ [m/sec] with $f_p = 0$).

6.1 Number of Penstock Segments

In all the above simulations, the number of penstock segments is chosen to be 50. Figure 15 shows the result of the simulation for scenario #1 for three different N values. As can be seen, the number of segments has influence on the simulation of the wave traveling times.

6.2 Pressure and Mass Flow Rate at Different Locations of the Penstock

Pressure and mass flow rate variations at different locations in the penstock for sudden valve closure ($T=0.5 \text{ sec} \leq 2L_P/a$) and initial water velocity of 1 [m/sec] are shown in Figure 16 and Figure 17, respectively. Notice the delay in reaching the peak values. Also notice that pressure at each location reaches its maximum when the mass flow rate reaches zero in that location. Figure 18 and Figure 19 show the pressure and mass flow rate variations at the same locations and conditions except for the valve closure time which has been increased to 3 seconds. Notice the change of behavior of these variables when $T > 2L_P/a$. Peak to peak variations of pressure is greater at the valve side whereas peak to peak variations of flow rate is greater at the head water side. The shape of the variations can be interpreted by the method of characteristics [7].

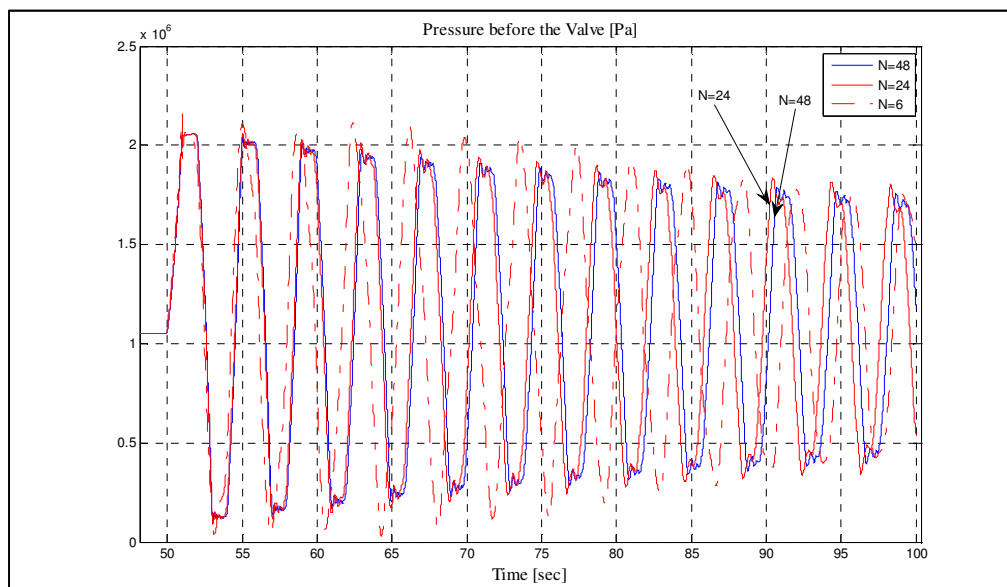


Figure 15 Simulation of Valve Uniform Closure for Different Number of Segments.

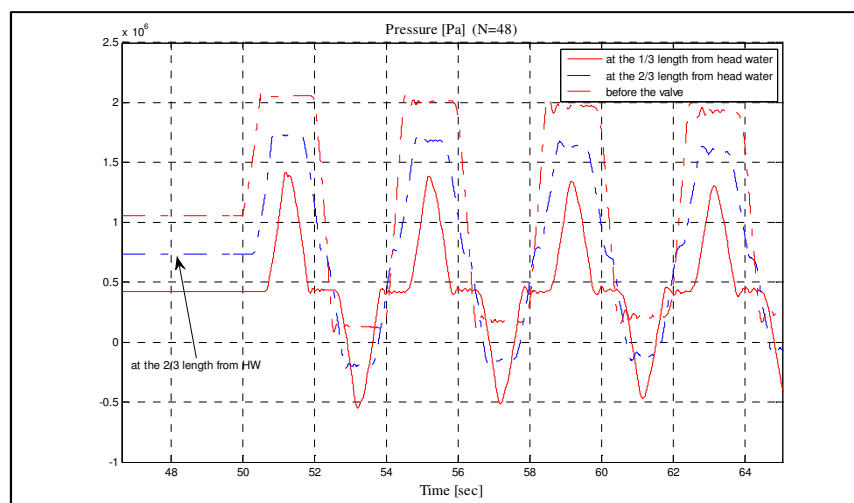


Figure 16 Pressure at different locations for valve closure time $T=0.5 \text{ sec}$.

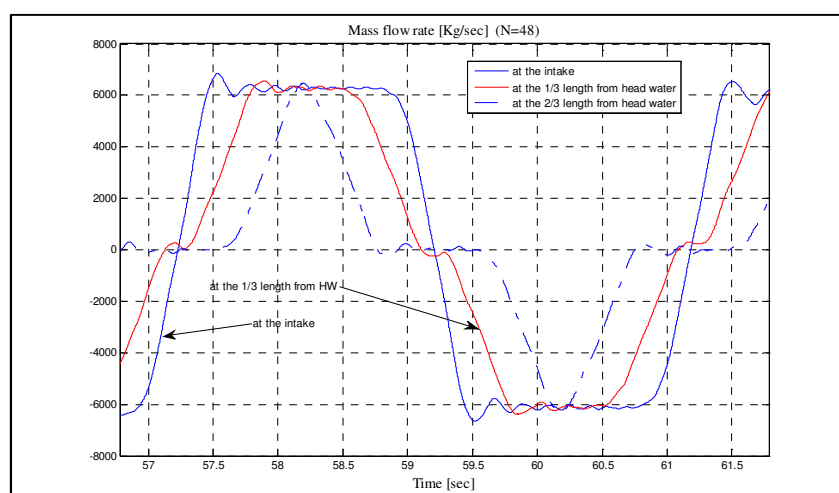


Figure 17 Flow rate at different locations for valve closure time $T=0.5$ sec.

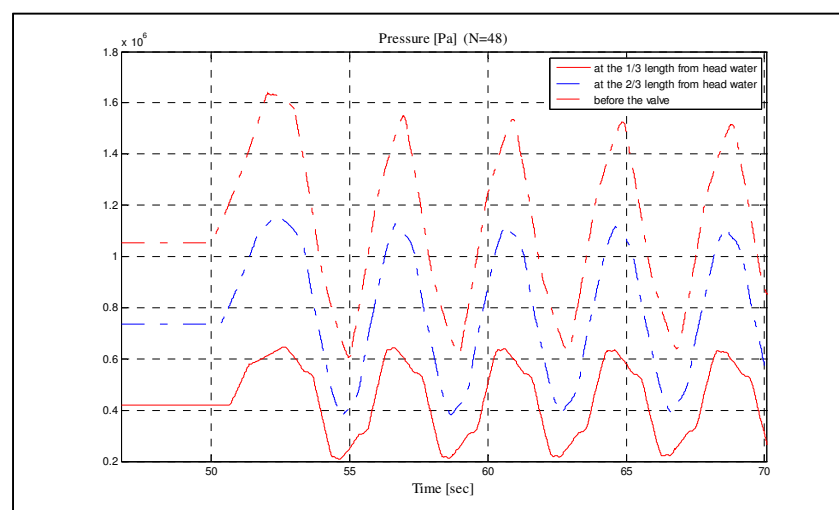


Figure 18 Pressure at different locations for valve closure time $T=3$ sec.

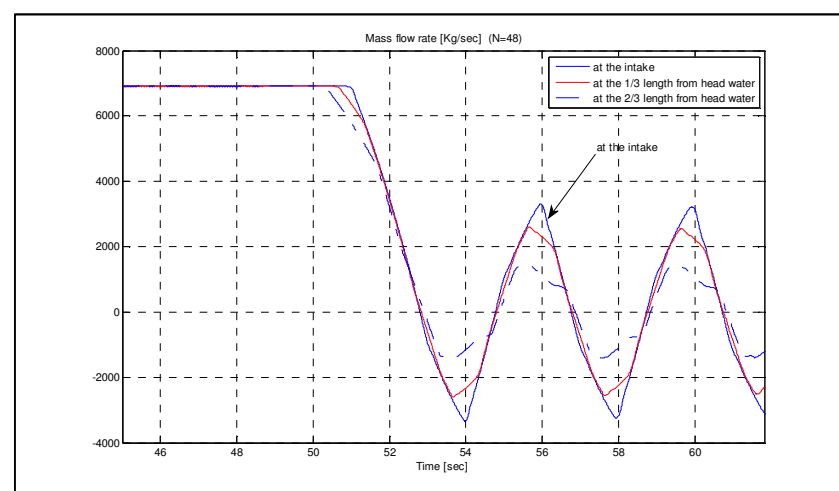


Figure 19 Flow rate at different locations for valve closure time $T=3$ sec.

6.3 Partial Valve Closure

Partial valve closure for scenario #1 is simulated in Figure 20. The valve starts closing at time $t=50$ sec from full open position (with a rate of full closure per one second) and closes until 90% open position.

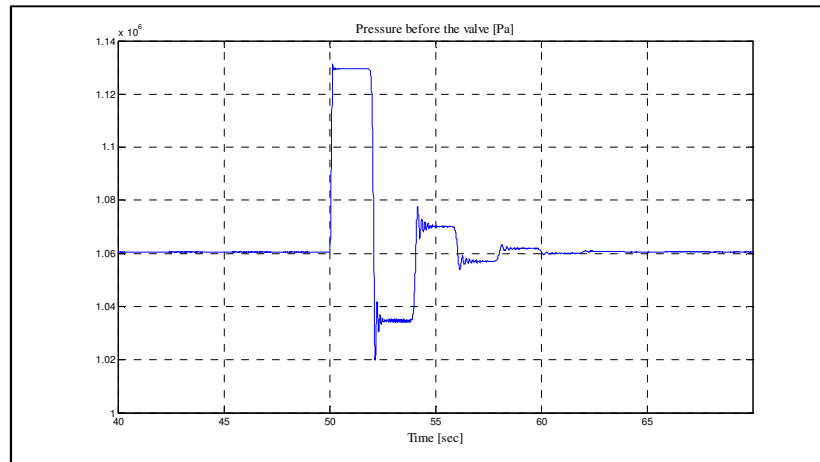


Figure 20 Simulation of Partial Valve Closure from Full Open to 90% Open Positions.

6.4 Options for ODE Solvers

All the simulations in Figure 10 to Figure 20 are done with the MATLAB “ode15s” solver with the following options:

```
options=odeset('MaxOrder',5,'RelTol',1e-6,'AbsTol',1e-6);
```

What happens if default options are used for “ode15s”? The simulation of Figure 20 is repeated with increased relative tolerance ($\text{'RelTol'}=1e-3$) and the result is given in Figure 21. As can be seen, with increased relative tolerance the “ode15s” encounters numerical errors which completely distort the solution in case of small valve changes. (For the case of the complete valve closure, the numerical errors become *relatively small compared to the large variations in the pressure before the valve* and the numerical errors don't seem to affect the result of the simulation significantly.)

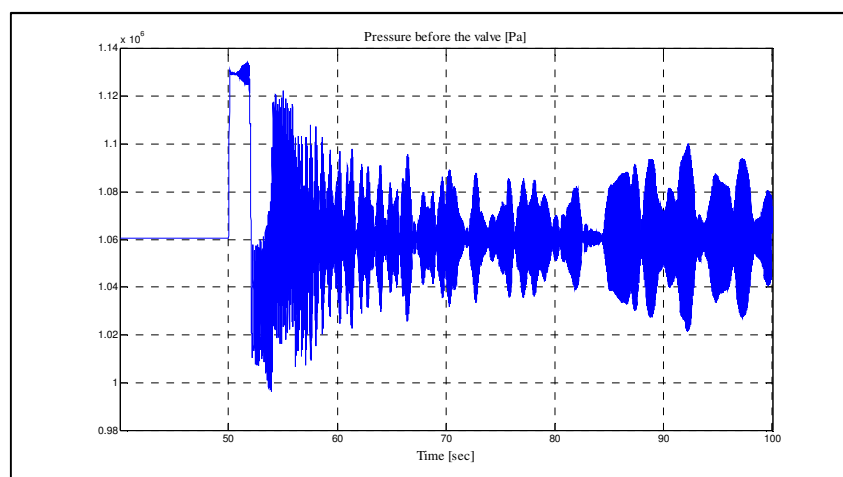


Figure 21 Simulation of Figure 20 with the Option $\text{'RelTol'}=1e-3$ for “ode15s”.

7 Simulation of a Complete Hydropower Generation Unit with Generator Connected to Infinite Bus

In this part the complete generation unit is simulated with both elastic and inelastic penstock models in parallel. The length of the penstock in these simulations will be 400 m and the speed of sound has been taken equal to 1000 m/sec inside the penstock. A transient droop controller with block diagram shown in the Figure 6 will control the turbine guide vanes and the generator is connected to an infinite bus. The simulation is done for two different scenarios: First guide vanes closing from 80% open position to 40% open position at $t=100$ sec will be simulated. In the second scenario the guide vanes reference will be constant and a generator terminal short circuit at $t=50$ sec with duration of 0.2 second will be simulated. A list of parameters and their values used for these simulations is given in Appendix I.

7.1 Change in the Guide Vanes Reference Signal

Results for this scenario are given in Figure 22 and Figure 23. The difference between the elastic model and the inelastic one appears in the transients. Nevertheless the only variable for which the effect of the traveling pressure waves is easily detectable is the pressure at the surge shaft junction (the local peaks from every 0.8 seconds in Figure 22).

7.2 Short Circuit at Generator Terminals

In this scenario the guide vanes opening reference is constant and at $t=50$ sec a short circuit happens at the generator terminals and recovers 0.2 seconds later. The results of this simulation are included in Figure 24 and Figure 25. As can be seen due to sluggish behavior of the waterway, the hydraulic parameters are not affected significantly. The important thing about simulation of this scenario is that “ode15s” was not able to solve it. The simulation is done with “ode45” with default options instead. “ode45” has an advantage over “ode15s” in this application. On the other hand, use of “ode45” for simulations in section 6 for complete valve closure (valve closure until 0.001 p.u. position) is quite slow and hence useless. This examples show that each numerical integration method has its own advantages and short comings.

8 Conclusion

Modeling of a high-head hydropower generation unit was considered in this work. It was shown how to use the “Finite Volume Method” and MATLAB to simulate the behavior of a penstock when elasticity of the penstock walls and compressibility of the water is taken into account. The “ode15s” ODE solver in MATLAB was used for the most of the simulations (except for the generator short circuit simulations). It was shown that under default options, especially the default relative tolerance, the solution will have some numerical errors which will distort the solution completely. It was suggested to reduce the relative tolerance option. For generator short circuit simulations, “ode45” is the right solver. However “ode45” has its own short comings when we want to apply it to simulations in Section 6.

The model introduced for the elastic penstock was validated in a classic penstock-valve problem with uniform valve closing. The responses of the model for different conditions were compared to Allievi charts [2]. It was found that except for high water velocities (higher than one or two m/s) the results almost agree. Obviously the Allievi charts in [2] are prepared for pipes with lower friction which shall be considered in mind when dealing with higher fluid velocities. A Fanning friction factor value of 0.04 was used for simulations throughout this paper.

A complete hydropower generation unit was simulated for both cases: elastic penstock model and inelastic penstock model. A classic transient droop controller was used for closed loop operation.

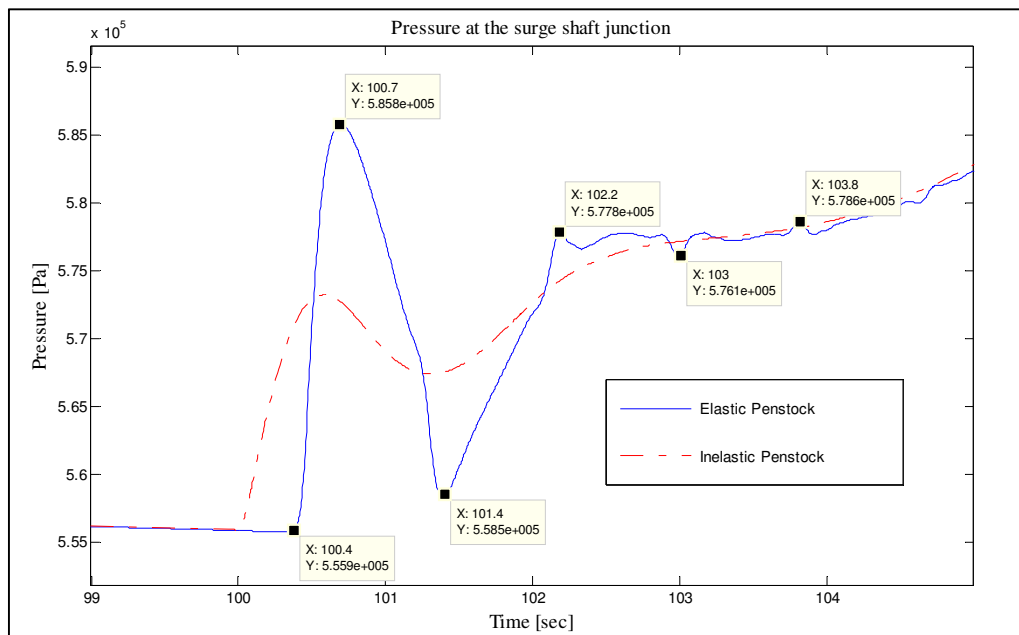


Figure 22 Simulation of the Change in the Guide Vanes Reference Signal.

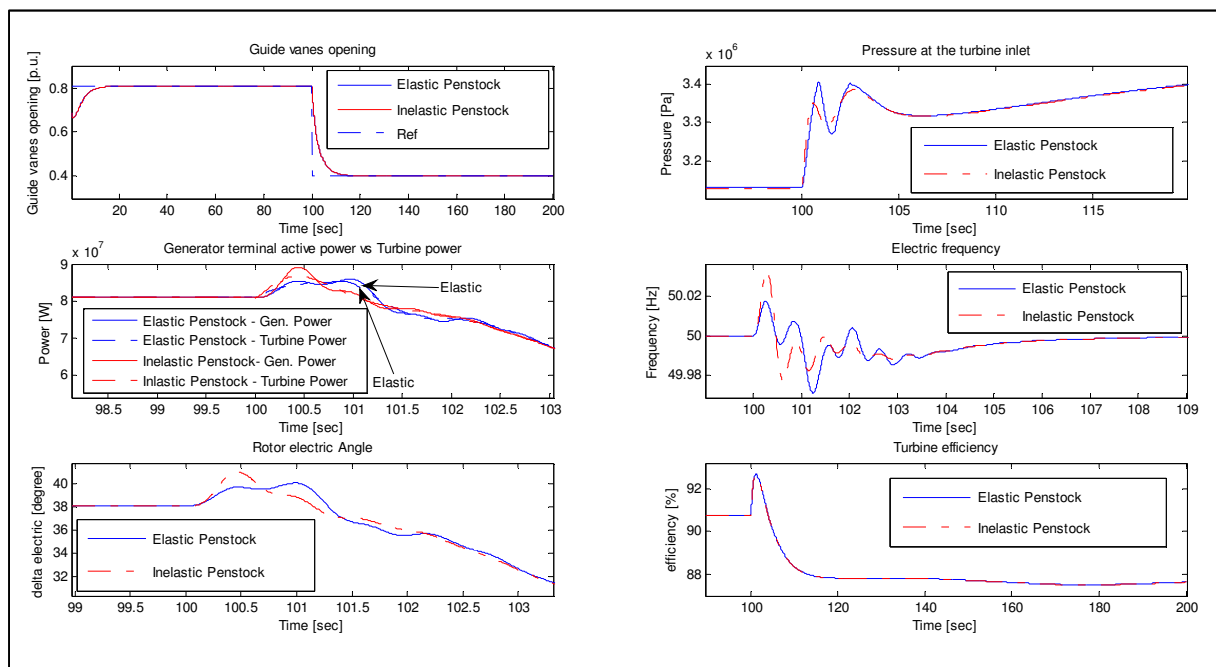


Figure 23 Simulation of the Change in the Guide Vanes Reference Signal (continued from Figure 22).

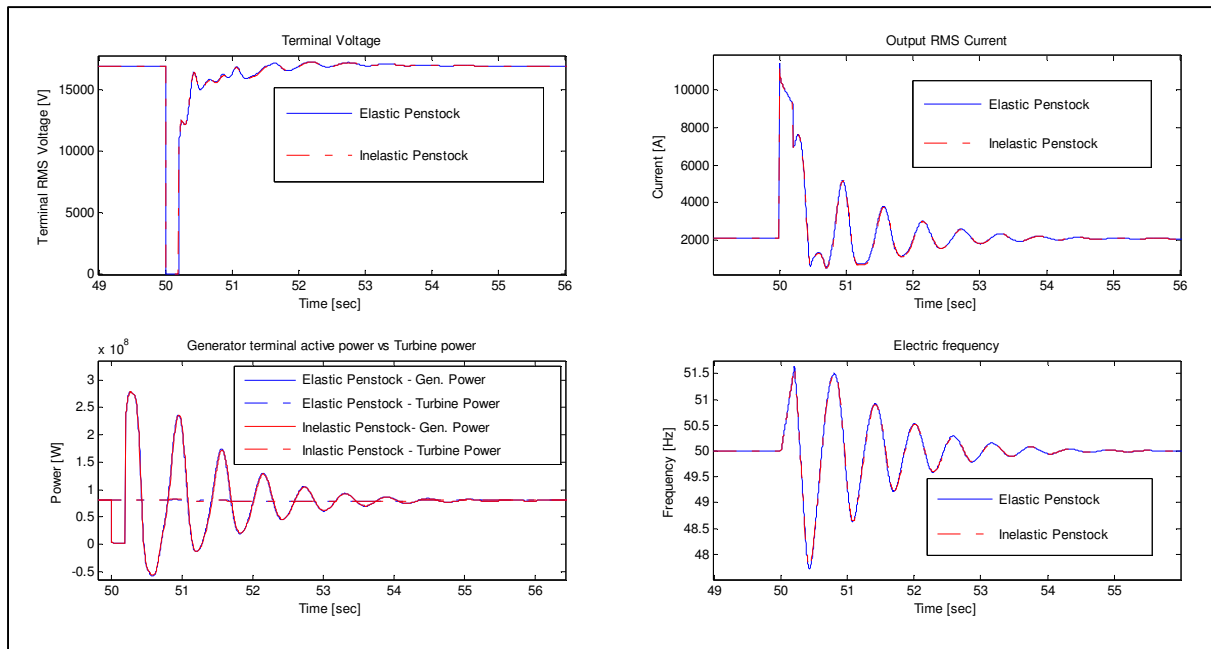


Figure 24 Simulation of Short Circuit in the Terminal Voltage.

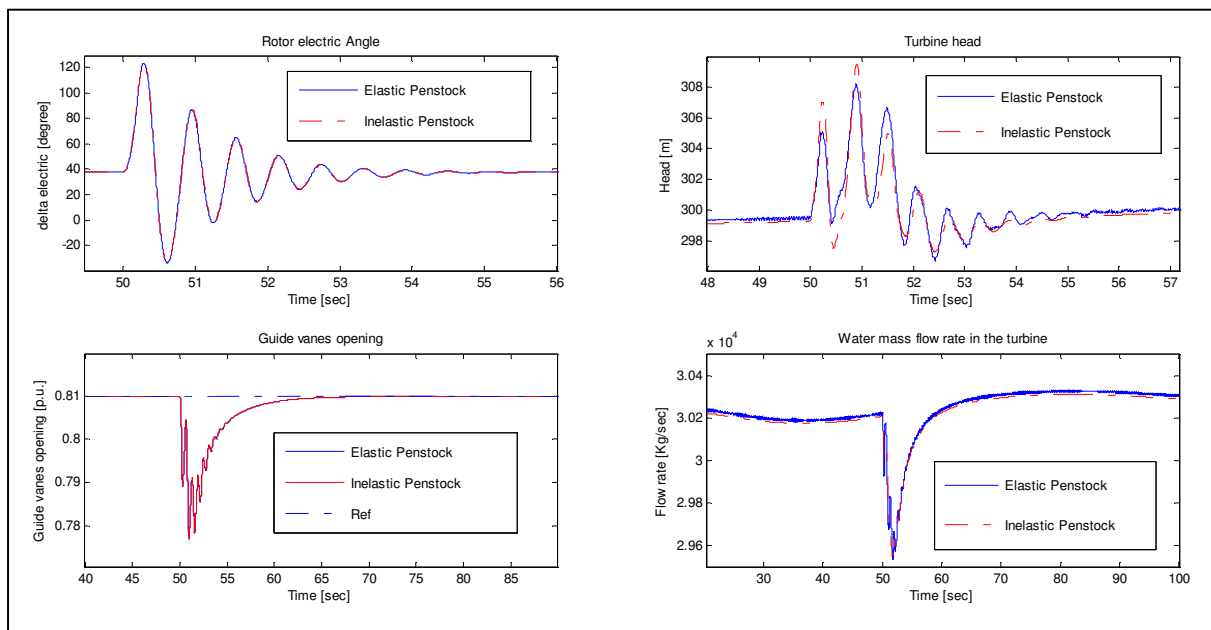


Figure 25 Simulation of Short Circuit in the Terminal Voltage (continued from Figure 24).

References

- [1] N. Kishor *et al.*, “A review on hydropower plant models and control,” *Renewable and Sustainable Energy Reviews*, vol. 11, pp. 776–796, Jun. 2007.
- [2] C.C. Warnick, *Hydropower Engineering*. Prentice-Hall: New Jersey, 1984.
- [3] *Water Hammer and Mass Oscillation (WHAMO) 3.0 User's Manual*, US Army Corps of Engineers: Construction Engineering Research Laboratories, 1998.
- [4] *Hydro Plant Library Version 2.0 User's Guide*, Modelon AB, 2010.
- [5] B. Honningsvåg *et al.*, *Hydropower in the New Millennium*. Lisse, The Netherlands : Swets & Zeitlinger B.V., 2001.
- [6] J. Arthur *et al.*, “Lesotho Highlands Water Project- Design of the 'Muela Hydropower Station,” *Proc. Instn Civ. Engrg*, pp. 43-53, 1997.
- [7] J. Parmakian, *Waterhammer Analysis*, 2nd ed. New York : Dover Publications, Inc., 1963.
- [8] H. K. Versteeg and W. Malalasekera, *An Introduction to Computational Fluid Dynamics: The Finite Volume Method*. Longman, 1995.
- [9] T. J. Chung, *Computational Fluid Dynamics*. Cambridge, UK: Cambridge University Press, 2002.
- [10] J. Machowski, *Power System Dynamics: Stability and Control*, 2nd ed. Chichester, UK: John Wiley & Sons, 2008.
- [11] B. Rahimi Sharefi, “Modeling for Control of Hydropower Systems,” M.S. thesis, Department of Electrical Engineering, Information Technology and Cybernetics, Telemark University College, Porsgrunn, Norway, 2011.

APPENDIX I

PARAMETERS FOR SIMULATIONS IN SECTION 7

Parameter	Value	Unit	Parameter	Value	Unit	Parameter	Value	Unit
Turbine Controller (Parameters of the controller are defined in Figure 6.)								
T_P	0.04	[sec]	T_r	1.75	[sec]	T_g	0.2	[sec]
δ	0.04	[-]	σ	0.1	[-]	\dot{Y}_{GV}^{MIN}	0.2	[1/sec]
\dot{Y}_{GV}^{MAX}	0.05	[1/sec]						
Penstock								
L_P	400	[m]	A_P^{atm}	7	[m ²]	θ_P	45*pi/180	[rad]
f_P	0.04	[-]	a	1000	[m/sec]			
Head/Tail Water Systems								
A_C	25	[m ²]	A_S	10	[m ²]	A_{TWT}	25	[m ²]
f_C	0.04	[-]	f_S	0.04	[-]	f_{TWT}	0.04	[-]
L_C	4500	[m]	L_{TWT}	300	[m]			
h_R	40	[m]	h_{DT}	5	[m]	h_{TW}	10	[m]
θ_C	0.2*pi/180	[rad]	θ_S	60*pi/180	[rad]	θ_{TWT}	0.5*pi/180	[rad]
Generator, Exciter and Bus (Exciter and bus parameters are defined in Figure 8)								
r	0.01	[Ω]	r_e	0.1	[Ω]	x_d	12	[Ω]
x_q	12	[Ω]	x'_d	1.7	[Ω]	x''_q	1.7	[Ω]
T'_{do}	6	[sec]	T''_{qo}	0.1	[sec]	x'_q	= x_q	[Ω]
x''_d	-	[Ω]	K_E	400	[-]	T_E	0.05	[sec]
K_{FE}	0.025	[-]	T_{FE}	1	[sec]	V_{tr}	17000	[V]
E_f^{MIN}	50000	[V]	E_f^{MAX}	50000	[V]	n_p	12	[-]
J	170000	[Kg. m ²]	ω_s	100 π	[rad/sec]]	V_S	15000	[V]
x_e	1.4	[Ω]						

Parameter	Value	Unit	Parameter	Value	Unit	Parameter	Value	Unit
Turbine								
Q_{td}	36	[m ³ /sec]	H_{td}	330	[m]	ω_m^{design}	$100\pi/6$	[rad/sec]

Turbine efficiency and discharge as a function of guide vanes opening at design head and design rotational speed (For more detailed model and data of turbine refer to [11].)

Y_{GV}	0.3	0.4	0.5	0.6	0.7	0.8	0.9	1
Percent of design discharge	38	49	60	70	80	88	95	100
Efficiency [%]	81.5	87.5	91	93	93	91	90	88

- [2]. Balino, J.L. et al. "The Differential Perturbative Method Applied to the Sensitivity Analysis for Water Hammer Problems in Hydraulic Networks." *Applied Mathematical Modeling* 25 (2001) 1117-1138.
- [3]. US Army Corps of Engineers. "Water Hammer and Mass Oscillation (WHAMO) 3.0 User's Manual." US Army Corps of Engineers: Construction Engineering Research Laboratories. September 1998.
- [4]. Modelon AB. "Hydro Plant Library Version 2.0 User's Guide." Modelon AB. 2010.
- [5]. IEEE working group on prime mover and energy supply models for system dynamic performance studies "Hydraulic Turbine and Turbine Control Models for System Dynamic Studies" *IEEE transactions on power systems*, Vol. 7, No. 1, February 1992.
- [6]. Versteeg H.K. & Malalasekera W. "An Introduction to Computational Fluid Dynamics: The Finite Volume Method" Longman, 1995.

Paper 11

Title: Modeling, Simulation and Control for an Experimental Four Tanks System using ScicosLab

Carlos Pfeiffer

Telemark University College, Norway

Keywords: Model Predictive Control, Four Tanks System, Kalman Filter, ScicosLab

During the last years, an interconnected four tanks system originally developed at Lund University has become popular for research and testing of advanced control schemes in universities across the world. In this system, water is pumped through two independent variable speed pumps, and flows are split using two three-way valves to feed the tanks. Different experimental flow configurations can be achieved by modifying the positioners of the valves. The system is very challenging, since it is nonlinear, it is multivariable with strong variables interactions, and it may present non-minimum phase characteristics for some configurations. Most published papers utilize a fourth order state space model to approximate the system. However, for laboratory scale systems the dynamics of the pumps may be important, and they should be considered.

In this work a six state variables nonlinear state space model is presented, considering the tanks and the pumps dynamics. The parameters of the model were fit using experimental data, and the resulting model was linearized and used to test a Model Predictive Controller on the experimental system. Since only the levels of two of the tanks were measured, a Kalman filter was used to estimate the state variables. All the simulations and the implementation of the control algorithms were performed using the free open-source software package ScicosLab.

Modeling, Simulation and Control for an Experimental Four Tanks System using ScicosLab

Carlos F. Pfeiffer
Høgskolen i Telemark
Porsgrunn, Norway

Abstract

For the last years, an interconnected four tanks system originally developed at Lund University[3] has become popular for research and testing of advanced control schemes in universities across the world. In this system, water is pumped through two independent variable speed pumps, and flows are split using two three-way valves to feed the tanks. Different experimental flow configurations can be achieved by modifying the valves settings. The system is very challenging, since it is nonlinear, it is multi-variable with strong variables interactions, and it may present non-minimum phase characteristics for some configurations. Most published papers utilize a fourth order state space model to approximate the system. However, for laboratory scale systems the dynamics of the pumps may be important, and they should be considered.

In this work a six state variables nonlinear state space model is presented, considering the tanks and the pumps dynamics. The parameters of the model were measured or fit using experimental data, and the resulting model was linearized and used to test a Model Predictive Controller on the experimental system. Since only the levels of two of the tanks were measured, a Kalman filter structure was used to estimate the state variables. All the simulations and the implementation of the control algorithms were performed using the free open-source software package ScicosLab 4.4.

1 System description

For the last years, an interconnected four tanks system originally developed at Lund University[3] has become popular for research and testing of advanced control schemes in universities across the world. In this system, water is pumped through two independent variable speed pumps, and flows are split using two three-way valves to feed the tanks, as described in figure 1. Different experimental flow configurations can be achieved by modifying the valves settings. The system is very challenging, since it is nonlinear, it is multi-variable with

strong variables interactions, and it may present non-minimum phase characteristics for some configurations. Most published papers utilize a fourth order state space model to approximate the system [3, 2, 4]. However, for laboratory scale systems the dynamics of the pumps may be important, and they should be considered, as described in the following section.

2 Model

The fundamental dynamic model for the level of a simple cylindrical tank comes from a mass balance, i.e. *the change of wa-*

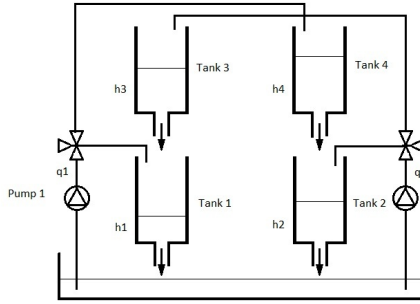


Figure 1: Four tanks interacting system

ter mass inside the tank = mass flow of water coming in - mass flow of water coming out:

$$\frac{dM(t)}{dt} = \dot{m}_{in} - \dot{m}_{out} \quad (1)$$

where $M(t)$ represent the variation of mass inside the tank, \dot{m}_{in} the total mass flow of water coming into the tank, and \dot{m}_{out} the total mass flow of water coming out the tank. The model can be expressed with volumetric flows by using the density of the liquid, ρ :

$$\frac{d\rho V(t)}{dt} = \rho \dot{q}_{in} - \rho \dot{q}_{out} \quad (2)$$

Considering ρ constant $dV(t) = A dh(t)$, where A is the area of the base of the tank, and $h(t)$ is the level:

$$A \frac{dh(t)}{dt} = \dot{q}_{in} - \dot{q}_{out} \quad (3)$$

Here a semi-empirical relation derived from Bernoulli's principle is often used to approximate the flow out of a tank as a function of the level: $q_{out} = k_o \sqrt{\Delta P}$, where ΔP is the pressure difference across the output orifice and k_o a constant depending on the characteristic of the output opening (orifice or valve). Using $\Delta P = \rho gh(t)$, where g is the Earth gravity constant, we can now approximate $q_{out}(t) = k_o \sqrt{\rho g} \sqrt{h(t)}$,

or $q_{out}(t) = c \sqrt{h(t)}$, where $c = k_o \sqrt{\rho g}$. By expressing the output flow this way it is straightforward to evaluate c experimentally. This approximation gives good results when the level (and therefore the difference of pressure) is not close to zero, and the diameter of the orifice is small.

Applying the mass balance equations to the four tanks configuration we obtain:

$$\frac{dh_1(t)}{dt} = -\frac{c_1 h_1(t)^{1/2}}{A_1} + \frac{c_3 h_3(t)^{1/2}}{A_1} + \frac{\gamma_1 q_1(t)}{A_1} \quad (4)$$

$$\frac{dh_2(t)}{dt} = -\frac{c_2 h_2(t)^{1/2}}{A_2} + \frac{c_4 h_4(t)^{1/2}}{A_2} + \frac{\gamma_2 q_2(t)}{A_2} \quad (5)$$

$$\frac{dh_3(t)}{dt} = -\frac{c_3 h_3(t)^{1/2}}{A_3} + \frac{(1 - \gamma_2) q_2(t)}{A_3} \quad (6)$$

$$\frac{dh_4(t)}{dt} = -\frac{c_4 h_4(t)^{1/2}}{A_4} + \frac{(1 - \gamma_1) q_1(t)}{A_4} \quad (7)$$

where q_1 is the total flow given by pump 1, q_2 is the total flow given by pump 2, and γ_1 and γ_2 are numbers between 0 and 1 representing the fraction of the total flows q_1 and q_2 going to tanks 1 and 2 respectively. Most publications assume that the dynamics of the pump is much faster than that of the tanks, modeling q_1 and q_2 as simply being proportional to the pumps voltages: $q_1 = k_1 v_1$ and $q_2 = k_2 v_2$. A more realistic model is given by the transfer function relating speed with input voltage for a DC motor, and calculating the water flow as proportional to the motor velocity. For systems with high inertia and viscous forces, the transfer function can be usually represented by an over-damped second order

system with transfer function:

$$\frac{\Omega(s)}{V(s)} = \frac{k_m}{(\tau_m s + 1)(\tau_e s + 1)} \quad (9)$$

Where $\Omega(s)$ is the angular velocity (rad/sec), $V(s)$ is the input voltage, τ_m is the time constant of the pumps mostly depending on mechanical parameters (moment of inertia and viscous forces), τ_e is a time constant mostly depending of electrical parameters (resistance, inductance) and k_m is the gain of the motor. In practice, for the variable speed pumps we expect τ_m to be much bigger than τ_e , and the transfer function for each pump could be approximated by first order systems. Using this simplification we can add two equations to the model:

$$\frac{dq_1(t)}{dt} = -\frac{1}{\tau_1}q_1(t) + \frac{k_1}{\tau_1}v_1(t) \quad (10)$$

$$\frac{dq_2(t)}{dt} = -\frac{1}{\tau_2}q_2(t) + \frac{k_2}{\tau_2}v_2(t) \quad (11)$$

where τ_1 and τ_2 represent the time constants of the pumps approximated as first order systems, and k_1 and k_2 are the gains of the pumps relating flow with voltage (considering steady state flow proportional to motor speed). These constants can be evaluated experimentally by using a system identification technique. The main contribution of adding these equations is that they consider the dynamics of the pumps, i.e., that the flows are not instantaneous functions of the pumps voltages.

3 Linear model

The four tanks and pumps dynamic model can be linearized around an operation point, resulting in the following model after

taking deviation variables:

$$\frac{dH_1(t)}{dt} = -\frac{c_1}{2A_1\sqrt{h_{1s}}}H_1(t) + \frac{c_3}{2A_1h_{3s}^{1/2}}H_3(t) + \frac{\gamma_1}{A_1}Q_1(t) \quad (12)$$

$$\frac{dH_2(t)}{dt} = -\frac{c_2}{2A_2\sqrt{h_{2s}}}H_2(t) + \frac{c_4}{2A_2h_{4s}^{1/2}}H_4(t) + \frac{\gamma_2}{A_2}Q_2(t) \quad (13)$$

$$\frac{dH_3(t)}{dt} = -\frac{c_3}{2A_3h_{3s}^{1/2}}H_3(t) + \frac{(1-\gamma_2)}{A_3}Q_2(t) \quad (14)$$

$$\frac{dH_4(t)}{dt} = -\frac{c_4}{2A_4h_{4s}^{1/2}}H_4(t) + \frac{(1-\gamma_1)}{A_4}Q_1(t) \quad (15)$$

$$\frac{dQ_1(t)}{dt} = -\frac{1}{\tau_1}Q_1(t) + k_1V_1(t) \quad (16)$$

$$\frac{dQ_2(t)}{dt} = -\frac{1}{\tau_2}Q_2(t) + k_2V_2(t) \quad (17)$$

Where $H_i(t) = h_i(t) - h_{is}$, $Q_i(t) = q_i(t) - q_{is}$, for $i = 1, 2, 3, 4$, h_{1s} and q_{2s} represent the steady state values for the tanks heights and the water flows on the operating point. For the deviation voltages, $V_1(t) = v_1(t) - v_{1s}$ and $V_2(t) = v_2(t) - v_{2s}$, where v_{1s} and v_{2s} are the pumps steady state voltages at the operating point.

This system of linear differential equations can be represented in matrix form as:

$$\frac{dX(t)}{dt} = \mathbf{A}X(t) + \mathbf{B}U(t) \quad (18)$$

where:

$$X(t) = [H_1(t)H_2(t)H_3(t)H_4(t)Q_1(t)Q_2(t)]' \quad (19)$$

Table 1: Tanks parameters

	Tank 1	Tank 2	Tank 3	Tank 4	Units
A_i	12.57	12.57	12.57	12.57	cm^2
h_{is}	7.0	7.0	8.3	3.1	cm
c_i	9.82	5.76	9.02	8.71	$\frac{cm^{5/2}}{s}$

Table 2: Pumps parameters

	Pump 1	Pump 2	Units
K_i	6.94	8.72	$\frac{cm^3/s}{V}$
τ_i	6.15	13.2	s

$\mathbf{A} =$

$$\begin{bmatrix} -\frac{c_1/A_1}{2h_{1s}^{1/2}} & 0 & \frac{c_3/A_1}{2h_{3s}^{1/2}} & 0 & \gamma_1/A_1 & 0 \\ 0 & -\frac{c_2/A_2}{2h_{2s}^{1/2}} & 0 & \frac{c_4/A_2}{2h_{4s}^{1/2}} & 0 & \gamma_2/A_2 \\ 0 & 0 & -\frac{c_3/A_3}{2h_{3s}^{1/2}} & 0 & 0 & \frac{1-\gamma_2}{A_3} \\ 0 & 0 & 0 & -\frac{c_4/A_4}{2h_{4s}^{1/2}} & \frac{(1-\gamma_1)}{A_4} & 0 \\ 0 & 0 & 0 & 0 & -\frac{k_1}{\tau_1} & 0 \\ 0 & 0 & 0 & 0 & 0 & -\frac{k_2}{\tau_2} \end{bmatrix} \quad \text{where} \quad (20)$$

$$\mathbf{B} = \begin{bmatrix} 0 & 0 \\ 0 & 0 \\ 0 & 0 \\ 0 & 0 \\ \frac{k_1}{\tau_1} & 0 \\ 0 & \frac{k_2}{\tau_2} \end{bmatrix} \quad (21)$$

4 Parameters Identification

The areas of the four tanks are calculated by measuring the diameters directly. All tanks have an internal diameter of six centimeters. The output orifices constants were evaluated experimentally by stabilizing the tanks at a level of 7 centimeters using independent PI controllers with valves settings $\gamma_1 = 0$ and $\gamma_2 = 0$, and measuring the output flows q_{is} . From here, $c_i = q_{is}/h_{is}^{1/2}$. To evaluate the parameters of the pumps, the valves were set at $\gamma_1 = 1.0$ and $\gamma_2 = 1.0$ to feed only tanks 1 and 2, keeping tanks 3 and 4 empty, and a step response identification technique was

used to fit the second order response. Since:

$$\frac{H_1(s)}{Q_1(s)} = \frac{k_{T1}}{\tau_{T1}s + 1}$$

$$k_{T1} = \frac{2h_{1s}^{1/2}}{c_1}$$

and:

$$\tau_{T1} = \frac{2A_1h_{1s}^{1/2}}{c_1}$$

and from equation 10:

$$\frac{Q_1(s)}{V_1(s)} = \frac{k_1}{\tau_1s + 1}$$

The response to a step in input voltage for tank one level is given by:

$$\frac{H(s)}{V(s)} = \frac{k_{T1}k_1}{(\tau_{T1}s + 1)(\tau_1s + 1)}$$

The time response for a voltage step of magnitude M is given by:

$$H_1(t) = k_1k_{T1}M \left(1 + \frac{\tau_1 e^{-\frac{t}{\tau_1}} - \tau_{T1} e^{-\frac{t}{\tau_{T1}}}}{\tau_{T1} - \tau_1} \right)$$

The parameters k_{T1} , τ_{T1} were evaluated using the values on table 1 and the time response to a step was used to fit the values of τ_1 and k_1 using a non-linear least squares parameter estimating routine. The same procedure was used with tank two to obtain the pump parameters indicated in table 2.

5 Open loop simulation

Simulation of the non-linear system is straightforward in ScicosLab. ScicosLab is an open source, free licensed software similar to matlab, available from [5]. The four differential equations describing the levels and the two differential equations describing the flows are programmed as a vector function and solved with the ScicosLab routine *ode*. A simulation for an step change on the pumps voltages of 1, $\gamma_1 = 0$ and $\gamma_2 = 0$ when $h_{1s} = h_{2s} = 7$ is shown on figures 2 and 3.

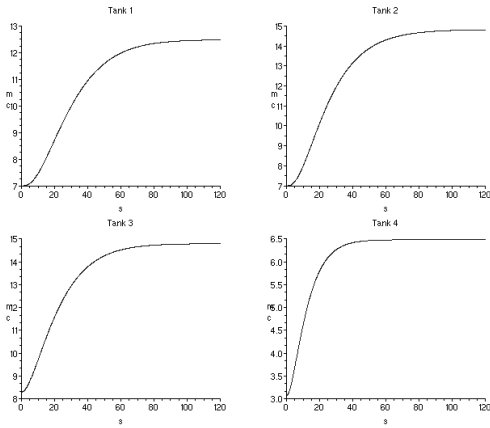


Figure 2: Tanks levels step response

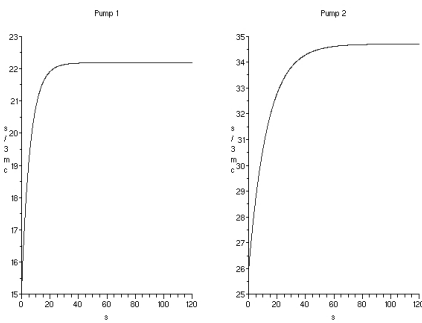


Figure 3: Pumps flows step response

6 Linear Model Predictive Control

Linear Model Predictive Control (MPC) requires a reasonable linear model of the system. ScicosLab does not include a MPC Toolbox with its standard distribution, but it can readily be programmed. For this work, the first MPC approach described in [1] was extended for multivariable systems to control the levels on tanks 1 and 2. The continuous state-space representation is given by equations 18, 19, 20, 21 and:

$$\mathbf{Y} = \mathbf{C}\mathbf{X} \quad (22)$$

with:

$$\mathbf{C} = [110000] \quad (23)$$

In order to eliminate steady state errors on the presence of persistent disturbances and model errors, the linear model is transformed to a differences system and augmented with integrators (one per each controlled output), producing the structure given by equations 24 and 25 [1].

$$\begin{bmatrix} \Delta X(k+1) \\ Y(k+1) \end{bmatrix} = \begin{bmatrix} \mathbf{A}_D & \mathbf{0} \\ \mathbf{C}\mathbf{A}_d\mathbf{I} \end{bmatrix} \begin{bmatrix} \Delta X(k) \\ Y(k) \end{bmatrix} + \begin{bmatrix} \mathbf{B}_d \\ \mathbf{C}\mathbf{B}_d \end{bmatrix} \Delta U(k) \quad (24)$$

$$Y(k) = [\mathbf{0I}] \begin{bmatrix} \Delta X(k) \\ Y(k) \end{bmatrix} \quad (25)$$

Linear MPC with receding horizons should minimize function 26, where n_p is the prediction horizon and n_c is the control horizon, R_k is a reference vector, Y_k is the output vector, and ΔU_k is the vector of inputs changes at the k sampling instant. Q and P are weighting matrices (in practice usually selected as diagonal matrices with positive

elements on the main diagonal):

$$\min_{\Delta U_1 \dots \Delta U_{n_c}} J = \sum_{k=1}^{n_p} (R_k - Y_k)^T Q (R_k - Y_k) + \Delta U_k^T P \Delta U_k \quad (26)$$

with $n_c \leq n_p$, $\Delta U_k = 0$ for $k = n_c + 1, n_c + 2, \dots, n_p$ and subject to constraints:

$$b_{1_i} \leq U_k \leq b_{1_s} \quad (27)$$

$$b_{2_i} \leq \Delta U_k \leq b_{2_s} \quad (28)$$

$$b_{3_i} \leq Y_k \leq b_{3_s} \quad (29)$$

where $b_{1_i}, b_{2_i}, b_{3_i}$ are lower bound vectors and $b_{1_s}, b_{2_s}, b_{3_s}$ are upper bound vectors. This MPC formulation requires values for all the state variables. Since only the levels of tanks 1 and 2 are measured, a Kalman filter structure was used to estimate the state vector (the covariance matrices were tuned by trial and error to obtain a satisfactory observer dynamics. Using a Kalman filter structure warrants a stable observer). ScicosLab provides tools to convert from a continuous state space representation to a discrete one and to solve the Riccati equations necessary for the Kalman filter design. It also includes two powerful quadratic programming routines to handle linear constraints: *quapro* and *qld*. Once the required system matrices and bound vectors are defined, the MPC algorithm implementation in ScicosLab can be stated with the following steps:

- Select a sampling time.
- Discretize the system (ScicosLab *cont2disc* function).
- Obtain a differences model and extend the discrete system with the outputs.

- Design an observer using a Kalman filter structure (ScicosLab *ricc* function).
- Define n_c, n_p, R_k, Q, P , and the lower and upper bounds of the constraints.
- Set up the Quadratic Programming problem defined by 26.
- Solve the Quadratic Programming problems (ScicosLab *quapro* and *qld* functions).
- Calculate the new input vector by adding ΔU_1 to the present input and feed it to the system.
- Update the control and prediction horizons and repeat the process.

7 Experimental System Control

Even though ScicosLab was not originally contemplated to work on line, it offers a way to add functions by compiling and linking C code. This facility was used to modify the routines given in the open toolbox provided in [6] to communicate with a National Instruments USB-6800 data acquisition system to read the tank levels and set the pumps voltages directly from ScicosLab, allowing the using of the Model Predictive Controller on line for sampling times of one second and larger.

For the experiments the non-linear model was linearized around levels values of 7 centimeters for tanks 1 and 2, and the resulting linear model parameters were kept constant for all the experiments (except the valve parameters γ_1 and γ_2 , which are set to their known corresponding values in each experiment). The MPC tuning parameters were tested by trial and error to get an acceptable performance, with a sampling time of 1 second. The developing of tuning control

techniques for MPC is a subject of ongoing research.

Figure 4 shows the levels for tanks 1 and 2 when a change of reference of 2 centimeters is applied in tank 1 and of 3 centimeters on tank 2, using values of $\gamma_1 = 0.9$ and $\gamma_2 = 0.9$ for the three way valves.

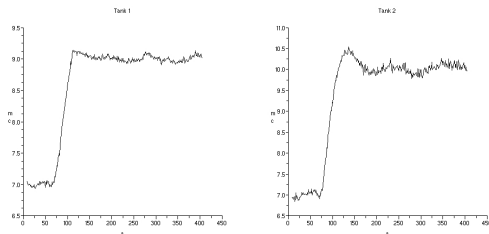


Figure 4: Tanks levels step response

Figure 5 shows the effect of applying not persistent disturbances consisting on blocking completely the output flow of water for several seconds, first in tank 1, and then on tank 2. For this experiment, $\gamma_1 = 1$, and $\gamma_2 = 0.5$, with a sampling time of 1 second and the same parameters for the MPC as the previous controller. The plots show

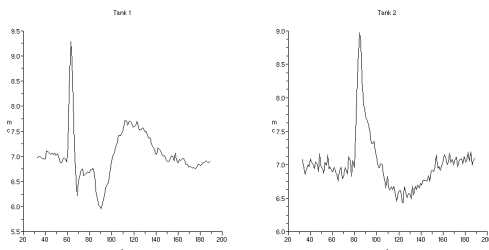


Figure 5: Tanks levels response to a disturbance

how the disturbance control on tank 1 does not affect the level on tank 2, but the control action to handle the disturbance on tank 2 affects tank 1, as it is expected by the interaction settings on the three ways valves.

8 Conclusions

A sixth order dynamical model of a four interacting tanks system with variable speed pumps was presented, and it was used to implement a linear MPC controller using ScicosLab. The controller was tested with success on an experimental system, communicating ScicosLab with a USB-6800 National Instruments Data Acquisition system using the NIDAQ-mx C API. It was showed that ScicosLab is capable for MPC developing and that it can also be used for on line control in research with good results.

References

- [1] L. Wang, *Model Predictive Control System Design and Implementation Using MATLAB* Springer, 2009, ISBN:1848823304
- [2] S. Dormido and F. Esquembre, *The Quadruple-Tank Process: An Interactive Tool for Control Education*, In Proceedings of the 2003 European Control Conference, Cambridge, UK.
- [3] K. H. Johansson, *The quadruple-tank process: a multivariable laboratory process with an adjustable zero*, IEEE Trans. on Control Systems Technology, vol 8, n° 3, may 2000, pp. 456-465.
- [4] T. Raff, S. Huber, Z. K. Nagy and F. Allgöwe, *Nonlinear Model Predictive Control of a Four Tank System: An Experimental Stability Study* Proceedings of the 2006 IEEE International Conference on Control Applications Munich, Germany, 2006, pp. 237-242.
- [5] ScicosLab <http://www.scicoslab.org>.

- [6] *DAQ Toolbox für ScicosLab* [http://
www.kybr.de/](http://www.kybr.de/)

Paper 12

Title: Modelling and control of a high head hydropower plant

Wenjing Zhou, Behzad Rahimi Sharefi, Bernt Lie, Bjørn Glemmestad
Telemark University College, Norway

Keywords: Modeling, simulation, control, hydropower

This paper describes an effective mathematical model of a hydropower plant and how a decentralized control strategy for frequency and terminal voltage can be simulated. Several dynamic equations are presented for each hydraulic element of a typical high head hydropower with ODEs (ordinary differential equations), as well as a fourth order model of synchronous generator with exciter is proposed for the modelling of generated electrical power and terminal voltage. This paper merged these two models and eventually results in a MIMO system. The frequency and terminal voltage were chosen as the control objectives according to the quality of power. For the control strategy, a PI controller coupled with droop characteristics was implemented for the frequency, and a decentralized controller with stabilizer was applied to terminal voltage control. The interactions of these two controllers are simulated and analyzed. The simulation results are presented and discussed.

Modelling and control of a typical high head hydropower plant

Wenjing Zhou, Behzad Rahimi Sharefi, Bernt Lie, Bjørn Glemmestad

Faculty of Technology, Department of Electrical Engineering, Information Technology and Cybernetics
Telemark University College, P. O. Box 203, N-3901
Porsgrunn, Norway

Abstract—This paper describes an effective mathematical model of a hydropower plant and how a decentralized control strategy for frequency and terminal voltage can be simulated. Several dynamic equations are presented for each hydraulic element of a typical high head hydropower with ODEs (ordinary differential equations), as well as a fourth order model of synchronous generator with exciter is proposed for the modelling of generated electrical power and terminal voltage. This paper merged these two models and eventually results in a MIMO system. The frequency and terminal voltage were chosen as the control objectives according to the quality of power. For the control strategy, a PI controller coupled with droop characteristics was implemented for the frequency, and a decentralized controller with stabilizer was applied to terminal voltage control. The interactions of these two controllers are simulated and analyzed. The simulation results are presented and discussed.

I. INTRODUCTION

Hydropower is a renewable and safe energy compared to thermal and nuclear power. In Norway, hydropower covers close to 100% of the electricity production, so it is of interest to utilize this energy as efficiency as possible. With this purpose, it is important to develop models for hydropower system in a way suitable for developing modern control strategy. Such a modelling work is normally done separately either for mechanical power or the synchronous generator in the plant at present. Few simulations of their interactions have been carried out, and this is another purpose of modelling.

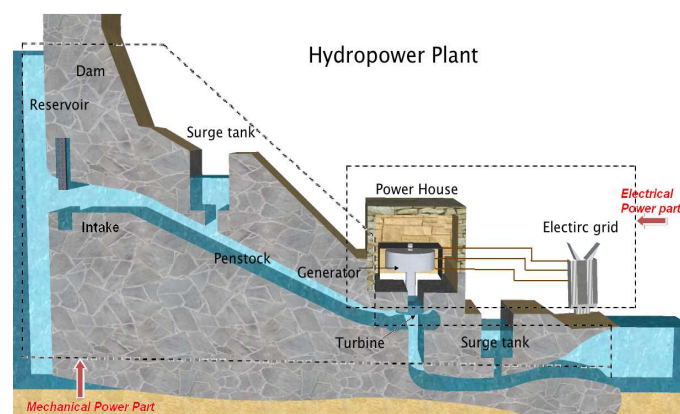


Figure 1. Overview of a typical hydropower plant.

The plant in Figure 1 is a typical high head hydropower plant in Norway and also the modelling and control object of this paper. Normally, a dam is built after the water reservoir to accumulate water. At the intake, there always is a gate to control water flows from the reservoir to water conduits. This gate has been assumed opened with a constant value and ignored in modeling. The function of the surge tank is briefly

to reduce water hammer pressure variations and keep the mass oscillations, caused by load changes, within acceptable limits and decrease the oscillations to stable operation as soon as possible [1]. There is an upstream surge tank and a downstream surge tank has been included in this paper. A water conduit after dam and a penstock after upstream surge tank guide the water flowing to the hydraulic turbine. There is another water conduit connecting downstream surge tank and downstream water reservoir. The hydraulic turbine is the mechanical part that transfers water kinetic power to mechanical power. There are two main kinds of hydraulic turbine in Norway: Francis turbine and Pelton turbine. For the Francis turbine, the water flows into the runner of the turbine through a guide vane with adjustable opening to control the rotation speed of the runner. For Pelton turbine, the water flows into runner bucket as a jet from a nozzle. The rotation speed is controlled by needle opening. The hydraulic system from reservoir to turbine supplies mechanical power. Modelling of it is called mechanical power modelling in this paper. Furthermore, there are several synchronous generators in the power house to transfer mechanical power to electrical power to the grid for peoples' everyday use. Modelling of them is called electrical power modelling. It is assumed the electrical part is a single machine connected to infinite bus (SMIB) model

II. MODELLING OF MECHANICAL POWER

The modeling process of mechanical power is shown in Figure 2. There are two reservoirs and two surge tanks, which are located respectively in upstream and downstream, a hydraulic turbine, water conduits and penstocks connecting the other elements. The mechanical power is the output from this system, and the gate opening is the manipulated variable. The gate here is an effective opening of the guide vane of Francis turbine or nozzles of Pelton turbine. It was assumed that the water head of the reservoirs are constant.

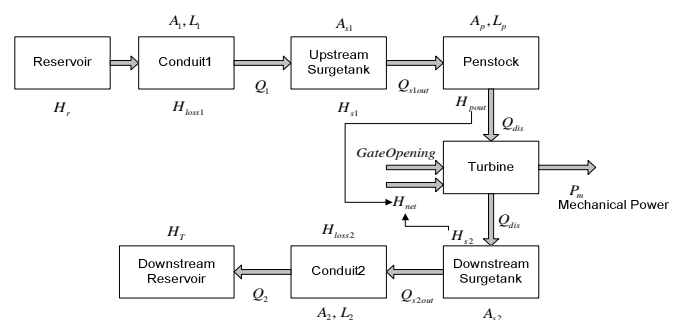


Figure 2. Flowchart for modeling mechanical power of a hydropower plant.

In this paper, the friction term of fluid, in water conduit and penstock model, is expressed as a head loss which is derived from Darcy–Weisbach equation considering that the direction of the flow can be inverted, and then it can be described as:

$$H_{loss} = f_r \cdot \frac{L}{D} \cdot \frac{\bar{v} \cdot |\bar{v}|}{2g} = f_r \cdot \frac{L}{D} \cdot \frac{\bar{Q} \cdot |\bar{Q}|}{2g \cdot A^2} \quad (1)$$

where:

A	Cross sectional area of pipe, m^2
D	Internal diameter of pipe, m
f_r	Friction factor, <i>dimensionless</i>
g	Gravity acceleration, m^2/s
L	Length of the pipe, m
\bar{Q}	Average volume flow, m^3/s
\bar{v}	Average fluid flow, m/s

A. Reservoir

Upstream reservoir is the water resource for the hydropower. After producing power, the water is gathered in downstream reservoir or directly flow into river. It has been assumed here the water levels of reservoirs are constant. In other words, H_r and H_T in Figure 2 are constant.

B. Penstock

Penstock is an enclosed pipe that delivers water to hydraulic turbine. Then Elasticity of water is only included in penstock model, not in all the models which can be an open volume. Penstock construction material can be cerement, plastic or other things, what just make a difference of friction in modelling. Furthermore, it is also assumed there is no water leakage. The dynamics of penstock have been simplified as just one discrete space element from a set of partial differential equations [2], which considered one-dimensional water flow through a chosen plane area [3].

$$\frac{dQ_{pin}}{dt} = \frac{g \cdot A_p}{L_p} (H_{s1} - H_{pout} - H_{lossp}) \quad (2)$$

$$\frac{dH_{pout}}{dt} = \kappa \cdot (Q_{pin} - Q_{pout}) \quad (3)$$

$$\kappa = \frac{a^2}{g \cdot A_p \cdot L_p} \quad (4)$$

where:

A_p	Cross sectional area of penstock, m^2
L_p	Length of the penstock, m
Q_{pin}	Inlet flow of penstock, m^3/s
Q_{pout}	Outlet flow of penstock m^3/s
H_{s1}	Water head of upstream surge tank, m
H_{pout}	Water head at Outlet of penstock, m
H_{lossp}	Head loss along penstock, m
a	Water pressure wave velocity, m/s

C. Surgetank

The surge tanks are open volume in this paper which means there is no air or water compressed when water level increases inside it. The surge tank equations are derived from the continuity of flow at the two junctions. The hydraulic losses at orifices of each surge tank have been neglected [4].

For upstream surge tank:

$$A_{s1} \cdot \frac{dH_{s1}}{dt} = Q_{s1in} - Q_{s1out} \quad (5)$$

For downstream surge tank:

$$A_{s2} \cdot \frac{dH_{s2}}{dt} = Q_{s2in} - Q_{s2out} \quad (6)$$

where:

A_{s1}	Cross sectional area of upstream surge tank, m^2
A_{s2}	Cross sectional area of downstream surge tank, m^2
Q_{s1in}	Inlet flow of upstream surge tank, m^3/s
Q_{s1out}	Outlet flow of upstream surge tank, m^3/s
Q_{s2in}	Inlet flow of downstream surge tank, m^3/s
Q_{s2out}	Outlet flow of downstream surge tank, m^3/s
H_{s2}	Water head of downstream surge tank, m

D. Water Conduits

The model of water conduit has been simply derived from Newton's second law without considering elasticity of water:

$$F = m \cdot a \quad (7)$$

$$\Delta p \cdot A = m \cdot \frac{dv}{dt} \quad (8)$$

The Δp is the pressure difference between inlet and outlet.

Taking the conduit1 as an example, its inlet pressure is from the reservoir, and its outlet pressure is equal to pressure from surge tank. Considering the head loss along the penstock, the Equation (3) can be developed as:

$$m \cdot \frac{dv}{dt} = \rho \cdot g \cdot (H_r - H_{s1} - H_{loss1}) \cdot A_1 \quad (9)$$

with $m = \rho \cdot L_1 \cdot A_1$, $v = \frac{Q_1}{A_1}$

Then the dynamic ODE of flow for conduit1 now can be stated as:

$$\frac{dQ_1}{dt} = \frac{g \cdot A_1}{L_1} (H_r - H_{s1} - H_{loss1}) \quad (10)$$

Correspondingly, the dynamic equation for the conduit2 which joins the downstream surge tank to the tail reservoir is:

$$\frac{dQ_2}{dt} = \frac{g \cdot A_2}{L_2} (H_{s2} - H_T - H_{loss2}) \quad (11)$$

where:

$A_{1,2}$	Cross sectional area of conduit 1,2, m^2
$H_{loss1,2}$	Head loss along conduit 1, 2, m
H_r	Water head of upstream reservoir, m
H_T	Water head of downstream reservoir, m
$L_{1,2}$	Length of the conduit1, 2, m
$Q_{1,2}$	Average volume flow along conduit1, 2 m^3/s

E. Hydraulic Turbine

The general mechanical power from water, no matter which kind of the turbine it is, can be stated as:

$$P_m = \eta \cdot \rho \cdot g \cdot H_{net} \cdot Q_{dis} \quad (12)$$

The net head is identical to the difference of water heads of two surge tanks minus some head loss:

$$H_{net} = H_{pout} - H_{s2} - H_{loss3} \quad (13)$$

The discharged flow into the turbine is related the type of turbine. It is all generally applied as an effective gate opening OP [5]. Then, the discharged flow is formulated as

$$Q_{dis} = k \cdot A_p \cdot OP \cdot \sqrt{H_{net}} \quad (14)$$

$$Q_{dis} = Q_{pout} \quad (15)$$

The flow before the turbine and after turbine is assumed identical. The gate opening OP is simulated as a linear function depends on time, every second it can move 1% of full opening.

$$\Delta OP = 1 \cdot \Delta t \quad (16)$$

Symbolist for Equation (12)-(16):

H_{net}	Net head to Turbine, m
H_{pout}	Outlet head of penstock, m
k	Gate constant, <i>dimensionless</i>
OP	Effective gate Opening, %
P_m	Mechanical power, W
Q_{dis}	Discharge flow to Turbine, m^3/s
η	Turbine efficiency

F. Model testing

A gate close situation is simulated. At time 200sec, the gate is closed from 50% to 35%, ramping down 1% per second. The resulting mechanical power is shown in Figure 3. There is an inverse response of power when gate closed. It is because the flow continuously reduced, but the water head is suddenly increased due to smaller passage. The pressure before turbine and net head across turbine, which is shown in Figure 4, should not be too high that it may damage the turbine or penstock. Therefore, the gate should be controlled very carefully.

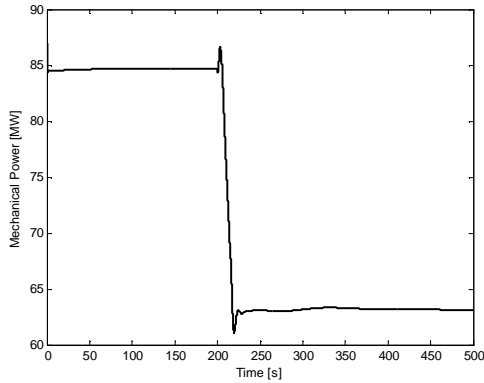


Figure 3. Mechanical power when gate is closed.

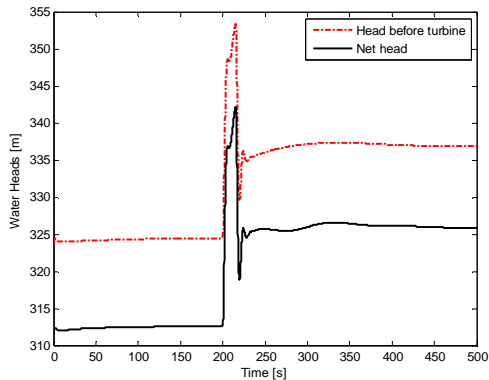


Figure 4. Water heads when gate is closed

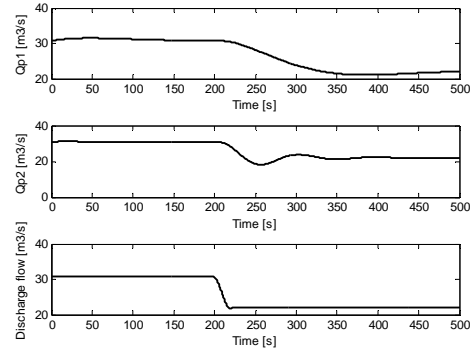


Figure 5. Flow rate when gate is closed

III. MODELING OF ELECTRICAL POWER

In this paper, a synchronous generator model is presented with simplification of Park transformation [6]. But it is enough to analyze the electrical transient. A fourth order model [7] with ODEs is as below:

Electrical equations:

$$T_{d0}' \cdot \frac{dE_q'}{dt} = (X_d' - X_q') \cdot I_d' - E_q' + E_{fd} \quad (17)$$

$$T_{q0}' \cdot \frac{dE_d'}{dt} = (X_q' - X_d') \cdot I_q' - E_d' \quad (18)$$

Terminal equations:

$$U_{td} = E_d' - R_a' \cdot I_d' - X_q' \cdot I_q' \quad (19)$$

$$U_{tq} = E_q' - R_a' \cdot I_q' + X_d' \cdot I_d' \quad (20)$$

$$P_e = E_d' \cdot I_d' + E_q' \cdot I_q' + (X_d' - X_q') \cdot I_d' \cdot I_q' \quad (21)$$

$$U_t = \sqrt{U_{td}^2 + U_{tq}^2} \quad (22)$$

Rotor motion equations:

$$\frac{d\delta}{dt} = \omega_0 \cdot (\omega - 1) \quad (23)$$

$$M \cdot \frac{d\omega}{dt} = P_{m,(p,u)} - P_e - Dp \cdot \frac{d\delta}{dt} \quad (24)$$

With δ and consider the voltage from infinite bus, the terminal voltages can also be stated as [8]:

$$U_{td} = -V_0 \cdot \sin \delta + R_e' \cdot I_d' + X_e' \cdot I_q' \quad (25)$$

$$U_{tq} = V_0 \cdot \cos \delta + R_e' \cdot I_q' - X_e' \cdot I_d' \quad (26)$$

The exciter here is simply treated as a second order [9] dynamic model:

$$T_E' \cdot \frac{dE_{fd}'}{dt} = K_E \cdot (U_r - U_t - U_s) - E_{fd}' \quad (27)$$

$$T_{FE} \cdot \frac{dU_s}{dt} = K_F \cdot \frac{dE_{fd}'}{dt} - U_s \quad (28)$$

Symbolist for Equation (17)-(28):

D_p	Damping coefficient, <i>dimensionless</i>
E_d'	d axis transient voltage, $p.u$
E_{fd}'	d axis field voltage, $p.u$

E'_q	q axis transient voltage, $p.u$
P_e	Electrical power, $p.u$
$P_{m(p,u)}$	Mechanical power, $p.u$
I_d	d axis armature current, $p.u$
I_q	q axis armature current, $p.u$
J	Generator inertia constant, <i>dimensionless</i>
K_E	Exciter gain, <i>dimensionless</i>
K_F	Stabilizer gain, <i>dimensionless</i>
R_a	Armature resistance, $p.u$
R_e	Equivalent resistance of transmission lines, $p.u$
T'_{d0}	d axis open circuit time constant, <i>second</i>
T'_{q0}	q axis open circuit time constant, <i>second</i>
T_E	Exciter time constant
T_{FE}	Stabilizer circuit time constant
U_t	Generator terminal voltage, $p.u$
U_{td}	d axis component of terminal voltage, $p.u$
U_{tq}	q axis component of terminal voltage, $p.u$
U_r	Reference voltage, $p.u$
U_s	Stabilizer voltage, $p.u$
V_0	Infinitive bus voltage, $p.u$
X_d	Synchronous reactance, $p.u$
X'_d	d axis transient reactance, $p.u$
X_q	q axis synchronous reactance, $p.u$
X'_q	q axis transient reactance, $p.u$
X_e	Equivalent reactance of transient line, $p.u$

A. Model Testing

For testing this model, a short circuit error situation is simulated at 1.1s and recovered at 1.2s, results shown in Figure 6 and Figure 7. Notice that the voltage control is in closed-loop during the simulation. The terminal voltage was suddenly set to zero because of the short circuit, and it led to unexpected oscillations of electrical power. In the meanwhile, the excitation voltage, the manipulated variable for terminal voltage, went up to increase the voltage to reference point again. Apparently, the change of terminal voltage has caused oscillation of electrical power. From Equation (24), it will result in oscillation of angular speed, equilibrium to oscillation of frequency which should be as stable as possible. To obtain a constant frequency normally requires control actions for mechanical power. Therefore, the voltage control and frequency control sequentially should be implemented simultaneously for the hydropower system. This paper only presented a decentralized control with two separate controllers, which was discussed in next section. The generated electrical power was assumed thoroughly consumed. There is no mathematical modeling of detailed electric grid with load included.

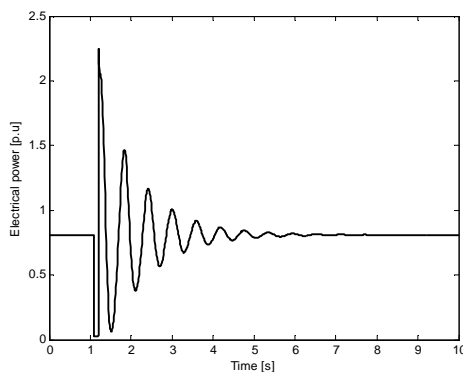


Figure 6. Simulated electrical power with a short circuit error

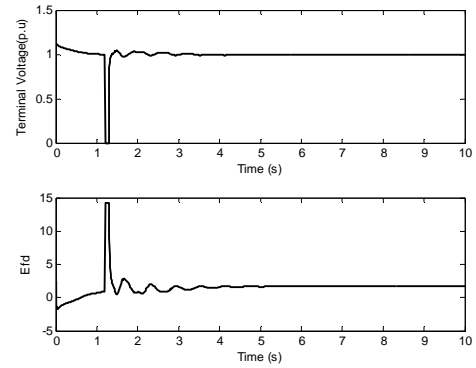


Figure 7. Simulated terminal voltage of excitation voltage with a short circuit error

IV. CONTROL STRUCTURE

The modeling results in a MIMO system, the mechanical power from water and excitation voltage of synchronous machine are the inputs, while the frequency and voltage are the outputs in this system. A traditional PI controller was implemented with this model for frequency and another controller for voltage. This interacted and controlled MIMO system working process is shown in Figure 8.

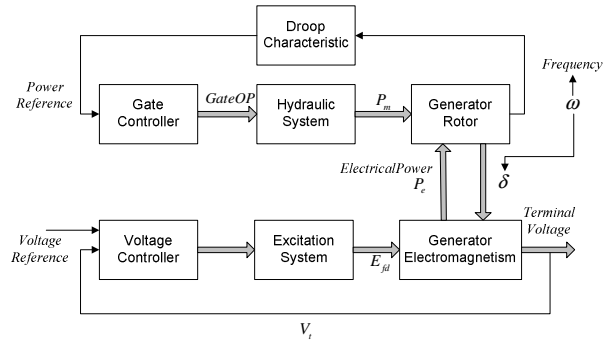


Figure 8. Flow chart of controlled MIMO hydropower system

A. Frequency Control

The frequency control is equal to the speed control or the active power control of the hydraulic turbine. The controller should comply with the main purpose, which is to keep the rotational speed stable and constant of the turbine-generator unit at any grid load. In other words, it should respond to any change of electrical power.

When a real hydropower plant is connected to an isolated load, in case of a load decrease, the excess power will accelerate the rotation of the turbine. Then the controller should reduce turbine speed that means deceleration of the water in the penstock and corresponding pressure rise and oscillations. However, to avoid it approaching to bearable pressure for turbine and penstock, closing rate should be limited. To fulfill and balance these two opposite demands, a PI controller has been implemented. Since the SMIB assumption, this PI controller was implemented with a droop characteristic, which is a traditional control method to decide how much a single machine should contribute to the network at present, for active power and frequency. The droop relationship [10] for them is described as:

$$\frac{\Delta f}{f_{nom}} = -Dr \cdot \frac{\Delta P}{P_{nom}} \quad (29)$$

Every simulation control interval, the function of droop characteristic will calculate deviation of frequency and obtain a reference power for PI controller as

$$P_{new} = -\frac{1}{Dr} \cdot \frac{f_{new} - f_{old}}{f_{nom}} \cdot P_{nom} + P_{old}, \quad P_{ref} = P_{new} \quad (30)$$

B. Voltage Control

The voltage control was carried out with the generator excitation control using a controller with a stabilizer. The controller was embedded in the second order model of exciter, which is shown in Equation (27), (28). The purpose of the controller is to hold the terminal voltage magnitude of a synchronous generator at a specific value. An increase in reactive power load of the generator should be accompanied by a drop in the terminal voltage magnitude. This voltage is rectified and compared to a set point signal. The difference of them input into a controller and then it controls the exciter field and increases the exciter voltage. Thus, the generator field current is increased, which results in an increase in the generated voltage [11].

V. RESULTS AND DISCUSSION

From Figure 8, it can be seen that the mechanical power, electrical power, frequency, phase angle and terminal voltage are interacting with each other. These mutual effects also can be seen from Equation (17) to Equation (26). Even with these effects, two decentralized controllers still perform working effectively with disturbances. Because this paper presumed it is a single machine to infinite bus system, the disturbances have been simulated as a suddenly frequency step change and voltage change in the infinite bus. These disturbances were added to the process compulsorily, not simulated as mathematical functions. That means during simulation process, when these disturbances happen, they would last for several seconds. In such a period, how a single machine in a hydropower plant response to the disturbance can be observed.

In all simulations with controllers, what should mention are the oscillations in the beginning, it is because when combining the electrical power model and mechanical power part, the system needs some time to be initialized. The physical meaning of this situation can be explained like what happens when a generator injects to the electrical grid.

- Simulation results with a frequency disturbance of 51Hz at period 25s to 35s.

As it can be seen in Figure 9, when the system got this disturbance, the gate moved towards to a smaller opening with its characteristic steps to get a smaller mechanical to reduce the frequency. In other words, it was to reduce the frequency. After the disturbance ends, the gate moved back to its working point when it was at 50 Hz. And consequently, the mechanical power was also raised up. After the gate finished its movements, the mechanical power got some waves. It is because of the dynamics of the hydraulic system.

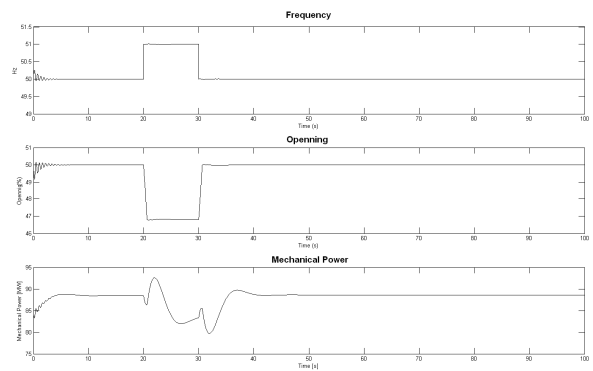


Figure 9. Simulation results of gate controller with a frequency disturbance

When the disturbance happened, there was a small effect to terminal voltage what is shown in Figure 10. The exciter maintained the terminal voltage quite well. It reduced to a smaller value, when got a disturbance. This is because the when the mechanical power is decreased, the electrical power will correspondingly should be reduced. Then, the excitation voltage should be smaller to keep the terminal voltage at its reference point. The control response of exciter can be seen rather faster than the gate. This is reasonable and practical. A turbine is mechanical equipment bearing high pressure and tons of water. Its movement is certainly slower than the electrical voltage generation with several windings.

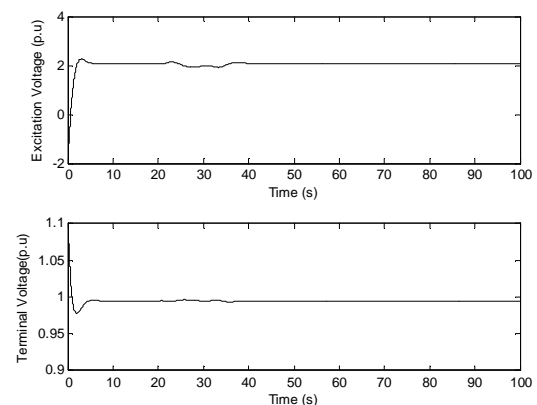


Figure 10. Simulation results of voltage controller with a frequency disturbance

- Simulation results with a voltage disturbance of 0.9 p.u at period 20s to 25s.

Firstly, the controlling of excitation voltage can be seen in Figure 11. It responded very quickly, and it went up to get a higher terminal voltage. Due to its quick response, the voltage also got a deviation after the disturbance ended. But again, the exciter forced it back to its nominal working point. This control result is acceptable.

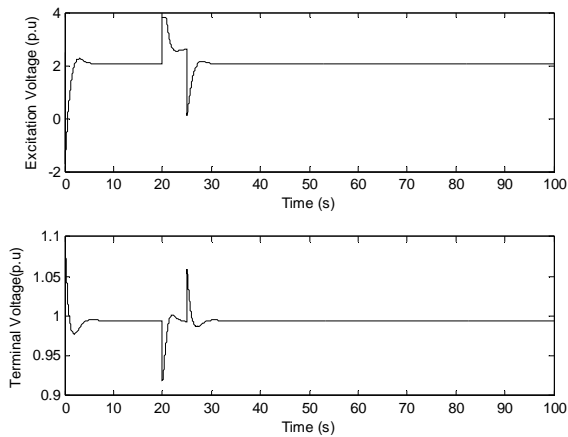


Figure 11. Simulation results of voltage controller with a voltage disturbance

However, when there was voltage disturbance, it caused some oscillations on the mechanical power control that can be seen in Figure 12. Terminal voltage changed means the electrical power changed, which is also presented in Figure 6; the frequency sequentially got a deviation from its nominal point. To control the frequency, the gate started to act. But because of interactions between electrical power control and mechanical power control, it caused some oscillations till the system went stable again.

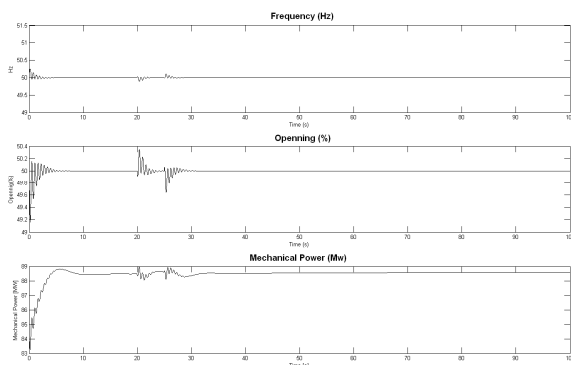


Figure 12. Simulation results of gate controller with a voltage disturbance

These simulations presented a simple model with a traditional and most common controller for power system. It shows there are still some interacting effects with two decentralized controllers. By this model, it can be analyzed why oscillations happen. Furthermore, since there are thousands of generators in the system and many different hydropower plants in the electrical net, to reduce oscillation in the electrical grid, to use less water make more power, a more advanced modern control strategy can be figured out with this modelling work.

VI. REFERENCES

- [1] Arne Kjølle, "Hydropower in Norway, Mechanical Equipment", Norwegian University of Science and Technology, 2001, Chapter 1.7.
- [2] "Hydraulic turbine and turbine control models for system dynamic studies", IEEE Trans. Power Syst, vol.7, pp.1167-179, Feb. 1992.
- [3] B.Strah, O.Kuljaca, Z.Vukic, "Speed and Active Power Control of Hydro Turbine Unit", IEEE Trans. Energy Conv, vol.20, No.2, June, 2005.
- [4] H. Fang, L.C., N. Dlakavu, Z. Shen, "Basic Modeling and Simulation Tool for Analysis of Hydraulic Transients in Hydroelectric Power Plant". IEEE Transactions on energy conversion. Vol. 23, pp.834-841, (2008).
- [5] Juan Garrido, A.Z., Francisco Vazquez, "Object oriented modelling and simulation of hydropower plants with run-of-river scheme: A new simulation tool". Simulation Modelling Practice and Theory, 2009. Vol. 17: pp. 1751-1752.
- [6] Park, R.H., "Two-reaction Theory of Synchronous Machines, Generalized Method of Analysis". Part I. AIEE Transactions 1929. Vol.48: pp. 716-727
- [7] Milano, F., Power System Modelling and Scripting. 2010: Springer, p. 325-326.
- [8] Jan Machowski, J.W.B., James R. Bumby, Power System Dynamics. Stability and Control. 2008, UK: John Wiley & Sons, Ltd. 455.
- [9] H.L.Zeynelgi, A.D., "Modelling and Simulation of synchronous machine transient analysis using SIMULINK". International Journal of Electrical Engineering Education. Vol.4, pp. 39.
- [10] Saadat, H., Power System Analysis. 2nd ed. 2002: McGraw-Hill Primis Custom Publishi. pp. 555-562
- [11] Sluis, P.S.a.L.v.d., Electrical Power System Essentials. 2008: John Wiley & Sons pp. 144.

Paper 13**Title:** Modeling of aluminum in water treatment process

Jani Tomperi
University of Oulu, Finland

Keywords: Aluminum, Water Treatment, Modeling, Variable Selection, MLR, PLS

Surface and groundwater by itself contains fairly little amount of aluminum, excluding some exceptions. However, aluminum sulfate is used as a flocculating agent in water treatment process to coagulate impurities of the water. Flocculated impurities can be removed for instance by filtering or skimming. The quality of water treatment process can be valued by measuring residual value of aluminum.

High quantity of aluminum in drinking water causes the pipeline corrosion and has negative influences to health. E.g. nerve damages, allergies and Alzheimer disease are connected to high intake of aluminum from food and drinking water. Aluminum may even be mutagenic and carcinogenic. Taking account of all these disadvantages it is essential to use proper dosage of aluminum sulfate in water treatment process to reach an optimal purification level of water and avoid high residual quantity in drinking water. In this paper residual value of aluminum in water treatment process is studied and modeled. The goals of the study are to find the most significant variables affecting to quantity of residual aluminum and create a prediction model to predict the residual aluminum in a water treatment process. The case process is a chemical water treatment plant in southern Finland. Plant uses mainly the surface water from the lake nearby.

On-line process data and laboratory measurement data is used in data analysis and modeling. Data covers the whole year 2010. Laboratory measurements are done at least once every working day. On-line process data is first hour averaged and combined with laboratory measurements data. Outliers and clearly incorrect values are manually filtered and interpolation is used to fill the missing data values. Every measuring variable in combined dataset is scaled between $[-2, 2]$ using a nonlinear scaling method. Forward variable selection method is used to select the significant variables. Dataset includes over 60 variables so variable selection is an important part of data analysis.

Prediction models are created using Multiple Linear Regression (MLR), Partial Least Squares (PLS) and neural network. Data processing and modeling are done with Matlab (Mathworks, Inc., Natick, MA).

PREDICTIVE MODEL FOR RESIDUAL ALUMINUM IN A WATER TREATMENT PROCESS

Tomperi Jani^{*1}, Pelo Marja², Juuso Esko¹.

¹ University of Oulu, Control Engineering Laboratory, P.O.Box 4300, FIN-90014 University of Oulu, Finland.

² Finnsugar Ltd, Sokeritehtaan tie 20, FI-02460 Kantvik, Finland.

* Corresponding author: jani.tomperi@oulu.fi, fax +358 8 553 2304, phone +358 8 553 2476.

Abstract: In water treatment processes aluminum salts are widely used as coagulation chemical due to their efficiency in coagulation and flocculation processes. Aluminum is proved to be at least a minor health risk and some evidence points that aluminum could have a positive affect to Alzheimer's disease. Therefore it is important to minimize the residual aluminum in drinking water or in water used at food industry, to be on the safe side. In this study data of a water treatment plant was analyzed and the residual aluminum in drinking water was predicted using Multiple Linear Regression (MLR) and Neural Network (NN) models. The purpose was to find out which variables affect to the amount of residual aluminum and create a simple and reliable prediction model which can be possibly used in an early warning system (EWS) or for automatic on-line control. A nonlinear scaling method was used to scale all measurement variables to range [-2...+2] before data-analysis and modeling. Results showed that it is possible to predict the baseline of residual aluminum in drinking water but peak values could not be predicted with a simple model. Variables that affected the most to amount of residual aluminum are among others: raw water temperature, raw water KMnO₄ and PAC/KMnO₄-ratio.

Keywords: *Water treatment process; Residual aluminum; Nonlinear scaling; Modeling; Multiple linear regression; Neural Network*

1. INTRODUCTION

1.1 Surface water treatment process

Surface waters are most commonly treated with chemical coagulation. Coagulant chemicals like aluminum or iron salts are added into the raw water followed by rapid mixing and decreasing slow mixing in chambers. In flocculation process the coagulant chemical reduces the electrical charge of hydrophobic particles and allows them to stick together and form larger particles, flocs. Flocs are removed from the water by sedimentation, dissolved air flotation or filtration processes. After floc removal water is passed to the next stage of treatment: oxidation, filtration, ozonation and disinfection. Coagulation, flocculation and filtration processes remove suspended and dissolved contaminants, harmful chemicals, turbidity and color components from the raw water. Also the bacterial and virus level can be reduced. The efficiency of the coagulation-flocculation process depends on raw water quality, coagulant chemical and dose, mixing

conditions and pH of the water. [WHO 2008, Driscoll and Letterman 1995]

1.2 Aluminum

Aluminum is the most abundant metal (8% by weight) in the Earth's solid surface and it is very reactive. Aluminum occurs naturally in water, soil and air. Due to its reactivity aluminum does not occur in soil as a free metal but combined in tens of different minerals.

Also in natural waters aluminum can occur in different forms. The concentration of aluminum in natural waters can vary significantly depending on various physicochemical and mineralogical factors. The aluminum intake level from drinking water varies according to the aluminum level in raw water and whether aluminum coagulants are used in water treatment process. Intake from food and water is unavoidable but only 5% of the total intake is from drinking water. Major part (5 mg/day) of the total intake is from food and its

additives. Contribution of intake from air is generally negligible. [WHO 2008, WHO 2003]

1.3 Aluminum in water treatment process

Aluminum salts are widely used as a coagulant chemical in water treatment processes to reduce organic matter, color and turbidity of the raw water. Aluminum has good ability to coagulate and flocculate both organic and inorganic compounds. However, using aluminum salts in water treatment process may lead to increased concentration of aluminum in drinking water. The residual aluminum also increases the water turbidity and may have some health effects to consumers. Aluminum hydroxide may also deposit on the walls of the pipes decreasing carrying capacity [Driscoll and Letterman 1995].

The field study of [Driscoll and Letterman 1995] suggested that to decrease the concentration of residual aluminum in drinking water it is necessary to maintain the pH of treated water near the pH of minimum aluminum solubility, remembering that this value varies with temperature. It was observed that the concentration of residual aluminum was affected by the pH of coagulation, the treated water pH, and the temperature of water. The aluminum concentration was proportional to the turbidity of the water. They suggested that the pH should be varied in response to seasonal changes in temperature. [Driscoll and Letterman 1995]

1.4 Health effects of aluminum

Reported minor symptoms of high level of residual aluminum in drinking water are nausea, vomiting, diarrhea, mouth and skin ulcers, rashes and arthritic pain. Symptoms are generally mild and short-lived. [WHO 2003]

There are very conflicting researches on more serious health effects of aluminum for humans and animals. Environmental factors, target groups etc. of the different studies varies greatly and therefore it cannot be said with certainty that the residual aluminum in drinking water by itself is the main affecting factor for serious health effects.

The report of World Health Organization at 1997 said that positive relationship between aluminum in drinking water and Alzheimer's disease cannot be totally dismissed. Three studies out of six

epidemiological studies showed positive relationship between aluminum in drinking water and dementia or Alzheimer's disease. It has been hypothesized that aluminum exposure is an increased risk factor for the development or acceleration of onset of Alzheimer's disease in humans. [WHO 2008, McLachlan et al. 1996] On the other hand, Canadian Study of Health and Aging claims that residual aluminum in drinking water does not increase the risk of Alzheimer's disease. [Leakey 2004]

2. DATA ANALYSIS

All data analyses were done with Matlab version 7.8 (The MathWorks Inc.) using Matlab Toolboxes and self-created scripts.

2.1 The water treatment plant

The data was collected from the water treatment plant of Finnsugar Ltd. in Kirkkonummi, Finland. This chemical treatment plant uses surface water from a lake nearby (Humaljärvi), an artificial lake (Pikkala) or mixture of these two sources as raw water. Before adding the coagulation chemical the pH of raw water is adjusted to the optimal value with calcium hydroxide. Water is treated with chemical flotation and PAC filtration. Aluminum based coagulation chemical PAX-14 (Kemira Kemwater) is used in coagulation process. Coagulation chemical dose is controlled as a function of raw water KMnO₄ (Potassium permanganate) value. After the filtration pH of the water is again adjusted to the optimal level for distribution. UV-radiation and sodium hypochlorite are used for disinfection.

During the period of data collection presented in this paper the long-term mean value of residual aluminum in drinking water produced in the water treatment plant of Finnsugar Ltd. was under half of the quality recommendation maximum target value (0.2 mg/l) defined in the Health Protection Act of the Finland's Ministry of Social Affairs and Health [FINLEX 2001]. Thus, a high amount of residual aluminum in drinking water is not a serious concern in Finnsugar Ltd water treatment plant. Even so, Finnsugar Ltd has a great interest to find out which variables effect to the amount of residual aluminum and use this information to minimize it.

2.2 Dataset

The original dataset included tens of online measurement variables and several laboratory measurements of the raw and drinking waters with good quality. Unnecessary and too rarely measured variables were left out and only measurements which could be used for prediction of residual aluminum in drinking water were left in the final dataset. Thus, the final dataset included 25 on-line measurement variables, 10 laboratory measurements of raw water and 6 measurement variables of drinking water. Measurements of drinking water were not used in modeling. Measured laboratory variables were

- pH
- KMnO₄
- turbidity
- hardness
- color
- conductivity
- smell
- chlorine
- bacteria
- aluminum

The dataset used in analysis and modeling covered a period of 16 months.

Laboratory measurements of the raw and drinking waters were done at least once in every working day. The on-line measurements were originally stored at 5 minutes interval to plant's database. The on-line measurements were averaged to one hour data before combined with the laboratory measurement data. Laboratory measurement values were combined to the corresponding hour of on-line measurement data. Missing data values were added by linear interpolation and few evident outliers were manually filtered out. Time delays were not taken into account in the data analysis because changes in the water treatment process are generally slow and delays between the different measurement points are negligible, according to process expert.

2.3 Nonlinear scaling

A dataset which contains several different measurement variables has to be scaled before data analysis to avoid incorrect results. In this work dataset was scaled between $[-2...+2]$ using a nonlinear scaling method.

Nonlinear mapping function has been developed to extract meanings of variables from measurement signals. These functions are called membership definitions. Membership definitions map the real values of variables to the range of $[-2...+2]$. Thus, a normal scaling to range $[-1...+1]$ is combined with handling of warnings and alarms. A trapezoidal membership function which is based on the support and core areas defined by fuzzy set theory is used to define the concept of feasible range. The support area is defined by the minimum and maximum values of the variable. The value range is divided into two parts by the central tendency value. The core area is limited by the central tendency values of the lower and upper part. The mapping function contains one monotonously increasing function for the values between -2 to 0 and one monotonously increasing function between values 0 to +2. Membership functions consist of two second order polynomial: one for the negative values and one for the positive values. Because the scaling idea is based on the membership functions of fuzzy set systems these values are called linguistic values. Detailed description of this nonlinear scaling method is presented in [Juuso 2010, Juuso 2011].

3. DATA MODELING

Prediction models were made to predict the amount of residual aluminum in drinking water. Models were created using a Multiple Linear Regression (MLR) and Neural Network (NN). Variable selection was done using a forward selection method. Also manually selected variables were used in modeling. The purpose of manual variable selection was to simplify and improve the performance of the created models.

3.1 Multiple Linear Regression

Multiple linear regression (MLR) can be used to describe the relationship between a set of independent variables and a dependent variable, to predict future scores on the dependent variable or to test specific hypotheses based on scientific theory or prior research. A linear equation is fitted to observe independent variables. MLR equation can be written as

$$Y = b_0 + b_1X_1 + b_2X_2 + \dots + b_nX_n + e \quad (1)$$

,where b_0 is a constant value, $X_1...X_n$ are independent variables, $b_1...b_n$ are corresponding regression coefficients and e is the error in prediction. MLR equation is thus weighted linear combination of the independent variables. [Matlab 2011, Tranmer and Elliot 2008, Audone and Giunta 2008]

3.2 Neural Network

The neural network modeling was done using the Matlab Neural Network Toolbox.

Multilayer perceptron (MLP) is a feedforward artificial neural network. MLP consists of at least three layers: an input layer, one or more hidden layers and an output layer. MLP utilizes a supervised learning technique called back-propagation for training a network. Data samples are used for training the network. [Pal and Mitra 1992, Beale et al. 2010]

The neural network used in this work consisted of measured variables as inputs, predicted value of residual aluminum as output and one hidden layer (5 neurons). Resilient back-propagation (trainrp) was used as the training function and mean squared error (mse) as the performance function. Hyperbolic tangent sigmoid (tansig) transfer function was used for the hidden layer, and the linear (purelin) transfer function for the output layer.

4. RESULTS AND DISCUSSION

4.1 General study

Before creating prediction models for the residual aluminum the combined on-line and laboratory measurement dataset was studied. The purpose was to find out significant correlations between measured variables and residual aluminum. As said earlier, all measurements were scaled with nonlinear scaling method and missing values were added by interpolation. Nonlinear scaling improved the ability to identify interdependencies of measurement variables and changes in one specific trend line compared to original data trends.

It was noticed that results of correlation determination varied depending on the order of the nonlinear scaling and data interpolation. In

Table 1 is shown variables which had highest correlation coefficient with residual aluminum when measurement dataset was not scaled or interpolated. Only laboratory measurements of raw water had high correlation to residual aluminum and on-line measurements had very low correlation coefficients. In Table 2 are the correlation coefficients when dataset was first scaled and then interpolated. Good correlation of some on-line measurements was now revealed. Number of variables with good correlation and values of correlation coefficients decreased when the original data was at first interpolated and then scaled.

Using only the scaled on-line and laboratory measurement data at the exact time of drinking water measurements sampling (I.e. interpolation did not affect to results of correlation calculation) improved slightly the correlation coefficients of residual aluminum.

Table 1. Correlation coefficients of the residual aluminum (original dataset).

Correlation coefficient	Variable
0.82	Raw water color (lab)
0.81	Raw water pH (lab)
0.79	Raw water KMnO ₄ (lab)
0.78	Raw water smell (lab)
0.76	Raw water smell, heated (lab)
0.37	Raw water conductivity (lab)

Table 2. Correlation coefficients of the residual aluminum (scaled and interpolated dataset).

Correlation coefficient	Variable
-0.61	Raw water temperature (on-line)
0.51	Raw water color (lab)
0.50	PAC/KMnO ₄ (on-line)
0.50	Raw water KMnO ₄ (on-line)
-0.37	Raw water pH (lab)

Data analysis showed that the residual aluminum in drinking water was also highly correlated with the turbidity and temperature of drinking water. These variables were ignored in data analysis and modeling because these measurements cannot be used in real life to predict the residual aluminum in drinking water as early stage of the water treatment process as possible.

Trend lines of residual aluminum and highest correlated variables are shown in Figure 1. Seasonal changes in raw water temperature are

clearly seen. The amount of residual aluminum is high when raw water is cold even if the raw water KMnO_4 and PAC-dosage are at low level. When raw water temperature is higher and raw water KMnO_4 rises the amount of residual aluminum is relatively low. This shows the fact that the effectiveness of the water treatment process on the view of residual aluminum is better when raw water is warmer. Winter and cold raw water causes challenges also to this water treatment process - like many other water treatment processes around the world.

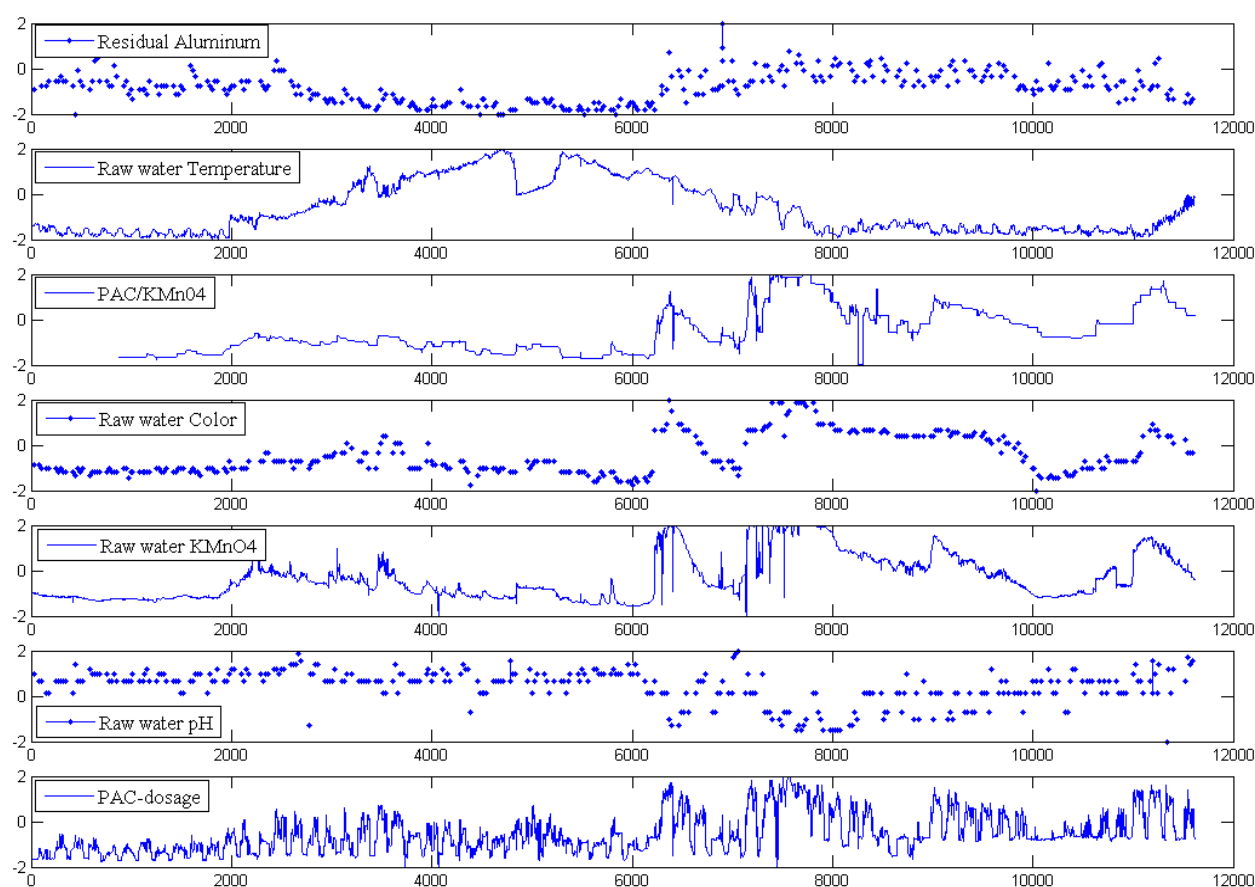


Figure 1. Trend lines of residual aluminum and measurement variables. From top to down: Residual aluminum, raw water temperature, PAC/ KMnO_4 , raw water color, raw water KMnO_4 , raw water pH and PAC-dosage.

4.2 Prediction models

Processing method of the dataset naturally affects also to accuracy of prediction models and the selection of processing method must be done carefully.

Prediction models were trained using $\frac{3}{4}$ of the data and tested using the final $\frac{1}{4}$ of the data. At first the variables for the modeling were selected by a forward variable selection method. Using these variables the best prediction model could not be created and the final variable sets were selected manually. This was done to create as simple as possible prediction model that could predict the residual aluminum reliably, not to create a perfect mathematical model. Created model could be thereby used easily for on-line control or in an early warning system (EWS) if necessary.

During modeling session it was noticed that there are several different combinations of measuring variables that could be used in modeling the residual aluminum with fairly good accuracy. Only the best results are presented in this paper.

In Figure 2 is shown the result of one MLR prediction model testing period. Variables used in model were *raw water temperature*, *raw water KMnO₄* and *PAC-dosage*. The baseline of the residual aluminum prediction is fairly good. Modeled residual aluminum follows the changes of measured residual aluminum but peak values could not be predicted. This is understandable taking into account which and how few variables were selected in model. Modeling period showed that the peak values of the residual aluminum could be predicted and the accuracy of the model improved only if some variables of drinking water laboratory measurements were used in the model.

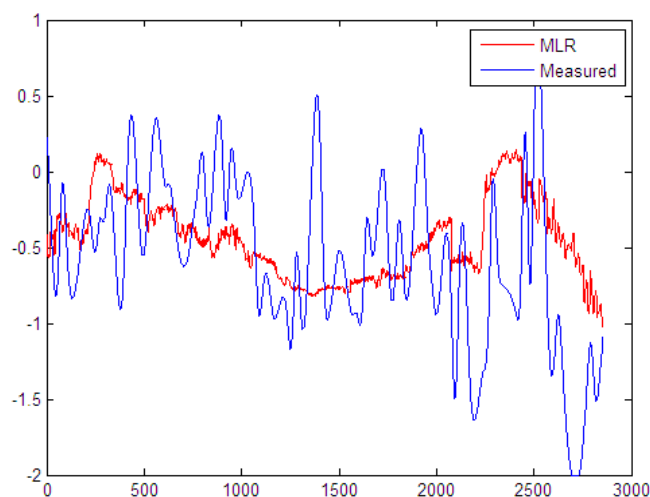


Figure 2. Testing period of the MLR model for the residual aluminum.

Increasing the number of variables does not improve the prediction result significantly. Using *raw water temperature*, *PAC/KMnO₄*, *raw water color*, *raw water KMnO₄* and *raw water pH* in a MLR model gave almost identical prediction accuracy than presented in Figure 2. This is encouraging result for creating the early warning system or on-line control. Same accuracy can be attained with fewer variables.

Also neural network was used in modeling. Result of the best neural network model for predicting the residual aluminum in drinking water is shown in Figure 3. *Raw water temperature*, *raw water KMnO₄*, *raw water pH* and *PAC-dosage* were used in the model. The accuracy of NN model is nearly the same as the accuracy of MLR model. The base line and changes are predicted fairly good but peak values could not be found.

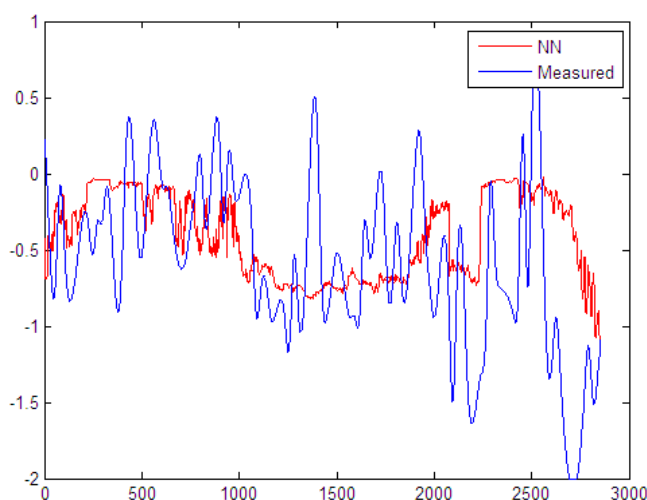


Figure 3. Testing period of neural network model for residual aluminum.

Nonlinear and linear models have been used also earlier to predict the residual aluminum in a water treatment process [Juntunen et al. 2010]. Methods and results were quite similar to presented in this paper but the prediction accuracy were slightly better. Although, the peak values of residual aluminum could not be predicted perfectly. Difference in prediction accuracy can be explained by variable selection and the goal of the work. [Juntunen et al. 2010] used partly different and more variables than it was used in the work presented in this paper. The aim seemed to be more to create a good prediction model for residual aluminum than to create a simple model that could be used in on-line control or an early warning system. Other significant differences were that the process data was averaged to 1 day data and compared to daily laboratory data, measuring period was only 275 days and the dataset was not scaled using nonlinear scaling method.

5. CONCLUSIONS

The purpose of this work was to analyze the data of the water treatment plant, find out which variables affect to the amount of residual aluminum in drinking water and create as simple and reliable prediction model for residual aluminum as possible. Clear correlations to residual aluminum were found and fairly good prediction models were created using only a few variables. Variables that had highest correlation to amount of residual aluminum were among others:

raw water temperature, raw water $KMnO_4$ and $PAC/KMnO_4$ -ratio.

The baseline of residual aluminum in drinking water can be predicted in fairly good accuracy with MLR and NN models presented in this paper. The accuracy could be improved by using different variable selection or using different prediction methods. Yet, the results were promising and an early warning system could be created based on these models to give additional information to the process personnel of the water treatment plant.

ACKNOWLEDGEMENTS

This work was done as a part of Development of a comprehensive water quality management system (POLARIS) –project. Contribution of relevant persons in Finnsugar Ltd and co-workers in POLARIS-project are greatly acknowledged. Also the funding of the TEKES (the Finnish Funding Agency for Technology and Innovation) and other partners of POLARIS is acknowledged.

REFERENCES

- Audone, B., Giunta, G. (2008). Multiple Linear Regression to Detect Shielding Effectiveness Degradations. *International Symposium on Electromagnetic Compatibility - EMC EUROPE 2008*. 8-12 Sept. 2008. pp. 1 – 6.
- Beale M.H., Hagan M.T. Demuth H.B., (2010). *Neural Network Toolbox TM 7 User's Guide*. Matlab MathWorks Inc. September 2010.
- FINLEX, (2001). Decree of the Ministry of Social Affairs and Health. Relating to the quality and monitoring of water intended for human consumption. No. 461/2000. Issued in Helsinki on 19 May 2000. 16pp.
<http://www.finlex.fi/en/laki/kaannokset/2000/en2000461.pdf>
- Driscoll C., Letterman R. (1995). Factors regulating residual aluminium concentrations in treated water. *Environmetrics*, Vol. 6, pp. 287-309.

Juntunen P., Liukkonen M., Pelo M., Lehtola M., Hiltunen Y. (2010). Modelling of residual aluminum in water treatment process. In *EUROSIM 2010*.

Juuso E. K. (2010). Data-based development of dynamic models for biological wastewater treatment in pulp and paper industry. In *SIMS 2010 – 51st Congress on Simulation and Modelling*, Oulu, Finland, 14-15 October 2010.

Juuso E. K. (2011). Intelligent Trend Indices in Detecting Changes of Operating Conditions, *Proceedings of UKSim 13th International Conference on Modelling and Simulation –UKSim 2011*, Cambridge,UK, 30 March – 1 April 2011, pp. 162-167.

Leakey H. (2004). Aluminium residual management in drinking water using selection criteria of aluminium based primary coagulants. M.Sc Thesis, Royal Roads University Victoria.

MATLAB. (2011). *Matlab Statistics Toolbox™ 7 User's Guide*. Matlab MathWorks Inc. April 2011.

McLachlan D.R.C., Bergeron C., Smith J.E., Boomer D., Rifat S.L. (1996). Risk for neuropathologically confirmed Alzheimer's disease and residual aluminum in municipal drinking water employing weighted residential histories. *Neurology*, Vol.46, pp. 401-405.

Pal S. K., Mitra S. (1992). Multilayer perceptron, fuzzy sets and classification. *IEEE Transactions on neural networks*, Vol. 3, No. 5, September 1992, pp. 683-697.

Tranmer M., Elliot M. (2008). Multiple Linear Regression. Catie Marsh Centre for Census and Survey Research. Teaching papers. 47 p.

WHO - World Health Organization. (2003). Aluminium in Drinking-water: *Background document for development of WHO Guidelines for Drinking-water Quality*.

WHO - World Health Organization. (2008). Guidelines for drinking-water quality [electronic resource]: incorporating 1st and 2nd addenda, Vol.1, Recommendations. – 3rd ed.

Paper 15

Title: Stability Analysis of AGC in the Norwegian Energy System

Ingvar Andreassen, Dietmar Winkler
Telemark University College, Norway

Keywords: energy generation, hydro power production, Modelica, Automatic Generation Control

The power system frequency in the Norwegian energy system should not deviate outside of 49.9 and 50.1 Hz. However, since 1995 a rising tendency has been seen in a frequency deviation outside this limit in the Norwegian energy system. A model of an energy system containing several hydropower plants, a power grid and an AGC (Automatic Generation Control) system was made. This model is based on the Modelica language and the hydro-power plant library HydroPlant from Modelon AB.

An AGC system is used to control the power production in an area, according to the production plan and the frequency response of the system due to actual frequency deviation. A stability analysis was performed on the model to investigate the influence of AGC to the power system model. This showed the conditions for which the AGC controller caused more instability to the system frequency.

Stability Analysis of AGC in the Norwegian Energy System

Telemark University College

Faculty of Technology

Porsgrunn, Norway

Ingvar Andreassen*

Dietmar Winkler†

Abstract

The power system frequency in the Norwegian energy system should not deviate outside of 49.9 and 50.1 Hz. However, since 1995 a rising tendency has been seen in a frequency deviation outside this limit in the Norwegian energy system. A model of an energy system containing several hydropower plants, a power grid and an AGC (Automatic Generation Control) system was made. This model is based on the Modelica language and the hydro-power plant library HydroPlant from Modelon AB.

An AGC system is used to control the power production in an area, according to the production plan and the frequency response of the system due to actual frequency deviation. A stability analysis was performed on the model to investigate the influence of AGC to the power system model. The PI controller of the AGC system model was tuned by an open loop step response test and by considering the power system as a second order oscillating process. It was found that a slow acting AGC regulation was favourable for the power system.

Keywords: *energy generation, hydro power production, Modelica, AGC tuning*

1 Introduction

The Norwegian energy company *Skagerak Energi* is evaluating the impact of introducing an AGC system in for the control of its power plants. The company wants therefore to investigate the impacts of an AGC system to the power system stability. A realistic model for the AGC system and high head hy-

dropower plants is therefore desirable. The model needs to include both, the dynamics of the waterways, as well as the non linearities of the specific AGC system such as rate limiters, sampling, deadbands, etc.

Skagerak Energy is an energy company with a core business in production, transmission of electric power and thermal energy. The company reported an annual mean production of 5400 GWh in 2009 by 20 fully owned and 25 partly owned hydro power plants. Skagerak Energy is partly owned by Statkraft with a 66.62% share and by the local municipalities with 33.38%.

1.1 Governing principals in the energy system

This section explains the governing principals in the energy system. This means the governing principles for turbine controllers, in addition to general energy net governing principals such as LFC (Load Frequency Control), ACE (Area Control Error) and AGC (Automatic Generation Control).

In an electrical power system, loads are switched on and off continuously. And because electricity cannot be stored efficiently in large amounts, there is a need of maintaining a balance between generated and consumed power. If the balance in real power deviates, the frequency will deviate instantly from the nominal value. If significant loss in generation occurs without an adequate response by the power system, then extreme frequency deviations can occur outside the working area of power plant [1].

To be able to control the frequency in the energy system, there is a need of several control actions, such as:

- Control actions on each power generating unit to maintain the power balance, without letting

*Contact: Ingvar.Andreassen@skagerakenergi.no

†Contact: Dietmar.Winkler@hit.no

the frequency deviate too much from the nominal value.

- A production plan based on statistics of the loads connected at different times, which shows what power plants that will contribute with a certain power to the grid in time.
- System control of the overall power production in each area, or cluster, of power plants.

The speed of a hydropower turbine is given by the amount of water that flows through the turbine, which is controlled by prime mover control [1], or turbine control. The mechanical energy supplied to the turbine by the water flow, and the electric load of the generator, will then give the frequency delivered from the generator. In a power system, or an energy network, the frequency is the same throughout the system. This means that all synchronous generators in the system are affected by lower rotational speeds at a lower grid frequency. The rotational speed and the active power output of a generator are controlled by the amount of mechanical energy supplied to the turbine, this can be explained by equation 1 [2]:

$$P_m = P_e + P_a \quad (1)$$

Where:

$$\begin{aligned} P_m &= \text{mechanical power [W]} \\ P_e &= \text{electrical power [W]} \\ P_a &= \text{accelerating power [W]} \end{aligned}$$

Hydro power turbine controllers (or hydro turbine governors) are control units which control the turbine output power, and it keeps the power output and power consumed by the grid load in balance. Turbine controllers have two main tasks which is turbine control, and turbine and generator protection [3].

1.2 Control function and sequences

The generator terminal voltage control is a separate control action that responds typically within a second or less [4]. The generator voltage control is a separate control system, not part of the turbine controller. The three different control actions mentioned in this section, the Turbine and Generator Protection, the Generator Voltage Control and the Turbine Control can be seen together in Figure 1.

This shows that the different controller action parts have different time scales, with a time difference of

ten times between each of the controller actions. This overall control system is quite complex, but due to the different time scales, the different control loops are virtually de-coupled from each other. This makes it possible in most cases to study each control loop individually [4, 1]. Power system frequency stability is impacted by both fast and slow dynamics; therefore the time frame for stability analysis of such a system is from a few seconds to several minutes [5, ch. 5].

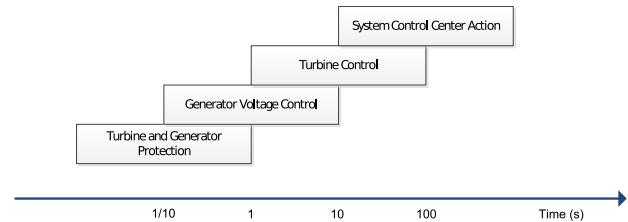


Figure 1: Different time scales of power system controls [4]

1.3 Turbine control and droop control

Normally, the turbine governors use basic PID structure to control, e.g., the guide vanes of a Francis turbine. One special thing about turbine governors is speed droop which makes it possible for the production units on the grid to share the load and “cooperating” in keeping a stable frequency. This is possible by changing the power reference to a changing frequency, and thus a change in power demand. The purpose of speed droop is to make power production units share the load in an equitable way [5]. More specifically, droop is the frequency drop, in percentage or in per unit of the rated frequency when the active power output of the generator rises from no load to maximum load of the rated power. The droop can be expressed mathematically in per unit by equation 2, [6]:

$$R_{gi} = -\frac{\Delta f / f_r}{\Delta P_{gi} / P_{gi,r}} \quad (2)$$

Where:

$$\begin{aligned} R_{gi} &= \text{droop or regulation of generator } i \text{ [pu]} \\ \Delta f &= \text{frequency change in the system [Hz]} \\ f_r &= \text{nominal rated frequency [Hz]} \\ \Delta P_{gi} &= \text{change in active generator power [MW]} \\ P_{gi,r} &= \text{nominal rated generator power [MW]} \end{aligned}$$

An example of the influence of droop at a power plant can be seen in Figure 2. This figure shows that due

to droop the active power balance will be restored at a different frequency than before a change in load.

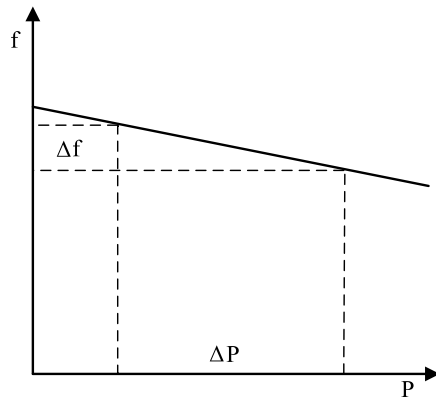


Figure 2: The droop and its influence on frequency and output power at a load rise.

Another parameter that is interconnected with droop is the network *power frequency characteristic*. This is a measure of the stiffness of the grid and it relates the frequency deviation from nominal frequency to the active power generation required to bring the produced and consumed power into balance. The network power frequency characteristic λ is expressed in equation 3, [6]:

$$\lambda = -\frac{\Delta P}{\Delta f} = \sum_i \frac{1}{R_{gi}} \cdot \frac{P_{gi,r}}{f_r} \quad (3)$$

1.4 Secondary control or Load Frequency Control (LFC)

Load Frequency Control (LFC) it is the control action that is implemented after the turbine controller (primary control). The control of frequency and generation is commonly referred to as Load Frequency Control (LFC) [5].

When a deviation in frequency occurs, due to imbalance of consumed and produced active power, the turbine controller increases or decreases the mechanical power to the generator, and thereby restores the active power balance. This prevents the frequency to deviate further. But as the turbine controller includes droop, the active power balance is restored at a different frequency than before the imbalance occurred (as explained by Figure 2). The LFC will then bring the system back to the nominal frequency by increasing or decreasing the mechanical power to the turbine-generator. This makes influences the kinetic energy, and thereby the frequency, so that the frequency is adjusted back to nominal frequency, from point I to point II, see Figure 3.

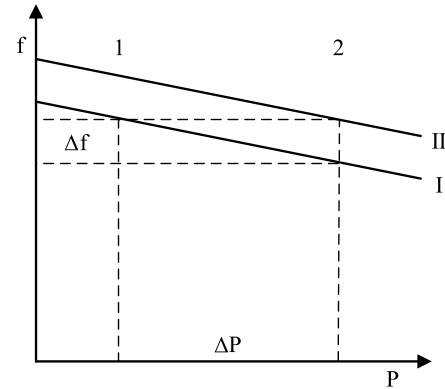


Figure 3: LFC control action. [2]

Load frequency control is also needed to restore the scheduled power interchanges with other control areas. LFC can be controlled manually by a Transmission System Operator (TSO), which is Statnett in Norway, or automatically by the Area Generation Control (AGC).

1.5 Area Control Error (ACE)

When the scheduled power exchange with the neighbouring control areas equals the actual power exchange, the balance in a control area is reached, and hence the ACE equals zero. The ACE can be explained as a comparison of the scheduled and the actual power exchange of a control area to its neighbouring control areas. To avoid the secondary control action of neutralising the primary control, the effect of the primary control action in a control area must be subtracted from the control area unbalance, the ACE. The definition of the ACE is given in equation 4, [2]:

$$ACE_i = (P_{ai} - P_{si}) + \lambda_i(f_a - f_s) = \Delta P_i + \lambda_i \Delta f \quad (4)$$

Where:

- ACE_i = Area Control Error [MW]
- P_{ai} = Actual power export [MW]
- P_{si} = Scheduled power export [MW]
- λ_i = Network power frequency characteristic [MW/Hz]
- f_a = Actual frequency [Hz]
- f_s = Scheduled frequency [Hz]
- i = Counter

1.6 Automatic Generation Control (AGC)

Area Generation Control (AGC) covers two main purposes [4]&[5, p. 601]:

- To regulate the frequency of interconnected control area power systems close to the nominal value
- To restore the scheduled power interchanges between different control areas in a power system.

This last function is commonly referred to as LFC [5, p. 601]. The AGC is the automated process of the secondary control of a power system and the automated process of bringing the Area Control Error of an area back to zero. This means that the goal of the AGC system is to produce power according to the scheduled production for each control area, corrected by the current frequency and droop settings in an area.

When considering two control areas, with one AGC controller controlling each control area, the system could look like shown in Figure 4

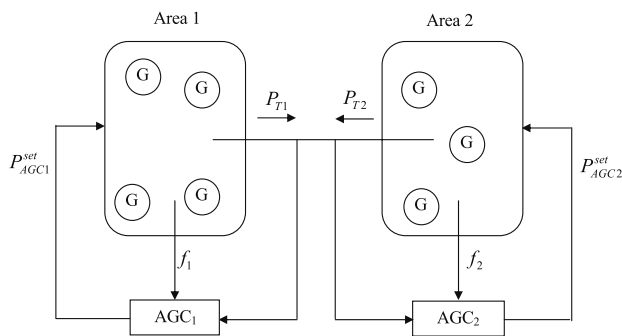


Figure 4: A system of two control areas, each controlled by an AGC [4]

In this system, the two AGC controllers will work as secondary controllers by adjusting the power reference for the generators in the area, where the power reference is denoted P_{AGC1}^{set} and P_{AGC2}^{set} . This means that each area needs its own AGC controller and controls the set-points of each turbine-generator in its area.

The AGC controller can have integral control [5, p. 606], where the integrator part of the controller makes sure that ACE will be brought to zero at steady state. It is commonly implemented as a proportional-integral (PI) controller [4].

Figure 5 shows an overview of how the AGC system works together with a power production unit, or primary control, where the AGC system controls the set-point of the unit's turbine controller.

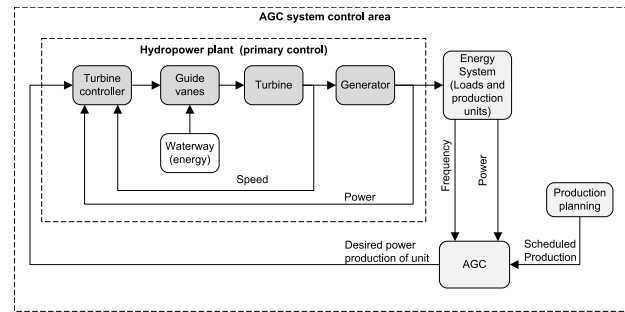


Figure 5: Total power system model, based on idea from [4]

2 Simulation model

A simulation model was created for the power production in a real control area controlled by Statkraft from Dalen in Telemark, Norway. The model consists of a control area with six production units that can be regulated by an AGC system, and one plant which is controlled manually only.

The following assumption were made for the model:

- A uniform frequency in the complete system model.
- Operation within AGC emergency operating limits, this means ACE within the dead band and command zone.
- AGC system running in Base (manual) or SCHR (regulation with bringing ACE towards zero) mode, or a combination of these.

Tools that were used for making the model and for simulations are the object oriented programming language Modelica¹. To be able to make the Modelica[®] model and to execute simulations, the computer program Dymola² was used. Components from the HydroPlant Library³ of Modelon AB were used to build the power production units. In addition, MATLAB⁴ was used to plot simulation results and to do some stability analysis.

2.1 Production unit models

The six main production units are located in three different plants. They are made anonymous and are

¹Modelica[®] is a registered trademark of the Modelica Association

²Dymola[®] is a registered trademark of Dassault Systèmes

³For more information on this library see: <https://modelica.org/libraries/HydroPlant>

⁴MATLAB[®] is a registered trademark of The MathWorks

called 1ABC, 2AB and 3A. Additional smaller production units are called The production units 4AB, 5A, 6A, 7A and 8A which were simplified by assuming them as one production unit. It was decided to make the power system model with having one production unit with a detailed waterway from the HydroPlant Library. This production unit is the unit 1B, which was the one with the most parameters available. Parameters for the model were collected from Statkraft and from [7]. Production unit 1B consist of a Francis turbine with nominal power of 108 MW, connected to a 120 MVA, 96 MW generator, and the turbine has a nominal net head of 377 m. The complete model of production unit A in plant 1 is shown in Figure 6.

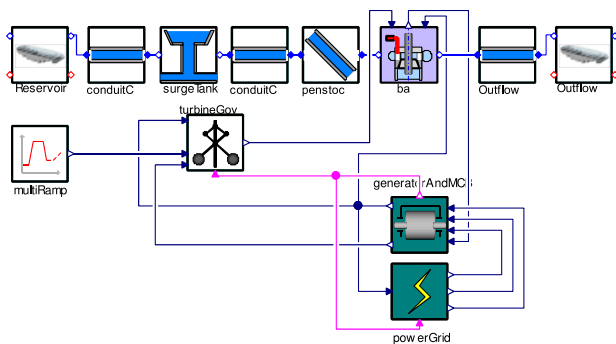


Figure 6: Model of plant 1 B, with waterway from HydroPlant Library

A simplified overview over the main components for the plant is shown in Figure 7, with elevations above sea level is for the different parts. Note that one back intake and the sand traps, gates and valves are not included in this figure, because it has little influence on the system dynamics and are therefore are not included in the model. The trash racks are considered in the model only as a contribution to the friction in conduit channel 1&2.

The rest of the waterways and turbines were simplified to ease the simulation. The simplified model was made by using a transfer function model to represent the dynamics in the water way and another transfer function to represent the time constant of the turbine governor and guide vane servo mechanism. The turbine was simplified by the using a gain together with a turbine efficiency table. Plant 1 was explained above, and unit 1A and 1C are almost identical to 1B. Production units 2A and 2B consist each of a Francis turbines with nominal power of 110 MW, connected to a 125 MVA, 100 MW generator, and have a nominal turbine net head of 209 m. Production unit 3B is the largest of the three types, which has a Francis

turbine with nominal power of 136 MW, which gives mechanical power to a 140 MVA, 120.4 MW generator, and where the nominal net head for the turbine is 264 m. The production units 4AB, 5A, 6A, 7A and 8A were assumed to have the dynamics of the largest of the units, unit 7A. This unit has a Francis turbine and a nominal generator power of 60 MW. The total nominal power of these six units simplified into one is 142.4 MW.

2.2 The AGC system model

Figure 8 gives an overview of the calculation of the AR (Anticipated Response to the units) and the UDG (Units Desired Generation). In the model, the AR was calculated by a model called AGC controller as it is shown in Figure 8. It shows the main components of the AGC system model such as ACE calculation model, Butterworth low-pass filter, PI controller, AGC dead-band, zero order hold sampling and DGS, which is the deviation from the schedule at the last ACE zero crossing. The UDG is calculated in the power plant models, to be able to simplify the structure of the system model.

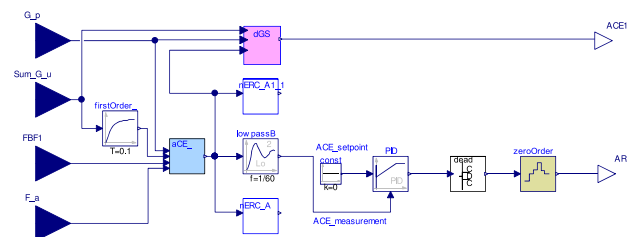


Figure 8: The AGC controller model

The ACE calculation is done according to eq. (3). The power frequency characteristic of the system, $\tilde{\lambda}$, is inserted into the ACE calculation.

The power frequency characteristic in ABB's AGC system is called Bias, or FBF, which can be expressed by $\tilde{\lambda}$ and is calculated as:

$$\tilde{\lambda} = -\frac{\Delta P}{0.1\Delta f} = \sum_i \frac{10}{R_{gi}\%} \cdot \frac{P_{gi,r}}{f_r} \quad (5)$$

Where:

$$R_{gi}\% = \text{Droop or regulation of generator } i \text{ } [\%]$$

The PI controller is a standard parallel PID controller with anti wind-up from Modelica standard library. The derivative part of the controller is not used, therefore the controller is of type PI. The goal of the AGC is to minimise the ACE, therefore the set-point is set

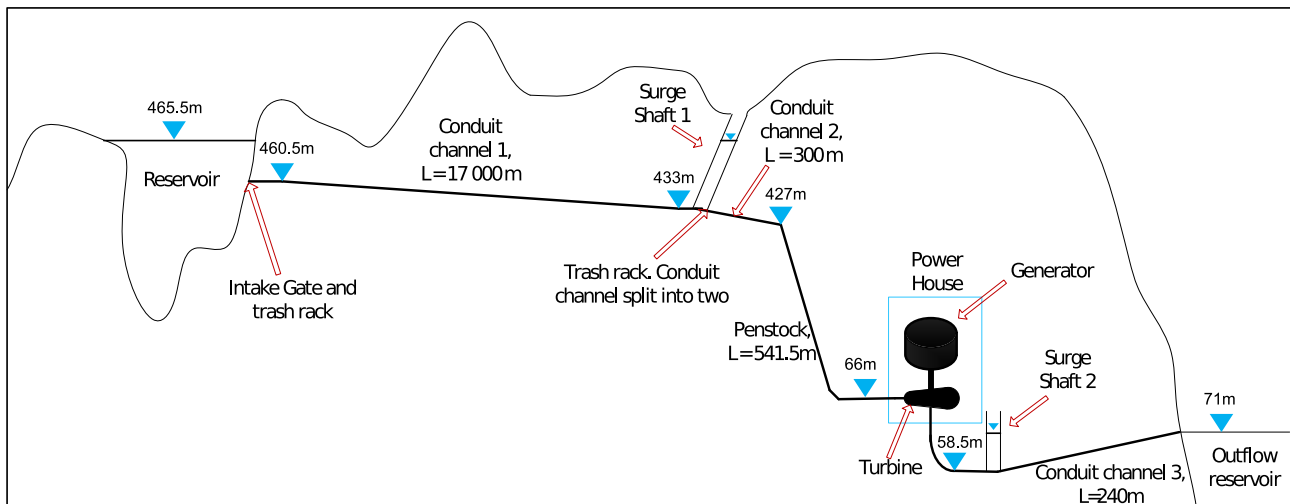


Figure 7: Overview of main parts and elevations above sea level of plant 1B, from information given by [7]

to a constant zero. The process measurement into the controller is the ACE value after passing the Butterworth filter, also known as FACE.

2.2.1 Non-linearities of the system

The AGC system has a sampling time of 5 seconds. The real plants use dead band for the power measurement back to the AGC system, and rate limiters are present in the system. The dead band zone function in the AGC system creates non linear dynamics. All this makes the system highly non linear, and these non linearities needed to be modelled to get similar system response as the real system. A rate limiter was used to model the guide vane opening and closing time constraints of the units. Additional rate limiters were used in the AGC system model, which had a slower response than those for the guide vanes. A dead band was made using Modelica, using absolute dead band, according to Figure 9.

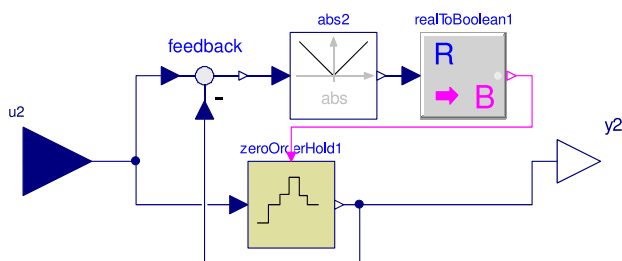


Figure 9: The dead-band model

2.3 The complete power system model

The complete power system model was put together by having one plant model for each of the power plants in the system with the production units inside the plant model. The system model is shown in Figure 10.

The system model also contains a production plan model and a plant data model. The production plan model makes it easier to change the set point change scenario. The plant data model can be used to change key parameters for the production units in the system.

3 Stability analysis

A stability analysis was performed on the AGC system model with the plants in the control area. This was done according to two scenarios with real data sets which were recorded in spring 2011. The stability of the production units in the model was analysed, as well as the stability of the total AGC system, where the goal is to minimise the ACE.

3.1 Tuning the AGC PI controller

The PI controller of the AGC system was tuned by using a method that is based on the so called Skogestad's method from [8]. The method is based on attaining a process model from information given by an open loop step response of the system, and then using classic control theory for mathematically designing the controller and parameters of the controller.

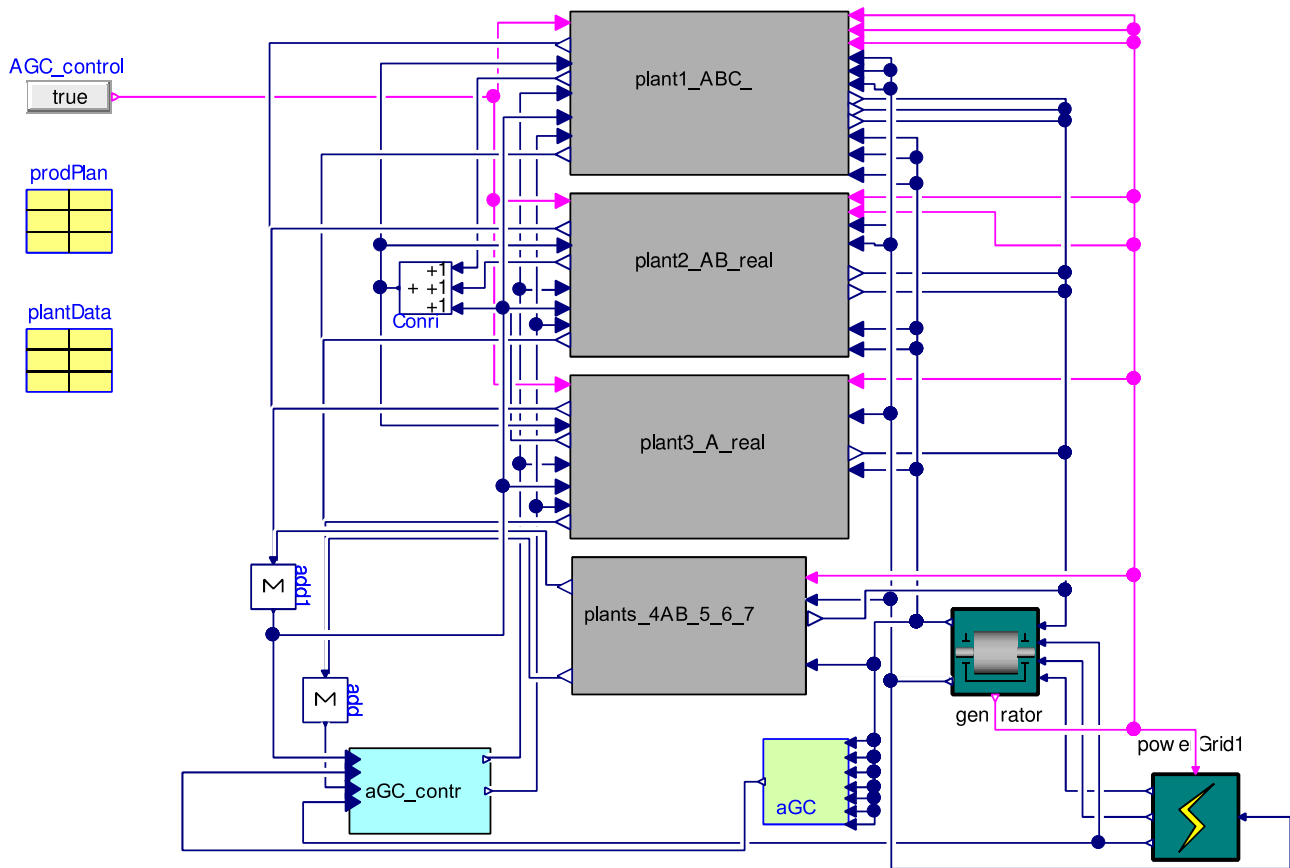


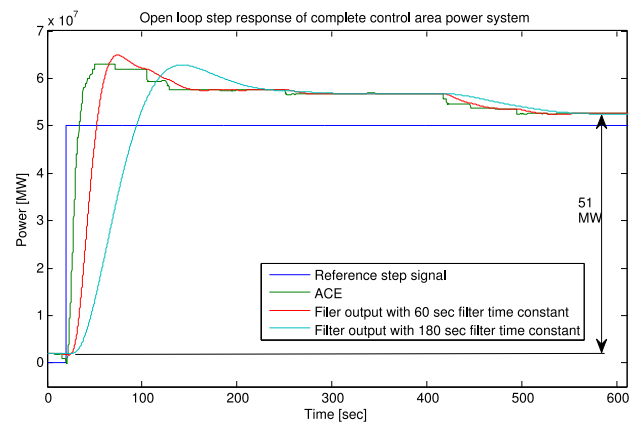
Figure 10: The complete AGC power system model

3.1.1 Identifying the process model

The complete power system model ran as open-loop, this means the output of the AGC PI controller was disconnected from the AR of the AGC, and a pure step signal with a height of 50 MW was inserted directly to the AR input to the plants. Before the step signal was initiated at 1000 seconds, the plants were all running close to a steady state of 85 MW each, which is in their normal operating area. At the time of 1000 seconds, the plants got a reference change of all together 50 MW by the AR. The step signal and the response are seen in Figure 3.1 and in Figure 3.2. The figures displays the process gain k and the process delay τ . The process time constant was found for a Butterworth filter time of 60 s and 180 s, because this filter time makes a significantly large difference in the system dynamics as the two figures show.

The process gain k is found by eq. (6) [9]):

$$k = \frac{\Delta y}{\Delta u} \quad (6)$$

Figure 11: Open-loop step response, finding process gain k

Where:

Δy = Output of the process

Δu = Reference control signal to the process

The process gain can then be found using information from Figure 11 by:

$$k = \frac{\Delta y}{\Delta u} = \frac{53 - 2}{50 - 0} = \frac{51}{50} = 1.02 \quad (7)$$

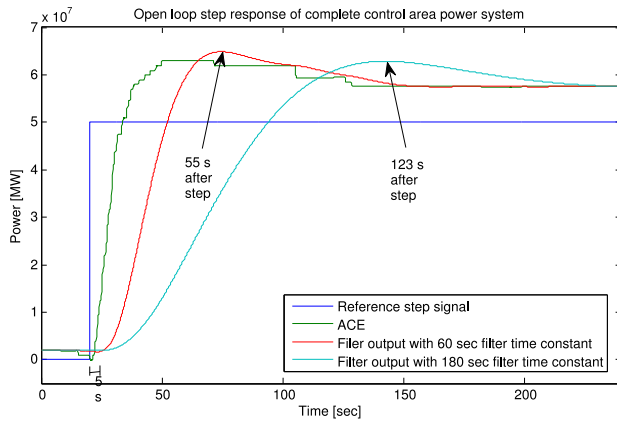


Figure 12: loop step response, finding time delay and time constants of the process

The open loop step response is shown also in Figure 12, where the response is magnified. It shows that the process delay τ is approximately 5 seconds, and it shows the time of the first peak of the process overshoots.

3.1.2 Identifying the controller parameters

The controller parameters were found according to method from [10]. The process model $h_p(s)$ has been found based on the previous section. The control system $h_c(s)$ together with the process in a basic feedback control system is shown in Figure 13.

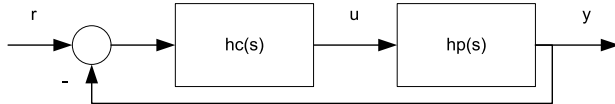


Figure 13: A basic feedback control system, by idea from [10]

The method suggests to set the response from the reference signal r to the measure output y is given by the following expression:

$$h_r(s) = \frac{y}{r} = \frac{1 - \tau}{1 + T_c s} \quad (8)$$

Where:

- T_c = Closed loop set point response time
- r = the reference process value

The user specified response time T_c is a tuning parameter which should be chosen as $T_c \geq \tau$, and [8] suggests to set $T_c = \tau$ as a starting point. The open loop step response is similar to the behaviour of a second order process, with a damping factor $\zeta = 0.6$.

By trial and error it was found that the time constant τ_0 of 13 s gives a similar response to that of the open loop test.

3.2 Testing the AGC PI controller parameters

The PI parameters found for the two filter time constants was then tested on the model. The scenarios tested are real case scenarios from spring 2011. The case presented here is using a Butterworth filter time constant of 60 s. The permanent droop setting was set to 6%, except only for unit 1C which had a 4% droop setting. The permanent droop setting in the production units in the grid model was set to 6%, the same as for most plants in the control area. Random load disturbance was added in the grid model to simulate varying grid frequency.

The production schedule initiated step changes in the modelled control area. At this particular time, the units 1A and 2B had step changes from 95 to 70 MW and 100 to 90 MW respectively. The three units 1A, 2B and 3A were set in AGC regulation mode but follow the production schedule. Where unit 3A had a constant scheduled production of 100 MW. Unit 2A is switched off and the other units in the control area were controlled in Base mode where 1B, 1C and 4,5,6,7,8 are set to constant 70, 80 and 55 MW respectively.

The real recorded data set shows that set point changes were initiated approximately 50 s before the change in the production plan. This was implemented in the ProdPlan model. A test was made for the calculated PI parameters from section 3.1.2 by Skogestad's method with $T_c = \tau$, which gave $K_p = 1.53$ and $T_i = 15.6$ s. This gave a very unstable and oscillating response. By using $T_c = 3\tau$ instead, a new $K_{pT_c} = 3\tau$ is found for the 60 s filter time constant as:

$$K_{pT_c=3\tau} = \frac{2\tau_0\zeta}{k(T_c + \tau)} = \frac{2 \cdot 13 \cdot 0.6}{1.02(3 \cdot 5 + 5)} = 0.76 \quad (9)$$

This shows much better performance, as shown in Figure 14. Still it is possible to get even less oscillations in the ACE by using $T_c = 5\tau$, or perhaps $T_c = 8\tau$, which gives the proportional gains $K_{pT_c=5\tau} = 0.51$ and $K_{pT_c=8\tau} = 0.34$. The simulation results when using these three proportional gains can be seen together with the real recorded ACE in Figure 14.

The real response has a one minute sampling time, which is too large to see the complete system dynamics. It seems like the simulated response is faster

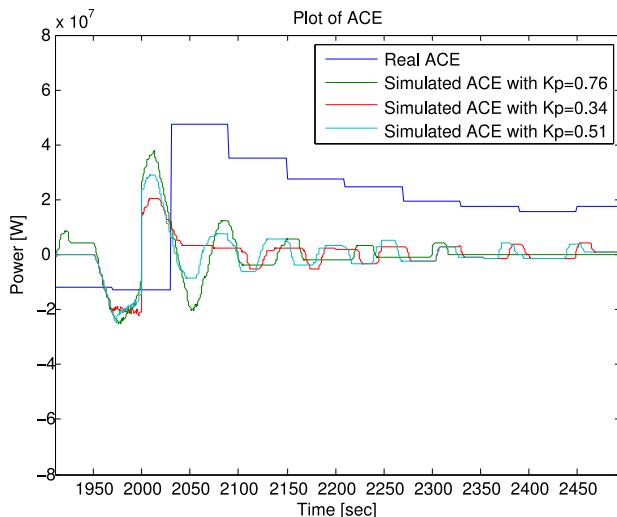


Figure 14: Real ACE, and simulated ACE with $K_p = 0.76, 0.51$ and 0.34

than the real response, the reason for this is not known. Nevertheless, a good for the model is to choose $T_c = 8\tau$, which gives $K_p = 0.34$.

It was also tested if a larger or smaller integral time T_i could give better control. $T_i = 10s$ gave more oscillations. Twice the T_i from Skogestad's tuning method gives $T_i = 31.2s$, but this did not improve stability or minimise ACE more. Therefore it can be said that a choosing PI parameters around $K_p = 0.34$ and $T_i = 15.6s$ could be a good choice for the minimising the ACE, this means using the tuning method from Skogestad with $T_c = 8\tau$.

The response at the production units was then observed when using the chosen AGC parameters $K_p = 0.34$ and $T_i = 15.6s$. The complete power plant with HPL waterway was used as unit 1A in this simulation, the result is shown in Figure 15.

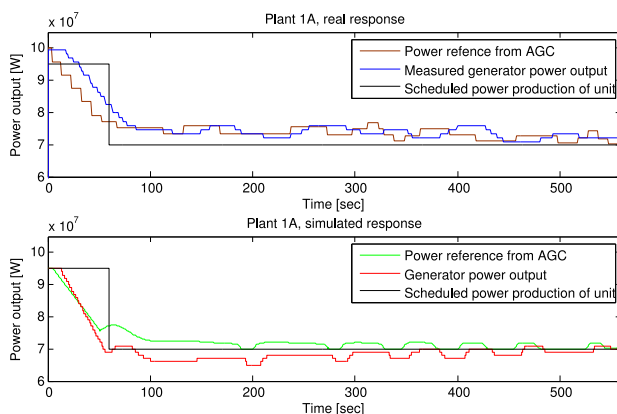


Figure 15: Response and simulated response with HPL waterway, production unit 1A

This shows somewhat the same dynamics, although slightly constant smaller oscillations are observed for the response in the model. This constant oscillation occurs due to the dead band in the AGC controller, which was set to 5 MW in all tests. The reason why this dead band has this much influence on the dynamics is because there are only three units in AGC regulation mode at this particular point in time. This means these three units have to share the additional contribution to control the ACE back towards zero. The size of the dead band zone of the AGC controller will therefore influence the stability whenever the system is close to steady state conditions. The power system frequency at this particular time can be seen in Figure 16.

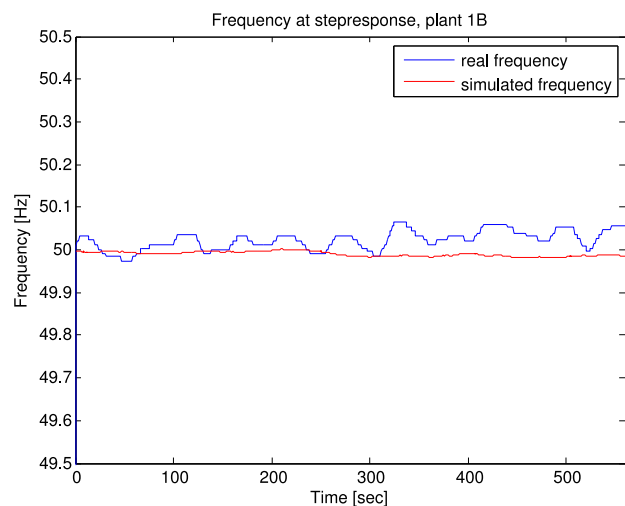


Figure 16: Frequency at step change, real and simulated

4 Discussion

As explained in Section 1.2, the power system frequency stability is impacted by both fast and slow dynamics, and the time frame for the stability analysis of such a system varies from a few seconds to several minutes [5]. The fast dynamics which have a time frame of a few seconds are for example the dynamics of the waterway, which give an inverse response at plant step change. The slow system dynamics are especially caused by the Butterworth filter time constant and the AGC rate limiter, but also the dead bands and AGC sampling time. The AGC tuning in Figure 14 shows a desired slow acting ACE regulation for the chosen PI parameters. By comparing this ACE regulation response with the faster ACE responses in the same figure, it can be seen

that a faster response by the PI controller was not favourable as it made an increasing ACE. This complies with the findings of [11] which conclude that “there is no particular economic or control purpose served by speeding up the AGC action”, from a perspective of utility operations, and that the AGC is desired to act “slowly and deliberately over tens of seconds or a few minutes”.

5 Conclusion

An assessment of the theory is that a common objective of AGC was found to be both to regulate the power interchange in or out of a control area and to control the frequency towards its nominal value. However, the definition of what the objective of an AGC system actually is seems to vary somewhat. Based on tests of the model and comparisons with the real recorded data, it seems like the AGC system model can be used for simulations of the AGC system. Model simulations show that the non-linearities of the system such as rate limiters, dead band, sampling and AGC control zone dead band makes much of the system dynamics, in addition to AGC Butterworth time constant.

The PI parameters in plant 1ABC was found to be outside the recommendations from Statnett’s FIKS⁵, where K_p are lower and T_i are higher than what is suggested. These units reaches their reference value later than what was the case for the other units, and this influence the overall AGC system response. The Butterworth filter in the AGC system makes by far the largest time constant in the system, as was seen in the open loop step response test. This Butterworth filter therefore decides how fast the system will regulate the ACE. However, we found that a slow acting AGC system is favourable, as it gave more stable operation and less ACE, which is the desired outcome. When tuning the AGC PI controller for the 60 s Butterworth filter time constant, it was found that the system had usable stability and a small ACE when using Skogestad tuning method parameters with $T_c = 8\tau$.

References

- [1] H. Bevrani, *Robust power system frequency control*. New York: Springer, 2009.
- [2] P. Schavemaker and L. Van der Sluis, *Electrical power system essentials*. Chichester: WileyBlackwell, 2008.
- [3] A. Kjølle, “Mechanical equipment,” *Norwegian University of Science and Technology, Trondheim*, 2001.
- [4] G. Andersson, “Dynamics and control of electric power systems,” 2007.
- [5] P. Kundur, N. J. Balu, and M. G. Lauby, *Power system stability and control*. New York: McGraw-Hill, 1994.
- [6] J. Machowski, J. W. Bialek, and J. R. Bumby, *Power system dynamics: stability and control*. Chichester: Wiley, 2008. 1. utg. med tittel: Power system dynamics and stability 2nd ed.
- [7] A. Solem and F. Vogt, *Norske kraftverker, bind 2*. [Oslo]: Teknisk ukeblads forlag, 1966.
- [8] S. Skogestad, “Simple analytic rules for model reduction and pid controller tuning,” *Modeling Identification and Control*, vol. 25, no. 2, pp. 85–120, 2004.
- [9] J. Balchen, M. Fjeld, and O. Solheim, *Reguleringsteknikk*. Tapir, 2004.
- [10] D. Di Ruscio, “System theory, state spece analysis and control theory,” *Lecture notes, Telemark University College, Porsgrunn, Norway*, 1996.
- [11] N. Jaleeli, L. VanSlyck, D. Ewart, L. Fink, and A. Hoffmann, “Understanding automatic generation control,” *Power Systems, IEEE Transactions on*, vol. 7, no. 3, pp. 1106–1122, 1992.

⁵Statnett, FIKS Funksjonskrav i kraftsystemet, Archived by WebCite® at <http://www.webcitation.org/5z6Ccshiu>

Paper 17**Title:** Considering culture adaptations to high ammonia concentration in ADM1

Wenche Bergland, Deshai Botheju, Carlos Dinamarca, Rune Bakke
Telemark University College, Norway

Keywords: anaerobic digestion, ADM1, ammonia, Syntrophic acetate oxidation, biogas

The Anaerobic digestion model No. 1 (ADM1) contains terms to calculate to what extent high ammonia content will inhibit anaerobic digestion (AD). It has, however, been observed that AD can adapt to much higher ammonia levels than predicted by ADM1. Schnürer et al. (1994; 1999) found that this adaptation is a result of the addition of an alternative pathway of acetate degradation by syntrophic acetate oxidizing organisms. This adaptation has great practical implications since many energy rich wastes available for biogas production have high protein content that will cause inhibiting ammonia levels during degradation. The aim of this study is to include high ammonia adaptation in ADM1 to make it applicable as a tool for design of AD of high ammonia and/or protein wastes.

Syntrophic acetate oxidation, which is not included in the original ADM1, is included here, by adding syntrophic acetate oxidizing organisms as a new state variable. Reaction stoichiometry is determined from basic biochemical reaction theory while information regarding reaction kinetics is not available. It is, however, known that this alternative pathway only occurs in processes with long sludge retention times (>20 d) and that it evolves slowly (over months). This indicates that these organisms have lower growth rates than the other organisms accounted for in ADM1.

Simulations show that the observed adaptations to high ammonia can be modeled by the simple modification of ADM1 proposed here. The predicted speed of adaptation is sensitive to both biomass yield parameter and the maximum specific growth rate. Changes in biogas production due to feed load changes are also reasonably well predicted. There is not yet enough experimental data available to estimate these parameters well. The model will be used to design experiments for improved parameter estimation.

Considering Culture Adaptations to High Ammonia Concentration in ADM1

Wenche Bergland*, Deshai Botheju, Carlos Dinamarca, Rune Bakke

Telemark University College, Faculty of Technology, P.O. Box 203, N-3901, Porsgrunn, Norway
(*e-mail: Wenche.Bergland@hit.no).

Abstract: The Anaerobic Digestion Model No.1 (ADM1) contains terms to calculate to what extent high ammonia concentration can inhibit anaerobic digestion (AD). It has, however, been observed that AD can adapt to much higher ammonia levels than predicted by ADM1. According to Hattori (2008) several syntrophic bacteria can oxidize acetate to form hydrogen thus creating an alternative pathway of acetate degradation. This adaptation has great practical implications since many energy rich wastes available for biogas production are comprised of high protein contents that produce inhibitory ammonia levels during degradation. The aim of this study is to include high ammonia adaptation in ADM1 to make it applicable as a tool for designing AD of high ammonia and/or protein containing wastes. Syntrophic acetate oxidation, which is introduced but not implemented in the original ADM1, is implemented here, by adding the concentration of syntrophic acetate oxidizing organisms as a new state variable. The reaction stoichiometry can be determined according to basic biochemical reaction principles but few details regarding reaction kinetics are available. Schnürer et al. (1997) has reported growth information of a mesophilic syntrophic acetate oxidizing bacteria, which is used here to estimate kinetic parameters. Simulations show that the observed adaptation to high ammonia can be implemented by the modified ADM1 structure proposed here. The predicted pace of adaptation seems to be most sensitive to the maximum specific growth rate (μ_m) of the syntrophic acetate oxidizing bacteria. A more complex model is required to simulate lag time during start up and inhibition; because no energy is available if the hydrogenotrophs are not situated in proximity to the acetate oxidizers. The model will be used to design experiments for improved process parameter estimation.

Keywords: Anaerobic digestion, ADM1, Ammonia, Biogas, Syntrophic acetate oxidation

1. INTRODUCTION

Anaerobic degradation of organic waste into biogas is carried out by a consortium of microorganisms, during which degradation of complex organic macro-molecules occurs by extracellular (disintegration, hydrolysis) and intracellular (acidogenesis, acetogenesis, methanogenesis) enzyme mediated biochemical reactions. The Anaerobic Digestion Model No.1 (ADM1) (Batstone et al., 2002), Figure 1, is a common platform of understanding in this area of research, developed by the International Water Association (IWA).

The ADM1 distinguishes these several stages of degradation, and includes an array of physico-chemical, chemical and biochemical processes. The last stage in the biodegradation process is the conversion of acetic acid and hydrogen to methane and CO₂ with about 70 % of the methane coming

through the acetic acid conversion pathway (Batstone et al., 2002). Specific groups of microorganisms (either bacteria or archaea) execute each of the above mentioned stages of biodegradation while maintaining their own growth rates.

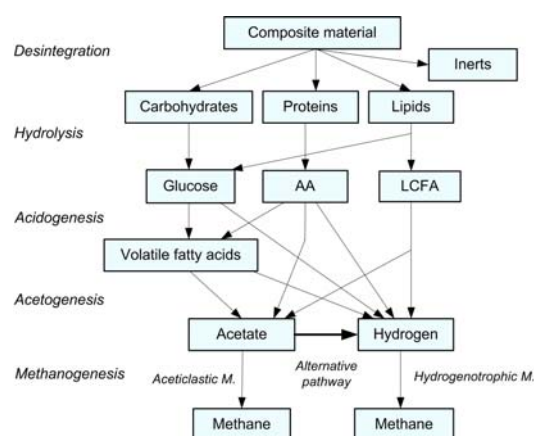


Figure 1. Modified COD flow diagram of the Anaerobic Digestion Model No.1 (Batstone et al., 2002) with the syntrophic acetate oxidizing pathway indicated.

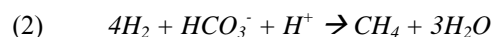
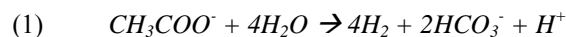
Due to the diversity of microbes naturally adopted to different environmental conditions and feed substrates, there are ranges of numerical values reported for the kinetic parameters of these microbial groups. ADM1 (Batstone et al., 2002) provides a comprehensive review list of such kinetic parameters based on various published studies. After rigorous use of this model during the last decade, a number of extensions and improvements have been suggested to enhance the usability of ADM1 (Kleerebezem & M., 2006).

Ammonia inhibition is a common problem encountered in anaerobic digesters fed high protein load. The process of acetic acid conversion to methane is carried out by a group of aceticlastic methanogenic archaea that is particularly vulnerable to ammonia inhibition. This vulnerability is already implemented in ADM1 by an inhibition function leading to a reduced rate of conversion when the ammonia concentration is high. This inhibition function predicts a 50 % inhibition when the free ammonia concentration is 30 mg/L. However it has been observed that AD can adapt to much higher ammonia levels than predicted by this ADM1 implementation, hence reducing the predictability of the model. This “metabolic adaptation” has important practical implications since many of the energy rich wastes available for biogas production have high protein contents that generate inhibitory ammonia levels during degradation.

Several studies (Karakashev et al., 2006; Schnürer et al., 1997; 2008; Song et al., 2010) have found that this adaptation is a result of an alternative pathway of acetate degradation by syntrophic acetate oxidizing organisms (Figure 1) which occurs when the aceticlastic methanogenic pathway is inhibited. This alternative pathway was first introduced by (Barker, 1936). Several microorganisms able to syntrophically oxidize acetate were reported lately (Hattori, 2008; Westerholm et al., 2010; Westerholm et al., 2011). The syntrophic acetate oxidizing pathway is catalyzed by different enzymes operating optimally in either the mesophilic or thermophilic ranges. This article describes the inclusion of this alternative biochemical process for mesophilic conditions, thus complements ADM1 to make it more suitable for modeling anaerobic biogas reactors fed substrates with high protein and/or ammonia contents.

2 METHODS

The following syntrophic acetate oxidizing reactions (Hattori, 2008) consists of reaction 1 undertaken by acetate oxidizers and reaction 2 which is undertaken by hydrogenotrophic methane producers already present in ADM1.



Reactions 1 and 2 together constitutes the syntrophic acetate oxidation, where both acetate oxidizing organisms and hydrogenotrophic methane producers are dependent on each other for utilizing the substrate (acetate) at hand.

The concentration of acetate oxidizing organisms is introduced as a new state variable in the modified ADM1 simulator using the program Aquasim 2.1f (Reichert, 1994). This group competes for the substrate with acetate utilizing methane producers (aceticlastic methanogenic archaea). The latter dominates when they are not inhibited by high free ammonia concentrations.

The reaction kinetics for reaction 1 is not readily available. Nevertheless, the reaction rate for enzyme driven biological reactions are generally approximated by a Monod type saturation function, as used for all other biochemical reactions in ADM1. The reaction rate of the uptake of substrate by the organism can be described as

$$(3) \quad \rho = k_m \cdot X \cdot \frac{S}{S+K_s} I_{pH} \cdot I_{H_2} \cdot I_{N-limit}$$

ρ = reaction rate of substrate ($\text{kgCOD}_S \text{ m}^{-3} \text{ d}^{-1}$), k_m = maximum substrate uptake rate constant ($\text{kgCOD}_S \text{ kgCOD}_X^{-1} \text{ d}^{-1}$), X = biomass concentration ($\text{kgCOD}_X \text{ m}^{-3}$), S = substrate concentration ($\text{kgCOD}_S \text{ m}^{-3}$), K_s = half saturation constant ($\text{kgCOD}_S \text{ m}^{-3}$), I = inhibition factor because of low pH, high hydrogen concentration or low nutrition level of ammonium. The inhibition factors have values between 1 and 0.

2.1 Estimating Parameters for Syntrophic Acetate Oxidizers

Three species are yet identified as mesophilic syntrophic acetate oxidizers following Equation 1. These are *Clostridium Utlunense* Strain BS (Schnürer et al., 1996), *Tepidanaerobacter acetatoxydans* sp. nov (Westerholm et al., 2011) and *Syntrophaceticus schinkii* gen. nov. sp. nov.

(Westerholm et al., 2010). The former is isolated from an anaerobic reactor fed pig manure, and data from a syntrophic experiment is reported by Schnürer et al. (1997). The syntrophic acetate oxidation by *Clostridium Utlunense* is in this work chosen to estimate parameters for Equation 3 to model reaction 1. The data in Figure 2 are recalculated from mmol (Schnürer et al., 1997) to kgCOD m^{-3} , assuming a reactor volume of 55.6 ml.

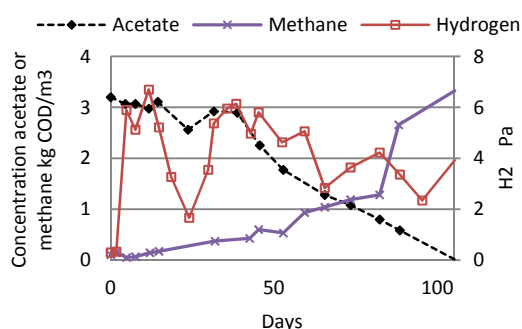


Figure 2. Experimental data from batch syntrophic acetate oxidation by *Clostridium Utlunense* and several hydrogen utilizing methanogens (Schnürer et al., 1997).

2.1.1 Parameters for Acetate Oxidation

The parameters k_m , K_s and I from Equation 3 are estimated as follows to model reaction 1.

2.1.1.1 Estimation of k_m and Y

The maximum substrate uptake rate (k_m) can be related to the maximum specific growth rate (μ_m), d^{-1} , of the organism by

$$(4) \quad k_m = \mu_m / Y.$$

Y is yield, $\text{kgCOD}_X \text{ kgCOD}_S^{-1}$, of biomass from substrate. μ_m can be calculated from observed doubling times of the organism under growth conditions without substrate limitations (Equation. 5). Doubling times are available for several species of syntrophic acetate oxidizing organisms under different feed and environmental conditions (Hattori, 2008).

$$(5) \quad \mu_m = \frac{\ln 2}{\text{doubling time}}$$

Clostridium Utlunense strain BS has 48 hours doubling time in pure pyruvate substrate but 480-600 hours (20-25 days) doubling time is estimated in a syntrophic co-culture, calculated from observed methane production rate. A lag time of approximately 2 months (Schnürer et al., 1996) has been observed in the syntrophic co-culture. The

methane was produced in stoichiometric amounts to the acetate consumed in the syntrophic oxidation with hydrogenotrophic methanogens. The yield seems therefore to be low for this process, which is consistent with the extreme low energy available according to (Schnürer et al., 1997). The energy available is estimated to be -17 kJ/mol for the acetate consumers and -17 kJ/mol for the hydrogen consumers. This is an existence at the utmost lowest energy level possible (20 kJ/mol for one proton transfer through the membrane) (Schnürer et al., 1997). Due to lack of experimental yield data it is assumed that the acetate oxidizers have a yield which is low but high enough to make growth possible. The yields according to this criterion are listed in Table 1.

Both Equation 4 and 5 are used to estimate k_m . The calculated values based on 20 and 25 days doubling time and low biomass yields are listed in Table 1.

Y	μ_m	k_m
0.01	0.035 and 0.028	3.5 and 2.8
0.03	0.035 and 0.028	1.17 and 0.93
0.05	0.035 and 0.028	0.7 and 0.56

Table 1. Calculated k_m values based on 20 and 25 days doubling time and assumed biomass yield factors.

2.1.1.2 Estimation of K_s

The half saturation constant K_s , $\text{kgCOD}_S \text{ m}^{-3}$, is set to model the concentration influence on the degradation rate of substrate. In ADM1 the recommended K_s is 0.1 - 0.5 $\text{kgCOD}_S \text{ m}^{-3}$ for the different organisms where the competing aceticlastic methanogens have 0.15 $\text{kgCOD}_S \text{ m}^{-3}$. The K_s value for the acetate oxidation is probable low because the rate seems to be unaffected by low acetate concentration (Figure 2). K_s can therefore not be estimated from parameter optimization of the acetate concentration in Figure 2. The K_s value can however not be too low because a low acetate concentration results in reduced available energy and the reaction stops. A value of 0.1 $\text{kgCOD}_S \text{ m}^{-3}$ for K_s is therefore assumed for these simulations.

2.1.1.3 Estimation of Inhibition

Inhibition can be caused from high hydrogen gas concentration and/or low pH. If the hydrogen gas concentration in the liquid increases, the Gibbs energy available for the reaction will be too small. Therefore no energy will be available for growth.

According to Schnürer et al. (1997) there are some indications that the syntrophic pathway by *Clostridium Utlunense* strain BS is mostly going through formate and not hydrogen. They have however measured the hydrogen pressure in the gas phase and it was between 1.6 and 6.8 Pa during syntrophic acetate oxidation. There can be super saturation (Pauss et al., 1990) of hydrogen in the liquid phase which gives a driving force of hydrogen from the liquid phase to the gas phase. The corresponding values in the liquid phase can be up to 70 times higher than if equilibrium is assumed. However when the observed hydrogen concentration in the gas phase is decreasing, it is more likely that the hydrogen concentration in the liquid phase is low and the phases are in equilibrium.

The calculated thermodynamic maximum of hydrogen pressure in the gas phase assuming equilibrium between the gas and liquid phase is 18 Pa (Schnürer et al., 1997) for the experiment in Figure 2. In the liquid this corresponds to the thermodynamic maximum being $2.14\text{E-}06 \text{ kgCOD m}^{-3}$ of hydrogen. The acetate oxidation will totally stop at and above this thermodynamic maximum, and be reduced (inhibited) at some degree before this level is reached.

The reduction in growth because of high hydrogen concentration can be modeled using an inhibition function. The inhibition function used for all hydrogen inhibition in ADM1 is Equation 6.

$$(6) \quad I = \frac{1}{1 + \frac{S}{K_I}}$$

The resulting inhibition factor, I , at different K_I factors is simulated in Figure 3.

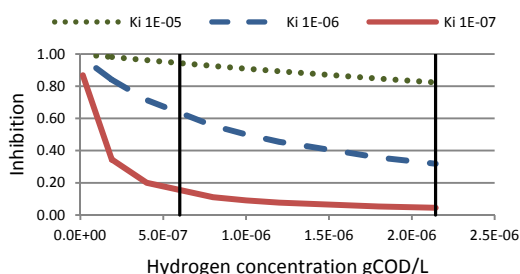


Figure 3. Inhibition simulated by Eq. (6) for 3 K_I values. The two vertical lines are assumed to be the observed levels for none and maximal inhibition (in Figure 2).

The assumed hydrogen concentration without inhibition is below $6\text{E-}07 \text{ kgCOD m}^{-3}$. This corresponds to the hydrogen levels during the last 40 days where the acetate consumption is linear in Figure 2. None of the three K_I values used in Figure 3 gives full inhibition at $2.14\text{E-}06 \text{ kgCOD m}^{-3}$ of hydrogen and no inhibition at $6\text{E-}07 \text{ kgCOD m}^{-3}$. To get a sharper cut the exponential inhibition function normally used for pH inhibition in ADM1 (Equation 7) is also tested.

$$(7) \quad I = \exp\left(-3\left(\frac{S-S_{LL}}{S_{LL}-S_{UL}}\right)^2\right)$$

Assuming no inhibition up to $6\text{E-}07 \text{ kgCOD m}^{-3}$ and full inhibition at and above $2.1\text{E-}06 \text{ kgCOD m}^{-3}$, $S_{LL} = 6\text{E-}07 \text{ kgCOD m}^{-3}$ and $S_{UL} = 2.1\text{E-}06 \text{ kgCOD m}^{-3}$. These parameters result in an inhibition factor as shown in Figure 4.

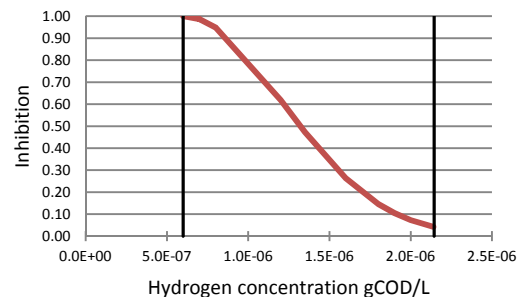


Figure 4. Simulated inhibition according to Eq. 7 as a function of hydrogen concentration in the liquid phase. The two vertical lines are assumed to be the observed levels for none and maximal inhibition in Figure 2.

Inhibition can also be caused by pH and is assumed to occur at pH lower than 7 because there is little energy for pumping protons against the concentration gradient over the cell membrane at lower pH. The same pH inhibition model as for aceticlastic methanogens is used.

2.1.1.4 Estimation of Decay Rates k_{dec}

The decay rate of the acetate oxidizer is unknown. A value of 0.02 d^{-1} is recommended for all the other organisms in ADM1. The growth is especially low for the acetate oxidizer because of the low available energy, so it is assumed that low decay may also occur. The value of 0.01 d^{-1} is therefore tested in addition to the typical decay rate of 0.02 d^{-1} .

2.1.2 Parameters for Hydrogenotrophic Methanogens

The hydrogen utilizing methanogens (Equation 2) also have little Gibbs energy available. According to Hattori (2008) and Schnürer et al. (1997) the acetate oxidizer and partner methanogens might share the extremely small energy exploited from the oxidation of acetate. This indicates that the growth rates and yields as recommended in ADM1 for hydrogenotrophic methanogens can be too high. The yield and k_m could therefore be reduced. The K_s value recommended in ADM1 for mesophilic high rate is however $2.5E-05 \text{ kgCOD}_S \text{ m}^{-3}$. Using this value and a maximum hydrogen concentration at stable conditions of $2.1E-05 \text{ kgCOD}_S \text{ m}^{-3}$ results in a maximum value for $(S/k_s + S)$ to be 0.46. Below the hydrogen level ($6E-07$) where no inhibition occurs for acetate consumption, the value is below 0.023. Since the reason for slow growth of the hydrogen consuming methanogens is the low hydrogen concentration, the parameters recommended in ADM1 for hydrogen utilizing methanogens are not altered.

2.2 Simulation

The kinetic and stoichiometric parameters for the new pathway added to ADM1 are listed in Table 2. These parameters are used in the simulations of the experiment (Figure 2), where the acetate oxidation is the main pathway instead of acetoclastic methanogenesis. The experiment is a batch lab-scale reactor, fed acetate, adjusted to pH 8 and with no stirring.

No	Inhibition	k_{dec}	Yield	K_s	μ_m	k_m
1i, 1ii	Equation 6	0.01	0.01	0.1	0.035	3.5
2i, 2ii	Equation 6	0.01	0.03	0.1	0.035	1.2
3i, 3ii	Equation 6	0.02	0.03	0.1	0.035	1.2
4i, 4ii	Equation 7	0.02	0.03	0.1	0.035	1.2
5i, 5ii	Equation 6	0.02	0.05	0.1	0.035	0.7

Table 2. Parameters used in the different simulations with (i) and without (ii) fixed initial biomass concentrations. All $K_i = 1E-06 \text{ kgCOD}_X \text{ m}^{-3}$.

The amounts of biomass in the start, X_{ox} and X_{h2} , are unknowns. Two approaches are tested; one optimizing the amount of biomass to fit the experimental data (no. 1i – 5i) and one using the same amount of biomass for all simulations $X_{ox} = 0.03 \text{ kgCOD}_X \text{ m}^{-3}$ and $X_{h2} = 0.04 \text{ kgCOD}_X \text{ m}^{-3}$ (no. 1ii – 5ii).

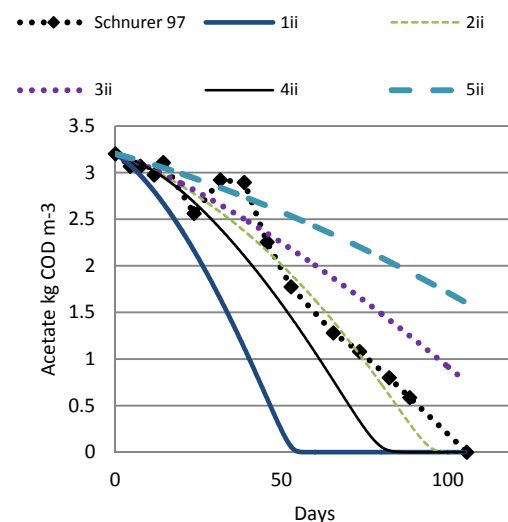
3 RESULTS

The simulated final biomass, with initial biomass X_{ox} and X_{h2} , which gave the best fit to experimental biogas production data for each case, are listed in Table 3.

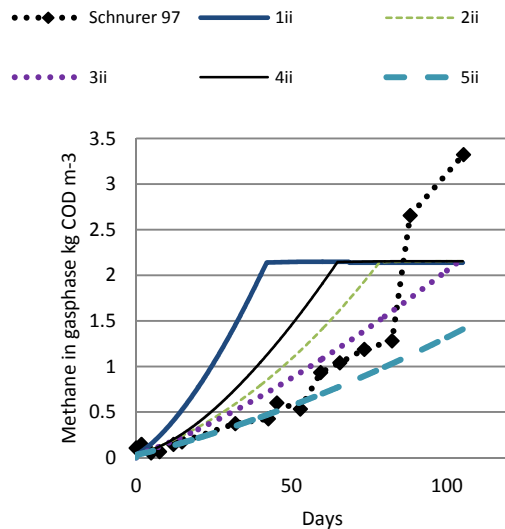
No	X_{ox} start	X_{h2} start	X_{ox} end	X_{h2} end
1i	0.005	0.007	0.018	0.072
2i	0.025	0.005	0.074	0.093
3i	0.04	0.005	0.046	0.08
4i	0.015	0.005	0.048	0.09
5i	0.06	0.007	0.073	0.076

Table 3. Optimized initial biomass concentration, $\text{kgCOD}_X \text{ m}^{-3}$, together with the simulated final biomass.

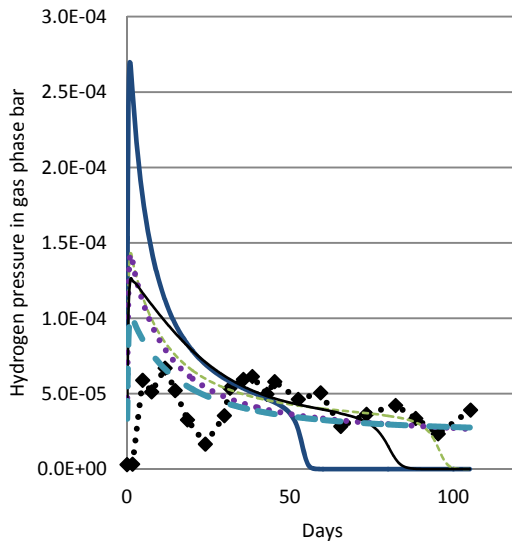
All these simulations results in rather equal curves and are represented by case 2ii in Figure 5. These results are compared to other simulations, all with the same initial biomass, to investigate only the effects of varying the new kinetic and stoichiometric process parameters and not of varying the biomass. The simulations with less good fit compared to case 2ii serves as a crude initial sensitivity analysis of the process parameters, as described in Table 2.



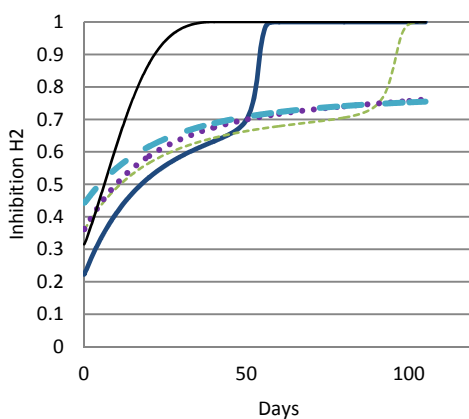
a) Acetate consumption



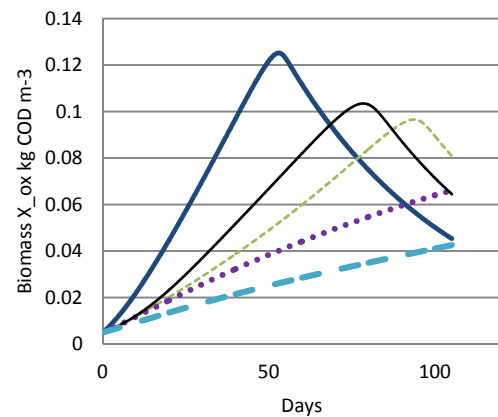
b) Methane consumption



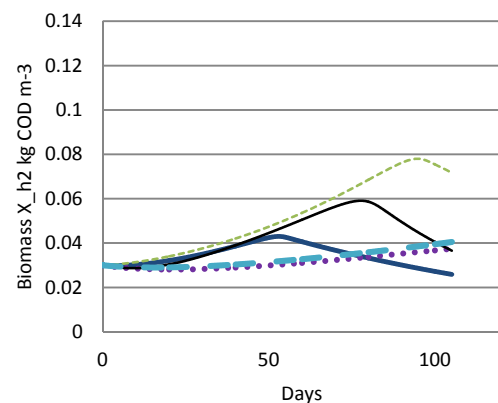
c) Hydrogen concentration in gas phase



d) Inhibition



e) Biomass of acetate oxidizers



f) Biomass of hydrogenotroph methanogens.

Figure 5 a-f. Simulations of substrate consumption and biogas production compared to measured values by Schnürer et al. (1997), where case 2i (Table 2 with fixed initial biomass $X_{ox}=0.03$ and $X_{h_2}=0.005$ kgCOD_X m⁻³) has the best fit. Simulated hydrogen caused inhibition and biomass accumulations are also presented.

The results in Figure 5 show clear effects from altering the new process parameters. Effects of decreasing yield which results in increasing k_m can be seen by comparing 3ii and 5ii or 1ii with 2ii. Both show a higher acetate consuming rate when the k_m is increased. Only K_{dec} is altered between simulation 2ii and 3ii. A clear reduction of the acetate consumption rate is observed when the degradation rate is increased. Decreasing the H_2 inhibition factor (simulation 3ii to 4ii) leads to faster substrate to biogas conversion. Repeating the simulation with a slower growth rate of syntrophic acetate oxidizers (doubling time of 25 days instead of 20 days) fit the experiment equally well as the simulations presented but with other initial biomass concentrations.

4 DISCUSSION

Biomass concentration in the experiments is unknown. Therefore parameter estimation is used to find the start amounts of biomass which can give a good fit while varying the other parameters. This is an important parameter particularly in batch experiments, and reduces the possibility to evaluate the fitness of the other parameters in Table 2. It is therefore not possible to evaluate the small variations in K_{dec} , biomass yield and inhibition parameter which were used. With optimized initial biomass concentrations, all tested parameter values gave reasonable good fit to the experiment. Choosing the same initial biomass concentration for all simulations, the effect of varying the parameters is more visible. The results show that the ranges of parameter values tested are all plausible.

The available Gibbs energy for the syntrophic acetate oxidizing reaction is very low and small changes in the hydrogen concentration in the liquid could be expected to stop the growth of the acetate oxidizers. The hydrogen concentration can in a short period increase to a high level if the hydrogen utilizing bacteria are not present close to the acetate oxidizers. This can lead to oscillating growth conditions for both co-cultures until they are positioned close to one another. This can be observed by oscillating hydrogen concentrations in the liquid phase. The measured hydrogen concentration in the gas phase has this oscillating nature. Since the hydrogen concentration in the liquid phase can be up to 70 times higher than what is estimated assuming equilibrium between gas and liquid phase (PAUSS et al., 1990), it can be assumed that the hydrogen concentration in the liquid phase oscillates even more. It is difficult to model this behavior and this will give an expected deviation between the experimental and the simulation results. A much more complicated ("biofilm") model is needed to model local concentration gradients.

A reported lag phase of 2 months for the bacteria *Clostridium Utlunense* before it "turns on" the syntrophic acetate oxidizing reaction also contributes to the slow adaption to high ammonium concentration. The lag phase is not included in the model but must be taken into consideration when simulating the reactor start-up phase. The model is therefore probably more suitable to simulate later stages of process development such as steady state. The estimated parameters should be compared to a

continuous flow experiment where the same bacteria are found in order to reduce the effect of the biomass concentration at the start. Such tests are planned.

An existence at the utmost lowest energy level possible makes the organism very vulnerable to high hydrogen levels which can occur at the starting phase or during changes in the operation parameters or feed composition. An exponential hydrogen inhibition function is probably not very correct because it cannot be assumed that the hydrogen is evenly spread in the liquid phase or that the hydrogen production is from the same bacteria during reactor instability. For general cases Equation 6 can therefore be recommended as a hydrogen inhibition function.

5 CONCLUSION

Adaptation to high ammonia levels in anaerobic reactors can be performed by several bacteria creating an alternative pathway when the aceticlastic methanogens are inhibited due to high free ammonia concentration.

The mesophilic syntrophic acetate oxidizer *Clostridium Utlunense* strain BS is here chosen to implement the alternative pathway in ADM1 when the aceticlastic methanogens are inhibited. Few details regarding reaction kinetics for the added pathway are available and parameters are therefore estimated from published experimental data. The amount of biomass applied is unknown (Schnürer et al., 1997) and therefore estimated by simulations here. The biomass at start of the published batch experiments, obtained by parameter estimation, was used to simulate gas production and composition throughout the experiments. The simulation gives reasonable good fit to experimental result of mesophilic syntrophic acetate oxidation reported (Schnürer et al., 1997) with all the variations tested here. It is therefore concluded that the syntrophic acetate oxidizing reaction pathway hereby included in the ADM1 is appropriate to simulate biogas production when the aceticlastic methanogens are inhibited by free ammonia.

More work is however needed to fine tune process parameters and to make the model also simulate the observed lag phase before the alternative pathway "kicks in". The lag phase can be due to the fact that this bacterium is reported to live at the lowest

available energy possible. Implications of this are not yet implemented in the model.

6 REFERENCES

Barker, H. A. (1936). On the biochemistry of the methane fermentation. *Archives of Microbiology* , 7 (1), 404-419.

Batstone, D., Keller, J., Angelidaki, I., Kalyuzhnyi, S., Pavlostathis, S., Rozzi, A., et al. (2002). The IWA Anaerobic Digestion Model No 1 (ADM1). *WATER SCIENCE AND TECHNOLOGY* , 45, 65-73.

Hattori, S. (2008). Syntrophic acetate-oxidizing microbes in methanogenic environments. *MICROBES AND ENVIRONMENTS* , 23, 118-127.

Karakashev, D., Batstone, D. J., Trably, E., & Angelidaki, I. (2006). Acetate oxidation is the dominant methanogenic pathway from acetate in the absence of *Methanosaetaceae*. *APPLIED AND ENVIRONMENTAL MICROBIOLOGY* , 72, 5138-5141.

Kleerebezem, R., & M., M. C. (2006). Critical analysis of some concepts proposed in ADM1. *WATER SCIENCE AND TECHNOLOGY* , 54, 51-57.

Pauss, A., Andre, G., Perrier, M., & Guiot, S. (1990). Liquid-to-gas mass-transfer in Anaerobic Processes - Inevitable transfer limitations of methane and hydrogen in the biomethanation process. *APPLIED AND ENVIRONMENTAL MICROBIOLOGY* , 56, 1636-1644.

Reichert, P. (1994). AQUASIM - A tool for simulation and data-analysis of aquatic systems. *WATER SCIENCE AND TECHNOLOGY* , 30, 21-30.

Schnürer, A., & Nordberg, A. (2008). Ammonia, a selective agent for methane production by syntrophic acetate oxidation at mesophilic temperature. *WATER SCIENCE AND TECHNOLOGY* , 57, 735-740.

Schnürer, A., Schink, B., & Svensson, B. (1996). *Clostridium ultunense* sp nov, a mesophilic bacterium oxidizing acetate in syntrophic association with a hydrogenotrophic methanogenic bacterium. *INTERNATIONAL JOURNAL OF SYSTEMATIC BACTERIOLOGY* , 46, 1145-1152.

Schnürer, A., Svensson, B., & Schink, B. (1997). Enzyme activities in and energetics of acetate metabolism by the mesophilic syntrophically acetate-oxidizing anaerobe *Clostridium ultunense*. *FEMS MICROBIOLOGY LETTERS* , 154, 331-336.

Schnürer, A., Zellner, G., & Svensson, B. (1999). Mesophilic syntrophic acetate oxidation during methane formation in biogas reactors. *FEMS MICROBIOLOGY ECOLOGY* , 29, 249-261.

Song, M., Shin, S. G., & Hwang, S. (2010). Methanogenic population dynamics assessed by real-time quantitative PCR in sludge granule in upflow anaerobic sludge blanket treating swine wastewater. *BIORESOURCE TECHNOLOGY* , 101, S23-S28.

Westerholm, M., Roos, S., & Schnürer, A. (2010). *Syntrophaceticus schinkii* gen. nov., sp nov., an anaerobic, syntrophic acetate-oxidizing bacterium isolated from a mesophilic anaerobic filter. *FEMS MICROBIOLOGY LETTERS* , 309, 100-104.

Westerholm, M., Roos, S., & Schnürer, A. (2011). *Tepidanaerobacter acetatoxydans* sp. nov., an anaerobic, syntrophic acetate-oxidizing bacterium isolated from two ammonium-enriched mesophilic methanogenic processes. *Systematic and Applied Microbiology* , 34, 260-266.

Paper 18

Title: Dynamic modelling of a pulp mill with a BLG plant - effects in the chemical recovery cycle

Christian Hoffstedt
Innventia AB, Sweden

Keywords: Gasification, pulp mill, dynamic, WinGEMS, black liquor

A modern chemical pulp mill has a considerable surplus of energy. The black liquor, containing dissolved lignin, extractives and residual cooking chemicals, is sent to the recovery line and later combusted in the rather inefficient recovery boiler, producing steam and electricity. A more thermal-efficient way of utilizing the energy in the black liquor is by gasification, producing a syngas that may be used for biofuel production. The next step for this technology is the construction of a demonstration plant in parallel with a recovery boiler. When the gasifier is of demonstration size, it will affect other parts of the pulp mill. This is important to know about when, for example, designing equipment. Data from the Chemrec pilot plant in Piteå, Sweden has been used in the model. The model mill is a BAT-mill (best available technique) with a black liquor gasification plant running in parallel with the recovery boiler. The simulations were carried out in WinGEMS. Realistic start-up and shut down procedures have been applied. The focus of the work was to study the dynamic effects in the recovery line and the lime kiln load as well as the build up time of salts in the mill liquors when operating a recovery boiler and a gasifier in parallel. The work was carried out within the BLGII (Black Liquor Gasification)-program.

Dynamic modelling of a pulp mill with a BLG plant – effects in the chemical recovery cycle

*Christian Hoffstedt and Niklas Berglin
Innventia AB, Box 5604, SE-11486 Stockholm, Sweden*

Abstract

A modern chemical pulp mill has a considerable surplus of energy. The black liquor, containing dissolved lignin, extractives and residual cooking chemicals, is sent to the recovery line and later combusted in the rather inefficient recovery boiler, producing steam and electricity. A more thermal-efficient way of utilizing the energy in the black liquor is by gasification, producing a syngas that may be used for biofuel production. One application of the technology is to apply it as a capacity booster to an existing mill with its recovery boiler in operation thus converting a part stream of the black liquor capacity. When operated in parallel with the recovery boiler, the gasifier system will affect other parts of the pulp mill, which are important to know about when, for example, designing equipment. The simulation tool used is WinGEMS and data from the Chemrec development plant in Piteå, Sweden has been used in the model. The model mill is a BAT- mill (best available technique) with a black liquor gasification plant running in parallel with the recovery boiler. The focus of the study has been to study the dynamic effects in the recovery line and the lime kiln load as well as the build up time of Cl/K in the mill liquors.

Introduction

A pulp mill that produces bleached kraft pulp generates 1.7–1.8 tonnes of black liquor (measured as dry content) per tonne of dry pulp. Black liquor represents a potential energy source of 250–500 MW per mill [1]. It is of great interest to convert the primary energy in the black liquor to an energy carrier of high value. Gasification takes place under partial oxidation and the inorganic chemicals can be regenerated in the gasifier and directly processed into green liquor, while the organic material is converted into syngas. Black liquor gasification is thus an interesting pathway for converting the energy in the black liquor into an high value energy carrier while regenerating the cooking chemicals [2].

This work investigates the steady state and dynamic effects in the chemical recovery line while operating a black liquor gasifier in parallel with a recovery boiler. When the BLG unit is of pilot plant size, the effects on the pulp mill are none or minor. But when scaling up the BLG unit to a demonstration plant and utilizing approximately 25% of the total amount of black liquor in the gasifier, it will have effects on the chemical recovery cycle. The results can be used for developing control strategies, calculating tank volumes and tracking component flow through the system.

This study is mainly focused on the effects on the lime kiln load and Cl/K levels in the mill liquors.

The simulation tool - WinGEMS

The simulation tools used in this work was WinGEMS (Pacific Simulation/Metso Automation), a tool specially focused on pulp & paper production. Both steady state and dynamic behaviour can be modelled. WinGEMS uses sequential numerical approximation to model transient behaviour in a process. To transfer the model from steady state to dynamic mode, volumes and residence time of each part of the mill is required. The volumes in a pulp mill are large and the residence time is long, often several hours in each step.

A converged model with steady state results, which also is the starting point of the dynamic simulations (at time = 0), is needed. Both high (80% full) and low (20% full) tank levels were studied. With high tank levels, the larger stock acts as a buffering liquor and the residence time is longer and process changes are spread out at a slower rate.

Mill boundary and design

The model used is a BAT-mill (best available technology), developed in the FRAM-program [3] and includes the entire pulp mill, from incoming wood too fully bleached and dried pulp.

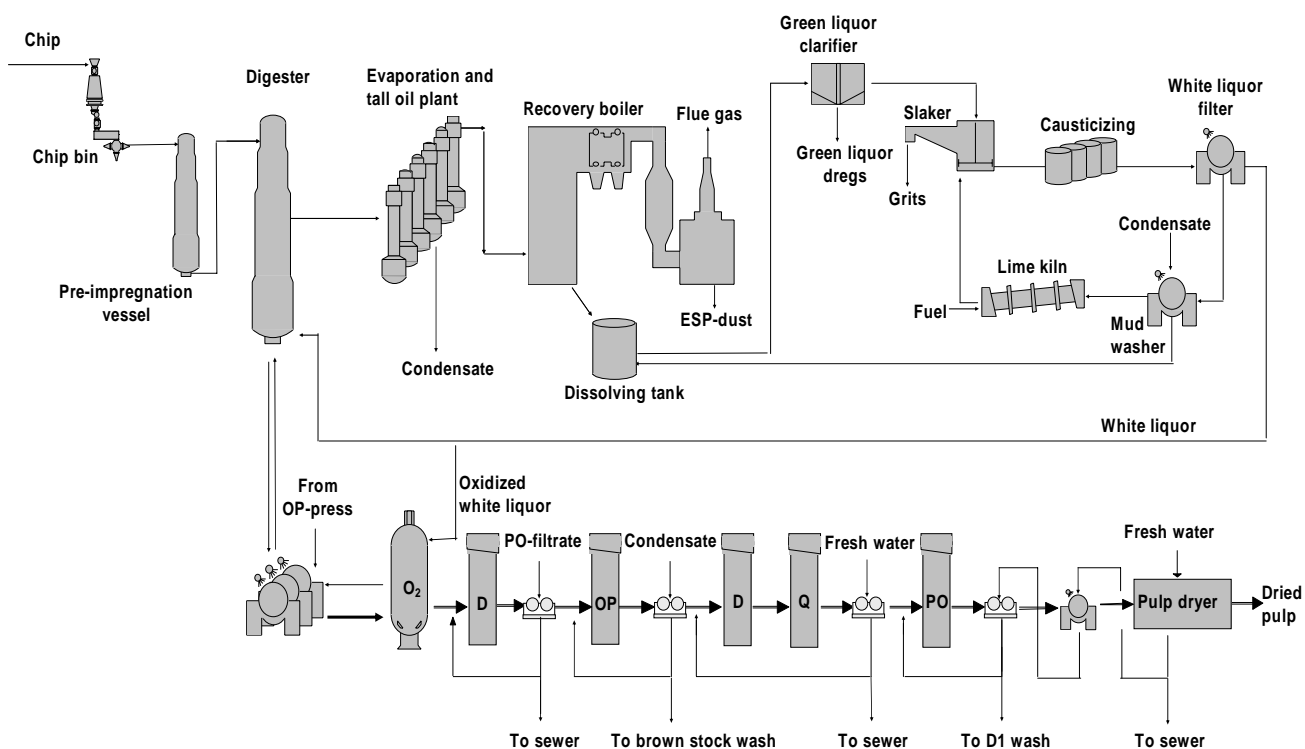


Figure 1. *Figure of a pulp mill simulation in WinGEMS*

The raw material is softwood and black liquor of 80% dry solids is fed to the recovery boiler and the gasifier. The black liquor has a lower heating value of 12.3 MJ/kg DS and the composition is presented in the table below.

Table 1. Black liquor composition

	Mass %
C	35.7
H	3.7
S	4.4
O	35.8
Na	19.0
K	1.1
Cl	0.3

A black liquor gasifier (BLG) system has been implemented in parallel with the recovery boiler. The black liquor is split before the recovery boiler to control the amount of black liquor to the gasifier. The gasifier is operated at around 30 bars and a temperature of 1050°C [4]. The BLG unit produces syngas and green liquor similar to the analysed green liquor from DP1, the development plant gasifier owned and operated by Chemrec in Piteå, Sweden. The gasification system designed by Chemrec [5] is outlined in figure 2 below.

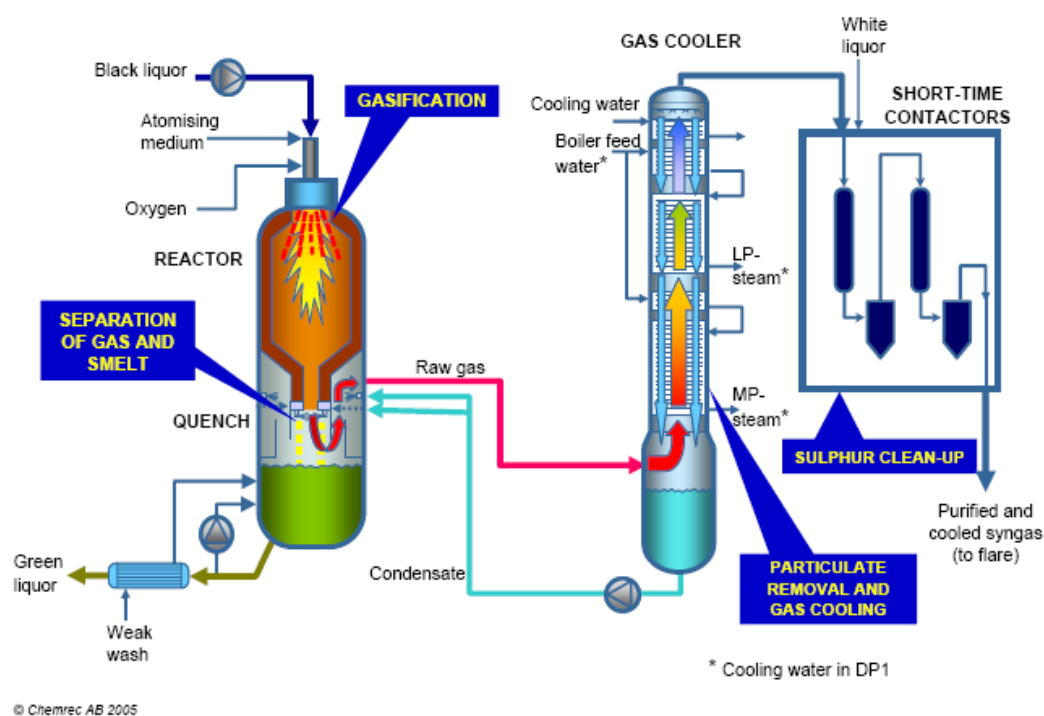
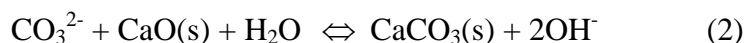
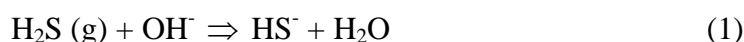


Figure 2. BLG system designed by Chemrec

In pressurized gasification, certain amounts of sulphur will form gaseous H_2S instead of Na_2S , leading to a higher proportion of carbonate in the green liquor. After a gas cleaning step the isolated H_2S is added to the white liquor as H_2S according to reaction (1) below. Reaction (2) below was used by the model to calculate the CaO demand to complete the causticising reaction. The required CaO demand is to take reaction (2) to the point where no additional carbonate can be converted into hydroxide. Hydroxide is needed in the wood digesting. Since the green liquor from black liquor gasification contains more carbonate, the CaO demand is higher. The CaO is produced in the lime kiln or added as make-up to the process, so the lime kiln load will be higher or more CaO make-up is needed.



For the dynamic simulations a simple controlling system has been set up. All effected parameters have a set point and the manipulated variable is changed stepwise with a small step size. The results from these simulations can then be used to develop a more advanced and effective control system. Realistic start-up and shut down procedures have also been applied. Thirty days of continued operation has been simulated with the step size of 30 minutes.

Results

As stated before, the green liquor produced in the BLG unit will give a higher load on the lime kiln. The steady state value for the lime kiln in this model, when 25% of the black liquor goes to the gasifier, is 264 kg CaO/BDt (per ton dry pulp produced), an increase with 9% compared with no gasifier. The result from the dynamic simulations showed that the peak in lime kiln load is 3% higher than the steady state with high tank levels and 4% with low tank levels. This effect is explained by several factors. It will take some time before the controlled weak wash flow is correct. Initially the flow will be too large, thus the white liquor flow will be larger and the required amount of CaO produced in the lime kiln will increase. The added sulphur to the white liquor consumes OH^- (reaction 1) so initially more OH^- is needed. This will require a higher load, the use of make-up chemicals or delaying the time for adding sulphur.

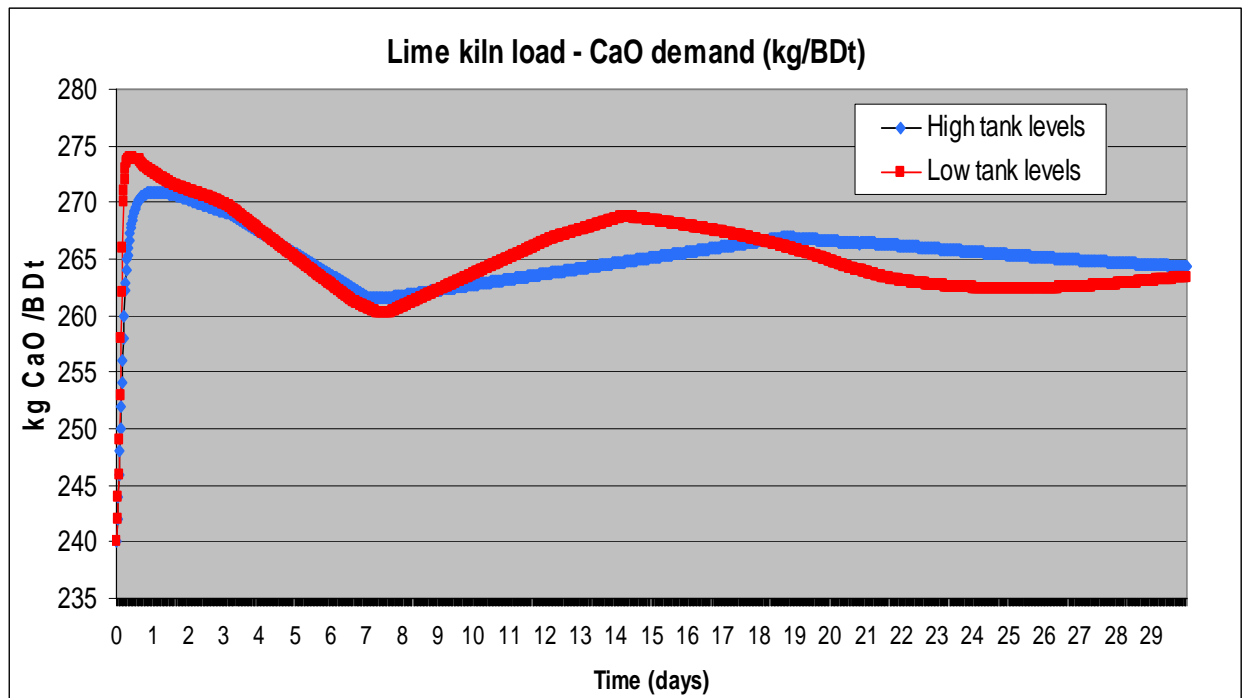


Figure 3. Lime kiln load when 25% of the black liquor is gasified

The load in the lime kiln may be close to its limit and the additional dynamic effect is important to take into the calculations when designing process equipment and calculating lime kiln fuel demand.

Extracting Cl and K from process is usually done by extracting ESP-dust from the recovery boiler. When sending black liquor to the gasifier, some of the Cl and K will bypass the recovery boiler. However, the Cl and K-levels in the mill liquors only showed a slight increase in the steady state results. This is explained by a higher concentration of Cl/K in the extracted ash. The long time trend in the dynamic simulations showed no significant increase in Cl/K levels and the build-up time was slow.

Since most pulp mills have sulphur in excess, the installation of a BLG-unit gives a great opportunity to purge some of the sulphur from the syngas to keep the sulphur level in the mill. The extraction rate of ESP-dust, which is the common way of purging excess sulphur, would then be lower and consequently decrease the need for adding make-up chemicals, since less alkali is lost with the dust. A lower extraction rate of ESP-dust does however result in higher levels of Cl and K. In the simulations, it was tested to extract 10% of the sulphur present in the syngas, corresponding to approximately 1 kg sulphur/BDt pulp produced and the results are presented in figure 4.

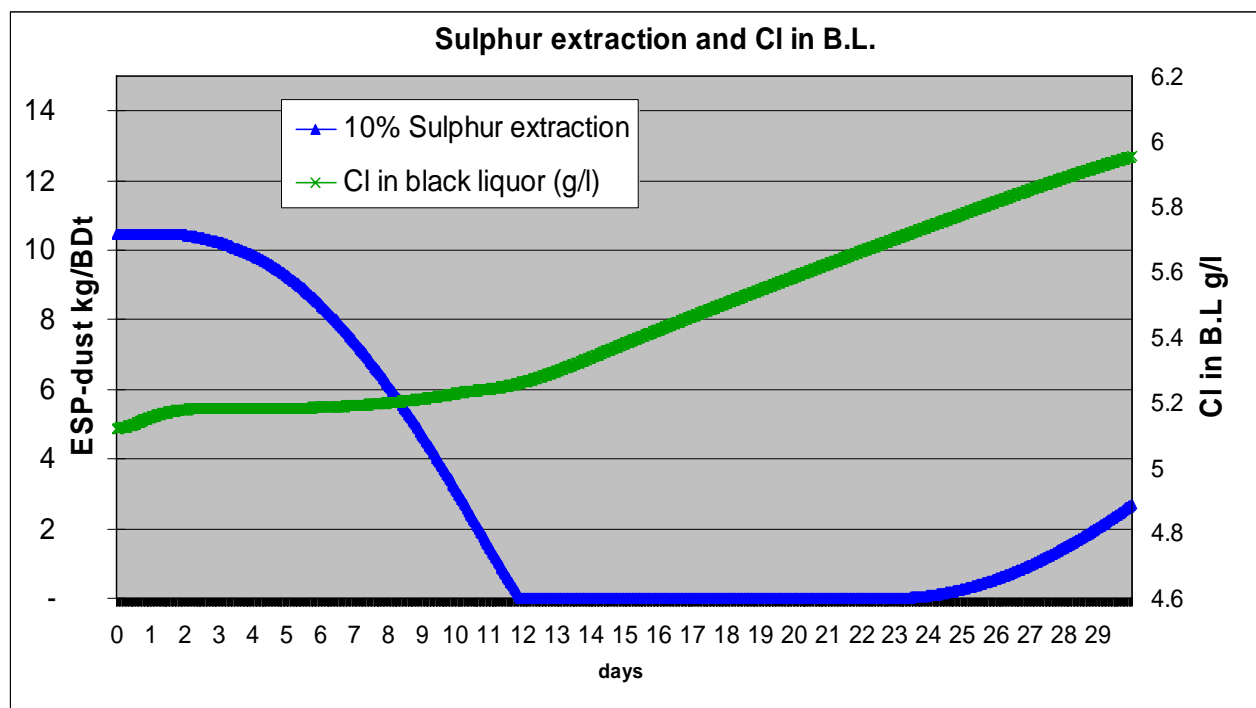


Figure 4. Cl in black liquor and ESP-dust extraction when extracting 10% of the sulphur in the syngas

The need for NaOH make-up decreased significantly, with approximately 75% during this period, which would mean a lower operating cost. However, after 30 days of operation the Cl and K-levels in both the white and black liquor was around 20% higher. High tank levels were used so with low tank levels the amount of Cl and K would be even higher. With these higher levels care must be taken to avoid corrosion problems in the recovery boiler after a longer operating period. This problem is isolated to when operating both a gasifier and recovery boiler. The gasifier is not as sensitive to Cl/K as the recovery boiler is and when only operating a gasifier, corrosion will not occur at these levels.

Conclusions

When sending 25% of the total black liquor to the gasifier, the lime kiln load will increase with 9% because of the green liquor composition. In addition, the dynamic effect at start-up will give a 3-4% extra load above the steady-state result, but most of this extra load should be possible to avoid with control measures and using make-up chemicals. The opposite effect is observed when shutting down the gasifier.

The Cl and K levels will increase in the white and black liquor. The increase is small, however, approximately 2%, when 25% of the black liquor is sent to the gasifier. This is a result of a higher concentration of Cl and K in the ESP dust extracted.

Black liquor gasification provides excellent opportunity for extracting sulphur from the syngas to reduce sulphur excess in the mill. This would decrease the purged ESP-dust and the need for make-up chemicals and thus improve the mill economy.

Decreasing the amount of ESP-dust will increase the Cl and K levels in the liquors. When a sulphur extraction rate from the syngas of 1 kg/BDt pulp was applied, the

simulations showed that after one month of operation the ESP-dust extraction rate and need for NaOH make-up decreased with approximately 75%. However, the Cl/K levels had increased with approximately 20% and there may be a risk of corrosion in the recovery boiler after longer operating periods.

Acknowledgements

The authors of this paper would like to thank the Swedish Energy Agency, Mistra, Smurfit Kappa Kraftliner AB, SCA Packaging AB, Södra Cell AB, Sveaskog, Chemrec AB and the County Administrative Board of Norrbotten for partial funding of this work through the BLG II research program [6].

References

1. Berglin, N., Ekblom, T., Lögdberg, S., “*Black liquor gasification with motor fuel production – BLGMF II*”, 2005
2. Larson, E., Consonni, S., Katofsky, R., “*A cost-benefit assessment of biomass gasification power generation in the pulp and paper industry*” – Princeton University, 2003
3. Dehlin, L., Berglin, N., et al. “*Bleached market kraft pulp mill – Reference and type mill*”, 2005
4. Carlsson, P., Marklund, M., Gebart, R., et al. “*Experimental investigation of an industrial scale black liquor gasifier. 1. The effect of reactor operation parameters on product gas composition*”, Fuel, In press, 2010
5. <http://www.chemrec.se>
6. Landälv, I., et al. *Populärvetenskaplig sammanfattning av BLGII-programmet 2007-2010*, 2010

Paper 19**Title:** DYNAMIC MODELLING APPROACH FOR DETECTING TURBIDITY IN DRINKING WATER

Petri Juntunen, Mika Liukkonen, Markku J. Lehtola, Yrjö Hiltunen
University of Eastern Finland, Finland

Keywords: Dynamic modelling, Water treatment, Water quality

The modelling of water treatment processes is of particular importance since water of low quality causes health-related and economic problems which have a considerable impact on people's daily lives. This not only increases the need for monitoring the process but also complicates the development of new methods for process diagnosis and monitoring. Nonetheless, the process is also considered challenging because of its complexity, dynamics and numerous contributory variables. It is essential to take process dynamics into account when data-driven applications are being developed, because successful modelling often requires an ability to adapt to changing conditions.

In water treatment there are observable cycles present which cause the process to be-have dynamically. The variation in water consumption is one of these, causing changes not only within a day but also within a week and even within a year. Year cycles can be distinguished even more clearly if surface water is treated, because the water temperature is observed to have some effects on the process. In addition to cyclic behaviour, other factors such as the addition of lime may cause sudden changes in turbidity.

Soft sensors which utilize process history can be used in replacing difficult and expensive measurements or in predicting the behaviour of a process in the future. They have proved to be efficient in process monitoring and control and therefore provide a potential means of estimating turbidity in drinking water, for example. In the paper, we will present a dynamic soft sensor based on multivariate regression for predicting turbidity of treated water. Because process data typically consist of a large number of variables, a group of them is selected adaptively before a dynamic predictive model is created, which is then used in estimating the degree of turbidity in the future.

Because of the dynamic character of the water treatment process, static process models may become inapplicable, which we will demonstrate using a case process. Our results show that the static model is not able to follow the changes in turbidity ($r = 0.4$), whereas the adaptive one can produce a reasonable estimate for it ($r = 0.75$). This dynamic behaviour is probably due to the cyclic behaviour of the process, which can also be seen in several process variables. In conclusion, dynamic models seem to provide a fruitful way of modelling the process.

DYNAMIC MODELLING APPROACH FOR DETECTING TURBIDITY IN DRINKING WATER

PETRI JUNTUNEN*, MIKA LIUKKONEN, MARKKU J. LEHTOLA, YRJÖ HILTUNEN

Department of Environmental Science, University of Eastern Finland, P.O. Box 1627, 70211 KUOPIO

*Corresponding author. E-mail: petri.juntunen@uef.fi, Tel.: +358 44 7185325

Abstract:

Turbidity is a common on-line measured quality parameter in water treatment plants for analyzing the general quality of purified water. In this paper, we introduce a dynamic method for predicting turbidity in drinking water. The goals of the work were to construct a real-time data-driven model to predict the turbidity in treated water and to find the most significant variables affecting turbidity. Our results show that the static model is not able to follow the changes in turbidity ($r = 0.40$), whereas the dynamic one can produce a reasonable estimate for it ($r = 0.75$).

Keywords: Water Treatment, Turbidity, Dynamic Modelling, Variable Selection, MLR.

1. INTRODUCTION

The modelling of water treatment processes is of particular importance since water of low quality causes health-related and economic problems which have a considerable impact on people's daily lives. This not only increases the need for monitoring the process but also complicates the development of new methods for process diagnosis and monitoring. Nonetheless, the process is also considered challenging because of its complexity, dynamics and numerous contributory variables. In real processes the correlation between simulated and experimental data has been poor, but expensive *in-situ* testing is needed (Baxter et al., 2001, Thomas, 1999, Maier & Dandy, 2000). It is essential to take process dynamics into account when data-driven applications are being developed, because successful modelling often requires an ability to adapt to changing conditions.

In water treatment there are observable cycles or episodic events present which cause the process to behave dynamically. The variation in water consumption is one of these, causing changes not only within a day but also within a week and even within a year. Year cycles can be distinguished even more clearly if surface water is treated, because the water temperature is observed to have some effects on the process (Bratby, 2006, Juntunen et al., 2010 a). In addition to cyclic behaviour, other factors such as rapid, previously unseen changes of lime feed or pH may cause sudden changes in turbidity (Juntunen et al., 2010 b).

There are many parameters which can be used to measure the quality of water. Turbidity is a common water quality parameter, the purpose of which is to measure impurities in water. In a physical sense, turbidity is the reduction of clarity in water due to the presence of suspended or colloidal particles and it is commonly used as an indicator for the

general condition of drinking water (WHO, 2006). Furthermore, turbidity has been used for many decades as an indicator of the efficiency of drinking water coagulation and filtration processes. For this reason, turbidity is an important operational parameter. High turbidity values refer to poor disinfection ability and possible fouling problems in distribution network, for example, so turbidity should be minimized (Letterman et al., 1999). However, turbidity is a quite sensible measurement and many variables and phenomena are influencing to the measurement. This makes turbidity challenging for modeling purposes.

Soft sensors which utilize process history can be used in replacing difficult and expensive measurements or in predicting the behaviour of a process in the future. They have proved to be efficient in process monitoring and control and therefore provide a potential means of estimating turbidity in drinking water, for example. However, the challenge for those models is to take the dynamic aspects into account (Valentin, 2001). On the other hand, it has been shown that adaptive applications can become imperative due to process dynamics (Liukkonen et al., 2011a-b). In the paper, we will present a dynamic soft sensor based on multivariate regression for predicting turbidity of treated water. Because process data typically consist of a large number of variables, a group of them is selected adaptively before a dynamic predictive model is created, which is then used in estimating the degree of turbidity in the future. The results of the dynamic model are compared to the traditional (static) MLR model.

2. MATERIALS AND METHODS

2.1 Process and data

Itkonniemi plant is one of the water treatment plants of Kuopio Waterworks. In the plant water is first bank filtrated. After filtration water is purified with chemical coagulation in a chemical purification process. After coagulation, the coagulated floc is separated by sedimentation or flotation followed by sand filtration. In final stage, water is disinfected by chlorination.

The experimental data were extracted from archived process measurements covering a period of 1017 days with a time step of 1 hour. The total number of variables used in the study is 64. 22 of the variables are hydrological and quality parameters of raw water, 38 of the variables are on-line measurements from the process and the rest of the variables are different time variables.

The process lags were defined semi-manually by calculating them based on the dimensions of unit operations and comparing the results to those from cross-correlation calculations. The embedded lags varied between 0-5 hours.

2.1 Linear regression

In multiple linear regression (Cohen, 1968), the purpose is to model the relationship between two or more explanatory variables and a response variable by fitting a linear equation to observed data samples. In principle, the MLR model with observations and variables is given in (1):

$$Y = e + a_0 + a_1 X_1 + a_2 X_2 + \dots + a_n X_n \quad (1)$$

where Y is the value for the response variable, X is the value of the predictor (explanatory) variable, $a_{0..n}$ equals the unknown coefficient to be estimated, and e signifies the uncontrolled factors and experimental errors of the model. The fitting works by minimizing the sum of the squares of the vertical deviations from each data point to the line that fits best for the observed data, which is also called least squares fitting.

2.2 Variable selection

The sequential forward selection method (Whitney, 1971), was used for the selection of variables in this case. In the approach, the variables are progressively included to larger and larger subsets so that the prediction performance for residual aluminium is maximized. To select p variables from the set of P variables: (1) Search for the variable that gives the best value for selected criterion. (2) Search for the variable that gives the best value with the variable(s) selected in stage 1. (3) Repeat stage 2 until p variables are selected.

2.3 Dynamic Soft Sensor

We have developed a dynamic approach to predict the turbidity of treated water, which can be utilized in an online

application. Because process data typically consist of a large number of variables, a group of them is selected adaptively before a dynamic predictive model is created. The method uses N previous values of turbidity with corresponding process data and p adaptively selected variables to create a p -dimensional regression model that can be used to predict the turbidity in the future. The regression can be used in creating the model. The algorithm consists of the following stages:

1. Selecting p variables using $1 \dots N$ samples using turbidity of treated water concentration as the output.
2. Training with $1 \dots N$ samples to obtain a model for the turbidity of treated water concentration using p selected variables, and prediction of the sample $N+1$ using p selected variables and the model.
3. Training with $2 \dots N+1$ samples to obtain an updated model for turbidity of treated water using p selected variables, and prediction of the sample $N+2$ using p selected variables and the model.
4. Repeat stages 2 to 3 until all samples within the subset of N rows have been predicted.
5. Go to stage 1 and select the next subset of variables using $N+1 \dots 2N$ samples, and repeat the loop until all samples have been predicted.

In this case, the value of p was 5 and the value of N was 24.

All data pre-processing and modelling was carried out using Matlab software, version R2000b (MathWorks, inc.).

3. RESULTS

In the modeling and variable selection phase the process and laboratory data were used to produce dynamic predictive model for turbidity.

The average correlation between the observed values of turbidity and those estimated by the dynamic model was 0.75 whereas using a static model we achieved a correlation of 0.40. With the dynamic model, the correlation varied between 0.40-0.91. A sample of the trends of the results is shown in Fig. 1.

The selected variables for the static model and the most frequently selected ones for the dynamic models are shown in table 1. The features of the most selected variables of the dynamic model are shown in Fig. 2.

Table 1. The most frequently selected variables during the modelling process.

Selection Round	Static Model		Dynamic Model
1.	Solvent Feed	Water	Filter Wash flow
2.	Filter Wash Flow		Line 600 1, Filtration Pressure
3.	Line 700, Filtration Pressure	700, Level in Sedimentation	Line 500, Level in Sedimentation
4.	Well 4, Surface		Line 600 6, Filtration Pressure
5.	Post lime feed		pH after Lime Feed

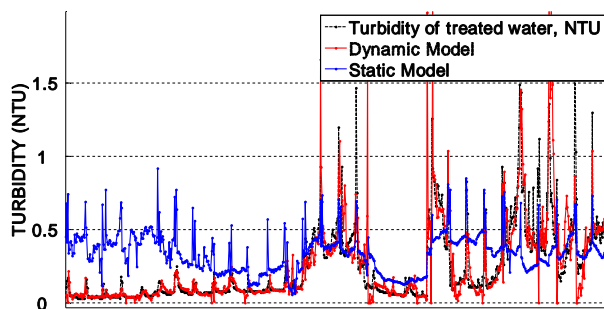


Fig.1. A sample period (approx. 1 month) of the modelled and measured turbidity.

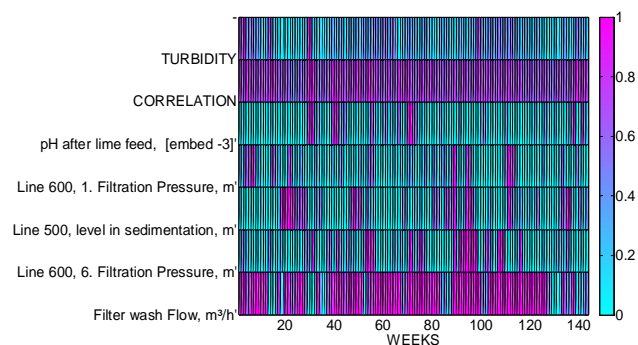


Fig. 2. The probability for being selected among the 5 most selected variables, correlation between the model and values of measured turbidity within a time window of one week.

4. DISCUSSION

Our results show that the static model is not able to follow the changes in turbidity ($r = 0.40$), whereas the adaptive one can produce a reasonable estimate for it ($r = 0.75$). In addition, the selected variables between the static and dynamic models vary remarkably. In conclusion, this study shows that the models produced for processes which have cyclic and/or episodic behaviour should have dynamic components in the models.

However, some periods with bad correlation diminishes the average value of the dynamic model. In those bad periods the correlation could reach as low as 0.4, whereas normally the correlation was between 0.7-0.9. Most of those bad periods seem to be situations in which turbidity has been low. One explanation for this phenomenon would be the limited accuracy of the turbidity meter when turbidity is < 0.1 NTU.

The soft sensor approach has two clear benefits: first, the selected variables represent the mostly affecting variables to the process personnel at each moment, which can help to increase the knowledge of the process and the potential problems. For example, in Fig. 3 we can see a 3-week episode around week 30 with exceptionally high level of turbidity. In the same period we can see that “pH after lime feed” variable has a strong probability to be selected. Further analysis showed that the pH level was exceptionally high during that period, which implicates an un-optimal pH control during that time.

Second, the soft sensor can predict the future turbidity in the process, which provides several potential applications such as optimize the running of the process. Furthermore, the soft sensor could be used as a tool for on-line water quality monitoring. The benefits of the applications would e.g. to get more knowledge of short-term changes online, to feed-forward control the post-processes of water treatment such as disinfection, or to optimize the sampling of water.

Furthermore, some phenomena of the water treatment processes usually have some non-linear elements (Maier et al., 2004). In this reason, experiments with non-linear regression methods are considerable to increase the performance of the dynamic models in the future.

5. CONCLUSIONS

In conclusion, dynamic models seem to provide a fruitful way of modelling the process. Because of the dynamic character of the water treatment process, static process models may become inapplicable, which is demonstrated by analyzing the case process. The results are promising considering the wider use of the dynamic data-driven variable selection and modelling in water treatment processes, and the potential of the method is large.

5. ACKNOWLEDGEMENTS

The research was supported by Maa- ja Vesitekniiikan tuki Ry, and the research material was produced in the POLARIS project financed by the Finnish Funding Agency for Technology and Innovation (Tekes), which the authors thank for its financial support.

REFERENCES

- Baxter, C.W., Stanley, S.J., Zhang, Q., 1999. Development of a fullscale artificial neural network model for the removal of natural organic matter by enhanced coagulation. *J Water SRT-Aqua* 48 (4), 129–136.
- Bratby, J.(2006) Coagulation and flocculation in water and wastewater treatment. IWA publishing. Cornwall
- Cohen, J., (1968). Multiple Regression as a General Data-Analytic System. *Psychological Bulletin*, 70:426-443.
- Juntunen, P. Liukkonen, M. Pelo, M. Lehtola, M. and Hiltunen, Y. (2010a) Modeling of Residual Aluminium. In Šnorek, M., Buk, Z., Čepel, M., Drchal, J. (Editors), Proceedings of the 7th EUROSIM Congress on Modelling and Simulation Vol.2: Full Papers (CD). Czech Technical University in Prague. ISBN 978-80-01-04589-3
- Juntunen, P. Liukkonen, M. Pelo, M. Lehtola, M. and Hiltunen, Y. (2010b) Modeling of Turbidity in Water Treatment Processes. In Juuso E. (editor), Proceedings of the 51st SIMS Congress on Modelling and Simulation. Finnish society of automation.
- Letterman, R. D, editor. (1999). Water Quality & Treatment, Handbook of Community Water Supplies. AWWA.
- Liukkonen, M., Hälikkä, E., Hiltunen, T., Hiltunen Y., (2011a). Adaptive Soft Sensor for Fluidized Bed Quality: Applications to Combustion of Biomass. *Fuel Processing Technology* (in press).
- Liukkonen, M., Hälikkä, E., Hiltunen, T., Hiltunen Y., (2011b). Dynamic Soft Sensors for NO_x Emissions in a Circulating Fluidized Bed Boiler. In: Desideri U., Yan J. (eds.), *Energy solutions for a sustainable world - Proceedings of the Third International Conference on Applied Energy*, pp. 1607-1620.
- Maier, H. R., & Dandy, G.C., (2000). Neural networks for the prediction and forecasting of water resource variables: a review of modelling issues and applications. *Environmental modeling and software*. Vol. 19, No. 5, pp. 485 -494.
- Maier, H. R. Morgan, N., Chow, C.W.K. (2004). Use of artificial neural networks for predicting optimal alum doses and optimal water quality parameters. *Environmental modeling and software*. Vol. 15, No. 5, pp. 105-124.
- Mathworks. *Using Matlab version 5*. (1998). The Mathworks Inc., Natick.
- Thomas, D. N., Judd, S. J., Fawcett, N. (1999). Flocculation modeling: A Review. *Water Research*. Vol. 33, No 7 pp. 1579 – 1579.
- Valentin, V., Denoeux, T. (2001). A Neural based Software Sensor for Coagulation Control in a Water Treatment Plant. *Intelligent Data Analysis*. 5:23-39.
- Whitney. A.W., (1971) A Direct Method of Nonparametric Measurement Selection. *IEEE Transactions on Computers*, C-20:1100-1103.
- World Health Organization. (2006) Guidelines for drinking-water quality [http://www.who.int/water_sanitation_health/dwq/gdwq3rev/en/] Vol. 1, Recommendations. – 3rd ed.

Paper 22

Title: DEVELOPING A COMPUTER PROGRAM FOR THE ESTIMATION OF THE INCOMING SUN BEAM BY DEFINING A SPECIAL COEFFICIENT FACTOR FOR DENİZLİ/TURKEY

Engin Çetin
Pamukkale University, Turkey

Keywords: Pyronometer, Visual C#.Net, Solar Radiation, Solar Estimation Methods

Hottel has presented in 1976 a method for estimating the solar beam radiation transmitted through clear atmospheres which takes into account zenith angle and altitude for a standard atmosphere with respect to four climate types. In this work a computer program is developed in Visual C#.Net using Hottel's estimation method. The developed computer program will estimate the incoming instantaneous solar beam radiation with respect to a given time period, incline, longitude and climate type of the region. On the other side, a pyronometer has been replaced to the Clean Energy Research Center at the Pamukkale University to measure the incoming sun beam for Denizli/Turkey. These measurements have been stored every hour into a database. Afterwards, using the developed estimation program the incoming solar beam to Denizli is calculated for defined time periods and stored to another database. Afterwards a special coefficient factor is calculated only for Denizli for a better estimation of the incoming sun beam. This is done by taking the correlation and mean value of both stored results for the same given time interval. The calculated coefficient factor can be used in the developed estimation program by multiplying the end results. This will give a more realistic solution of the estimated incoming sun beam for Denizli.

Developing a Computer Program for the Estimation of the Incoming Sun Beam by Defining a Special Coefficient for Denizli/Turkey

G. Uckan, H. K. Ozturk, E. Cetin

Energy Research and Application Center, Pamukkale University
Denizli-Turkey, phone: +90 258 296 3203, e-mail: guckan@pau.edu.tr, hkozturk@pau.edu.tr, engincetin@pau.edu.tr,

Introduction

Hottel has presented in 1976 a method for estimating the solar beam radiation transmitted through clear atmospheres which takes into account zenith angle and altitude for a standard atmosphere with respect to four climate types. In this work a computer program is developed in Visual C#.Net using Hottel's estimation method. The developed computer program will estimate the incoming instantaneous solar beam radiation with respect to a given time period, incline, longitude and climate type of the region. On the other side, a pyronometer has been replaced to the Clean Energy Research Center at the Pamukkale University to measure the incoming sun beam for Denizli/Turkey. These measurements have been stored every hour into a database. Afterwards, using the developed estimation program the incoming solar beam to Denizli is calculated for defined time periods and stored to another database. Afterwards a special coefficient factor is calculated only for Denizli for a better estimation of the incoming sun beam. This is done by taking the correlation and mean value of both stored results for the same given time interval. The calculated coefficient factor can be used in the developed estimation program by multiplying the end results. This will give a more realistic solution of the estimated incoming sun beam for Denizli.

Using Hottels Estimation Method for Calculating the Incoming Sun Beam to Denizli

Hottel has developed a estimation method [1] in 1976 for estimating the solar beam radiation transmitted through clear atmospheres which takes into account zenith angle and altitude for a standard atmosphere for four different climate types [4]. The instantaneous solar beam can be calculated by using Eq.1.

$$G_{cnb} = G_{on} * \tau_b, \quad (1)$$

Where G_{cnb} represents the solar beam which is coming to the normal at clear sky. " G_{on} " denotes the solar constant and will be taken as 1367 kWh/m^2 . The needed " τ_b " parameter will be calculated by using Eq.2.

$$\tau_b = a_0 + a_1 \exp(-k/\cos\theta_z). \quad (2)$$

The parameters a_0 , a_1 and k can easily be calculated from the Eq. 3-5 given by Hottel.

$$a_0 = 0.4237 - 0.00821 (6-A)^2, \quad (3)$$

$$a_1 = 0.5055 + 0.00595 (6.5-A)^2, \quad (4)$$

$$k = 0.2711 + 0.01858 (2.5-A)^2. \quad (5)$$

The parameter A represents the altitude of the area where the measurement will take place. The zenith angle " θ_z " can be calculated from the Equation 6 given below.

$$\cos\theta_z = \cos\delta \cos\Phi \cos\omega + \sin\delta \sin\Phi, \quad (6)$$

here " δ " represents the declination angle which will be calculated from Eq. 7.

$$\delta = 23,45 * \sin(360 * (284 + n) / 365). \quad (7)$$

As seen in Eq. 7, " n " is the day number. For the 1st of January n will be taken "1". The latitude angle Φ will be given to the system through a form, which was developed in C#.Net. The latitude value has to be given to the program, from the user side. In Eq. 6, " ω " represents the angle of the time period. The time period angle can be found from Eq. 8.

$$\omega = (GZ - 12) * 150, \quad (8)$$

" GZ " stands for the solar time and will be calculated from Eq. 9.

$$GZ = YSZ + [4(Ls - Lloc)] / 60 + E / 60 + DET. \quad (9)$$

In Eq. 9, " YSZ " represents the local time, " $Lioc$ " represents the longitude of the measurement place, and " Lst " represents the local standard time constant which will be taken 30° for Turkey. The parameter " DET " is the energy saving correction factor and will be taken "0" from end of March until end of November.

Developing the Estimation Program Using C#.Net

In this work, an estimation program is developed using the equations and parameters developed by Hottel. These estimation programs are also useful in developing simulation programs for real systems [5]. The estimation program is realized using Visual C#.Net. This program

will perform the estimation of the incoming instantaneous solar beam radiation according to the given time period, latitude, longitude and four different climate types selected according to the region. Using forms which have been developed in C#. Net, parameters like; Hour, day number inside the year, date in days-months, latitude and longitude of the place where the measurement will take place are given to the program. Pressing the related button the program will run and estimation of the coming sun beam will be calculated.

Flowchart of the Solar Estimation Program.

One of the first steps to calculate the coming solar beam radiation is to calculate the transmittance of the atmosphere. For this the needed steps are given in Fig.1.

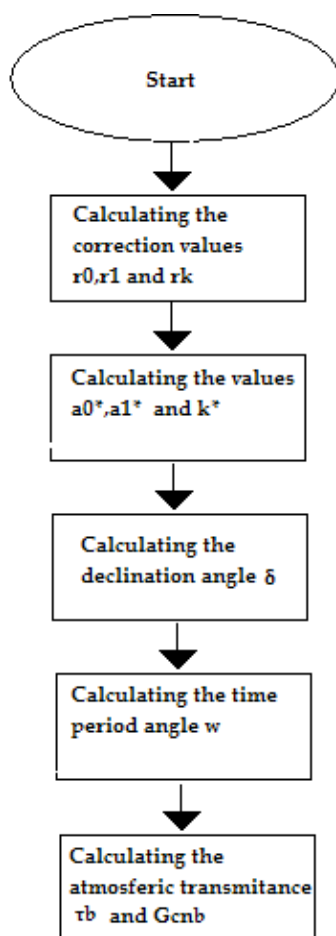


Fig.1. Flowchart of the program which will estimate the transmittance of the atmosphere according to a given time period.

The developed estimation program will run and the transmittance of the atmosphere will be calculated. After processing these five main steps seen in Fig. 1. The estimation of the coming solar beam can be calculated easily using Eq.1.

Developing the Forms and Writing the C#.Net Codes

The forms which are developed using C#.Net are one of the most important part of the work. These forms will be the main visual part of the estimation program. According to the parameters which will be given by the user using textboxes, the program will start to run by clicking one of the buttons seen in Fig.2. This process will give new output variables like; Zenith angle, atmospheric transmittance or the estimation of the solar beam radiation seen in Fig.3

Fig.2. An operator interface screen for the developed software.

After pressing one of the buttons the background codes written in C#.Net will start to run and the output values will display on the form given in Fig.3. The climate type which is written into the textbox by the user, will be used inside the background codes of the form to perform the according climate type parameters. These parameter values are called as the climate correction factors and are presented by Hottel [1] as seen in Table.1.

Table 1. Hottel's presented climate correction table for four different climate types.

Climate Type	r0	r1	r2
Tropical	0.95	0.98	1.02
Midlatitude summer	0.97	0.99	1.02
Subarctic summer	0.99	0.99	1.01
Midlatitude winter	1.03	1.01	1.00

Fig. 3 shows the display output of the from given in Fig. 2, after the button is clicked for starting the calculation process.

Fig.3. Display of the output values after pressing the buttons.

Again seen in Fig. 3, label objects are displaying the output results on the form under Analyze Data. These results will be the declination angle, zenith angle, atmospheric transmittance and the estimated solar radiation beam.

Measurements Done for Denizli Using a Pyranometer

The measurement of the incoming solar beam radiation to Denizli is done using a pyranometer. This equipment is replaced at the Clean Energy House of the Pamukkale University. The measurements have been done to take an overview of the coming solar beam radiation to Denizli in real time. These results will be used to compare with the estimated solar radiation results [6] calculated using the developed estimation program. This will be useful to define a special coefficient for Denizli. The coefficient named as the “correction factor” will be used for a closer estimation. All measurements are taken periodically and stored to a database. A measurement example taken from the Celan Energy House is seen in Fig.4. The measurement was made for a sunny day, for two different types of solar panels. One form a stable solar panel which was is fixed with a stable angel due to the horizon and the other one form a rotating panel.

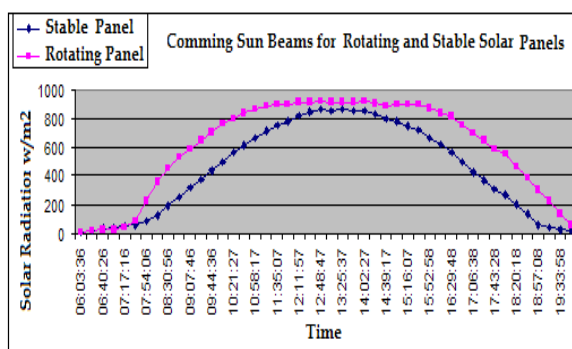


Fig.4. Solar radiation measurements using pyranometer for moving and stable solar panels.

The purple line represents the data taken from the rotating solar panel where the blue line represents the measurements taken from the stable solar panel.

Definig the Correction Factor

As described before, the correction factor will be used to get a closer estimation output from the developed estimation program. This is done by multiplying the estimated value with the correction factor seen in Eq.10.

$$\text{Closer Est. Output} = (\text{Est. Program Output}) * (\text{Correction. Factor}) \quad (10)$$

Dividing the measured result with the estimated program output ; The correction factor will be realized as seen in Eq.11.

$$\text{Correction. Factor} = (\text{Measured Pyranometer Result}) / (\text{Est. Program Output}) \quad (11)$$

This correction factor will be developed taking the mean value of the measured results from the pyranometer and divide it with the mean value of the estimated program results. In this way for each month a different correction factor can be defined. The daily results of the estimation program for February are given in Fig.5. After using the correction factor we get a closer estimated result for February seen in Fig.6.

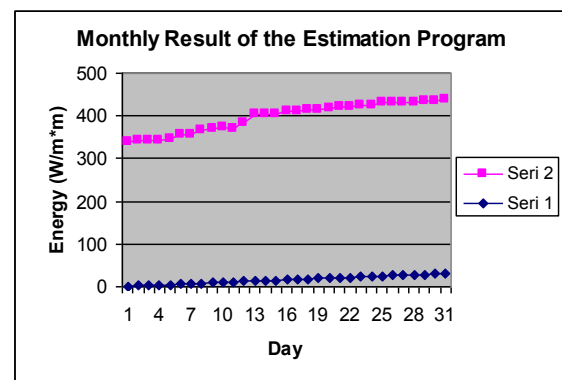


Fig.5. Daily results taken from the estimation program for February

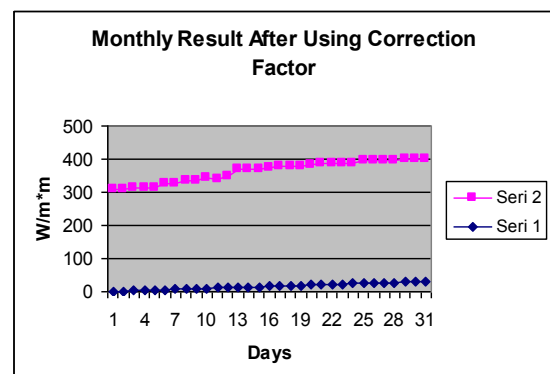


Fig.6. Daily results February which are taken from the estimation program after using the correction factor.

Conclusions

Hottel's estimation method is useful for places where measurement can not be made because of not suitable conditions. Hottel's estimation method gives close results to real measurements, but it can still be improved by defining correction factors for special cases or places. Therefore a special coefficient renamed as correction factor is defined for every month. In this work the correction factor is developed for a closer estimation result of the coming solar beam to Denizli. These measurements are done for February 2011 using a pyranometer replaced at the Clean Energy House at the Pamukkale University. They are stored to a database file. Afterwards the mean values of the daily stored results taken from the pyranometer are divided with the mean value of the daily results taken from the developed estimation program. The result of this division will give the correction factor of the related month. Different correction factors can be defined for different months to get a better estimation result which is closer to the real measurements done using a pyranometer.

Acknowledgement

The authors gratefully acknowledge the support provided by the Council of Scientific Research Projects of PAU.

References

1. **Hottel HC.** A Simple Model for Estimating the Transmittance of Direct Solar Radiation Through Clear Atmosphere // *Solar Energy*. – Elsevier, 1976. – No. 18 – P.129-134.
2. **Cetin E., Yilanci A., Oner Y., Colak M., Kasikci I., Ozturk HK.** Electrical Analysis of a Hybrid Photovoltaic-Hydrogen/Fuel Cell Energy System in Denizli, Turkey // *Energy&Buildings*. – Elsevier, 2009. – No. 41. – P.975–981.
3. **Vasarevicius D., Martavicius R.** Solar Irradiance Model for Solar Electric Panels and Solar Thermal Collectors in Lithuania // *Electronics and Electrical Engineering*. – Kaunas: Technologija, 2011. – No. 2(108). – P.3–6.
4. **Duffie J. A., William A., Beckman W. A.** *Solar Engineering of Thermal Processes*. - A Willey-Interscience Publication, 1991. - 944 p.
5. **CIRAS.** Computer Simulation and Decision Making. - CIRAS News. – 2001 - No. 32(2) – P.1-4.
6. **Tasdemiroglu E., Sever R.** Estimation of Total Solar Radiation from Bright Sunshine Hours in Turkey // *Energy*. – Elsevier, 1989. – No. 14(12) - P.827-830.
7. **Fernández-García A., Zarza E., Valenzuela L., Pérez M.** Parabolic-Trough Solar Collectors and Their Applications // *Renewable and Sustainable Energy Reviews*. – Elsevier, 2010. – No. 14(7) – P.1695-1721.
8. **Kalogirou S. A.** *Solar Thermal Collectors and Applications*. // *Progress in Energy and Combustion Science*. – Elsevier, 2004. – No. 30(3) – P.231-295.

Paper 24

Title: OMSketch — Graphical Sketching in the OpenModelica Interactive Book, OMNotebook

Mohsen Torabzadeh-Tari, Jhansi Reddy Remala, Peter Fritzson
Linköping university, Sweden

Keywords: OMSketch, DrControl, DrModelica, modeling, simulation, OMNotebook, teaching, interactive

In this paper we present a new functionality for graphical sketching in the OpenModelica interactive book, OMNotebook, which is part of the OpenModelica environment and used mainly for teaching. The new functionality is called OMSketch and allows the user to edit and draw shapes and figures within the electronic book. This allows teachers to prepare more pedagogic course material and students to make graphical notes in addition to the current textual ones.

The active electronic notebook, OMNotebook, is already used as basis for two course materials, DrModelica and DrControl for teaching the Modelica languages and control theory respectively. Electronic notebooks can be an alternative or complement compared to the traditional teaching method with lecturing and reading textbooks. Experience shows that using such an electronic book will lead to more engagement from the students. OMNotebook can contain interactive technical computations and text, as well as graphics. Hence it is a suitable tool for teaching, experimentation, simulation, scripting, model documentation, storage, etc.

OMSketch — Graphical Sketching in the OpenModelica Interactive Book, OMNotebook

Mohsen Torabzadeh-Tari, Jhansi Reddy Remala, Martin Sjölund, Adrian Pop, Peter Fritzson

PELAB – Programming Environment Lab, Dept. Computer Science
 Linköping University, SE-581 83 Linköping, Sweden
mohsen.torabzadeh-tari@liu.se {jhare950}@student.liu.se
 {martin.sjoland, adrian.pop, peter.fritzson}@liu.se

Abstract

In this paper we present a new functionality for graphical sketching in the OpenModelica interactive book, OMNotebook, which is part of the OpenModelica environment and used mainly for teaching. The new functionality is called OMSketch and allows the user to edit and draw shapes and figures within the electronic book. This allows teachers to prepare more pedagogic course material and students to make graphical notes in addition to the current textual ones.

The active electronic notebook, OMNotebook, is already used as basis for two course materials, DrModelica and DrControl for teaching the Modelica languages and control theory respectively. Electronic notebooks can be an alternative or complement compared to the traditional teaching method with lecturing and reading textbooks. Experience shows that using such an electronic book will lead to more engagement from the students. OMNotebook can contain interactive technical computations and text, as well as graphics. Hence it is a suitable tool for teaching, experimentation, simulation, scripting, model documentation, storage, etc.

Keywords: OMSketch, DrControl, DrModelica, modeling, simulation, OMNotebook, teaching, interactive

1 Interactive OMNotebook

In this paper we introduce a research project for making the modern object-oriented equation-based modeling and simulation environment OpenModelica more user friendly and effective with graphical sketching ability, **Error! Reference source not found..**

The electronic OMNotebook, part of the OpenModelica platform, offers a common platform for learning programming languages as well as given the opportunity to experiment with physical phenomena.

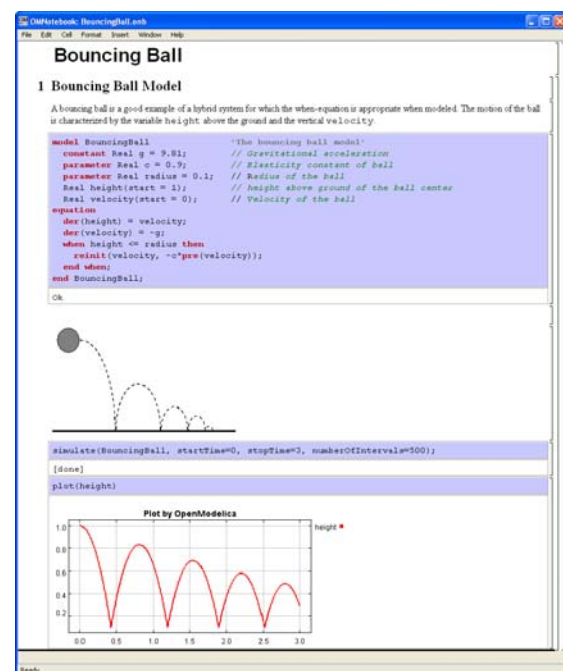


Figure 1. Bouncing ball example with movement animation in OMNotebook

This kind of interactive courses based on electronic books allow experimentation and dynamic simulation as well as execution of computer programs. The OMNotebook can contain program code **Error! Reference source not found.**, text, links, pictures, video, virtual and scientific visualizations and with introduction of OMSketch plug-in drawing and sketching possibilities in the same tool. OMNotebook is an active electronic book that makes it is possible to integrating applied sciences in physics, human biology, mathematics and computer science.

1.1 Qt Platform

Qt from Trolltech, [4], is a cross platform application providing a framework for developing large scale web-base, mobile and stand alone applications. Qt also provides SDK (Software Development Kit) for developing

user defined graphical applications, which are provided in both C++ and Java.

One main reason for choosing Qt for developing the sketch plug-in was that the interactive book, OMNotebook was already implemented using Qt which is well suited for GUI applications. Another reason for justifying this choice is that Qt is distributed under open source license conditions. Qt SDK version 4.7 was used to develop OMSketch application in this work.

1.2 Structure of the Paper

Section 2 is presenting an overall structure of OMSketch and Section 3 the used Qt constructs and classes. In Section 4 a detailed OMSketch structure is explained with implementation details. Finally some concluding words and future work are presented in the Section 5 and 6 respectively.

2 Graphical Editor

OMSketch is an environment for graphical editing, providing simple and complex shapes that can be drawn according to user choice. The user can also export the drawn shapes as standalone files (in png or jpg format) making it even more user friendly.

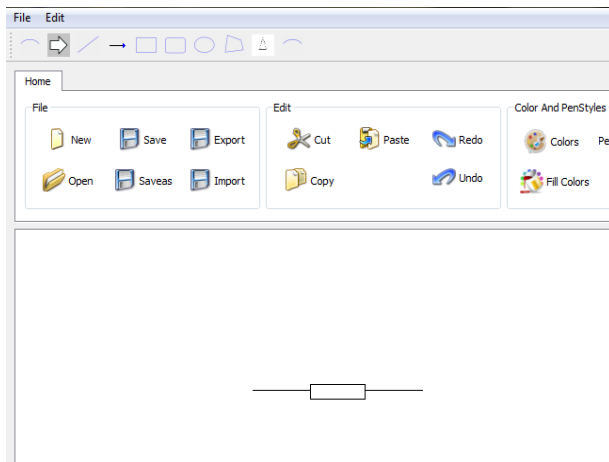


Figure 1. Illustrating usage of OMSketch when drawing a resistor like shape

In Figure 1 the OMSketch plug-in is used for drawing a resistor like component. In the same figure also the File, Edit and Color and Pen Styles tabs are shown that will be explained more in detail in the coming sections.

2.1 OMSketch Structure

OMSketch editor provides different shapes, colors and styles that can be used to draw both simple and complex shapes. The drawn shapes can also be exported or

embedded into OMNotebook. In Figure 2 the different developed classes are shown in a UML diagram.

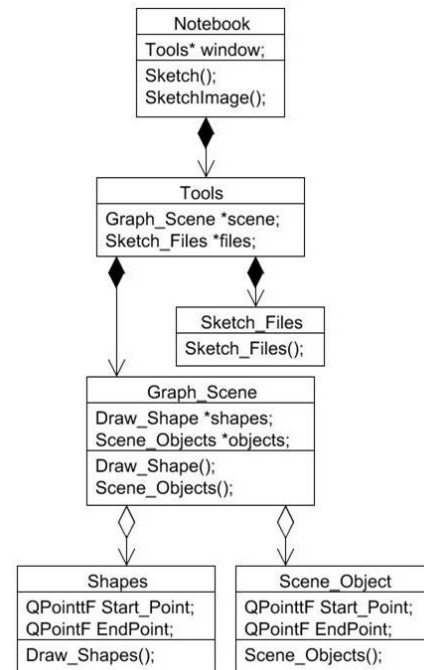


Figure 2. UML diagram for OMSketch classes

As shown in Figure 2 the OMSketch is invoked from OMNotebook with the starting class `Tools`. The underlying class `Graph_Scene` provides functions for drawing shapes and managing them, with the `SceneObjects` containing relevant functions for searching in the shapes in a scene. The `SketchFiles` class provides functions to read and write corresponding OMSketch files.

2.2 Shape Management

Every object in the `Shapes` class has the same method and variables for treating the standard shapes. For irregular shapes some more methods and variables are added. The standard shapes are `Draw_Line`, `Draw_Rectangle`, `Draw_RoundRect`, and `Draw_Ellipse`. All these classes inherit the Qt class `QGraphicsPathItem` and also contain get and set methods, like `GetStartPnt`, `GetEndPoint`, `setStartPoint`, or `setEndPoint`. The setting classes can for example be used for choosing pen color, width or style.

2.3 Tools class

The `Tools` class is the main class of OMSketch and responsible for the layout, shown in Figure 3. This class inherits `QMainWindow` class of Qt, providing methods for managing the contents of a `Scene` object. It

also provides methods for managing Menus, TabWidgets, DialogBoxes, and the drawing area.

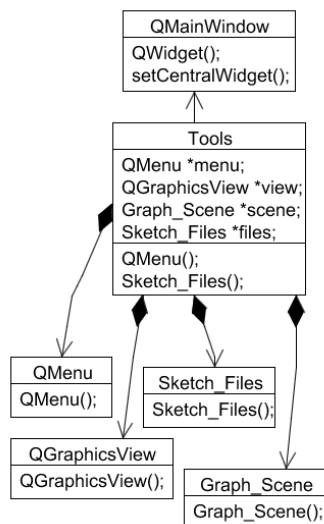


Figure 3. UML diagram of Tools class

The file management part is responsible for creating temporary files for importing and exporting shapes to and from OMNotebook. It is also providing the ability to export shapes as a standalone file, for example in png or jpg format.

2.3.1 GraphScene

The GraphScene class is the main drawing class of OMSketch application, also shown in Figure 4.

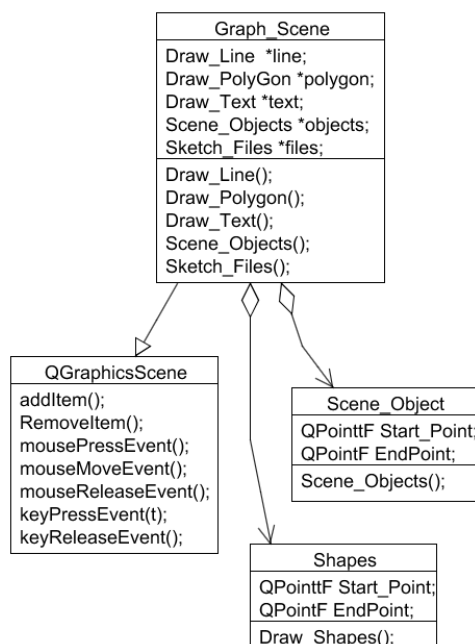


Figure 4. UML diagram of GraphScene

This class inherits `QGraphicsScene` class from Qt and is responsible for user interactions like MouseEvents, or keyBoardEvents and also for drawing and managing the shapes.

2.3.2 SceneObject

The `SceneObjects` class is a type of template class that holds information about the shape in a scene, like a unique id, coordinates or styles. The main purpose of this class is for quick searching of shapes in a scene, writing the shapes to the files, reading the shapes from the file.

2.3.3 Shapes

Every shape is an object of its respective class and contain the methods set and get for handling attributes such as coordinates, pen styles, brush styles. All shapes (except the text class) are inheriting the Qt class `QGraphicsPathItem` class. The text shape inherits `QGraphicsTextItem` class.

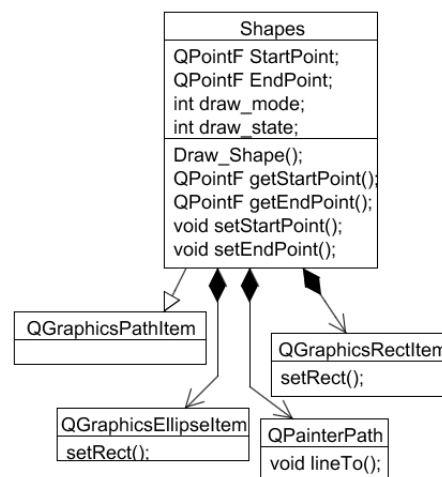


Figure 5. UML diagram of Shape class

2.3.4 SketchFiles

The `SketchFiles` class manages reading and writing of shapes to a file. This class contains methods to parse the shape information and provide the relevant information to save or open a file.

3 Used Qt API's and classes

In the coming sections different Qt classes are mentioned that has been used in OMSketch.

3.1 QMainWindow

The `Tools` class of OMSketch inherits `QMainWindow` class which provides methods for managing window

frame work. The layout can be enriched with components like menu bars, toolbars and/or status bars.

3.2 QGraphicsScene

This is the main class responsible for the actual drawing. It is a container class with methods for drawing shapes, mouse and keyboard events.

3.3 QGraphicsItem

This is the base class for all graphical items (shapes) in Qt. The `QGraphicsScene` class uses `QGraphicsItem` for adding shapes into the scene. Every item has methods for user interactions like mouse events and/or rotations and transformation.

3.4 QGraphicsView

`QGraphicsView` provides a widget to display the `QGraphicsScene`.

3.5 QMenu

`QMenu` class provides methods for adding items to the menu lists. `QMenuBar` is the most common type of `QMenu` providing drop down.

3.6 QAction

`QAction` provide methods for triggering a specific action when a menu item is clicked on.

3.7 QPainter

`QPainter` is the base class for low leveling painting on the widgets.

3.8 QFileDialogBox

The `QFileDialogBox` class provides a widget when the user wants for example to save or open a file.

3.9 QPen and QBrush

`QPen` and `QBrush` provide pen and brushes for drawing graphical shapes.

4 OMSketch Layout

The layout of OMSketch managed by `Tools` class consists of menu bar, tab widget and drawing area, see Figure 6.

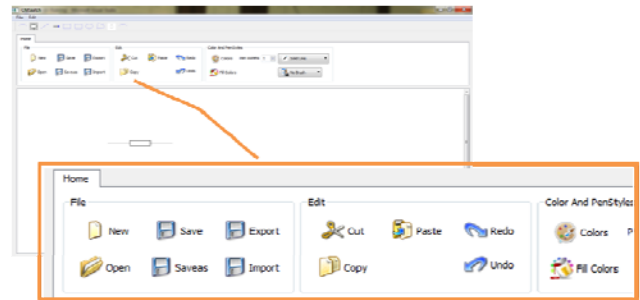


Figure 6. OMSketch Home tab zoomed

Each tab is formatted into panels and each plane consists of different tasks to select. The drawing area is auto adjusted according to the window size. Scroll bar are added automatically as the drawing area size increases. The main layout is managed by `QMainWindow` class that has methods to organize the menus, widgets. The flow diagram can be shown as follows:

4.1 Menus

In Qt the menu items are instances of `QMenu` class. The code snippet of initializing of these classes can be shown as follows:

```
fileMenu =
    menuBar()-> addMenu(tr("&File"));
editMenu =
    menuBar()-> addMenu(tr("&Edit"));
toolMenu =
    menuBar()-> addMenu(tr("&Tools"));
```

In the above code `fileMenu` is an object of `QMenu`, and `menuBar()` is a method of `QMainWindow` class to which a menu item is added to. The method returns the menu item, which is passed into `fileMenu` object. Similarly the `editMenu` and `toolMenu` objects are instantiated

4.2 Tab Widget

Tab widgets are specialized for designing widgets and graphical items by using the available space more efficiently. The first tab is titled as "Home" tab which is divided into File, Edit, and Styles. The Home tab is implemented using `QGroupBox`.

The Styles is using four Qt widgets, `QPushButton`, `QLabel`, `QComboBox` and `QSpinBox`. `QLabel` is used for labeling pen widths. For selecting pen widths `QSpinBox` is used. `QComboBox` is used for choosing the pen and filling styles.

The following code illustrates the implementation of tab widgets in OMSketch application.

```
tabWidget = new QTabWidget();
tab_widget = new QWidget();
tab_layout = new QHBoxLayout();
```

```
tab_widget -> setLayout(tab_layout);
tabWidget -> addTab(tab_widget, "Home");
```

The first line of the code initializes the tab widget object. In the second line a `QWidget` object is initialized and a `QHBoxLayout` is added to it. Finally the `addTab` method is used for adding the Home tab.

4.3 Drawing Area

The drawing area is an instance of `QGraphicsView` widget, which is added to a horizontal widget. The horizontal widget is then added to a `QWidget` which is in its turn added to `QMainWindow`.

The below code shows the implementation of drawing area.

```
view = new QGraphicsView(scene);
scene -> setSceneRect(0,0,1200,800);
hlayout -> addWidget(view);
main_widget -> setLayout(hlayout);
setCentralWidget(main_widget);
```

The `setSceneRect` method sets the coordinates of the drawing area. Then this view is added to a horizontal layout and the layout to widget. This widget is added to central widget.

5 Future Work

The usability of the OMNotebook can be further enhanced with an equation and symbol editor for writing mathematical equations.

Animations and more interactive geometries are also on the wish list of desired features. The user can then play with the fundamental axioms and theorems in programmable geometries.

6 Conclusions

In this paper we presented a new functionality for graphical sketching in the OMNotebook. The new functionality is called OMSketch and allows the user to edit and draw shapes and figures within the electronic book. This allows teachers to prepare more pedagogic course material and students to make graphical notes in addition to the current textual ones.

7 Acknowledgements

This work has been supported by EU project Lila and Vinnova in the ITEA2 OPENPROD project. The Open Source Modelica Consortium supports the OpenModelica work.

References

- [1] <http://www.openmodelica.org> [accessed 2011-08-03]
- [2] Peter Fritzson. *Principles of Object-Oriented Modeling and Simulation with Modelica 2.1*, 940 pages, Wiley-IEEE Press, 2004.
- [3] Modelica Association. *The Modelica Language Specification Version 3.2*, May 2010. <http://www.modelica.org>.
- [4] <http://www.qtnokia.com> [accessed 2011-08-12]

Paper 25**Title:** Modeling digestate nitrification

Yanni Qin, Deshai Botheju, Knut Vasdal, Rune Bakke
Telemark University College, Norway

Keywords: ASM 3, cow manure, digestate, nitrification, simulation

A simplified adaptation of Activated Sludge Model no. 3 (ASM 3) is used to simulate a biological nitrification process carried out in a laboratory scale 10 L volume bio-reactor fed anaerobically digested cow manure effluents. Nitrification is applied to enhance the fertilizer quality of such digestates by converting unstable ammonical N into nitrates. This study aims at using the nitrified digestate as an organic fertilizer in greenhouses for ecological food production.

The behavior of the laboratory bio-reactor was closely resembled by the simulations carried out using the ASM 3 adaptation. Despite the fact that ASM 3 model was originally developed for domestic waste water treatment processes, it can successfully be adopted for simulating the digestate nitrification, without modifying the values of kinetic and stoichiometric constants. Process simulations carried out using this model facilitate to assess and optimize different process variables such as feed rate, hydraulic retention time, extent of aeration, alkalinity content, etc. Modeling and simulations in this regard can significantly boost the knowledge gain of the study while restricting the costly experimental efforts to the most relevant scenarios. Simulations are also helpful to operate the process at minimum energy consumption and hence at the maximum profitability.

Simulation of digestate nitrification based on cow manure

Deshai Botheju^{1*}, Yanni Qin¹, Knut Vasdal²
Rune Bakke¹

¹Telemark University College, Faculty of Technology, P.O. Box 203, N-3901, Porsgrunn, Norway
(*e-mail: Deshai.Botheju@hit.no).

²Lukseffjellvien 507, 3721, Skien, Norway

Abstract: Activated Sludge Model no. 3 (ASM 3) is used to simulate digestate nitrification carried out in a laboratory scale 13 L bio-reactor fed anaerobically digested cow manure effluents. Nitrification is applied to enhance the fertilizer quality of such digestates through the conversion of unstable ammonical N into nitrates.

Observed behavior of the laboratory bio-reactor is closely resembled by the simulations carried out using ASM 3 model. Despite the fact that ASM 3 was originally developed for domestic wastewater treatment processes, this study confirms that the model can successfully be used for simulating digestate nitrification, without modifying the originally suggested values of kinetic and stoichiometric parameters. Process simulations carried out using this model can facilitate to assess and optimize different process variables such as feed rate, hydraulic retention time, sludge age, extent of aeration and alkalinity content. Modeling and simulations in this regard may significantly boost the knowledge gain of the study while restricting the costly experimental efforts to the most relevant scenarios. Simulations are further helpful to operate the process at minimum energy consumption, hence with enhanced profitability.

Keywords: ASM 3 model, Cow manure, Digestate, Nitrification, Simulation.

1. INTRODUCTION

The use of anaerobically digested manure as a farmland fertilizer is dually affective. While this practice greatly reduces the need for costly synthetic mineral fertilizers (Vu et al., 2007), it does also avoid the release of nutrients as a waste into the environment that often causes serious pollution in natural water bodies mainly through eutrophication (Lægrend et al., 1999; Bernet et al., 2000). During anaerobic digestion, chemically bound nitrogen in organic compounds (such as proteins, amino acids and nucleic acids) is released in ammonical N form (NH₄-N) (Luostarinen et al., 2006). Although the direct spreading of digested (or sometimes raw) manure in farmlands has been the practice until now (Luostarinen et al., 2006; Yamamoto et al., 2006), it is not without several drawbacks. NH₄-N is unstable at above-neutral pH conditions, especially at elevated temperatures (Tchobanoglous et al., 2003); hence nutrient nitrogen can be lost as ammonia gas (NH₃), causing an air pollution problem as well. Direct spreading of such manures in farmlands can further cause severe odors within the immediate surroundings. This is due to the reason that these digestates are often not fully stabilized during the anaerobic process. Contamination of food products with harmful metal toxicants and microorganisms are other issues in some cases of manure spreading in farmlands (Franco et al., 2006; Vu et al., 2007). Recent virulent outbreak of food borne illness caused by *E. coli* bacteria might, according to some media reports, have originated from manure fertilizers. Cattle intestine is a rich

source of various *E. coli* strains including *Escherichia coli* O157:H7 (Trochimchuk et al., 2003) which can cause several gastrointestinal diseases including *hemolytic uremic syndrome* reported in Europe during the summer of 2011.

Biological nitrification can be used to convert unstable NH₄-N into nitrate. Nitrate (NO₃-N) is a stable and easily available N source for plants. Considering the above aspects, it has previously been shown that the use of post-anaerobic nitrification is a useful value addition process for producing high quality, aesthetically sound, odor-neutral and safe organic fertilizers from anaerobic digestates (Botheju et al., 2010). Improved sedimentation, substantial removal of toxic heavy metals, and enhanced hygienization ability of aerobic processes are among the other advantageous outcomes (Botheju et al., 2010). In Norway, anaerobic digesters associated with domestic wastewater are legally bound to incorporate a hygienization unit, often implemented as a micro-aerobic bioreactor, in order to achieve greater pathogen destruction (Botheju and Bakke, 2011). That law does not, however, apply to farm manure handling and biogas reactors. Enhanced sedimentation of particulate matter and self heat generation can be the main reasons leading to efficient pathogen destruction in biological nitrification.

One aim of the current article is to showcase this post anaerobic nitrification concept with the use of digested cow manure from a dairy farm in Norway. The specific aim of the modeling part of the study is to determine if such manure digestate nitrification processes can be adequately modeled

and simulated using the standard Activated Sludge Model no. 3 (ASM 3 – Gujer et al., 1999), without resorting to parameter estimations/modifications. Note that the standard ASM 3 model is originally developed for domestic wastewater treatment processes. The overall objective of this study is to design an efficient nitrification process to convert cow manure digestate into a liquid organic fertilizer which is to be used in greenhouses for ecological food production.

2. EXPERIMENTAL

A semi-UASB type anaerobic digester of 0.2 m³ volume was established in a dairy farm (Skien, Norway) in a pilot project for investigating the feasibility of introducing farm scale biogas generators to the Norwegian farming community. This digester is a hybrid between UASB, anaerobic filter and a gas-lift reactor. The design was based on a laboratory scale model which had been developed in Telemark University College. The pilot reactor was fed semi-continuously the liquid fraction of partially digested (pre-stored) cow manure. The liquid fraction was screened out using a 1.4 mm stainless steel mesh. Feed rate of 20 L/d and a hydraulic retention time of 10 days were used (average figures over a period of time). Operating temperature was 24 °C.

The effluent coming out from the aforementioned pilot biogas reactor was used as the feed substrate for the laboratory scale 12.8 L nitrification reactor used in this study. This bioreactor is made of acrylic and equipped with aeration diffusers at the bottom and a 1.5 L conical settling section at the top which is intended for achieving total biomass retention. The reactor was further equipped with dissolved oxygen (DO) and temperature probes, as well as tube connections for feeding, sampling, effluent removal and recycling. A magnetic stirrer was used at the bottom to ensure intensive mixing and avoid sludge sedimentation. A peristaltic pump (*Ismatec*[®]) together with a timer device was used to feed the manure digestate semi-continuously into the reactor. Reactor temperature was maintained at 26±1 °C (laboratory temperature). The used nitrification inoculum was a mixture of sludge from a nitrifying wastewater treatment facility (ESSO petroleum refinery at *Slagentangen*, Vestfold, Norway), and sludge from another bench scale nitrification reactor operated on a synthetic nutrient feed. Fig. 1 presents a schematic illustration of the digestate nitrification bio-reactor. Feeding pattern of the reactor during an operational duration of 61 days is shown in Table 1. These conditions were imitated during the model simulations.

Analytical

Different N species of NH₄-N, NO₃-N and NO₂-N were analyzed using a Flow Injection Analyzer (*Perstorp Analytical, Alpkem Flow Solution 3000*). This analyzer was connected to *WinFLOW V4* software and an automatic sampler. Further, measurements of pH, alkalinity, chemical oxygen demand (COD), dissolved oxygen, temperature, solids contents (TSS, VSS, TS and VS) were also obtained using standard analytical techniques (APHA, 1989).

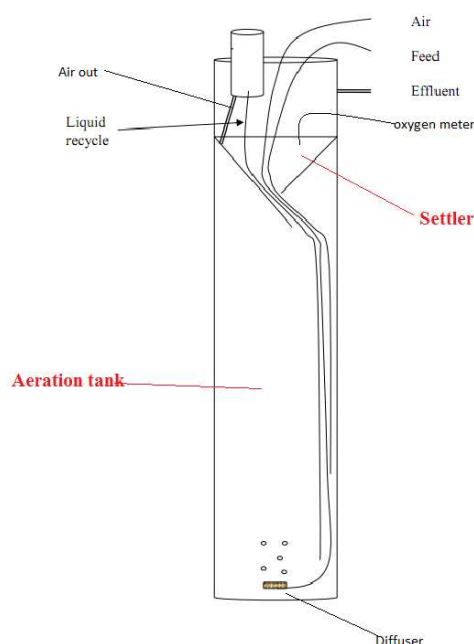


Fig. 1: Schematic view of the nitrification reactor where “air out” goes to a small recycle chamber in which it is separated from liquid that flow back down the liquid recycle line.

Table 1: Feed properties and reactor operating conditions.

Operation period (d)	Flow rate (ml/d)	NH ₄ -N (mg/L)	Alkalinity (M-HCO ₃ ⁻)	TCOD (g/L)	SCOD (mg/L)	pH
1-4	168	1200	180.9	46.5	7535	8.3
5-9	448	1200	180.9	46.5	7535	8.3
10-14	784	1200	180.9	46.5	7535	8.3
16-38	1120	1000	181.2	46.5	7535	8.3
39-46	1120	1280	180.1	42.1	7224	7.9
47-61	1120	1400	230.5	42.1	7224	7.6

3. MODELING AND SIMULATION

The digestate nitrification bioreactor was modeled as a completely mixed reaction zone with a sludge recycling stream to represent the sedimentation section. A full description of the used model is available elsewhere (Botheju et al., 2010). Equations 1-3 represent the basis of the reactor model simulated here. They describe the dynamics of soluble (s) components, particulate (p) components and oxygen, respectively. Since the experimental reactor was operated under presumed complete sludge retention condition, the recycle ratio is given the value of unity for the particulate components.

$$\frac{dC^s}{dt} = \frac{q}{V} (C_{in}^s - C^s) + S^T \cdot r_b \quad (1)$$

$$\frac{dC^p}{dt} = \frac{q}{V} C^p_{in} + S^T \cdot r_b \quad (2)$$

$$\frac{dC_{O_2}}{dt} = \frac{1}{V} [q \cdot C_{in,O_2} + V \cdot k_L a (C_s - C_{O_2}) - q \cdot C_{O_2}] + S^T \cdot r_b \quad (3)$$

The stoichiometric matrix (S^T), the reaction rates matrix (r_b) and the numerical values of all kinetic coefficients were taken from the ASM 3 model (Gujer et al, 1999). Table 2 summarizes some of the main parameter values used in the simulations. The symbolic notations are described in *Nomenclature* section. Influent concentration matrix (C_{in}) was based on the feed analysis shown in Table 1, which includes the time variations also. The oxygen mass transfer coefficient ($k_L a$ –Table 2) is chosen by using the model simulations themselves so that the simulated oxygen concentration of the reactor matches the measured dissolved oxygen values.

Table 2: Some of the principle parameter values used in simulations.

Parameter	Value
Reactor volume, V [L]	12.8
Flow rates, q [ml/d]	168-1120
O_2 saturation coefficient at 25 °C, C_s [mg/L]	8.5
Autotrophic max. growth rate, μ_A , [d^{-1}]	1
NH_4^+ -N saturation for autotrophes, K_{a,NH_4} [g/m^3]	1
O_2 saturation for nitrifiers, K_{a,O_2} [g/m^3]	0.5
HCO_3^- saturation for nitrifiers, $K_{a,alk}$ [mol/m^3]	0.5
Aerobic endogenous respiration rate of autotrophes, b_{a,O_2} [d^{-1}]	0.15
Oxygen mass transfer coefficient, $k_L a$ [d^{-1}]	165

Developed model is simulated using a program script written in Matlab 7.0. The *Ode15s* solver is used for solving the set of ordinary differential equations generated from Eq 1-3. It was found that the *ode45*, another common solver available in Matlab, cannot be used due to the stiffness of this model.

4. RESULTS AND DISCUSSION

4.1 Predictability of ASM 3

Fig. 2 shows the measured and model predicted NO_3 -N and NH_4 -N concentrations (mg/L) under varied input loads. No parameter estimation was attempted except for the oxygen mass transfer coefficient, $k_L a$, which was selected based on observed dissolved oxygen measurements. Aeration efficiency is unique for any given reactor application /geometry. Both the simulations and the experimental measurements indicate a complete conversion of NH_4 -N under the operating conditions tested. This confirms the ability of post anaerobic nitrification to produce a stable nitrate N fertilizer product based on cow manure digestates.

ASM 3 model considers biological nitrification as a single stage process where ammonical N (NH_4 -N) is directly converted to nitrate N (NO_3 -N). In reality, nitrification is basically a two stage process where nitrite (NO_2 -N) is first

generated as an intermediate. This would not, however, make a significant disparity when simulating nitrification systems with minimal nitrite accumulation, like the case being discussed here. Measured NO_2 -N concentrations during the experiment were always below 10 mg/L; and most often were close to 1 mg/L (Fig. 2). In some rare situations, nitrite accumulation might be promoted by applying low oxygen supplies (below 1 mg/L), higher temperatures (above 30 °C), higher pH (above 7.9) and low sludge age conditions (Chuang et al., 2007). ASM 3 in the present form cannot be used for such cases. Modifications have been suggested to include two stage nitrification in ASM 3 (Iacopozzi et al., 2007; Kaelin et al., 2009). Such modifications seem irrelevant for the present application unless there is a need to simulate some process failure cases. It is therefore concluded that the standard ASM 3 is adequate for digested manure nitrification simulations.

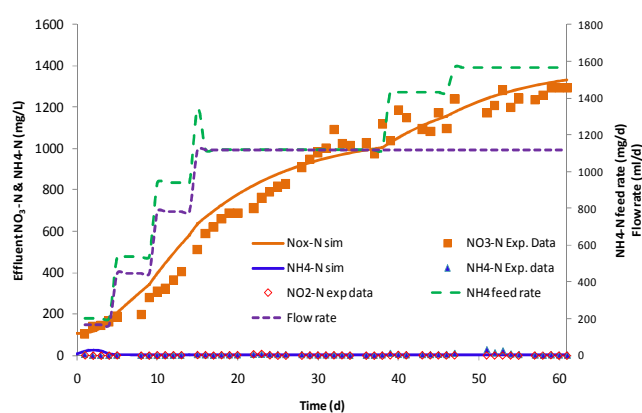


Fig. 2: Simulated and observed behaviour of digestate nitrification.

4.2 Simulations based analysis

Despite the fact that the dissolved oxygen level is above 1 mg/L throughout the experiment (Fig. 3), significant nitrogen loss due to anoxic denitrification activity is noted in simulations (Fig. 3). High concentration of heterotrophic biomass in the system can offsets the effect of the oxygen inhibition function used in the rate equation for anoxic growth in the ASM 3 model. In practical terms, this can be analogue to oxygen depleted conditions occurring inside activated sludge flocs even when the dissolved oxygen concentration of the bulk phase is sufficiently high, leading to a certain level of denitrification activity.

Nitrification reactions need adequate buffer capacity (or alkalinity) to proceed. If the feed stream does not have enough buffer capacity itself, supplementation is essential. According to this study, it is noted that cow manure digestate can be completely nitrified without addition of extra buffer capacity. Neither simulation nor measurements indicated any alkalinity deficiency (Fig. 3), but both showed that the most of the feed alkalinity is consumed for nitrification. Feed digestate has an average alkalinity level of 11.8 g HCO_3^- /L and pH of 8.0. The pH of the nitrified product is about 6.5. These alkalinity and pH values are well suited for the process as well as for the product. Extreme pH values can distort the

soil condition, therefore near neutral pH is preferable. Low and near neutral pH values observed in this study also avoid any significant N loss in NH_3 form. The optimum pH condition for the growth of nitrifiers is reported to be 7.5-8.0 (Willers et al., 1998; Colliver and Stephenson, 2000), but the results of this study show strong nitrification at lower pH. Avoiding the need for additional chemical supplements greatly enhances the process economy and preserves the green /organic nature of the proposed concept.

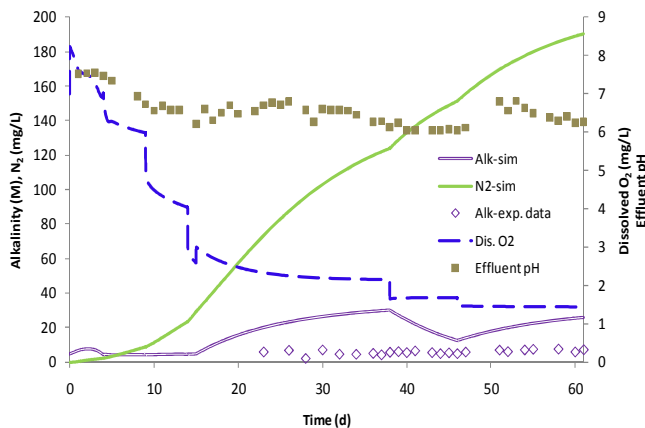


Fig 3. Measured reactor pH, alkalinity (measured and simulated), simulated N_2 and O_2 levels, during 61 d operation.

A simulation of the nitrification reactor until it reaches steady state under the last used feed and operating conditions in the experiment is presented in Fig. 4. The reactor reached steady state after about 75 days. Autotrophic nitrifying biomass concentration (XA) is about 1/8 of the amount of heterotrophic biomass (XH) present in the system, shown by the simulation. Nitrifying organisms are known for their slower growth rate (Bernet et al., 2000; Colliver and Stephenson, 2000). The simulation model used the values of 1 and 2 d^{-1} for the maximum specific growth rates of autotrophic and heterotrophic biomasses, respectively (Table 2).

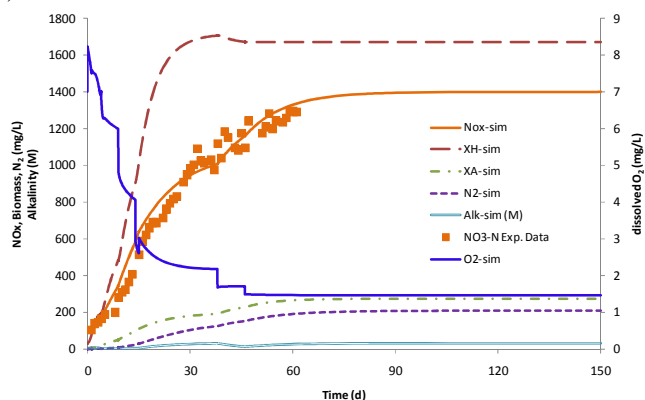


Fig. 4: Simulated steady state performance of the nitrification reactor.

Total active biomass concentration of the reactor is about 1900 mg/L, according to the simulations (Fig. 4). The active biomass is only a fraction of the total MLVSS concentration. It is generally accepted that MLVSS concentration must be

higher than 1500 mg/L to maintain a successful nitrification process (Coffman, 2011). Simulated autotrophic biomass concentration at day 61 suggests a specific nitrification rate of 0.44 g-N/g-XA.d . Reactor operating temperature of $26 \pm 1^\circ\text{C}$ (lab temperature) is within the reported optimum temperature range of $25\text{-}30^\circ\text{C}$ for nitrification (Neufel et al., 1986; Colliver and Stephenson, 2000).

4.3 N mass distribution analysis

The following analysis is performed on the N mass distribution of the reactor, based on measured and simulated figures.

Input fractions of N

Total $\text{NH}_4\text{-N}$ input from feed digestate = 70.3 g
(summation of measured $\text{NH}_4\text{-N}$ feed rates (mg/d) over 61 days)

Total N input associated with suspended solids (Xss)
= total suspended solids input (measured) over 61 days $\times 0.01 = 13 \text{ g}$
(0.01 is the yield of $\text{NH}_4\text{-N}$ due to the hydrolysis of suspended solids; as specified in ASM 3)

Total N input associated with organic soluble substrate (SS)
= total soluble substrate input (measured) over 61 days $\times 0.03 = 13.2 \text{ g}$
(0.03 is the yield of $\text{NH}_4\text{-N}$ (release) due to the uptake of SS; as specified in ASM 3)

Total input of N over the 61 days period = 96.5 g

Output fractions of N

$\text{NO}_3\text{-N}$ produced and taken out from the reactor during 61 days period = 56.4 g (measured and simulated - Fig. 2)

N_2 produced and exited the reactor during 61 days period = 6.4 g (simulated - Fig. 3)

$\text{NH}_4\text{-N}$ and $\text{NO}_2\text{-N}$ fractions in the effluent stream are deemed negligible (Fig. 2).

Total retention of suspended solids is assumed.

Total output of N over the 61 days period = 62.8 g

Accumulated fractions of N

Accumulated $\text{NO}_3\text{-N}$ on day 61 = 17.1 g (measured)

Accumulated N_2 on day 61 = 2.4 g (simulated - Fig. 3)

Accumulated $\text{NH}_4\text{-N}$ in Xss on day 61 = 15.4 g (simulated)

Total accumulation of N in the reactor = 34.9 g

According to this N mass distribution analysis, N balance closes with only 1 % difference between the input fraction and the summation of output fraction and accumulated fraction. It reveals that about 27 % of the input N load comes through suspended solids and soluble organic substrate.

Nearly half of that 27 % is embedded in suspended solids (including biomass cells present in the digestate). Out of the total N input, a 76 % is recovered as NO₃-N; while this amount becomes 105 % if only the NH₄-N input is considered. Generation of considerable amounts of NH₄-N due to the mineralization of solids was reported by other authors too (Meknassi et al., 2000; Botheju et al., 2010). Denitrification consumed 9 % of the total N input. About 15 % of the N input remains embedded in suspended solids. Assimilated N in biomass should represent a considerable portion of this solid embedded N. To what extent N assimilation can be reduced to obtain more nitrate is not clear. Denitrification, however, can be reduced by maintaining higher oxygen levels, at the expense of energy for aeration.

5. CONCLUSIONS

Anaerobically digested cow manure can successfully be nitrified to produce an improved quality stable fertilizer product. The process can be carried out without pH adjustments or buffer capacity supplements.

Activated sludge model no. 3 can be used, without modifications or parameter alterations, to model and simulate nitrification processes based on cow manure digestates.

ACKNOWLEDGEMENT

The study is supported by the Norwegian Ministry of Agriculture. Authors acknowledge various supports by the staff members of Telemark University College, Faculty of Technology.

NOMENCLATURE

C	-concentration
C_s	-O ₂ saturation concentration
$k_L a$	-aeration coefficient
p	-particulate component
q	-flow rate
r_b	-reaction rate vector
S	-stoichiometric matrix
s	-soluble component
S^T	-matrix transpose of S
t	-time
V	-reactor volume

REFERENCES

- APHA, AWWA, and WPCF (1989). Standard methods for examination of water and wastewater, 17th ed., Washington DC.
- Bernet, N., Delgenes, N., Akunna, J. C., Delgenes, J. P. and Moletta, R. (2000). Combined anaerobic aerobic SBR for the treatment of piggyery wastewater. *Water Research*, 34 (2), pp. 611 - 619.

- Botheju, D. and Bakke, R. (2011). Oxygen effects in anaerobic digestion - A review. *Open Waste Management Journal*, 4, pp. 1 - 19.

- Botheju, D., Svalheim, Ø. and Bakke R. (2010). Digestate nitrification for nutrient recovery. *Open Waste Management Journal*, 3, pp. 1 - 12.

- Chuang, H-P., Ohashi, A., Imachi, H., Tandukar, M. and Harada, H. (2007). Effective partial nitrification to nitrite by down-flow hanging sponge reactor under limited oxygen condition. *Water Research*, 41, pp. 295 - 302.

- Coffman, M. (2011). Wastewater systems operator certification study manual, Surface Water Quality Bureau, New Mexico Environment Department, Chapter 13, p. (13-6).

- Colliver, B. B. and Stephenson, T. (2000). Production of nitrogen oxide and dinitrogen oxide by autotrophic nitrifiers. *Biotechnology Advances*, 18, pp. 219 - 232.

- Franco, A., Schuhmacher, M., Roca, E. and Domingo, J. L. (2006). Application of cattle manure as fertilizer in pastureland: Estimating the incremental risk due to metal accumulation employing a multi-compartment model. *Environment International*, 32, pp. 724 - 732.

- Gujer, W., Henze, M., Mino, T. and van Loosdrecht, M. C. M. (1999). Activated sludge model No. 3. *Water Science and Technology*, 39 (1), pp.183 - 193.

- Iacopozzi, I., Innocenti, V., Marsili-Libelli, S. and Giusti, E. (2007). A modified Activated Sludge Model No. 3 (ASM 3) with two-step nitrification denitrification. *Environmental Modelling & Software*, 22, pp. 847 - 861.

- Kaelin, D., Manser, R., Rieger, L., Eugster, J., Rottermann, K. and Siegrist, H. (2009). Extension of ASM 3 for two-step nitrification and denitrification and its calibration and validation with batch tests and pilot scale data. *Water Research*, 43, pp. 1680 - 1692.

- Lægreid, M., Bøckman, O. C. and Kaarstad, O. (1999). Agriculture fertilizers and the environment, CABI publishing in association with Norsk Hydro ASA.

- Luostarinen, S., Luste, S., Valentin, L. and Rintala, J. (2006). Nitrogen removal from on-site treated anaerobic effluents using intermittently aerated moving bed biofilm reactors at low temperatures. *Water Research*, 40, pp. 1607 - 1615.

- Meknassi, Y. F., Tyagi, R. D. and Narasiah, K S. (2000). Simultaneous sewage sludge digestion and metal leaching: effect of aeration. *Process Biochemistry*, 36 (3), pp. 263 - 273.

- Neufel, R., Greenfield, D. J. and Rieder, B. (1986). Temperature cyanide and phenolic nitrification inhibition. *Water Research*, 20 (5), pp. 633 - 642.
- Tchobanoglous, G., Burton, F. L. and Stensel, H. D. (2003). Meltcalf & Eddy, Inc.'s *Wastewater Engineering: Treatment, Disposal, and Reuse*, 4th Edition, Tata McGraw-Hill Publishing company Ltd., pp. 65, 580.
- Trochimchuk, T., Fotheringham, J., Topp, E., Schraft, H. and Leung, K. T. (2003). A comparison of DNA extraction and purification methods to detect *Escherichia coli* O157:H7 in cattle manure. *Journal of Microbiological Methods*, 54, pp.165 - 175.
- Vu, T. K. V., Tran, M. T. and T.T.S. Dang. (2007). A survey of manure management on pig farms in Northern Vietnam. *Livestock Science*, 112, pp. 288 - 297.
- Willers, H. C., Derikx, P. J. L., Have, P. J. W. and Vijn, T. K. (1998). Nitrification limitation in animal slurries at high temperatures. *Bioresource Technology*, 64, pp. 47 - 54.
- Yamamoto, T., Takaki, K., Koyama, T. and Furukawa, K. (2006). Novel partial nitrification treatment for anaerobic digestion liquor of swine wastewater using swim bed technology. *J. Bioscience and Bioengineering*, 102 (6), pp. 497 - 503.

Paper 27**Title:** Trend analysis in dynamic modeling of water treatment

Esko Juuso

University of Oulu, Finland

Keywords: Trend analysis, dynamic models, nonlinear systems, water treatment, linguistic equations, statistical analysis

Temporal reasoning is a very valuable tool to diagnose and control slow processes. Identified trends are also used in data compression and fault diagnosis. Although humans are very good at visually detecting such patterns, for control system software it is a difficult problem including trend extraction and similarity analysis. In this paper, an intelligent trend index is developed from scaled measurements. The scaling is based on monotonously increasing, nonlinear functions, which are generated with generalised norms and moments. The monotonous increase is ensured with constraint handling. Triangular episodes are classified with the trend index and the derivative of it. Severity of the situations is evaluated by a deviation index which takes into account the scaled values of the measurements. Case studies are from water treatment. Modelling and simulation of biological wastewater treatment in pulp and paper industry requires hybrid models since the operating conditions can fluctuate drastically. A compact dynamic simulation is realized with linguistic equation (LE) models. The models consist of two parts: interactions are handled with linear equations, and nonlinearities are taken into account by membership definitions. The same scaling approach is used in trend analysis and modeling. The resulting model has a cascade structure with specialized LE models. The trend analysis is used model selection and model adaptation to activate recursive modeling.

Trend analysis in dynamic modeling of water treatment

Esko K. Juuso* Ilkka Laakso**

* Control Engineering Laboratory
Department of Process and Environmental Engineering
P.O.Box 4300, FI-90014 University of Oulu, Finland
(email: Esko.Juuso@oulu.fi)

** Stora Enso Fine Paper, P.O.Box 196, FI-90101 Oulu, Finland
(email: Ilkka.Laakso@storaenso.com)

Abstract: Temporal reasoning is a very valuable tool to diagnose and control slow processes. Although humans are very good at visually detecting such patterns, for control system software it is a difficult problem including trend extraction and similarity analysis. In this paper, an intelligent trend index is developed from scaled measurements. The scaling is based on monotonously increasing, nonlinear functions, which are generated with generalised norms and moments. The monotonous increase is ensured with constraint handling. Triangular episodes are classified with the trend index and the derivative of it. Severity of the situations is evaluated by a deviation index which takes into account the scaled values of the measurements. Case studies are from wastewater treatment. Modelling and simulation of biological wastewater treatment in pulp and paper industry requires hybrid models since the operating conditions can fluctuate drastically. A compact dynamic simulation is realized with linguistic equation (LE) models, which consist of two parts: interactions are handled with linear equations, and nonlinearities are taken into account by membership definitions. The same scaling approach is used in trend analysis and modelling. The resulting model has a cascade structure with specialized LE models. The LE based trend episodes and deviation indices provide good tools for detecting changes in operating conditions to be used in data and model selection and model adaptation.

Keywords: Trend analysis, dynamic models, nonlinear systems, water treatment, linguistic equations, statistical analysis.

1. INTRODUCTION

In the pulp and paper industry, a huge amount of water flows through different processes. Waste water treatment within Finnish pulp and paper industry is most commonly done in an activated sludge plant, which is a complex biological process, where several physical, chemical, and microbiological mechanisms simultaneously affect purification results. Limits of the emissions are defined by authorities. A lot of process measurements are available, but measurement sets do not include sufficient information on special features of the influent nor on microbial composition of the sludge. Populations of microorganisms are highly important, e.g. sludge bulking cause especially poor treatment efficiency results when biosludge escapes from secondary clarification.

Process simulators are used to test different control methods safely in changing process conditions without disturbing the process. However, a reliable process model is essential for process simulations. For activated sludge plants, modelling is even more demanding since the condition of the biomass need to be modelled as well. Mechanistic models have been two decades in active use. The first Activated Sludge Models (ASM) was presented in 1987 (Henze et al., 1987). However, the use has been limited by complexity of the models. Lindblom (2003) reduced the ASM1 to an

activated sludge plant in pulp and paper industry. The model purpose, defined at the beginning of the procedure, influences the model selection, the data collection and the model calibration. In the model calibration a process engineering approach, i.e. based on understanding of the process and the model structure, is needed. (Gernaey et al., 2004)

Black-box, stochastic grey-box and hybrid models are useful in wastewater applications for prediction of the influent load, for estimation of biomass activities and effluent quality parameters. These modelling methodologies thus complement the process knowledge included in white-box models with predictions based on data in areas where the white-box model assumptions are not valid or where white-box models do not provide accurate predictions. (Jansen et al., 2009)

Many variables are normally measured in a plant, but some of them are strongly cross-correlated. Data-based analysis has been used for variable selection (Teppola et al., 1997; Mujunen et al., 1998; Oliveira-Esquerre et al., 2002). Clustering data for detection of operating conditions has been used in (Heikkinen et al., 2008b) and (Heikkinen et al., 2008a) to get basis for specialised submodels. As the sludge settling properties have remarkable effects on the

treatment results, modelling of the diluted sludge volume index (DSVI) is important (Heikkinen et al., 2008b).

Linguistic equation (LE) modelling methods used in chemical water treatment (Ainali et al., 2002; Joensuu et al., 2004, 2005) have been extended to biological wastewater treatment. The nonlinear scaling approach presented in (Juuso, 2004, 2010b) is the basis of these models. Hybrid models combine mechanistic models (Jansen et al., 2009), data-driven models (Keskitalo et al., 2009; Heikkinen et al., 2009), and intelligent analysers (Juuso et al., 2009). The models are aimed for process control (Halttunen, 2009). The hybrid models introduced in (Juuso, 2009a) provide a good solution. The LE models developed for the intelligent analysers are the basis of the hybrid approach as well. Mechanistic part is mainly devoted to analysing the effects of the fluctuations in the influent wastewater. The models of the clarifiers originate from material balances.

The multimodel LE system consists of three interactive models: load, biomass and treatment. The slow changes of the operability of the biomass, is the heart of the system. The load, nutrients, oxygen and temperature are used in the model of the sludge settling. The biomass population can be assessed by DSVI. The LE models provide continuous smooth transitions between the submodels. The models can be tuned with genetic algorithms (GAs) (Juuso, 1999a, 2004). The improved coding presented in (Juuso, 2009b), which does not require penalty functions, and the new nonlinear scaling methodology based on generalised norms and skewness provides good results for the LE modelling (Juuso, 2010b).

Dynamic models should be adapted to the condition of the biomass, which changes slowly. Trends have earlier used in selecting the submodels in multilevel modelling of a lime kiln (Juuso, 1999a,b). Temporal reasoning is a very valuable tool to diagnose and control slow processes. Manual process supervision relies heavily on visual monitoring of characteristic shapes of changes in process variables, especially their trends. Although humans are very good at visually detecting such patterns, for control system software it is a difficult problem. (Kivikunnas, 1999; Kivikunnas et al., 1996) Intelligent trend indices based on LE models were introduced in (Juuso, 2011a).

This paper applies the intelligent trend analysis in biological wastewater treatment. Working point variables, load nutrition balances and treatment results are analysed to detect changes in operating conditions of an activated sludge plant.

2. TREND ANALYSIS

2.1 Trend episodes

Fault diagnosis is a special area of detecting operating conditions. Typical reasoning systems have three components: a language to represent the trends, a technique to identify the trends, and a mapping from trends to operational conditions (Dash et al., 2003). The fundamental elements are modelled geometrically as triangles to describe local temporal patterns in data (Fig. 1). The elements are defined by the signs of the first and second derivative, respectively. These elements, which are also

known as triangular episodic representations (Cheung and Stephanopoulos, 1990), have their origin in qualitative reasoning and simulation (Forbus, 1984; Kuipers, 1985). An interval-halving scheme to facilitate automatic extraction of temporal features from sensor data in terms of the trend language of primitives was presented in (Dash et al., 2001).

Detecting changes is important for data compression, process control and fault diagnosis. Linear regression combined with fuzzy reasoning can be used in detecting significant changes up or down in process variables (Poirier and Meech, 1993). The episodes shown in Figure 1 provide features for more detailed analysis. Trend extraction methods are based on polynomials, linear segments, wavelets and B-splines, and also neural networks are used. Similarities between trends are analysed for example with sequence matching, decision trees, pattern recognition and hidden Markov models, see (Maurya et al., 2007).

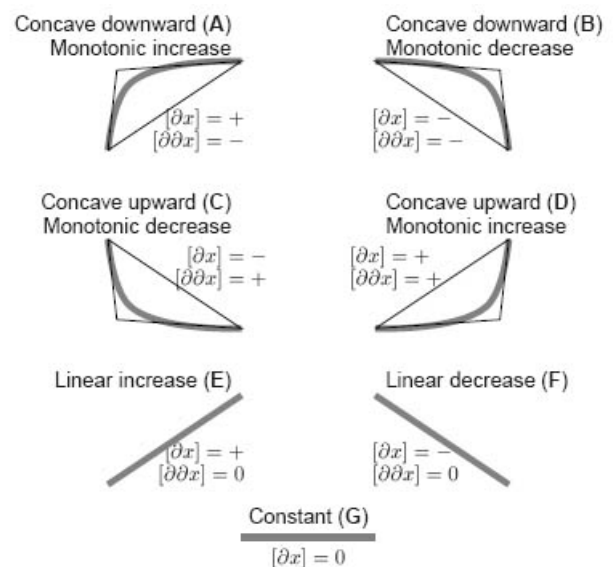


Figure 1. Triangular episodic representation: seven basic types of episodes used for interval description, each episode type is denoted by a letter from the set A, B, C, D, E, F, G (Kivikunnas, 1999).

2.2 Trend extraction

Piecewise linear regression is used for data compression. In the swinging door method, each new measurement value is compared to the active linear trend, and a new trend is started if the value does not fit to the deviation threshold. The trends are reconstructed from the archived spot values by linear interpolation between archived points at the original sampling instants. (Thornhill et al., 2004)

In a top-down approach, a line is fitted to all partitions of signal. The data set halved into two sets if the fitting error is large. The lower cut-off for the window size is two, where the line certainly can be fitted. A complimentary bottom-up approach starts from the finest partition, and adjacent segments are merged to create larger segments with minimised merging cost criteria. Merging is stopped when the minimum merging cost exceeds the maximum allowed error. (Maurya et al., 2007)

Polynomial regression can be used for finding nonlinear episodes. The data set is divided into pieces of equal length and a polynomial is fitted in each segment for uniform sample time (Konstantinov and Yoshida, 1992). Different orders and coefficients correspond to different shapes. The order of the polynomial is increased until desired fitness is achieved or the maximum allowed order is reached.

Time series of measurements contain effects of many distinct contributions: slow trends, different kinds of equipment faults, periodic disturbances and changing sensor noise (Stephanopoulos and Han, 1996). Also outliers and structural breaks need to be analysed to find true trends (Metz, 2010). Generalised norms provide useful tools for analysing different effects (Lahdelma and Juuso, 2008a). Trend removal on the basis of the user defined window (moving average or median) can be included to the pre-processing if the variation around the trend is important for the modelling.

2.3 Similarity analysis

In early research, similarity analysis was based on matching the sequence of primitives or the sign of the first derivative, i.e. if all the signs in both sequences are not the same then the two trends are considered different. A more detailed analysis uses additional information on the signs of the second derivative and the quantitative deviation between the signals. Outliers need to be removed in this analysis. Similarity measures can be based on distance measures, e.g. the Euclidean distance between the data sets. These approaches have been extended to several distance measures, non-uniform time scaling (time-warping) and non-uniform amplitude-scaling. Also stochastic hidden Markov models are used in trend matching. (Maurya et al., 2007) Resolution, fine or coarse, has a strong effect on results (Stephanopoulos and Han, 1996).

2.4 Fuzzy logic

The trend extraction method of Cheung and Stephanopoulos is called qualitative scaling (Cheung and Stephanopoulos, 1990). It generates a hierarchical multiscale structure of trend descriptions over different time scales from process data. Stephanopoulos et al. (Stephanopoulos et al., 1997) have applied the methodology in data analysis of fermentation processes. Their system consists of a wavelet signal decomposition that acts as a noise removing filter, a triangular representation of smoothed process variables, and a search algorithm that uses decision trees comparing Shannon's entropy for each branch in the tree. Trend analysis was applied to a pilot scale fermentation process in (Kivikunnas et al., 1996).

3. DATA ANALYSIS

Generalised moments and norms introduced in (Lahdelma and Juuso, 2008a,b) are the basis of the nonlinear scaling methodology (Juuso, 2009b; Juuso and Lahdelma, 2010) and the new intelligent trend indices (Juuso et al., 2009; Juuso, 2011a).

3.1 Generalised moments and norms

A norm defined by

$$\|^\tau M_\alpha^p\| = (\tau M_\alpha^p)^{1/p} = \left(\frac{1}{N} \sum_{i=1}^N |x_i^{(\alpha)}|^p\right)^{1/p}, \quad (1)$$

where $\alpha \in R$ is the order of derivation, the order of the moment $p \in R$ is non-zero. The signal is measured continuously, and the analysis is based on consecutive equally sized samples. Duration of each sample is called sample time, denoted by τ . The number of signal values $N = \tau N_s$ where N_s is the number of signal values which are taken in a second. This norm, which has the same dimensions as the signal $x^{(\alpha)}$, is defined in such a way that $-\infty < p < \infty$, i.e. the definition includes the l_p norms defined for $1 \leq p < \infty$. This norm introduced in (Lahdelma and Juuso, 2008a) is a Hölder mean, also known as the power mean. The norm values increase with increasing order, i.e. for the l_p and l_q norms holds

$$(\tau M_\alpha^p)^{1/p} \leq (\tau M_\alpha^q)^{1/q}, \quad (2)$$

if $p < q$. The increase is monotonous if all the signals are not equal.

The absolute mean $\|x^{(\alpha)}\|_1$, the rms value $\|x^{(\alpha)}\|_2$, and the absolute harmonic mean, $\|x^{(\alpha)}\|_{-1}$, are special cases where the order is 1, 2 and -1, respectively. When the order $p \rightarrow 0$, we obtain from (1) the absolute geometric mean, $\|x^{(\alpha)}\|_0$. The norm (1) represents the norms from the minimum to the maximum, which correspond the orders $p = -\infty$ and $p = \infty$, respectively. When $p < 0$, all the signal values should be non-zero, i.e. $x \neq 0$. Therefore, the norms with $p < 0$ are reasonable only if all the signal values near the zero are removed. (Lahdelma and Juuso, 2008a, 2010)

The normalised moments,

$$\gamma_k = \frac{E[(X - E(X))^k]}{\sigma_X^k}, \quad (3)$$

are generalised by replacing the expectation value $E(X)$ with the norm (1) as the central value:

$$\gamma_k = \frac{E[(X^{(\alpha)} - \|^\tau M_\alpha^p\|)^k]}{\sigma_X^k}, \quad (4)$$

where σ_X is calculated about the origin, and k is a positive integer. The feature γ_3 is called the coefficient of skewness, or briefly skewness, and the feature γ_4 as the coefficient of kurtosis. The skewness is a measure of asymmetry: $\gamma_3 = 0$ for a symmetric distribution. (Juuso and Lahdelma, 2010)

3.2 Nonlinear scaling in modelling

Membership definitions provide nonlinear mappings from the operation area of the (sub)system to the linguistic values represented inside a real-valued interval $[-2, 2]$, denoted as the linguistic range, see (Juuso, 2004). The membership definitions consist of two second order polynomials: one for negative values, $X \in [-2, 0]$, and one for positive values, $X \in [0, 2]$:

$$\begin{aligned} f_j^- &= a_j^- X_j^2 + b_j^- X_j + c_j, \quad X_j \in [-2, 0], \\ f_j^+ &= a_j^+ X_j^2 + b_j^+ X_j + c_j, \quad X_j \in [0, 2]. \end{aligned} \quad (5)$$

The values X_j are called *linguistic values* because the scaling idea is based on the membership functions of fuzzy

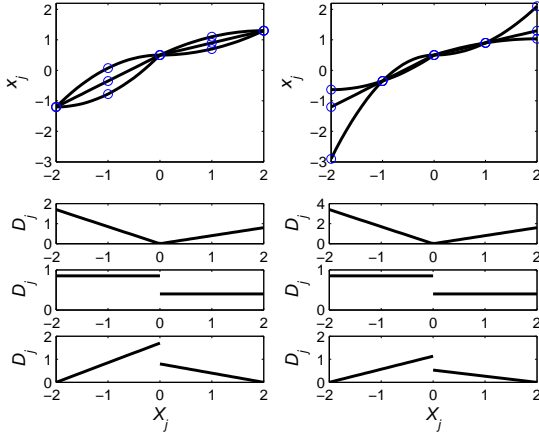


Figure 2. Feasible shapes of membership definitions f_j and corresponding derivatives D_j : coefficients adjusted with core (left) and support (right). Derivatives are presented in three groups: (1) decreasing and increasing, (2) asymmetric linear, and (3) increasing and decreasing.

set systems. The coefficients of the polynomials are defined by the corner points of the feasible range.

As the membership definitions are used in a continuous form, the functions $f_j^-(X_j)$ and $f_j^+(X_j)$ should be monotonous, increasing functions in order to produce realisable systems. In order to keep the functions monotonous and increasing, the derivatives of the functions f_j^- and f_j^+ should always be positive (Fig. 2).

The inequalities for the core and the support are satisfied with

$$\begin{aligned} (c_l)_j - \min(x_j) &= \alpha_j^- (c_j - (c_l)_j), \\ \max(x_j) - (c_h)_j &= \alpha_j^+ ((c_h)_j - c_j) \end{aligned} \quad (6)$$

if the coefficients α_j^- and α_j^+ are both in the range $[\frac{1}{3}, 3]$. Corrections are done by changing the borders of the core area, the borders of the support area or the centre point. Additional constraints for derivatives can also be taken into account. The coefficients of the polynomials can be represented by

$$\begin{aligned} a_j^- &= \frac{1}{2}(1 - \alpha_j^-) \Delta c_j^-, \\ b_j^- &= \frac{1}{2}(3 - \alpha_j^-) \Delta c_j^-, \\ a_j^+ &= \frac{1}{2}(\alpha_j^+ - 1) \Delta c_j^+, \\ b_j^+ &= \frac{1}{2}(3 - \alpha_j^+) \Delta c_j^+, \end{aligned} \quad (7)$$

where $\Delta c_j^- = c_j - (c_l)_j$ and $\Delta c_j^+ = (c_h)_j - c_j$. Membership definitions may contain linear parts if some coefficients α_j^- or α_j^+ equals to one (Fig. 2).

The best way to tune the system is to first define the working point and the core $[(c_l)_j, (c_h)_j]$, then the ratios α_j^- and α_j^+ from the range $[\frac{1}{3}, 3]$, and finally to calculate the support $[\min(x_j), \max(x_j)]$. The membership definitions of each variable are configured with five parameters, including the centre point c_j and three consistent sets: the corner points $\{\min(x_j), (c_l)_j, (c_h)_j, \max(x_j)\}$ are good

for visualisation; the parameters $\{\alpha_j^-, \Delta c_j^-, \alpha_j^+, \Delta c_j^+\}$ are suitable for tuning; and the coefficients $\{a_j^-, b_j^-, a_j^+, b_j^+\}$ are used in the calculations. The upper and the lower parts of the scaling functions can be convex or concave, independent of each other. Additional constraints can be taken into account for derivatives, e.g. locally linear function results if continuous derivative is chosen in the centre point. The continuity requirement limits the ranges of the ratios α_j^- and α_j^+ if the functions are adjusted by moving the centre point (Juuso, 2010b). Inequalities (6) should be satisfied also after changing c_j , which may require iteration.

3.3 Corner points with generalised moments and norms

The value range of x_j is divided into two parts by the central tendency value c_j and the core area, $[(c_l)_j, (c_h)_j]$, is limited by the central tendency values of the lower and upper part. The approach based on (4) is used for estimating the central tendency value and the core area. Derivation is not used for the process measurements, i.e. $\alpha = 0$. The central tendency value is chosen by the point where the skewness changes from negative to positive, i.e. $\gamma_3 = 0$. Then the data set is divided into two parts: a lower part and an upper part. The same analysis is done for these two data sets. The estimates of the corner points, $(c_l)_j$ and $(c_h)_j$, are the points where the direction of the skewness changes. The iteration is performed with generalised norms. Then the ratios α_j^- and α_j^+ are restricted to the range $[\frac{1}{3}, 3]$ moving the corner points $(c_l)_j$ and $(c_h)_j$ or the upper and lower limits $\min(x_j)$ and/or $\max(x_j)$. The linearity requirement is taken into account, if possible.

The nonlinear scaling methodology based on generalised norms and skewness provides good results for the automatic generation of scaling functions (Juuso and Lahdelma, 2010). Sensitivity to small faults and anomalies was increased considerably. The approach was tested with normal, Poisson and Weibull distributions and with two applications of condition monitoring. The scaling approach can be extended to recursive use (Juuso, 2011b).

3.4 Intelligent indices

Trend analysis provides useful indirect measurements for high level control. For any variable j , a *trend index* $I_j^T(k)$ is calculated from the scaled values X_j with a linguistic equation

$$I_j^T(k) = \frac{1}{n_S + 1} \sum_{i=k-n_S}^k X_j(i) - \frac{1}{n_L + 1} \sum_{i=k-n_L}^k X_j(i), \quad (8)$$

which is based on the means obtained for a short and a long time period, defined by delays n_S and n_L , respectively. The index value is in the linguistic range $[-2, 2]$ representing the strength of both decrease and increase of the variable x_j . (Juuso et al., 2009)

The derivative of the index $I_j^T(k)$, denoted as $\Delta I_j^T(k)$, is used for analysing triangular episodic representations (Fig. 1). An increase is detected if the trend index exceed a threshold $I_j^T(k) > \epsilon_1^+$. Correspondingly, $I_j^T(k) < -\epsilon_1^-$ for

a decrease (Fig. 3). These trends are linear if the derivative is close to zero: $-\epsilon_2^- < \Delta I_j^T(k) < -\epsilon_2^+$. Concave upward monotonic increase (D) and concave downward monotonic decrease (B) are dangerous situations. Concave downward monotonic increase (A) and concave upward monotonic decrease (C) mean that an unfavourable trend is stopping. (Juuso, 2011a)

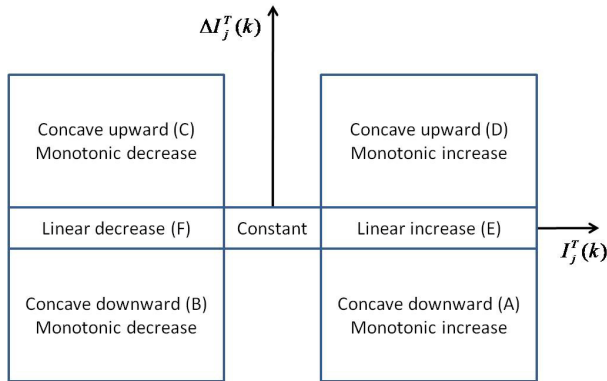


Figure 3. Triangular episodic representations defined by the index $I_j^T(k)$ and the derivative $\Delta I_j^T(k)$.

The trend detection logic is similar to a typical PI type linguistic equation (LE) controller (Juuso, 1999a). The system could be implemented as a fuzzy set system by generating the membership functions (Juuso, 2004). In the present system, fuzzy logic is used only for explaining the progress of the analysis.

Severity of the situation can be evaluated by a *deviation index*

$$I_j^D(k) = \frac{1}{3}(X_j(k) + I_j^T(k) + \Delta I_j^T(k)). \quad (9)$$

This index has its highest absolute values, when the difference to the set point is very large and is getting still larger with a fast increasing speed (Juuso et al., 2009). This can be understood as an additional dimension in Figure 3.

The trend analysis is tuned to applications by selecting the time periods n_L and n_S . Further fine-tuning can be done by adjusting the weight factors w_1 and w_2 used for the indices $I_j^T(k)$ and $\Delta I_j^T(k)$. The thresholds $\epsilon_1^+ = \epsilon_1^- = 0.5$.

4. ACTIVATED SLUDGE PLANT

In biological wastewater treatment, the biological state of the biomass influences on the purification result and subsequent process phases. The model based optimisation and control concept is aimed for detecting process conditions and comparing control actions to improve operation of an activated sludge plant (Fig. 4). On-line measurements and laboratory analysis are combined to build indirect measurements and intelligent dynamic models. Intelligent methods are needed in the models of the aeration basin. Uncertainty handling is an essential part of the models. The concept is tested in connection to industrial purification processes at the pulp mill of Stora Enso Fine Paper in Oulu.

The scaled measurement values can be used as intelligent indices. In this study, they are used in the trend analysis to

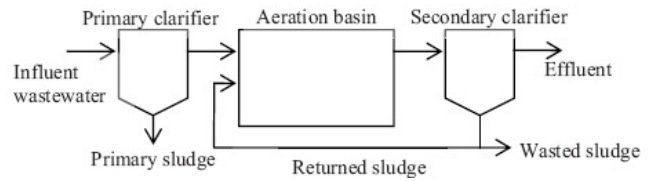


Figure 4. Activated sludge plant.

calculate trend indices to find trend episodes and deviation indices for long periods: $n_S = 30$ days and $n_L = 360$ days. The weight factor $w_2 = 5$ for all variables discussed. The weight factor $w_1 \in [1, 1.5]$ is variable specific.

4.1 Measurements

Measurements were extracted from databases of the process and laboratory data. Influent quality depends on suspended solids (SS), chemical oxygen demand (COD), biological oxygen demand (BOD) and concentrations of nitrogen and phosphorus. In pulp and paper industry, additional nitrogen and/or phosphorus dosing is needed to keep the biomass in good condition. Changes in biomass population may cause sludge bulking which is seen as deterioration of sludge settling properties, described with sludge volume index (SVI) or diluted sludge volume index (DSVI). For example, if there is lack of oxygen or nutrients compared to biomass population, filamentous sludge leads into poor settling properties.

Changes in activated sludge process are slow, especially recovering from the bulking state to normal operation takes time. There are significant seasonal effects, e.g. temperature is typically some degrees lower in winter time. On the other hand, cooling problems may cause temperature rise in summer time. In addition pH and dissolved oxygen profile have obvious effects to the biomass population. Considerable changes of influent quality can be seen in conductivity.

The control variables such as sludge age, COD/nutrient rate, sludge loading, and recycle ratio can be derived from the measurements. The treatment efficiency is assessed by reduction of total nitrogen, total phosphorus, and total COD.

Effective time delays are taken into account, and an additional challenge is that these time delays are varying. Naturally, the delays depend on the flow rates, but also the changes of kinetics have their effects. Moving the points with the number of delays is complicated when the time delays are not constants. A variable time delay based on the flow defines a variable time window $[(T_D)_{min}, (T_D)_{max}]$ for calculating the moving averages of the scaled measurements. The window is essential in this kind of applications, where the process is distributed.

In the data analysis, all these measurements are scaled with the nonlinear scaling approach presented in Section 3.2. Only the measured values are taken into account, since some of the measurements are collected very infrequently. Missing values are handled as not-a-numbers in calculating the norms (1) and moments (4). The calculated operating point variables, the load and the nutrients can be used directly for predicting the treatment results. (Juuso, 2010a)

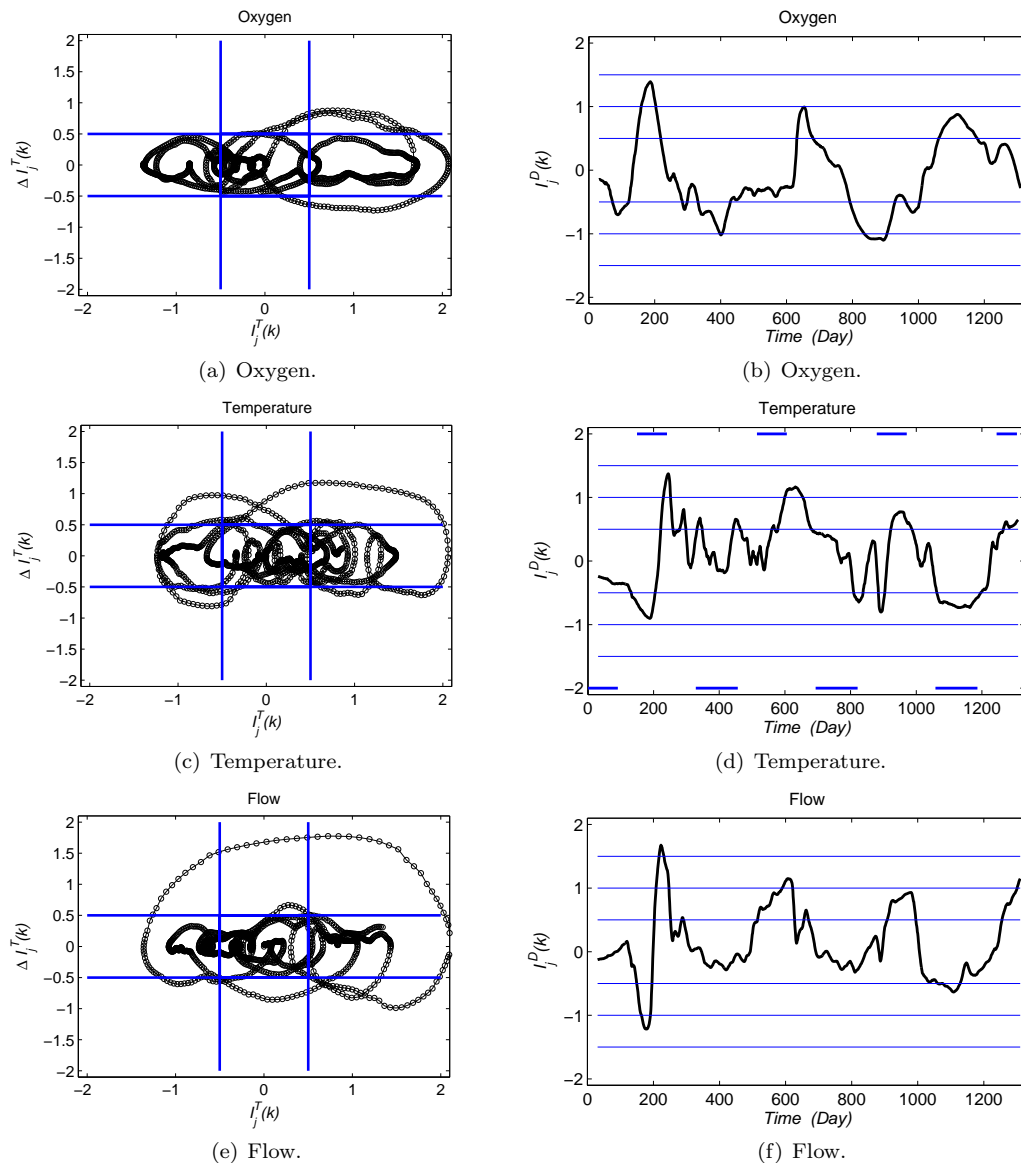


Figure 5. Trend episodes (left) and deviation indices (right) for working point variables.

4.2 Operating conditions

The operating conditions are classified by oxygen, temperature and flow. As the flow comes from the production process, it cannot be made suitable for the treatment process (Fig. 5(f)). The process stoppages can be seen as fast changes of trend episodes (Fig. 5(e)). The temperature should be kept in optimal range. However, in summertime heat exchanger and additional cooler water have not been sufficient to do that, when the flow has been very high. Correspondingly, in winter time the temperature of the basin has decreased when the flow has been on a lower level. Early warning of these temperature changes is provided by the trend episodes (Fig. 5(c)) and the deviation indices (Fig. 5(d)).

The normal levels are the best both for the temperature and the oxygen: too high and low temperatures affect to the biomass; too low oxygen levels are harmful and too high levels mean excess energy consumption. The period of low temperature is during the long stoppage of the process,

and high temperatures are related to high flow in summer time. One period of high oxygen and three periods of low oxygen were detected in (Juuso, 2010a). Increasing oxygen levels are here detected with the trend episodes (Fig. 5(a)) and the deviation indices (Fig. 5(b)).

4.3 Load and nutrients

Load and nutrient should be balanced since both an exceptionally high load and excess nutrients cause problems. The data set of three years and eight months starting from January 2005 includes examples of these problems. For most of time during the first year the feed of nutrients was on a high level, and then it was decreased to a low level during the second year (Juuso, 2010a). During the first autumn, there was a high peak of nutrient feed period of high nutrient feed when the load was fairly low. The nutrient feed returned to normal by the spring. However, later the load was strongly increased, which have caused an opposite situation. Changes of load levels are early detected with the trend episodes (Fig. 6(c)) and the deviation indices

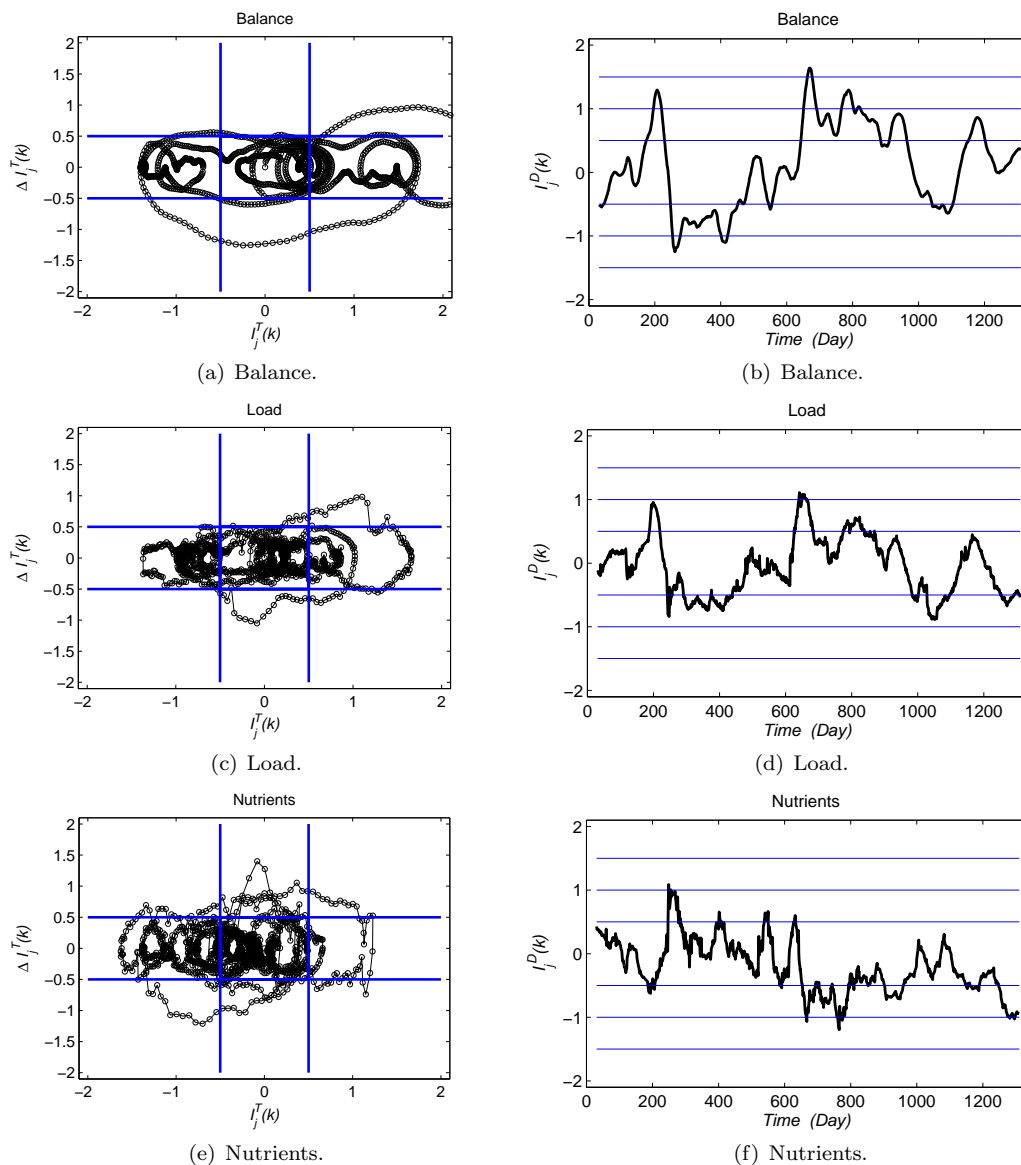


Figure 6. Trend episodes (left) and deviation indices (right) for load and nutrients balance.

(Fig. 6(d)). Corresponding changes of the nutrition levels are seen in Figures 6(e) and 6(f).

Averages obtained from longer time periods have been used in calculating the load nutrients balance. The changes of the balance are clearly seen in the deviation index (Fig. 6(a)): the low levels detected when $250 < t < 450$ were corrected before $t = 600$, but after that the increase of the load was not balanced when $630 < t < 680$. Too low nutrition levels were kept until $t = 950$. Better results were obtained only when the load went down.

4.4 Treatment results

Treatment results are here analysed by comparing the COD reduction and DSVI values: the deviation index should be high for the COD reduction and low for the DSVI. The load and the nutrients should be balanced, i.e. the difference of the load and nutrient level should be close to zero (Fig. 6(b)). Too high nutrient level compared to the load causes poor settling seen as an increase of the DSVI,

which continues as an oscillating behaviour when $250 < t < 480$ (Fig. 7(d)). The treatment result is on the normal level, but the deviation index already indicates reduced performance (Fig. 7(b)). The treatment result improves when the nutrient feed corresponds better the load level. Even high flow around $t = 600$ is acceptable if it does not cause considerable increase in temperature, compare Figures 7(b) and 5(f). Very good operation achieved when $480 < t < 620$ and again when $650 < t < 750$. These periods end when the nutrient level becomes lower (Fig. 6(f)).

Generally, too low nutrient level causes problems in settling (Fig. 7(d)). Very good operation is lost, and the biomass gets into a weak condition when the oxygen level goes down (Fig. 5(b)) and the temperature up (Fig. 5(d)). The worst conditions results when also the flow goes up on the third summer: COD reduction is low (Fig. 7(b)) and DSVI high (Fig. 7(d)). Recovering takes a long time although the nutrient load balance and the operating conditions are good. The balance level is high when $t = 940$,

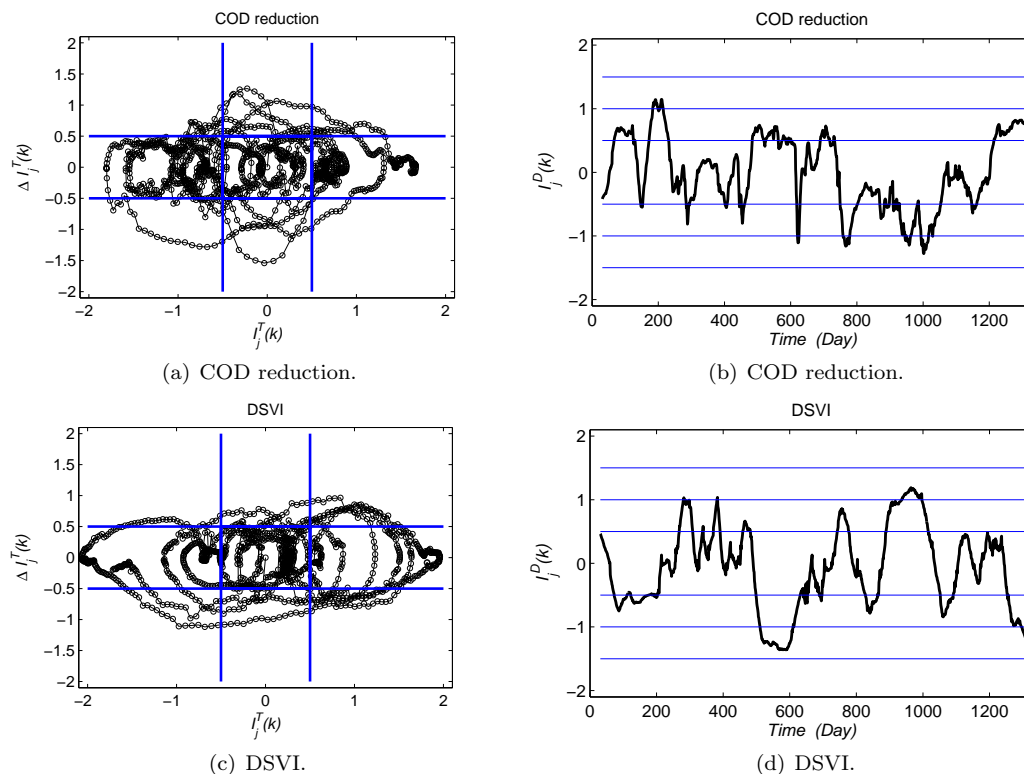


Figure 7. Trend episodes (left) and deviation indices (right) for the treatment results.

but goes gradually to appropriate range when t goes to 1000. However, the worst conditions both in the COD reduction and the DSVI continue the whole period, 60 days. The high load when $t = 1200$ reduces performance. Finally, good treatment results are reached just in the end of the time period (Figs. 7(b) and 7(d)).

Problems of simple data-driven modelling approaches are clearly understood by comparing these results. The operation of the treatment process depends strongly on the condition of the biomass, whose changes are fairly slow as can be seen from the DSVI values (Fig. 7(d)). The variable time delays and modelling of the slow changes of the biomass are necessary to understand the operation. The intelligent analysers presented in (Juuso et al., 2009) are promising tools for on-line detection, and the method of defining the parameters further improves the sensitivity. The trend episodes and the deviations indices provide early warning about the changes.

5. CONCLUSIONS

The LE based trend analysis provides good tools for detecting changes in operating conditions. The nonlinear scaling methodology based on generalised norms and skewness is an important part of the methodology. The analysis demonstrates the problems of simple data-driven modelling in this application. The hybrid structure is essential: load, biomass and treatment need their specialised models where the condition of the biomass is the key part. The data sets for developing these specialised submodels can be chosen with the intelligent trend analysis. In future research, the trend analysis will be used for shorter time periods to develop advanced control solutions. By choosing specific time periods and weight factors the intelligent

trend analysis can be done parallel in several time scales, which are needed for control, fault diagnosis and performance monitoring.

REFERENCES

- Ainali, I., Piironen, M., and Juuso, E. (2002). Intelligent water quality indicator for chemical water treatment unit. In *Proceedings of SIMS 2002 - the 43rd Scandinavian Conference on Simulation and Modelling, September 26-27, 2002, Oulu, Finland*, 247–252. Oulu.
- Cheung, J.T.Y. and Stephanopoulos, G. (1990). Representation of process trends - part I. A formal representation framework. *Computers & Chemical Engineering*, 14(4/5), 495–510.
- Dash, S., Rengaswamy, R., and Venkatasubramanian, V. (2001). A novel interval-halving algorithm for process trend identification. In *Preprints of 4th IFAC Workshop on On-line Fault Detection and Supervision in the Chemical Process Industries, June 7-8, Jeju Island, Korea*, 173–178.
- Dash, S., Rengaswamy, R., and Venkatasubramanian, V. (2003). Fuzzy-logic based trend classification for fault diagnosis of chemical processes. *Computers and Chemical Engineering*, 27, 347–362.
- Forbus, K. (1984). Qualitative process theory. *Artificial Intelligence*, 24, 85–168.
- Gernaey, K.V., van Loosdrecht, M.C.M., Henze, M., Lind, M., and Jørgensen, S.B. (2004). Activated sludge wastewater treatment plant modelling and simulation: state of the art. *Environmental Modelling & Software*, 19, 763–783.
- Halttunen, S. (2009). Model based on-line system in activated sludge process treating pulp and paper wastewaters. In I. Troch and F. Breitenecker (eds.), *6th Vienna*

- Conference on Mathematical Modelling - MATHMOD 2009, February 11-13, 2009, Argesim Report no. 35, 1027–1032. Argesim.*
- Heikkinen, M., Heikkinen, T., and Hiltunen, Y. (2008a). Modelling of activated sludge treatment process in a pulp mill using neural networks. In *The 6th International Conference on Computing, Communications and Control Technologies: CCCT 2008, Orlando, Florida, USA, June 29th - July 2nd 2008.*, 6 pp.
- Heikkinen, M., Latvala, T., Juuso, E., and Hiltunen, Y. (2008b). SOM based modelling for an activated sludge treatment process. In *Tenth International Conference on Computer Modelling and Simulation, EUROSIM/UKSim, Cambridge, UK, April 13, 2008.*, 224–229. The Institute of Electrical and Electronics Engineers IEEE.
- Heikkinen, M., Poutiainen, H., Liukkonen, M., Heikkinen, T., and Hiltunen, Y. (2009). SOM-based subtraction analysis to process data of an activated sludge treatment plant. In I. Troch and F. Breiteneker (eds.), *6th Vienna Conference on Mathematical Modelling - MATHMOD 2009, February 11-13, 2009, Argesim Report no. 35, 1021–1026. Argesim.*
- Henze, M., Jr., C.P.L.G., Gujer, W., Marais, G.V.R., and Matsuo, T. (1987). Activated sludge model no. 1., IAWQ scientific and technical report no. 1. London, UK.
- Jansen, J.L.C., Keskitalo, J., and Juuso, E. (2009). Oxygen uptake rate measurements as a tool for deterministic modelling of pulp and paper wastewater treatment plants. In I. Troch and F. Breiteneker (eds.), *6th Vienna Conference on Mathematical Modelling - MATHMOD 2009, February 11-13, 2009, Argesim Report no. 35, 1008–1013. Argesim.*
- Joensuu, I., Piironen, M., and Juuso, E. (2004). Adaptive feedback controller for dosage of water treatment chemicals. In K. Leiviskä (ed.), *Proceedings of AFNC'04 - the 2nd IFAC Workshop on Advanced Fuzzy/Neural, September 16-17, 2004, Oulu, Finland*, 127–131. Finnish Automation Society, Helsinki.
- Joensuu, I., Piironen, M., and Juuso, E. (2005). Dynamic simulator for dosing of water treatment chemicals. In L. Puigjaner and A. Espuna (eds.), *Proceedings of European Symposium on Computer Aided Process Engineering-15 (Escape-15), Barcelona, Spain, May 29 - June 1, 2005, Computer-aided chemical engineering, 20A*, 301–306. Elsevier, Amsterdam.
- Juuso, E. and Lahdelma, S. (2010). Intelligent scaling of features in fault diagnosis. In *Proceedings The 7th International Conference on Condition Monitoring and Machinery Failure Prevention Technologies, 22-24 June, 2010, Stratford-upon-Avon, UK*, 15 pp. BINDT.
- Juuso, E., Latvala, T., and Laakso, I. (2009). Intelligent analysers and dynamic simulation in a biological water treatment process. In I. Troch and F. Breiteneker (eds.), *6th Vienna Conference on Mathematical Modelling - MATHMOD 2009, February 11-13, 2009, Argesim Report no. 35, 999–1007. Argesim.*
- Juuso, E.K. (1999a). Fuzzy control in process industry: The linguistic equation approach. In H.B. Verbruggen, H.J. Zimmermann, and R. Babuska (eds.), *Fuzzy Algorithms for Control, International Series in Intelligent Technologies*, 243–300. Kluwer, Boston.
- Juuso, E.K. (1999b). Intelligent dynamic simulation of a lime kiln with linguistic equations. In H. Szczerbicka (ed.), *ESM'99: Modelling and Simulation: A tool for the Next Millenium, 13th European Simulation Multiconference, Warsaw, Poland, June 1-4, 1999*, pp. 395–400. SCS, Delft, The Netherlands.
- Juuso, E.K. (2004). Integration of intelligent systems in development of smart adaptive systems. *International Journal of Approximate Reasoning*, 35, 307–337.
- Juuso, E.K. (2009a). Hybrid models in dynamic simulation of a biological water treatment process. In J. Kunovský, P. Hanáček, F. Zboril, Al-Dabass, and A. Abraham (eds.), *Proceedings First International Conference on Computational Intelligence, Modelling and Simulation, 7- 9 September 2009, Brno, Czech Republik*, 30–35. IEEE Computer Society.
- Juuso, E.K. (2009b). Tuning of large-scale linguistic equation (LE) models with genetic algorithms. In M. Kolehmainen (ed.), *Revised selected papers of the International Conference on Adaptive and Natural Computing Algorithms - ICANNGA 2009, Kuopio, Finland, Lecture Notes in Computer Science*, volume LNCS 5495, 161–170. Springer-Verlag, Heidelberg.
- Juuso, E.K. (2010a). Data-based development of dynamic models for biological wastewater treatment in pulp and paper industry. In *SIMS 2010 Proceedings, The 51st Conference on Modelling and Simulation, Oulu, 14-15 October, 2010*, 9 pp.
- Juuso, E.K. (2010b). Data-based development of hybrid models for biological wastewater treatment in pulp and paper industry. In *Proceedings of 7th EUROSIM Congress on Modelling and Simulation, Prague, September 6-10, 2010*, 10 pp.
- Juuso, E.K. (2011a). Intelligent trend indices in detecting changes of operating conditions. In *2011 UKSim 13th International Conference on Modelling and Simulation, DOI 10.1109/UKSIM.2011.39*, 162–167. IEEE Computer Society.
- Juuso, E.K. (2011b). Recursive tuning of intelligent controllers of solar collector fields in changing operating conditions. In S. Bittani, A. Cenedese, and S. Zampieri (eds.), *Preprints of 18th IFAC World Congress, Milano, Italy, August 28 - September 2, 2011*, 12282–12288. IFAC.
- Keskitalo, J., Sorsa, A., Heikkinen, T., and Juuso, E. (2009). Predicting COD concentration of activated sludge plant effluent using neural networks and genetic algorithms. In I. Troch and F. Breiteneker (eds.), *6th Vienna Conference on Mathematical Modelling - MATHMOD 2009, February 11-13, 2009, Argesim Report no. 35, 1014–1020. Argesim.*
- Kivikunnas, S. (1999). Overview of process trend analysis methods and applications. In *Workshop on Applications in Chemical and Biochemical Industry, Aachen, Germany, Sept. 15, 1999*, <http://www.erudit.de/erudit/events/tc-a/erudit-tca-2-Kivikunnas-13050.PDF>, 443–452.
- Kivikunnas, S., Ibatici, K., and Juuso, E.K. (1996). Process Trend Analysis and Fuzzy Reasoning in Fermentation Control. In B.G. Mertzios and P. Liatsis (eds.), *Proceedings of IWISP'96 - Third International Workshop on Image and Signal Processing on the Theme of Advances in Computational Intelligence, 4-7 November*

- 1996, Manchester, UK, 137–140.
- Konstantinov, K.B. and Yoshida, T. (1992). Real-time qualitative analysis of the temporal shapes of (bio)process variables. *American Institute of Chemical Engineers Journal*, 38(11), 1703–1715.
- Kuipers, B. (1985). The limits of qualitative simulation. In *Proceedings of Ninth Joint International Conference on Artificial Intelligence (IJCAI-85)*, 128–136.
- Lahdelma, S. and Juuso, E. (2008a). Signal processing in vibration analysis. In *Proceedings The Fifth International Conference on Condition Monitoring and Machinery Failure Prevention Technologies, 15-18 July 2008, Edinburgh, UK*, 867–878. BINDT.
- Lahdelma, S. and Juuso, E. (2008b). Vibration analysis of cavitation in kaplan water turbines. In *Proceedings 17th IFAC World Congress, Seoul, Korea*, volume 17, 13420–13425. IFAC. [Http://www.ifac-papersonline.net/](http://www.ifac-papersonline.net/).
- Lahdelma, S. and Juuso, E. (2010). Generalised lp norms in vibration analysis of process equipmentss. In *Proceedings The 7th International Conference on Condition Monitoring and Machinery Failure Prevention Technologies, 22-24 June, 2010, Stratford-upon-Avon, UK*, 13 pp. BINDT.
- Lindblom, E. (2003). *Dynamic modelling of nutrient deficient wastewater treatment process. M.Sc. Thesis.* Lund University, Lund, Sweden. TEIE-5175.
- Maurya, M.R., Rengaswamy, R., and Venkatasubramanian, V. (2007). Fault diagnosis using dynamic trend analysis: A review and recent developments. *Engineering Applications of Artificial Intelligence*, 20, 133–146.
- Metz, R. (2010). Filter-design and model-based analysis of trends and cycles in the presence of outliers and structural breaks. *Cliometrica*, 4(1), 51–73.
- Mujunen, S.P., Minkkinen, P., Teppola, P., and Wirkkala, R.S. (1998). Modeling of activated sludge plants treatment efficiency with PLSR: a process analytical case study. *Chemometrics and Intelligent Laboratory Systems*, 41(1), 83–94.
- Oliveira-Esquerre, K.P., Mori, M., and Bruns, R.E. (2002). Simulation of an industrial wastewater treatment plant using artificial neural networks and principal component analysis. *Brazilian Journal of Chemical Engineering*, 19(4), 365–370.
- Poirier, P.J. and Meech, J.A. (1993). Using fuzzy logic for on-line trend analysis. In *2nd IEEE Conference on Control Applications, Vancouver, B.C.*, 83–86.
- Stephanopoulos, G. and Han, C. (1996). Intelligent systems in process engineering. *Computers and Chemical Engineering*, 20(6-7), 743–791.
- Stephanopoulos, G., Locher, G., Duff, M.J., Kamimura, R., and Stephanopoulos, G. (1997). Fermentation database mining by pattern recognition. *Biotechnology and Bioengineering*, 53(5), 443–452.
- Teppola, P., Mujunen, S.P., and Minkkinen, P. (1997). Partial least squares modeling of an activated sludge plant: A case study. *Chemometrics and Intelligent Laboratory Systems*, 38(2), 197–208.
- Thornhill, N.F., Choudhury, M.A.A.S., and Shah, S.L. (2004). The impact of compression on data-driven process analyses. *Journal of Process Control*, 14, 389–398.

TOWARDS MULTI FUEL SOFC PLANTS

Masoud Rokni¹, Lasse Clausen and Christian Bang-Møller
 Technical University of Denmark,
 Dept. Mechanical Engineering,
 Thermal Energy Systems, 2800 Lyngby, Denmark

ABSTRACT

Complete Solid Oxide Fuel Cell (SOFC) plants fed by several different fuels are suggested and analyzed. The plants sizes are about 10 kW which is suitable for single family house with needs for both electricity and heat. Alternative fuels such as, methanol, DME (Di-Methyl Ether) and ethanol are also considered and the results will be compared with the base plant fed by Natural Gas (NG). A single plant design will be suggested that can be fed with methanol, DME and ethanol whenever these fuels are available. It will be shown that the plant fed by ethanol will have slightly higher electrical efficiency compared with other fuels. A methanator will be suggested to be included into the plants design in order to produce methane from the fuel before entering the anode side of the SOFC stacks. Increasing methane content will decrease the needed compressor effect and thereby increase the plant power.

Keywords: SOFC, multi fuel, methanator, methanol, DME, ethanol

INTRODUCTION

The Solid Oxide Fuel Cell (SOFC) is an electro-chemical reactor currently under development by several companies for power-heat generation application. Depending on the type of the electrolyte they are operating at temperature levels of more than about 750°C up to 1000°C. Due to material cost, the lower temperature alternative is now being developed for market entry during this decade. This would also be in advantage for the BoP (Balance of Plants) components.

The biggest advantage of the SOFC in comparison with other types of fuel cells may be in its flexibility in using different types of fuels. However, in planar SOFCs one needs to pre-process most kind of fuels in order to break down the heavier hydro-carbons which may otherwise poison the solid oxide fuel cells. The sulphur content in the fuels must also be removed before entering the anode side of the SOFC. Such pre-processing can be done in two different catalytic reactors operating at different temperature levels indicated by reactor manufacturers.

SOFC – based power plants have been studied for a while and some companies, such as Wärtsilä,

are trying to realize such systems for CHP (Combined Heat and Power) applications; see e.g. [1]. The SOFC is also combined with CC (Combined Cycles) in the literature to achieve ultra high electrical efficiencies, see e.g. [2–3]. Due to the current operating temperature of the SOFC stacks, hybrid SOFC and GT (Gas Turbine) systems have also been studied extensively in the literature, e.g. in [4] for CHP (Combined Heat and Power). Characterization, quantification and optimization of hybrid SOFC–GT systems have been studied by e.g. [5]. In [6] modeling results are compared with measured data for a 220 kW hybrid planar SOFC–GT power plant. Details on design, dynamics, control and startup of such hybrid power plants are studied in [7]. While hybrid SOFC–GT plants have been extensively studied by many researchers, the investigations on combined SOFC and ST (Steam Turbine) are very limited see [8].

Fuel pre-reforming can be done in different reactors such as ASR (Adiabatic Steam Reformer) and CPO (Catalytic Partial Oxidation). The disadvantages of an ASR reactor is that it needs superheated steam during start-up (depending on the operating temperature of the reactor, i.e. 400°C), which is an extremely power consuming

¹Corresponding author: Phone: +45 45255 4124, Fax: +45

procedure. During normal operation steam is available after the anode side of the SOFC stacks, which can be recycled into the system. In a CPO reactor some of the fuel is burned to reach the reformer temperature (exothermic), which in turn decreases the plant efficiency. In this study both ASR and CPO reforming processes are applied for the plant fed by natural gas, which is assumed to be the base cases when comparison with alternative fuels is carried out.

SOFC plants fed by alternative fuels are designed and suggested. The alternative fuels are assumed to be methanol, DME and ethanol which do not produce any CO₂ at consumption side. A methanator is applied in these plants to increase the amount of methane prior to SOFC anode side. Increasing the amount of methane increases the extent of the endothermic reforming reactions and thus decreases the excess air flow which is used to cool down the SOFC stacks.

METHODOLOGY

The results of this paper are obtained using the simulation tool DNA (Dynamic Network Analysis), see [9], which is a simulation tool for energy system analysis. In DNA the mathematical equations include mass and energy conservation for all components, as well as relations for thermodynamic properties of the fluids involved. The program is written in FORTRAN. The component library includes models of various components such as; heat exchangers, burners, turbo machinery, dryers and decanters, energy storages engines, valves, controllers, as well as more specialized components and utility components. The user may also implement additional components. For example fuel cell model, methanator model and reformer model are included in this study as is going to be described below.

Modeling of SOFC

The SOFC model used in this investigation is based on the planar type developed by DTU-Risø and TOPSØE Fuel Cell. The model is calibrated against experimental data in the range of 650°C to 800°C (operational temperature) as described in

[10]. The model matches exactly the experimental data. The outlet temperatures (anode and cathode sides) are assumed to be the same as the operating temperature. The operational voltage (E_{FC}) is expressed as

$$E_{FC} = E_{Nernst} - \Delta E_{act} - \Delta E_{ohm} - \Delta E_{conc} - \Delta E_{offset} \quad (1)$$

where E_{Nernst} , ΔE_{act} , ΔE_{ohm} , ΔE_{conc} , ΔE_{offset} are the Nernst ideal reversible voltage, activation polarization, ohmic polarization, concentration polarization and the offset polarization respectively. The activation polarization is expressed as Butler–Volmer equation (see [11]). The activation polarization is isolated from other polarization to determine the charge transfer coefficients as well as exchange current density from the experiment by curve fitting technique. It follows,

$$\Delta E_{act} = \frac{RT}{(0.001698T - 1.254)F} x \sinh^{-1} \left[\frac{i_d}{2(13.087T - 1.096 \times 10^4)} \right] \quad (2)$$

where R , T , F and i_d are the universal gas constant, operating temperature, Faradays constant and current density respectively. Ohmic polarization depends on the electrical conductivity of the electrodes as well as the ionic conductivity of the electrolyte and can be described as

$$\Delta E_{ohm} = \left(\frac{t_{an}}{\sigma_{an}} + \frac{t_{el}}{\sigma_{el}} + \frac{t_{ca}}{\sigma_{ca}} \right) i_d \quad (3)$$

where $t_{an} = 600 \mu\text{m}$, $t_{el} = 50 \mu\text{m}$ and $t_{ca} = 10 \mu\text{m}$ are the anode thickness, electrolyte thickness and cathode thickness respectively. σ_{an} , σ_{el} and σ_{ca} are the conductivity of anode, electrolyte and cathode respectively.

$$\sigma_{an} = 10^5 \quad (4)$$

$$\sigma_{ca} = \frac{5.760 \times 10^7}{T} \exp \left(-\frac{0.117}{8.617 \times 10^{-5} T} \right) \quad (5)$$

$$\sigma_{el} = 8.588 \times 10^{-8} T^3 - 1.101 \times 10^{-4} T^2 + 0.04679 T - 6.54 \quad (6)$$

Concentration polarization is dominant at high current densities for anode – supported SOFC, wherein insufficient amounts of reactants will be transported to the electrodes and the voltage will

then reduce significantly. Neglecting the cathode contribution (see e.g. [12]), it can be modeled as

$$\Delta E_{conc} = B \left(\ln \left(1 + \frac{p_{H_2} i_d}{p_{H_2O} i_{as}} \right) - \ln \left(1 - \frac{i_d}{i_{as}} \right) \right) \quad (7)$$

where B is the diffusion coefficient which is calibrated against experimental data and found to be,

$$B = \left(0.008039 X_{H_2}^{-1} - 0.007272 \right) \frac{T}{T_{ref}} \quad (8)$$

In the above equations p_{H_2} and p_{H_2O} are the partial pressures for the H_2 and H_2O respectively, while T_{ref} is the reference temperature (1023 K). The anode limiting current density is defined as

$$i_{as} = \frac{2F p_{H_2} D_{bin} V_{an}}{R T t_{an} \tau_{an}} \quad (9)$$

where V_{an} and τ_{an} are the porosity and tortuosity of the anode and are the physical characteristics as 30% and 2.5 μm in the experimental setup. The binary diffusion coefficient is given by

$$D_{bin} = \left(-4.107 \times 10^{-5} X_{H_2} + 8.704 \times 10^{-5} \right) \left(\frac{T}{T_{ref}} \right)^{1.75} \frac{P_{ref}}{P} \quad (10)$$

which is also calibrated against the experimental data. P_{ref} is the reference pressure as 1.013 bar and X_{H_2} is the mass reaction rate of H_2 . Finally the current density i_d is directly proportional to the amount of reacting hydrogen according to the Faraday's law;

$$i_d = \frac{\dot{n}_{H_2} 2F}{A} \quad (11)$$

where \dot{n}_{H_2} is molar reaction rate of H_2 . The area A is the physical property of the cell and is 144 cm^2 .

Modeling of Methanator

The reforming process is assumed to reach chemical equilibrium by minimizing the Gibbs free energy as described in [14]. A similar procedure is also applied for modeling the

methanator. The Gibbs free energy of a gas (assumed to be a mixture of k perfect gases) is given by

$$\dot{G} = \sum_{i=1}^k \dot{n}_i \left[g_i^0 + RT \ln(y_i p) \right] \quad (12)$$

where g_i^0 , R , T and y_i are the specific Gibbs free energy, universal gas constant, gas temperature and molar fraction respectively. Each atomic element in the inlet gas is in balance with the outlet gas composition, which yields the flow of each atom has to be conserved. For N elements this is expressed as

$$\sum_{i=1}^k \dot{n}_{i,in} A_{ij} = \sum_{m=1}^w \dot{n}_{m,out} A_{mj} \quad \text{for } j = 1, N \quad (13)$$

The N elements correspond to H, C and O in this pre-reforming process. A_{mj} is the number of atoms of element j (H, C, O, N) in each molecule of entering compound i (H_2 , CH_4 , CO , CO_2 , H_2O , O_2 , N_2 and Ar), while A_{ij} is the number of atoms of element j in each molecule of leaving compound m (H_2 , CH_4 , CO , CO_2 , H_2O , N_2 and Ar). The minimization of Gibbs free energy can be formulated by introducing a Lagrange multiplier, μ , for each of the N constraints obtained in Eq. (13). After adding the constraints, the expression to be minimized is then

$$\phi = \dot{G}_{tot,out} + \sum_{j=1}^N \mu_j \quad (14)$$

$$\times \left(\sum_{i=1}^k \dot{n}_{i,out} A_{ij} - \sum_{m=1}^w \dot{n}_{m,in} A_{mj} \right)$$

The partial derivation of this equation with respect

to $\dot{n}_{i,out}$ can be writes as

$$\frac{\partial \phi}{\partial \dot{n}_{i,out}} = g_{i,out}^0 + RT \ln(y_{i,out} p_{out}) + \sum_{j=1}^N \mu_j A_{ij} \quad \text{for } i = 1, k \quad (15)$$

At the minimum each of these is then zero. An additional equation is added to make sure that the summation of molar fractions of the outlet gases is to be the unity.

RESULTS

Plants Fed by Natural Gas

The first configuration studied is shown in Fig. 1a. The fuel (NG) is preheated in a heat exchanger before it is sent to a desulfurization unit to remove the sulfur content in the NG. This unit is assumed to be a catalyst, operating at a temperature of 200°C. Thereafter the heavier carbon contents in the NG are broken down in a CPO type pre-reformer catalyst. Before that the fuel must be preheated again to reach to the operational temperature of the CPO catalyst. The CPO catalyst needs additional air which is supplied by a small pump as shown in the figure. This air is also preheated before entering the pre-reformer. It is assumed that the supplied NG is pressurized and therefore no pump is needed for the fuel. The pre-reformed fuel is now sent to the anode side of the SOFC stacks. Due to the exothermal nature of the CPO catalyst, no preheating of the fuel is required after the reformer. The fuel has a temperature of about 650°C before entering the stacks. The operating temperature of the SOFC stacks as well as outlet temperatures is assumed to be 780°C. The used fuel after the SOFC stacks is used to preheat the fuel as well as the air needed for CPO reformer by using two separate heat exchangers.

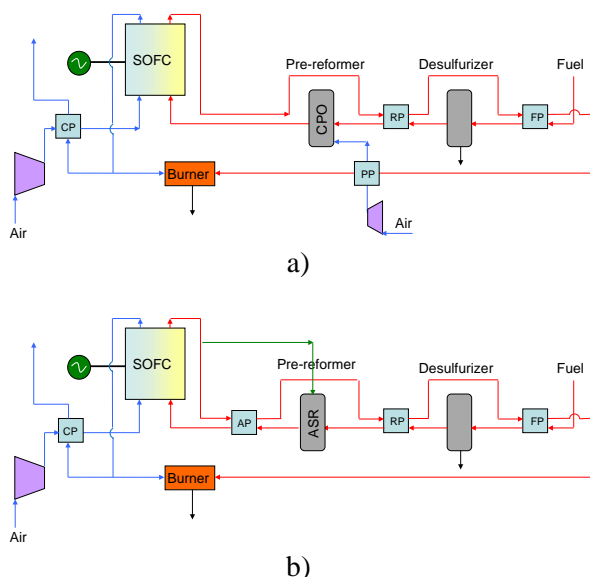


Figure 1. The complete SOFC plant fed by natural gas, a) with CPO reformer b) with ASR reformer.

On the other side, air is compressed in a compressor and then preheated in a recuperator to about 600°C before entering the cathode side of the SOFC stacks. Part of the air after the cathode side is used to preheat the incoming air. Thus it is assumed that the entering temperatures shall not be less than 600°C. Lower entering temperature may shut down the stacks automatically. Since the fuel in the SOFC stacks will not be utilized completely the rest of the fuel together with the air coming out of the cathode side are sent to a burner (catalytic burner) for further burning.

As mentioned earlier the ASR reformer needs super heated steam for operation. Such steam must be supplied to the reformer externally during start-up. However, during normal operation steam is available after SOFC stacks due to reactions of hydrogen and oxygen. Therefore, the stream after the anode side of SOFC is recycled as shown in Fig. 1b. There are three alternatives for such a recirculation unit, a pump, a turbocharger and an ejector. In a real plant, due to high temperature of this stream (more than 700°C) the cost of a pump working will be rather expensive. This is also true for a turbocharger which is working at such mass flows and pressures. Moreover, using an ejector brings up problems associated with the size and dimensioning of the ejector (due to combination of pressure drop and mass flows). Based on these facts and for the sake of simplicity an ejector is used in this investigation. In order to have a proper oxygen-carbon-ratio (~2), 50% of the anode outlet is recycled. Due to endothermic nature of the ASR reformer a heat exchanger is used to raise the temperature of the reformed fuel to 650°C prior to anode side of the SOFC stacks.

The main parameters for the plant are set in table 1. Number of stacks is assumed to be 10 meaning that each stack would produce 1kW electric power with 74 cells. The aim is to produce 10kW net power which is enough for a family house in Scandinavian countries. Thus electric power production by SOFC stacks is set to 10kW.

The pressure drops in the cathode sides as well as the component on the path of air (heat exchanger), is assumed to be 0.005 bars. The pressure drop in the anode side as well as the components in the path of fuel (heat exchangers, desulfurizer and reformer) is assumed to be 0.001 bars. These

values are the setting values for the program, however, pressure drops are a function of channel sizes and mass flows and the channel geometry is not known. Therefore, these values are calculated based on the available data for each channel mass flow and dimensions.

The SOFC plant provides direct current and must be converted to AC through a converter. Further, the efficiency of the DC/AC converter is assumed to be 100%. In reality there would be some losses through the converter and efficiencies of 97% could be assumed for plants of such sizes studied in this investigation. The inlet temperatures of both pre-reformers are assumed to be 400°C. For the CPO case the inlet air to the pre-reformer is thus preheated to this temperature as well.

Set points Parameter	CPO	ASR
Compressor intake T [°C]	25	25
Compressor $\eta_{\text{isentropic}}$	0.60	0.60
Compressor $\eta_{\text{mechanical}}$	0.95	0.95
SOFC cathode inlet T [°C]	600	600
SOFC cathode outlet T [°C]	780	780
SOFC utilization factor	0.80	0.80
SOFC number of cells	74	74
SOFC number of stacks	10	10
Δp in the fuel side [bar]	0.005	0.005
Δp in the air [bar]	0.001	0.001
Fuel inlet temperature [°C]	25	25
Desulfurizer operation T [°C]	200	200
SOFC anode inlet T [°C]	650	650
SOFC anode outlet T [°C]	780	780
Burner efficiency	0.97	0.97

Table 1. Main parameters for design point calculations.

The main calculated parameters are provided in Table 2.

Parameter	CPO	ASR
Net power output [kW]	9.85	9.85
SOFC plant efficiency [%]	48.1	55.8
Fuel consumption [kJ/s]	20.48	17.66
Net power consumption [W]	147.2	152.4
Burner outlet T [°C]	1170.0	951.7

Table 2. Net powers and efficiencies for the plants fed by natural gas.

The plants net powers and thermal efficiencies (based on LHV, Lower Heating Value) are shown in Table 2. The net power output of both plants is similar. The efficiency of the ASR plant is considerably higher than the corresponding CPO plant. The reason is the additional air needed for CPO reformer which is provided by the reformer compressor. This is reflected in higher fuel consumption for the CPO plant. Further, the temperature of the burner for the CPO plant is considerably higher than the ASR plant. This means that the heat generation for the CPO would be more than the ASR plant. This of course is justified by lower plant efficiency.

As mentioned previously, the inlet temperature of both reformers are assumed to be 400°C. However, one could assume other temperatures than this; therefore, Fig 2 is presented to study the plant efficiency versus reformer inlet temperature. As can be seen the plant efficiency with ASR pre-reformer does not change significantly when the inlet temperature is increased to 550°C. On the other hand, the plant efficiency increases when the CPO pre-reformer inlet temperature is increased. As mentioned previously, the reason that the inlet reformers temperatures assumed to be 400°C was that the oxygen-carbon-ratio for the CPO and steam-carbon-ratio for ASR would be about 2, thus carbon deposition is avoided. Note that, increasing CPO inlet temperature means that supplied air to the reformer is decreased, while recycle for ASR kept constant.

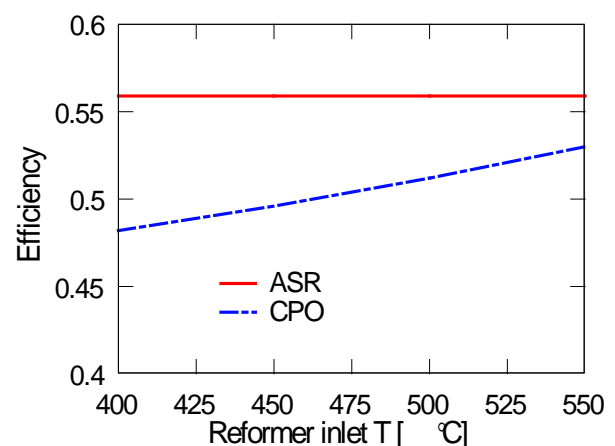


Figure 2. Plant efficiency as function of reformer inlet temperature.

Plants Fed by Alternative Fuels

The alternative fuels to be used here are methanol, ethanol and DME. These fuels can be produced from different sources such as biomass, natural gas and coal. At production side there will be CO₂ emission wherein its amount depends on the production source. In this way emission is centralized which means that the CO₂ emission can be captured. However, such capturing utility at consumer side will be difficult and extremely costly. From now on the phrase alternative fuels refer to methanol, DME and ethanol. Fuel properties are shown in Table 3.

Fuel	Chemical composition	LHV [MJ/kg]	LHV [MJ/L]
Methanol	CH ₃ OH	19.9	15.8
DME	CH ₃ OCH ₃	28.8	19.3*
Ethanol	C ₂ H ₅ OH	28.9	22.8

Table 3. Comparison between the fuels.

*Liquid (above 5 bar).

All these fuels can be directly fed to the anode side of the fuel cell without the need for desulfurizer and pre-reformer, since there is no sulfur and heavier hydrocarbons in these fuels. Thus the complete plant would be much simpler than the corresponding plant fed by natural gas, see Fig. 3. Both the fuel and air are preheated to 600°C before entering the SOFC stacks. In order to increase the oxygen-carbon-ratio some of the fuel is recycled after the anode side of the SOFC stacks.

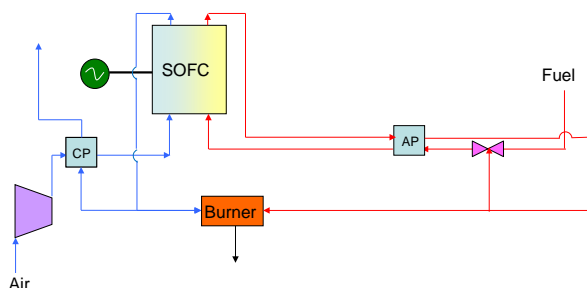


Figure 3. The complete SOFC plant fed by alternative fuels, methanol, DME and ethanol.

In order to have a fair comparison, number of stacks is chosen to be the same as in the case for

natural gas (10 stacks). Other assumptions are also the same as in the case for natural gas as shown in Table 1, such as pressure drops in the heat exchangers and burner efficiency.

Power production, plant efficiency and amount of fuel recycle (after anode) are presented in Table 4. As can be seen from table 3., the power produced by DME and ethanol are almost similar and slightly higher than the case with natural gas, while the power produced by methanol is slightly lower than the case with natural gas.

Fuel	Efficiency [%]	Net Power [kW]	Recycle [%]
Methanol	49.3	9.73	41
DME	50.3	9.94	37
Ethanol	54.1	9.93	38

Table 4. Comparison between the fuels.

The plant fed by ethanol has the best efficiency (~54%) while the plant fed by methanol has the lowest efficiency (~49%).

It might be interesting to mention that the power production by ethanol and DME are rather similar but the efficiency of the plant fed by ethanol is much higher than the case for DME. The reason is that the chemical reactions in the SOFC stacks are exothermic meaning that heat is going to be produced. Therefore, in order to keep the temperature of the SOFC stacks at the same level additional excess airflow is needed to cool down the SOFC stacks. This excess air is provided by the air compressor. For the case fed by DME it requires much higher air flow than for the case fueled by ethanol to cool down the SOFC stacks.

Effect of Methanator

As discussed above the mass flow of the air is considerably higher than the stoichiometry value and the reason is to cool down SOFC stacks and keep their temperature at the desired value. It might then be interesting to discuss possibilities to decrease the air mass flow somehow without affecting the operating temperature of the fuel cells. One possibility is to increase the amount of methane in the fuel prior to the anode side. Due to reforming reactions (methane and water, CO₂) and its endothermic (demanding heat) property then

heat can be absorbed from the cells. Increasing methane content in the fuel will then result in more such reaction, which in turn results in more heat will be absorbed. Thus the air flow will be decreased. This can be achieved by adding an adiabatic Methanator into the plant as shown in Fig. 4. Fuel is preheated to 300°C and then is entered into the Methanator wherein the amount of methane is increased before entering to the anode side of the SOFC stacks. To avoid carbon deposition additional steam (available after SOFC stacks) is recycled and then mixed with incoming fuel as shown in the figure.

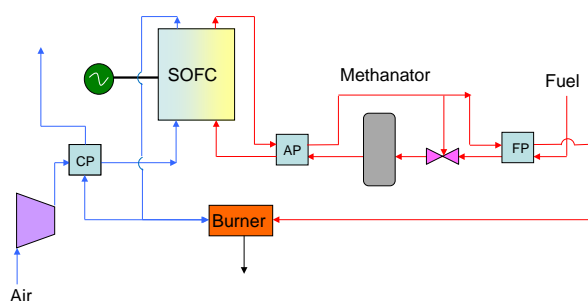


Figure 4. Suggested complete SOFC plant with Methanator when alternative fuels are used.

For the sake of safety a heat exchanger is used after the Methanator in case that the temperature of the fuel is not less than about 600 ~ 650°C. In fact, the temperature after the Methanator is about 600°C, which alleviates the need for the anode pre-heater (AP).

The results for such plant with the adiabatic Methanator is shown in Table 4 in terms of plant efficiency, net power produced and fuel consumption. As can be seen the plant efficiency fed by ethanol does not change considerably whether a Methanator is used or not. However, the plant efficiency fed by DME is increased slightly (by 1 point percentage) when a Methanator is used. Finally, the plant fed by methanol increased by about 2 point percentage when a Methanator is used compared with the corresponding plant without Methanator. Thus it can be concluded that the use of Methanator has a significant effect on plant efficiency and depends on the fuel type and molecular bounds.

Table 5 shows also that the plant fed by methanol needs significantly higher fuel mass flow (about

31% more) than DME and ethanol to provide the same net power of about 10kW.

Fuel	Efficiency [%]	Net Power [kW]	Fuel [kg/h]
Methanol	51.3	10.13	3.5712
DME	51.3	10.13	2.466
Ethanol	54.2	10.14	2.466

Table 5. Comparison between the fuels in a plant with Methanator.

CONCLUSIONS

A SOFC plant with about 10kW net power running by several fuels is studied. In the plant fed by natural gas both ASR and CPO pre-reformers were used to quantify their influence on plant efficiency. It was shown that the plant with ASR reformer had higher efficiency than the plant with CPO pre-reformer, 55.8% versus 48.1%. The reason was that the CPO pre-reformer burned some of the fuel to reach the reactor temperature and therefore, less fuel was available for the SOFC stacks and consequently less power was produced by the plant compared to corresponding ASR plant.

A general plant fed by alternative fuels (methanol, DME and ethanol) was also studied to compare the plants in terms of plant efficiency. It was shown that ethanol had a significantly higher plant efficiency compared with the corresponding plants fed by methanol and DME, 54.1% compared to 49.3% and 50.3%, respectively.

It was also concluded that using an adiabatic Methanator could increase plant efficiency fed by methanol significantly, while its effect on plant efficiency fed by DME was marginal. The use of adiabatic Methanator had no significant effect on plant efficiency when the plant was fed by ethanol. Such conclusions are valid under assumptions made here, such as number of stacks, temperature after the methanator or amount of recycled fuel. Other assumptions may slightly change the conclusions drawn here which are not discussed here.

REFERENCES

- [1] Fontell, E., Kivisaari, T., Christiansen, N., Hansen, J.-B. and Pålsson, J. 2004, "Conceptional study of a 250 kW planar SOFC System for CHP Application", *J. Power Sources*, Vol. 131, pp. 49 – 56.
- [2] Rokni, M., 2003, "Introduction of a Fuel Cell into Combined Cycle: A Competitive Choice for Future Cogeneration", *ASME Cogen – Turbo*, IGTI vol. 8, pp. 255 – 261.
- [3] Riensche, E., Achenbach, E., Froning, D., Haines, M. R., Heidug, W. K., Lokurlu, A., and von Andrian, S., 2000, "Clean Combined-cycle SOFC Power Plant – Cell Modeling and Process Analysis", *J. Power Sources*, Vol. 86, pp. 404 – 410.
- [4] Pålsson, J., Selimovic, A. and Sjunnesson, L., 2000 "Combined Solid Oxide Fuel Cell and Gas Turbine System for Efficient Power and Heat Generation", *J. Power Sources*, Vol. 86, pp. 442 – 448.
- [5] Subramanyan, K. and Diwekar, U. M., 2005 "Characterization and Quantification of Uncertainty in Solid Oxide Fuel Cell Hybrid Power Plants", *J. Power Sources*, Vol. 142, pp. 103 – 116.
- [6] Roberts. R. A. and Brouwer, J. 2006, "Dynamic Simulation of a Pressurized 220 kW Solid Oxide Fuel-Cell – Gas-Turbine Hybrid System: Modeled Performance Compared to measured Results", *J. Fuel Cell Science and Technology*, Vol. 3, No. 1, pp. 18 – 25.
- [7] Rokni, M., Fontell, E., Ylijoki, Y., Tiisonen, O., Hänninen, M., 2005, "Dynamic Modeling of Wärtsilä 5kW SOFC System", Ninth International Symposium on Solid Oxide Fuel cell (SOFC IX), Quebec, Eds. S.C. Singhal and J. Mizusaki, pp. 865 – 875.
- [8] Rokni, M., 2010, "Plant Characteristics of an Integrated Solid Oxide Fuel Cell Cycle and a Steam Cycle", *J. Energy*, Vol. 35, No. 12, pp 4691 – 4699.
- [9] Elmegaard, B, Houbak, N, 2005, "DNA – A General Energy System Simulation Tool," Proceeding of SIMS 2005, Trondheim, Norway.
- [10] Petersen, T.F., Houbak, N. and Elmegaard, B., 2006, "A Zero-Dimensional Model of a 2ND Generation Planar SOFC With Calibrated Parameters", *Int. J. Thermodynamics*, Volume 9, issue 4, pp. 161–168.
- [11] Keegan, K. M., Khaleel M., Chick L. A., Recknagle K., Simner S.P. and Diebler J., 2002, "Analysis of a Planar Solid Oxide Fuel Cell Based Automotive Auxiliary Power Unit", *SAE Technical Paper Series No. 2002-01-0413*.
- [12] Kim, J.W. and Virkar, A.V., 1999, "The Effect of Anode Thickness on the Performance of Anode – Supported Solid Oxide Fuel Cell", *Proc. of the Sixth Int. Symp. On SOFCs*, (SOFC – VI), PV99 – 19, The Electrochemical Society, pp. 830 – 839.
- [13] Elmegaard, B, Houbak, N, 1999, "On the Implementation of Energy Simulators with Emphasis on Chemical Equilibrium Gasifier Models", Proceedings of ECOS'99 (ISBN: 4-9980762-0-5), pp. 258-263, Tokyo.
- [14] Smith J.M., Van Ness, H.C., Abbott, M.M., Introduction to Chemical Engineering Thermodynamics, 7th ed., Boston:McGraw-Hill; 2005.

Paper 29**Title:** Etiology of Rey generator stator core failure and study of its rehabilitation integrity

Kourosh Mousavi Takami
 Pasad Parang Co.

Keywords: generator, core sheet, breakage top teeth, stator

Rey stator core failure reported in Nov. 2010 and generator CB was manually opened. Mitsubishi 1 is a 102 MVA air cooled GE design, operating at 11 kV and is run by gas turbine. The operator observed high temperature in stator and decreased load to reduce it. Temperature stabilized when load reduced to 20% of nominal value. A group of broken core sheets between conductor and air gap was found after precise inspections and removing the rotor. The damage was worst at the armature end (drive end) but extended to the entire length of the core and caused sheets deformed. The area involved was between the tooth tips and two sides of the slot. Core teeth vibration, increasing of negative phase current due to single phase earth fault or breaker failure, unbalanced load, over or under excitation, loosening of core due to tooth vibrations, coating destruction, rod-finger and wedge loosening and etc. can cause core failure in the generator. Vibration of teeth tips is the main supposition of their physical breakage. For evaluation of stator rehabilitation integrity, several parameters such as core arrangement method, strip quality, sheet thickness, coating material and integrity, coil forming method, end core arrangement, pressures on the stator core etc. are studied in theory and by Finite Element Method (FEM). FEM results showed that using of new type sheets with nonhomogenous strips with higher loss in machine stator, created higher back of core, axial and unbalanced fluxes. Axial flux increased end core temperature and caused a limitation on loading. Furthermore, use of different strip with nonhomogenous thickness, permeability and coating at each segment caused unbalanced flux, increased eddy currents, axial flux, end core temperature, bearings vibration etc and is led to reduction generator life.

Etiology of Rey generator stator core failure and study of its rehabilitation integrity

Kourosh Mousavi Takami

PhD in electric power engineering, Simulation and Modeling; pasadinfo@yahoo.com

Pasad Parang Co.

Keywords: generator, core sheet, breakage top teeth, stator

Abstract

Rey stator core failure reported in Nov. 2010 and generator CB was manually opened. Mitsubishi 1 is a 102 MVA air cooled GE design, operating at 11 kV and is run by gas turbine. The operator observed high temperature in stator and decreased load to reduce it. Temperature stabilized when load reduced to 20% of nominal value. A group of broken core sheets between conductor and air gap was found after precise inspections and removing the rotor. The damage was worst at the armature end (drive end) but extended to the entire length of the core and caused sheets deformed. The area involved was between the tooth tips and two sides of the slot.

Core teeth vibration, increasing of negative phase current due to single phase earth fault or breaker failure, unbalanced load, over or under excitation, loosening of core due to tooth vibrations, coating destruction, rod-finger and wedge loosening and etc. can cause core failure in the generator. Vibration of teeth tips is the main supposition of their physical breakage.

For evaluation of stator rehabilitation

integrity, several parameters such as core arrangement method, strip quality, sheet thickness, coating material and integrity, coil forming method, end core arrangement, pressures on the stator core etc. are studied in theory and by Finite Element Method (FEM). FEM results showed that using of new type sheets with nonhomogenous strips with higher loss in machine stator, created higher back of core, axial and unbalanced fluxes. Axial flux increased end core temperature and caused a limitation on loading. Furthermore, use of different strip with nonhomogenous thickness, permeability and coating at each segment caused unbalanced flux, increased eddy currents, axial flux, end core temperature, bearings vibration etc and is led to reduction generator life.

1. Introduction

Large scale generators are used in 70 large combustion [gas (17), steam (15) and combined cycle (38)] power plants (with 215 gas and 95 steam unit of generators) and 24 hydroelectric power stations (48 units of generators) in Iran. Most of them have worked

more than 20 years. Iranian peak load is about 40,000 MW in July-August while total nominal capacities of installed power plants are more than 60,000 MW. Rey, Isfahan, Montazer Ghaem, Tarasht, Be'asat, Neka, Bandar Abbas etc. are older group of power stations that have been serviced more than 30 years.

Iran currently tends to install combined cycle power plants with SIMENS [turbine (frame 5), control system (Teleperm XP), protection (Siprotec 7MU6 series) and AVR (Siprotec)], ANSALDO [generators], ABB [control system, AVR (UNITROL series) & protection (Relion family; REG, RET, REL, REF types)] equipments.

Some of older generators are damaged and repaired several times. For example, Neka generator is damaged by stator core failures. Stator core sheet loosed and vibrated, so finally coating of sheet was destroyed. Due to this phenomenon, the core color is changed to brown. On the other hand, impure hydrogen accelerated damaging non coated sheets in Neka generator. Also, electrical discharges in the tip of damaged teeth make ozone in the gap between stator and rotor. Ozone makes up with hydrogen solution in cooling air and vented from the stator.

Electro Magnetic Core Imperfection Detection (ELCID) is used to monitor of flux distribution in stator cores. With using an automatic motive unit, this equipment slowly moved in to the longitudinal axis of generator to measure of flux distributions in the teeth of stator sheets. External surfaces and slots of stator sheets are monitored and fluxes measured. This mentioned test is performed both in before and after repairing. As know, up to 3 sheets allowed to be short circuited. This can be increased to 5 sheets for it group of cores that have stator yoke length more than 300 mm.

In practice, mica and Araldite glues is used to fill of gaps between loose laminations.

During the 60-70 decade both rotor& gap hydrogen cooled and stator water cooled large scale generators were damaged due to end overheating [1]. High leading power factor in

500 MW CEGB generators damaged cores by melting and some of them lead to restricted long term loading by end overheating problems, reported in 1968. Fault length estimated over than 17 feet.

Because of cost of rehabilitations and repairing, core failures are very expensive. In the other hand, loss of revenue incurs a great loss due to outage of generator is the second problem.

Core failure in Pacificorp Hunter unit I in Nov. 2000 occurred and incurred US\$ 270. Also, about 1 million\$ incurred due to net electricity price that had not been produced for about 6 months.

In one of the generator failure, about 500 kg core sheet melted before conductor coli insulation broken and stator earth fault relay or 95-100% stator protection devices sensed it.

As reported by electricity utilities, most of stator core damage is related to end core overheating problems, increasing of eddy current in core laminations, interlaminar voltages, temperatures, top teeth vibrations etc.

Several machines damaged by core end and back of core and a lot of them damaged by core fault damages.

A number of on-line, off line sensors need to monitor of generator. Periodic off line tests help to preventive maintenance. Current, voltage, vibration, partial discharges, stator winding vibration, air-gas gap flux density, gas humidity, decomposition elements of insulation in the cooling gas, water purity, temperature of core/windings/ gas, and so on are candidate of on line monitoring. DCS is used to monitor and processing of mentioned parameters.

Additionally other periodic off-line test such as electric tests of insulation and core components (HIPOT, MEGGER, RSV, ELCID), visual inspection of commutators and dc field collectors, and so forth are intended.

2. Information source

According to information laid before the Rey Power station, by responsible manager, a forced outage occurred on Mitsubishi Unit 1

on 4th November 2010, in which the generator stator core was severely damaged. The rebuilt stator will be restored to service on Sep. 2011. Author claimed that Rey power station incurred about 23 million USD in net purchased power costs, in relation to the generator outage for 150 days. However, 50-60% of this cost is paid for fuel (gas) and operations.

Mitsubishi 1 is a 102 MVA air cooled GE design, Mitsubishi generator operating at 11 kV. The core is 2.66 m diameter 3.21 m long. The laminations are of 0.45 mm varnished core plate, 1/3 and 2/3 lapped, 10 segments per layer, located on 27 semi-circular insulated rods. Each lamination locates on 3 rods. Several (about 30) insulated tie rods pass through axial holes in the core approximately mid-way between the tooth tips and the back of core. The stator core is split into packets separated by radial cooling ducts.

Flux screen and shunt plates has not been used in this generator.

2.1.Etiology

Unit 32 was operating at 85 MW at time of fault. First indications of trouble were incepted when the stator core RTD alarmed at 105 °C. Later vibration alarm operated because the vibration level had risen to 0.133 mm 5 displacement, which is over the alarm level of 0.127mm. Shortly, afterwards a winding alarm annunciated. The unit tripped manually due to high temperature alarm.

Broken tooth metal spill out over the end plates and cooling ventilation duct. There was some damage at several locations at stator tooth over axial lengths between 20 cm and 110 cm in the form of corrosion, broken and deformed tooth tips and sheets between the stepped core sheets and a through internal surface of stator core.

The causes of the failure have not been determined. But vibrations or I beam lift off caused to loose of core sheets. Vibration origination can be from the: field current deviations, 2nd harmonic due to breaker pole non discrepancy or single or two phases earth fault, etc.

The thru bolt insulation also had core iron

impressions down its length. The bolt was apparently loose enough to vibrate and hit the core hard enough to cut small grooves into the insulation.

Location of initial fault is thought to be 15-25 cm from stator end (drive end), in the area between the stator core tooth tips, upper side of slot and over the supporters. Evidence of the root cause is considered likely to have been destroyed during the failure. Tooth breakage started from drive end of machine. It is related to core assembling by manufacturer. Core is assembled from drive end side and most of pressure is focused on its side.

Case of core failure on the machine with clamp loosening can be an alternative. Therefore, the core failure cannot strictly be said to be unprecedented. Nor could the core failure be claimed to be unpredictable, since, should a through bolt become loose, eventually a core fault would become a distinct possibility.

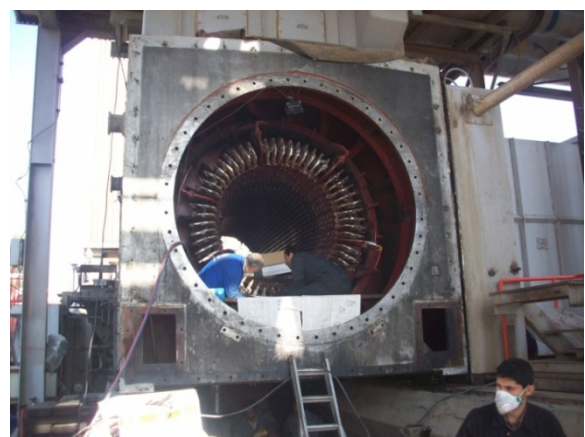
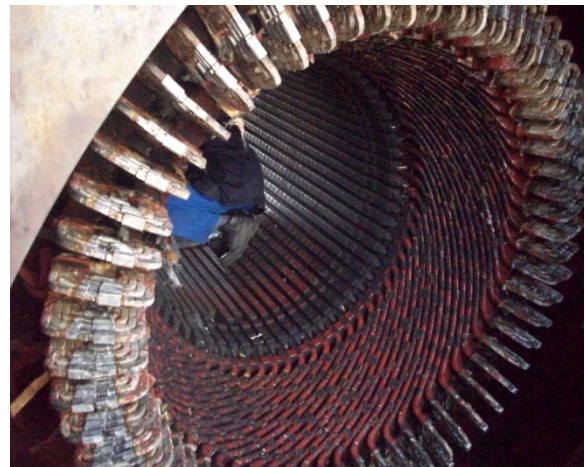




Figure1. Rey 85 MW generator, defects on the tooth of cores.

3. Theoretical analysis

To find problem sources in Rey generator, several cases are investigated. Results of investigation are considered in the following sections.

3.1. Eddy current

Eddy current can be one of reasons of changing color in core sheets of Rey generator [3-18]. Flux rate in the magnetic circuit of stator core is limited by eddy current losses. Thinner laminations and added impurities such as silicon in core sheets minimize eddy current effects. Strip laminations are coated by organic or non organic insulations in core production processes. After strip changing to core with several slots and mounting it into the generator housing, varnish insulation is used before assembling and additional liquid insulations are sprayed to stator after

mounting.

Insulations detritions due to vibrations or mechanical damage caused break down in top teeth and increases local eddy current losses. Local eddy current led to hot spot in the stator. Static ring flux test or HIPOT is used to identify of local hot spot locations. Due to interlaminar breakdown between core sheet surfaces that is resulted to hot spot, is more difficult to identify.

Rey generator has no melted iron, but changed color makes us think about the reason? Is overheating due to eddy current losses?

Stator cores are made in laminated sheets with thickness less than 0.6 mm, this is 0.45 mm in Rey. Each layer in on circle of stator is made within several segments. Cores positioned layer by layer and fixed by rods. Joints offset of each layers are half or one third of the pitch of a segment. By this overlap flux at butt joints can flow in low reluctances path.

3.2. breakdown by external objects

Nut, bolt, washer and something like these unknown metallic pieces rotate in stator-rotor gap. After a long or short time, these external pieces vibrate on the laminations and damage interlaminar insulations. Neighboring sheets physically contacted together and local hotspot created.

Interlaminar voltage is rarely low and as a typical value, for a 0.35 mm sheets is 50 mV for a large two pole machine. Then, if damage extended to several laminations, fault can occur. During routine test or overall of generator and with visual inspection teeth damaged surfaces are detected. In most conditions, sheet insulation can be modified and repaired.

Using electrolyte, sheet edges can be etched by phosphoric acid, after surfaces cleaning, epoxy resin is influenced between sheets by capillary action. Araldite adhesive and mica are used to fill space between laminations.

3.3. Vibration led to breakdown

Vibration of tip teeth is the main suppositions of teeth physically breakage. In core assembly step should be ensure that core fastened tightly and uniformly packed. No tooth and sheets of stator should be free to vibrations. Due to none uniformly laminations in thickness either lamination thickness deviations or coating thickness led to poor packing.

Due to rolling of strip in cold rolling process, middle of strip is thickest and edges are thinnest or vice versa. Depending to kind of roll bending force this thick or thin area can be changed, it can be in the middle or in the corners. According to rolling procedure and standards, this mentioned deviation should not exceed from 6- 10 μm in the cross of strip. Optimal cross of strip is about 1.2 meter and its roll length is more than 5000 meter.

Strip is cut in core building step by punch or laser. Large lamination segments cut so that yoke will be aligned in the rolling direction. Edge of punched area will be thinner than other part. Therefore, teeth tip that are between each punch are thin and the middle of each core is thicker than edge and teeth tips.

These sheets thickness deviations caused a vibration sources when machine is running in nominal or over speeds. Loose tooth laminations are the main source of vibrations. So, if this loose tooth is subjected by radial air cooling flow, it imposes axial forces that tending to separate and break of tooth. After fatigue time has elapsed, tooth is broken and as an external body vibrates in the stator. Broken teeth causes more damage to teeth and it can be visible in the vent duct of cooling system.

Rey generator experienced this phenomenon. A big mass of broken teeth has been gathered in the ventilation side of cooling system.

The maximum vibration of the stator core and core frame should be less than 50 μm peak to peak (unfiltered), with no natural resonance within the frequency ranges about 40–65 Hz and 80–120 Hz for 50 Hz systems. The problems associated with high vibrations are premature stator core inter-laminar and stator

winding insulation wear, and structural problems with the core and frame. Tight core and to have good mechanical coupling between the core and frame maintain generator in low vibration in keybars and other retainers. Low absolute vibrations and low relative vibration between the core and frame, with the two components in phase, is a good indicator that the core and frame structure is sound.

Disassembled sheets in Rey generator cleaned by rough blaster and coated just in one side. It made lamination thickness deviations or coating thickness led to poor packing

3.4. End region overheating

Magnetic flux in the core of stator has two different components, radial and peripheral.

There are peripheral components in the end part of stator core. Axial flux in the stator core tends to make circulating eddy current in the plane of sheets. In large generators, flowing peripheral currents in the stator and rotors create axial flux in the end part of stator core and coils. This flux induces great eddy current in the end part core of stator and core clamping plates.

Mentioned radial and peripheral eddy currents dissipate high value losses in the bottom of slot regions. Because of higher power rating in large generators, these losses are greater.

Several different methods suggested minimizing of eddy current losses:

- To use a flux divertors in the end part of core sections. Conducting screen is one of these devices.
- To increase of reluctance in rotor and stator gap. By employing of this method, end core flux profile will be homogenous.
- To make the core sheets to several segments.
- To increase of rotor teeth resistances for current and losses reduction. Pistoye slots in the rotor teeth elongate the path of eddy current flowing.
- Extra insulations of core sheets.

An appreciate design of end core regions modifies thermal, magnetically and

mechanical stresses. Several instructions have been suggested to decrease of core losses that are titled in the following:

Low loss steel, to use of laser method and low side effect punch and die quality, to remove rough edge after punching, better cleaning after punching, to clean of superficial imperfections of varnish and insulation process, optimization of overlapping and segmentations, decrease of building factors with improvement in core building, to apply of uniform core pressure and to find the optimized position of maintainer bars and etc. Some suggestions such as: uniform pressures, better insulations, optimized punch forces and cutter sharpness can be considered in Rey generator repairing process. Although, did not attend to new core coating thickness and strip losses caused to none uniform packing. Because of that rated pressure of core packing has not been requested by repairing contractor from Mitsubishi (main manufacturer of this machine), none uniform packing crated and teeth vibration is foreseen.

According to site test of generator by manufacturer and utilities in the world, end core interlaminar voltage may be about 40-50 times higher in the main body of core under transient and steady state modes.

Consequently, it can claim that core end very susceptible to attack by defected interlaminar insulations. Change of color and discoloration is one of significant indication of defected sheets. It is seen at the both core ends and behind of slots. Although between surfaces, at the butt joint positions and etc. sign localized overheating.

3.5.Shell leakage flux

Some part of fluxes perfuse to the outer part of coils and tends to link with peripheral component of core frame. Leaked flux oriented by armature magnetic field doesn't compose with core and makes eddy current losses in end core regions. Axial part of core frame contributes with flux as a squirrel cage, return path of flowed flux links trough peripheral parts. Although, this is not a boost that keybars and cores are in contribution to

make a reaction torque along with core frame. Due to lower impedance of core, back of core current, to complete of peripheral path, tend to link via core not with frame path.

When core is subjected with elliptical forces and torque reaction, conduction of back of core can be significant. Key bars movement resulting in consequential arcing at the back of core. To use of copper strip between frame and key bars and connecting those to a circular copper ring at each end of cores, make them as a squirrel cage. In this case, circumferential currents tend to flow through the copper strip rather than frame or cores.

To ensure that currents will always take the back of core path, it is recommended by some of manufacturer that welds the key bars to the back of core. Most usual method to protect of core is to use of semi insulated core. In key bar earthed, earth leakage flow to earth when core to key bar breakdown occurred.

Here a question, which one of the mentioned methods is the best solution.

In most of events, due to core grounding and making of back of core arc, frame weld to core. With presence of back of core arc, not only damage is limited to back of core but also interlaminar insulation is stressed and breakdown will occur. An example in this case, at the bottom of slot, axial vent duct or on the tooth, where there are weakness in insulations, back of core arc may be developed.

If the fed energy to breakdown be sufficient, damage will be significant.

After long times occur numerous interlaminar breakdowns resulted to rise in the core end losses.

3.5.1. End region shield flux

There is no shield flux screen in Rey generator. Here is shown that how can reduce axial and back of core flux effects by this device.

Geoff et al. in IEEE had a serious discussion on the end region shield flux effects. This

section is a glimpse on their research and readers are welcome to their studies.

Main flux is distributed in air gap and main body of stator and rotor, a part of produced flux by end regions is linked from the end cores of stator and rotor. End-windings of the stator and rotor, and the core-end fringe effects increase the end region effects. These effects made stray fluxes that enter to the core of stator in the tooth and just behind the bottom of the slot, in an axial direction and induce eddy currents in the core teeth and the back of core. However, axial flux rapidly turns to the direction of radial flux and adds to it. Because of heating by eddy current losses and stray fluxes, those made with additional fluxes, heating in end cores are increased and form magnetic saturation in the end cores.

In order to interaction variations between stator and rotor magnetic fields, power factor ($\cos\phi$) and generator rotor angle (δ) can change the both mentioned effects.

Two mentioned fluxes oppose each other in the lagging power factor series, and then reduce heating and losses. Unlike in leading power factor series, fluxes add to each other with vector summation and increase losses in end of core regions.

Several techniques are used to compensate of additional created heating such as: special slotting, stepping of core packets, and ventilation methods are fulfilled on the core-ends. Also, special flux shielding or shunting is done to stop excessive flux from entering the core in the axial direction.

To use of thinner core in the end part of stator core set is other plan. Thinner cores in end part have lower losses and more ventilation is made. Thinner core strip and increased ventilation add to the magnetic reluctance of the core-end in the axial direction and help reduce the tendency for flux to penetrate the core-end axially.

Key generator has not been equipped by flux screen to shield of end part. This shield is performed by copper, because of that copper has lower electrical resistance and is a poor conductor against magnetic flux.

Due to induce of eddy current in the end core flux screen, heat in copper shield and retaining ring nose are increased. Since shield is normally isolated from earth and is well cooled, help to reduce the axial flux into the core end and consequently decrease losses on its part. Also, flux shield exposed with axial flux and losses dissipated in this shield. Key generator needs to flux screen and efficient cooling circuit to reduce of heat up in core end part.

Other solution to reduce of core end losses is to split the tooth into smaller sections by split cut in the radial direction, away from the slot bottom. This method reduces losses and heating up by reduction in eddy current effect in the teeth. The slitting depth can be about 15 cm, more or less, depending to end region design. Slits numbers are vary from one to three.

Axial flux is shielded by other method that titled on flux shunt devices. Flux shunt prevent to link axial from the end cores. Flux shunt is made by a highly flux magnetically permeable and laminated arrangement of additional core plate that diverts end-region flux from the core-end, to avoid excessive heating in the stator core iron. End core design and cooling circuit have to be done with consider to flux shunt losses.

Back of core burning is other effect that can occur in turbo or hydro generator machine. With arcing between key bar and core burn the cores. Two shorting straps are welded to all of key bars around the stator end core in the both sides. Squirrel cage is made by those key bars and straps. These straps short any flowing current between each adjacent key bar. This prevents to flow the current through the core, when is flowing from the each key bar to adjacent one.

Flux leakage that pass from the back of core and influenced to key bars are the origin of this current. This is more marked in the core end part because of additional flux.

One of the noticeable reasons that ensure for well flux shielded end core is that end core is not oversaturated in magnetic flux. This is the main reason of back of core burning, particularly in the leading power factors.

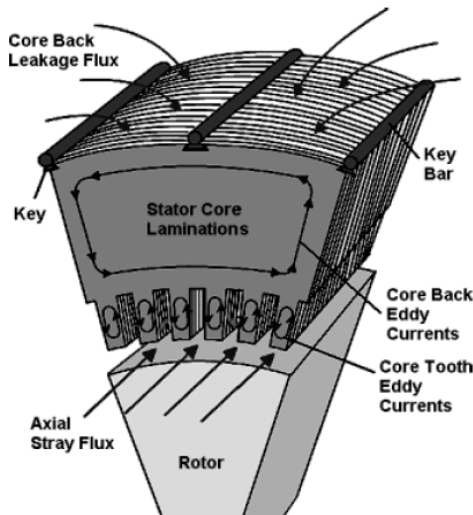


Figure 2. Stator core section [1]

4. Transient disturbances

Because of pole slipping (by changing of two end side of voltage angles or load angles), conductor swing that is lead to line clashing, etc transient condition is incepted and stator currents may well rise to several times rather than to steady state values.

By rotor dampers this over current will damp in short times and core fluxes are not increased. It means change in core flux is not significant for short term short circuits.

Eddy current of rotor damper keep the flux linkages constant.

End windings ampere turns and damping currents in the rotor damper windings supplement and amplify them, because of their same direction. Therefore, axial flux and in the back of core leakage flux at the ends of the core will considerably increase.

Consequently, due to this applied stress by short circuit and over flux in end regions, interlaminar insulation will be more highly stressed and at insulation weakness areas tend to break down.

Stresses make a transient vibration between frame and core and periodic contacts between the core at its ends and the core frame keybars is increased. These phenomena complicate the interlaminar insulation health conditions and end winding and cores stabilities.

5. Capacitance between interlaminated cores.

In the core of end regions small spit marks that are so small and might not be seen, are found. Those are found in the back of core, on the teeth, in the slots in vent ducts and between surfaces, indeed anywhere where there might be points of insulation weakness.

Microscopic spots crowd as spot welds and sometimes extends to several laminations.

End core laminations those are parallel plates and make a capacitor whose are short circuited by core to key bars contacts.

Each time contacts between core to frame is broken, inductive currents flow to open circuited core capacitors. Voltage across the laminations give to raise and potential increased in this local broken part of connections.

Capacitive charging process go on until create a break down in the opened interlaminar core capacitors. May discharge don't occur in first and stored capacitive energy rise to reach to initial inductive energy and oscillatory oscillations that lead to discharge is started.

Base of this dispute established on this rule that, the higher quality the interlaminar insulation, the bigger the increase of stored charge between the laminations before breakdown occurs and the larger the capacity lead to large interlaminar break.

This occurrence can be modeled in laboratory. Two laminated plates put in parallel contacts (as a capacitor), an inductance is serried by this and a battery as supply of this circuit is added in series within model. A switch is included to circuit to control and switching of model. It makes an inductive/capacitive simply model.

Switch is closed and after few minutes is opened; in opening time breakdown occur at the weakest point of insulation.

Insulation is inserted to broken point and repeat the switching, next weakest point is broken again: this time the flash will be slightly brighter, and so on. Consequently, if the energy input is sufficient to produce welding at the point of breakdown, it is done.

6. Coolant gas decomposition

Hydrogen gas is the main coolant in large

scale generators, but not in Rey generator. It subject to the high temperatures of an electric arc disassociates into atomic hydrogen H, which is extremely reactive. This disassociation may provide a possible link between the localized core burning at the ends of machines - including the spitting mentioned above - and a full scale core fault.

Hydrogen arcs are localized [3] and are characterized by a very high rate of heat transfer which cannot be accounted for by conduction, convection or radiation. A process of disassociation happens in which the molecule H_2 is converted into atomic hydrogen H, with the absorption of heat from the arc. Subsequently the hydrogen atoms recombine in the presence of a catalyst, giving up their heat to the catalyst in the process. Metals such as iron are good catalysts and may be heated to incandescence or be melted at some distance from the arc (3-5 cm). Heat transfer rates are about 11 times greater than might be expected from Hydrogen in its molecular form. Large quantities of hydrogen gas are not required to transfer large quantities of heat. The efficiency of the heat transfer process is high (82% 3mm from a metal surface to 55% at 35mm). The energy is transferred preferentially to metal in the vicinity of the arc causing greater damage than might be expected in air.

Whilst the disassociation of hydrogen is well understood and indeed is exploited in the hydrogen arc welding process, it has not been proven definitively to be a factor in core fault propagation. Nevertheless, the core failures in large machines have involved arcing in a hydrogen atmosphere and therefore it is entirely logical to believe that disassociation of hydrogen does play a part.

7. Simulation

COMSOL software has been used to simulate of the presented model [2].

It is often possible to model magnets, generator with magneto statics or AC power electromagnetic. The term "statics" implies that the time rate of change of the magnetic field is slow.

The magneto statics is done for 2D in-plane

and 2D axisymmetric models and 3D as well.

7.1. Governing equations

Start with Ampère's law for static cases:

$$\nabla \times H = J.$$

The current is: $J = \sigma v \times B + J^e$

Where J^e is an externally generated current density and v is the velocity of the conductor.

Using the definitions of magnetic potential, $\nabla \times A = B$.

and the constitutive relationship, $B = \mu_0(H + M)$, you can rewrite Ampère's law as:

$$\nabla \times (\mu_0^{-1} \nabla \times A - M) - \sigma v \times (\nabla \times A) = J^e$$

In the 2D case there are no variations in the z direction, and the current is parallel to the z -axis. Therefore you can add a term $-\sigma \Delta V/L$ to the definition of the current where ΔV is the potential difference over the distance L . This leads to:

$$J = \sigma v \times B + \sigma \frac{\Delta v}{L}.$$

In 2D, that equation simplifies:

$$-\nabla \cdot \left(\mu_0^{-1} \nabla \times A_z - \begin{bmatrix} -M_y \\ M_x \end{bmatrix} \right) + \sigma v \cdot \nabla A = \sigma \frac{\Delta v}{L} + J_z^e$$

The axisymmetric case uses another form of the contribution of the current coming from a potential difference $-\sigma (V_{loop}/(2\pi r))$ because current is present only in the azimuthal direction. The above equation then becomes, in cylindrical coordinates,

$$-\left[\frac{\partial}{\partial r} \right]^T \left[r \mu_0^{-1} \begin{bmatrix} \frac{\partial u}{\partial r} \\ \frac{\partial u}{\partial z} \end{bmatrix} + \mu_0^{-1} \begin{bmatrix} 2 \\ 0 \end{bmatrix} u - \begin{bmatrix} M_z \\ -M_r \end{bmatrix} \right] + r \sigma \left[V \cdot \begin{bmatrix} \frac{\partial u}{\partial r} \\ \frac{\partial u}{\partial z} \end{bmatrix} \right] + 2\sigma V_r u = \sigma \frac{V_{loop}}{2\pi r} + J_\phi^e$$

The dependent variable u is the nonzero component of the magnetic potential divided by the radial coordinate r , that is,

$$u = \frac{A_\phi}{r}$$

The application mode performs this transformation to avoid singularities at the symmetry axis.

The specific power output in a large turbo generator is some 70 MW per meter of active

length of core and the heat content of 1 gram of silicon steel at its melting point is approx 1330 J/gm.

Therefore if the energy output from 1m length of core were to be diverted into a single core hotspot the core could, in theory, melt at a rate of 54 kg/second, ignoring radiation, convection and conduction losses. But in Rey generator, melted core has not been seen and author did not take to account its energy in simulation.

8. Results and discussion

Simulation has been done in COMSOL software. Results are shown in the following figures.

Figure 1 shows magnetic flux in Mitsubishi air cooled generator with 0.45 mm thickness of strips. Figure shows a balance flux in stator and rotor cores. Flux distributed regularly in stator cores and has no extra axial and back of core fluxes. Those are neglected. Electricity conductivity of cores are considered with 1.12×10^7 [S/m] and relative permeability is 4000. 142150 triangles are the mesh results.

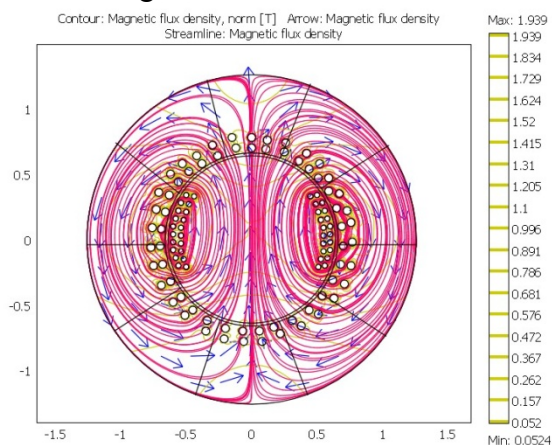


Figure 3. Core magnetic flux density for Mitsubishi 0.45 mm strip.

Figure 4 shows isoflux contours for Mitsubishi generator with 0.45 mm thickness of strips. It shows how flux is concentrated in 4 different parts. It is altering with field winding locations.

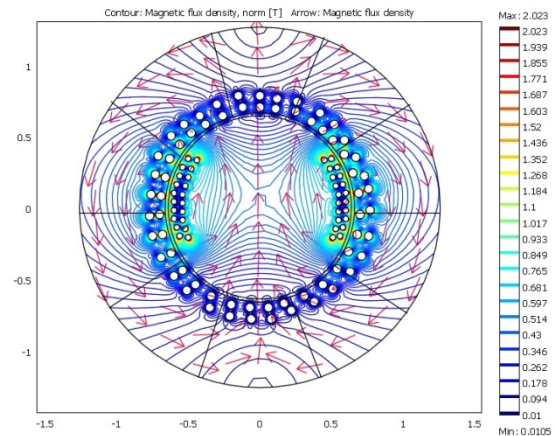


Figure 4. Iso flux contour for Mitsubishi 0.45 mm strips.

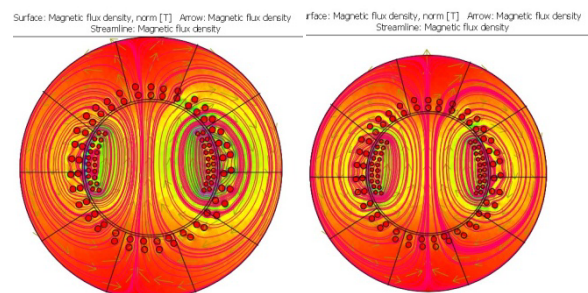


Figure 5. Imbalanced flux due to use of 5 from 10 strip segments (left side) and take turn (one bad and one good) in right have lower permeability.

Figure 5 shows flux distribution when is used different segments in good and bad quality of strips. Right of figure is used by 5 segments by bad and others are good. So second figure (right one), strips set by alternation, one good and one bad. It showed this is better than left figure one in flux balancing and make lower vibration in machine.

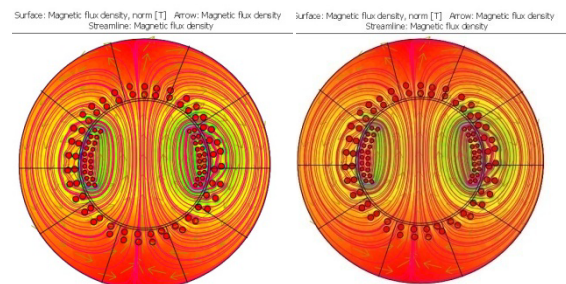


Figure 6. Imbalanced flux due to use of 3 from 10 strip segments (left side) 1 from 10 in right.

Figure 6 show other core setting. Left figure is showing that 3 segments in let of machine are bad and 7 others are good. This changed to 1 bad in left and others with good in right machine.

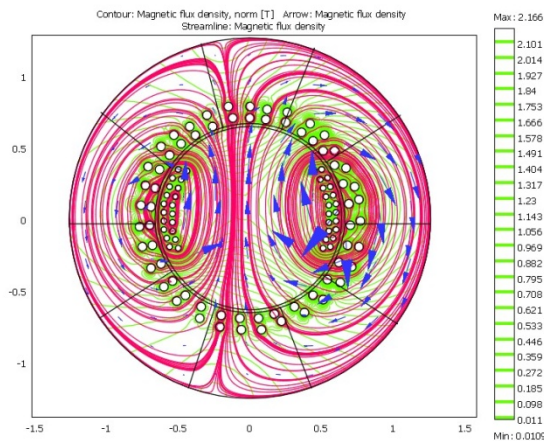


Figure 6. Core magnetic flux density with new and older cores with 4 strips in 0.5 mm and lower permeability and 6 other ones have 0.45 mm thickness.

Flux density show that there are back of core and axial flux in generator, if is used with different thickness in core segments. Those created in absence of flux screen and shunt plate.

If core losses increase from 1.2 w/kg to 4 w/kg at 0.1% of total strips in two different side of generator, back of core flux and axial flux are significantly increased.

Locally eddy current losses increase and higher temperature reduce core life times.

Key generator repair contractor set most of higher thickness and losses with rougher coating at the end of stator cores. It will increase end core temperature and reduce loading.

Figure 7 shows relative permeability versus magnetic intensity. It shows in Mitsubishi stator cores higher flux is created in 10000 of permeability. If stator core quality is decreased, flux density is reduced. Lower flux density leads to lower efficiency of machine.

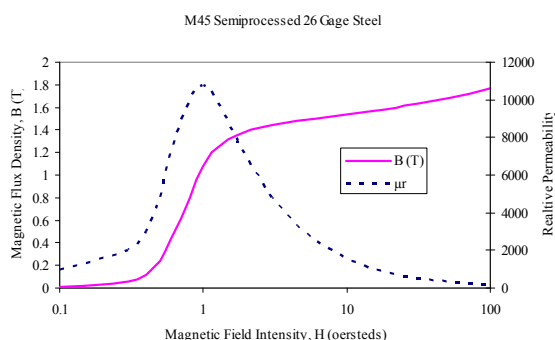


Figure 7. Magnetization curves and relative permeability

It have seen that there are mechanisms capable of producing transiently very high interlaminar voltages and causing localized breakdowns, both in the form of spot welds or meandering breakdowns.

Furthermore it is clear that hydrogen or air gas, the stator coolant on large machines, can act as an extremely efficient heat transfer medium if it disassociates in the presence of an arc.

Bearing in mind the high energy densities present in the stator core and the possibility of the presence of inter-laminar breakdowns causing increased eddy currents, localized heating and further breakdown, it is remarkable how relatively infrequent major core failures are. Generally speaking, design and manufacturing techniques are fit for purpose and only exceptionally does some particular set of circumstances lead to a truly dramatic fault of the kind described in this working paper. One moment's relaxation in preparation of the laminations, a little lack of attention in core building, careless insertion and wedging of the conductor bars and it might be a different story.

9. Conclusions

These observations of incipient core damage on machine, suggest strongly the mechanisms at work in this type of internal core fault to be:

- Tooth vibration due to harmonics.
- Over or under excitation in long times that is led to vibrations.
- Unbalanced flux.
- A loose tie rod that allows transverse vibration of the rod and its insulation under the influence of the rotating radial/circumferential magnetic field in the axial duct.
- Destructions of insulation because of vibration and eventual thinning to the extent that the through bolt makes contact with lamination edges at one or more points along its axial length.
- Given core to frame contacts that correspond with tie rod to lamination contacts,

a circulating radial/axial eddy current with high local losses at tie rod to lamination and lamination to yoke points will result

- Eventually a runaway core fault may be established.

Generally speaking core faults of this type in the body of the core are unlikely in machines where core clamping is by a cantilever arrangement involving the core end plate and the core fingers and where the through bolts are dispensed with. The exception is when a conducting foreign body lodges in one of the axial vent ducts.

But in rehabilitation process that has been done by Iranian repair workshop the following problems are considered:

- Non homogenous sheet distribution in core setting.
- To accumulate of new higher losses w/ kg cores in the end core of generators.
- Non homogenous coating (coat sprayed by car painting nozzles and pickled by hard grains) and one side coat in rehabilitated and repaired sheets.
- Higher losses and thickness in new sheets create the higher magnetic reluctance.
- Unbalanced flux is made in cores.

Author suggests installing a diagnostic to identify of defects in generator, as well. It has to monitor: stator bar vibration, air gap monitoring, and magnetic flux measuring.

10. References

1. Geoff Klempner, Operation and maintenance of large turbo generators, 2004, published by John Wiley & Sons, Inc., Hoboken, New Jersey., Hoboken, New Jersey, Canada.
2. Comsol software manual book, Stockholm, Sweden, 2011.
3. D. Zorbas, Electric Machines-Principles, Applications, and Control Schematics. West, 1989.
4. M. G. Say, Alternating Current Machines. Pitman Publishing, 1978.
5. T. Wildi, Electrical Machines, Drives and Power Systems. Prentice Hall.
6. V. del Toro, Electric Machines and Power Systems. Prentice Hall, 1985.
7. M. Liwschitz-Garik and C. C. Whipple, Electric Machinery, Vols. 1-2. Van Nostrand.
8. A. E. Fitzgerald and C. Kingsley, Electric Machinery. McGraw-Hill, 1971.
9. For a text describing the practical issues related to operation and maintenance of both turbogenerators and hydrogenerators, see Isidor Kerszenbaum, Inspection of Large
10. Synchronous Machines. IEEE-Press, 1996.
11. Tavner, P. J., Anderson A.F.: Generator Core Failures - IEE Proceedings - Electrical Power Applications- November 2005 - Vol 152, Issue 6, p. 1427-1439
12. M. Tari, K. Yoshida, and S. Sekito, "HTC Insulation Technology Drives Rapid Progress
13. of Indirect-Cooled Turbo Generator Unit Capacity," /Toshiba Corp., and R. Brutsch, J. Allison, and A. Lutz, IEEE PES 2001 Summer Power Meeting, Vancouver, BC. Von Rolltola Incorp.
14. K. Sedlazeck, W. Adelman, H. Bailly, I. Gahbler, H. Harders, U. Kainka, W. Weiss, B. Scholz, S. Henschel (Germany), R. Chianese, P. Hugh Sam, R. Ward, L. Montgomery (United States) Siemens Power Generation, U. Schuberth, and H. Spies (Germany), "Influence of Customer's Specifications upon Design Features of the EPR Turbogenerator," Framatome Advanced Nuclear Power, CIGRE' 2002, Paris.
15. IEEE/ANSI C50.13 -1989, "Requirements for Cylindrical-Rotor Synchronous Generators."
16. H. Feichtinger, "Case History of a 18Mn-18Cr Retaining-ring Affected by Stress Corrosion Cracks," HFC-Consulting, Zürich (ch); G. Stein and I. Hucklenbroich, VSG Energie- und Schmiedetechnik GmbH, ESSEN (D), EPRI Generator Retaining-Ring Workshop, December 8-9, 1997, Miami, FL.
17. A. G. Seidel, "Surface Indications on 18Mn-18Cr Retaining-ring," Houston Lighting and Power Company, EPRI Generator Retaining-Ring Workshop, December 8-9, 1997, Miami, FL.